



MONASH
University



DOCTORAL THESIS

**Born from binary mergers:
Supernova SN 1987A and R Coronae Borealis
stars**

Athira Menon

Supervisor: Prof. Alexander Heger

Co-Supervisor: Associate Prof. Amanda Karakas

*A thesis submitted in fulfillment of the requirements
for the degree of Doctor of Philosophy*

in the School of Physics & Astronomy

May 25, 2018

Copyright Notice

©Athira Menon

Under the Copyright Act 1968, this thesis must be used only under the normal conditions of scholarly fair dealing. In particular no results or conclusions should be extracted from it, nor should it be copied or closely paraphrased in whole or in part without the written consent of the author. Proper written acknowledgement should be made for any assistance obtained from this thesis. I certify that I have made all reasonable efforts to secure copyright permissions for third-party content included in this thesis and have not knowingly added copyright content to my work without the author's permission.

Declaration of Authorship

I, ATHIRA MENON, hereby declare that this thesis contains no material which has been accepted for the award of any other degree or diploma at any university or equivalent institution and that, to the best of my knowledge and belief, this thesis contains no material previously published or written by another person, except where due reference is made in the text of the thesis.

This thesis includes 1 original paper published in peer reviewed journals, 1 submitted publication and 1 manuscript in press. The core theme of the thesis is ‘products of mergers of binary stars’. The ideas, development and writing up of all the papers in the thesis were the principal responsibility of myself, the student, working within the ‘School of Physics and Astronomy, Monash University’ under the supervision of Prof. Alexander Heger.

The inclusion of co-authors reflects the fact that the work came from active collaboration between researchers and acknowledges input into team-based research.

I have renumbered sections, equations and figures of the published paper in order to generate a consistent presentation within the thesis. In the case of Chapters 2, 3, and 4 my contributions to the work are as summarised in the following table on Page iv.

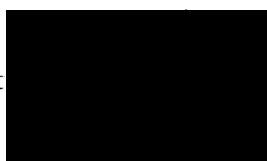
Student signature:



Date: 25th May, 2018

The undersigned hereby certify that the above declaration correctly reflects the nature and extent of the student’s and co-authors’ contributions to this work. In instances where I am not the responsible author I have consulted with the responsible author to agree on the respective contributions of the authors.

Main Supervisor signat



Date: 27 May 2018

Chapter	Publication	Status	Student contribution	Co-authors and contribution	Co-authors, Monash student
2	The quest for blue supergiants: binary merger models for the evolution of the progenitor of SN 1987A	Published in MNRAS, May 2017	75%. Concept, running simulations, analysing results, writing manuscript	Alexander Heger, 25% Concept, analysing results and feedback on manuscript	N
3	Explosions of binary merger progenitors for peculiar Type II supernovae	In press	60%. Concept, contacting authors for data, progenitor models, analysing results, writing manuscript	Victor Utrobin, 35% Explosion simulations, result analyses and, Section 3.2.2 and Figures 3.3-3.8 in manuscript Alexander Heger, 5% Feedback on manuscript	N
4	Low-metallicity CO+He WD post-merger models for RCB stars and their connection to low-density graphite grains	Submitted to MNRAS, October 2017	75%. Concept, running simulations, analysing results writing manuscript	Amanda Karakas, Maria Lugaro & Carolyn Doherty, 20% Concept, analysing results and feedback on manuscript. Christian Ritter, 5% Code installation and debugging.	N

“The fairest thing we can experience is the mysteries. It is the fundamental emotion which stands at the cradle of true art and true science... the mystery of the eternity of life, and the inkling of the marvellous structure of reality, together with the single-hearted endeavor to comprehend a portion, be it ever so tiny, of the reason that manifests itself in nature.”

Albert Einstein

“Be humble for you are made of earth. Be noble for you are made of stars.”

Serbian quote

Summary

This thesis explores the mergers of binary stars, belonging to two ends of the mass spectrum: on the high mass end, forming the majority of the thesis, is the merger that led to the formation of the massive progenitors ($16 - 25 M_{\odot}$) of Supernova SN 1987A and other peculiar Type II supernovae (Type II-pec SNe). On the low mass end is the merger of close binary white dwarfs (WDs) that led to the formation of the hydrogen-deficient carbon-rich R Coronae Borealis (RCB) stars ($0.9 - 1 M_{\odot}$).

SN 1987A, which exploded in the Large Magellanic Cloud, is the most well-observed supernova in literature. Its origin, however, has been highly debated due to the peculiar nature of its light curve and progenitor. Unlike the light curves of typical Type II SNe which have a long plateau phase, the light curve of SN 1987A was dome-shaped. Its progenitor star thus was not a cool red supergiant (RSG) but a hot, compact blue supergiant (BSG), identified in photographic plates as Sk $-69^{\circ}202$, with a radius of $R = 30 - 50 R_{\odot}$ and effective temperature $T_{\text{eff}} = 15 - 18 \text{ kK}$.

This is the first study in which we have demonstrated within a self-consistent framework, that a binary merger evolutionary model can explain both, the observational constraints of Sk $-69^{\circ}202$ and the light curve of SN 1987A. We find that binary merger models provide a much better fit to the light curve of SN 1987A than the single-star models in current literature.

The evolutionary model for Sk $-69^{\circ}202$ was built using the stellar evolution code KEPLER and is based on a binary merger scenario, in which a primary RSG star of mass $M_1 = 15 - 17 M_{\odot}$, containing a helium (He)-depleted core, merges with a main-sequence secondary star of $M_2 = 2 - 8 M_{\odot}$. During the merger, an accretion stream from the secondary star penetrates the He core of the primary and results in the partial dredge-up of the He shell from the core to the surface. The evolution of the merged star was followed until just prior to the collapse of its iron core. Of the 84 binary systems we investigated, spanning three initial parameters— M_1 , M_2 , and the fraction of the He shell of the primary dredged up (f_{sh}), 59 of the final models ended up as BSGs. Six of these were identified as progenitor candidates for SN 1987A, as they matched the observational characteristics of Sk $-69^{\circ}202$, such as its position on the Hertzsprung Russel diagram, the ratios of nitrogen to carbon and oxygen, of helium to hydrogen, and the lifetime of the star as a BSG.

Using the 1D radiation hydrodynamic code CRAB, we next simulated the explosions of these binary merger models, for SN 1987A and two other Type II-pec SNe, SN 1998A and

SN 2006V. The model that best reproduces the characteristics of Sk -69°202 and whose explosion matches its light curve, was formed from the merger of a system of masses $M_1 = 16M_\odot$, $M_2 = 7M_\odot$ and with a He core dredge up of $f_{\text{sh}} = 50\%$. This model has a radius of $37R_\odot$ and an ejecta mass of $20.6M_\odot$. The same model with different explosion parameters also fits the light curve of SN 1998A, a more luminous supernova than SN 1987A. In the case of SN 2006V, which is also a more luminous counterpart of SN 1987A, the explosion of a yellow supergiant progenitor with a radius of $150R_\odot$ and ejecta mass of $19.1M_\odot$ reproduces the light curve. This indicates that not all progenitors of Type II-pec SNe are necessarily BSGs.

The next system we studied were R Coronae Borealis (RCB) stars, which are expected to originate from the mergers of carbon-oxygen and helium white dwarfs (WDs). RCBs are near-solar mass hydrogen-deficient carbon-rich supergiants, that are predominantly metal-poor. They have $^{16}\text{O}/^{18}\text{O}$ ratios of 1 – 25, which are some of the lowest values of this ratio measured in any star, and are also enhanced in fluorine and the heavy-elements produced by the slow(s)-neutron capture process, compared to solar. In a previous work, post WD-merger stellar evolution models of RCBs constructed at solar-metallicity could reproduce the above chemical signatures. In this work, we construct new post WD-merger models with a realistic metallicity that matches RCB stars, of $[\text{Fe}/\text{H}] = -1.4$ ($Z = 0.0028$) and an alpha-enhanced initial composition. We adopted the same methodology as the previous work, the main feature of which was the inclusion of an artificial mixing routine during the post-merger evolution of the models. The new models presented in this work have $^{16}\text{O}/^{18}\text{O}$ ratios of 9.5 – 30, $^{12}\text{C}/^{13}\text{C}$ ratios of 1500 – 7000 and enhancements in F and s-process elements, which match the observational constraints of RCBs. We further performed an element-by-element comparison between our models and RCBs and also explored the possibility that some pre-solar graphite grains may have formed in the outflows of RCB stars. Our RCB models can reproduce the range in elemental abundances measured in RCBs and reproduce most of the observed isotopic ratios in our selected sample of pre-solar graphite grains, except for C and Al.

Acknowledgements

A PhD, as I saw it, was the last time I would be a full-time student. I also saw it as my last opportunity to fulfill my desire to continue the training I left off as a child in the Indian classical dance form, Bharatanatyam. What started as a hobby became one half of my expression, my thoughts and my identity, while the other half was science. It is I think, more than a coincidence that Bharatanatyam is called the ‘Cosmic Dance’, whose patron deity Nataraja keeps the rhythms of the Universe, its cycles of creation and destruction, through the rhythm of his anklets and drum.

In ways I couldn’t foresee, the two halves became so deeply intertwined that it was impossible to go through a single day without engaging both science and dance. I went on to complete my training in Bharatanatyam, perform in a 3-hour solo concert that was my graduation in the art form and conclusively demonstrate how the progenitor of SN 1987A was from a binary merger, both from an evolutionary perspective and from its explosion.

What made this journey possible was the support and encouragement of many people.

I want to first thank my supervisor, Prof. Alexander Heger, for his guidance, his support and for cheering me on. I am his first PhD student at Monash University, and for both of us this was an insightful experience of mentoring and being mentored. Over the years, I felt more as a colleague than a student, as I began taking ownership of my work and independently scouting for projects and collaborators. I want to thank Alex for giving me this freedom and advising me when I needed it. I especially thank him for promoting my work as my own, and making sure that my achievements received due recognition. He has always been in the front row to attend my talks, give me feedback for them and has even supported my commitment to my dance-training.

I would like to thank my co-supervisor, Associate Prof. Amanda Karakas, for bringing up the idea about revisiting my Masters work for a second PhD project. She has a superb memory for references and could easily pull out a paper she read from a decade ago. I also thank her for our conversations about University and work matters, giving me useful perspectives about them. To the colourful Prof. John Lattanzio, thank you for convincing me to join MoCA. None of this would have been possible without that hour-long Skype call on a rainy Mumbai day in 2013. I thank him for his warm company and the many invitations to his house parties where I tried many of his delectable wines from his famous cellar. I am especially grateful to him for taking me to the hospital when I first arrived in Melbourne

and caught a severe case of the flu. And also, for introducing me to Gregory David Roberts (Shantaram).

I thank my collaborators Dr. Victor Utrobin for his patience in answering my many questions about the mechanisms of supernovae and useful discussions about SN 1987A. I also thank Dr. Maria Lugaro and Dr. Carolyn Doherty, for their insights and feedback about my work and Dr. Christian Ritter for helping me out with setting up and debugging MESA and NUGRID tools. I would also like to acknowledge the input of two of my peers, Dr. Thomas Constantino and Dr. Christian Ritter, who have helped me with installing and debugging the codes I used in my thesis. Couldn't have done it without your patient help!

I acknowledge the financial support from the Australian Government for the Australian Postgraduate Award (APA) and the International Postgraduate Research Scholarship (IPRS) from Monash. I also thank Monash University and all those involved in the 3-minute thesis competition, which awarded me a generous cash prize for winning the second place in the competition and also for being voted by the audience as their favourite contestant. I would like to thank the friends I made at Monash University, especially Rebecca, Ben and Grace. And our taskmaster secretary Jean Pettigrew for getting things done so well.

My dance Guru, Dr. Chandrabhanu– thank you for being such a dedicated teacher. You are the reason I could find myself again, without being lost in the intimidating and sometimes exhausting labyrinth that science can be. Thank you for motivating me to train hard everyday, to re-discover my passion for dance and for all the philosophical/spiritual conversations that interspersed our classes. And of course, for the grand finale on October 14th, 2017, my arangetram, where I danced my heart out and kept nothing for myself, but gave it all to the audience. I could see you smiling proudly and that just made me confident to give more.

My parents, who have seen me grow, from the child who read the Childcraft series to becoming a practitioner of science. I thank them for their steadfast pride in me and their dream to one day call me 'Dr. Athira Menon'. I thank my partner Sriram Chandrasekaran, for listening and questioning with wonder and enthusiasm about the Universe and its workings, and especially about the now too-often repeated, 'SN 1987A'. Thank you for being my cheerleader and reminding me how truly spectacular Astrophysics is. I look forward to our life together.

And finally, my obeisance to the divine art of Bharatanatyam. Thank you for making me a better scientist and a better human being.

Dedicated to...

My twin halves: the Cosmos and Bharatanatyam, and my teachers: Mom, Dad and my Guru, Dr. Chandrabhanu.



FIGURE 1: Nataraja as enshrined in the temple of Chidambaram.
Artist: Athira Menon, Picture credit: Shripathy Hadigal.

Abbreviations and symbols

AGB	Asymptotic giant branch
BSG	Blue supergiant
SN/SNe	Supernova/Supernovae
pre-SN	Pre supernova
RCB	R Coronae Borealis
RGB	Red giant branch
RSG	Red supergiant
RLOF	Roche Lobe Overflow
WD	White dwarf
DD	Double degenerate
FF	Final He-flash
E	Explosion energy of supernova
f_{sh}	fraction of He shell of He core of primary dredged up
$\log L$	Surface luminosity
M_1	Mass of the primary star
M_2	Mass of the secondary star
M_{ej}	Mass of supernova ejecta
M_{Ni}	Mass of ^{56}Ni in the ejecta
R_L	Roche Lobe radius
$R_{\text{pre-SN}}$	Radius of pre-SN model
T_{eff}	Effective surface temperature
v_{Ni}	velocity of nickel mixing velocity

Contents

Copyright Notice	ii
Declaration of Authorship	v
Summary	viii
Acknowledgements	x
Dedicated to...	xii
Abbreviations and symbols	xiii
1 Introduction	1
1.1 The days of their lives	3
1.1.1 Low mass stars $0.08 \lesssim M/M_{\odot} \lesssim 0.8$,	4
1.1.2 Intermediate mass stars $0.8 \lesssim M/M_{\odot} \lesssim 8$	4
1.1.3 Massive stars $M/M_{\odot} \gtrsim 8$	6
1.1.4 Other factors affecting stellar evolution	7
1.2 The end of massive stars: core collapse supernovae	9
1.2.1 Supernova 1987A	13
The progenitor, Sk -69°202	14
The explosion	15
1.3 Born-again stars: R Coronae Borealis stars	17
1.3.1 Pre-solar graphite grains	18
1.4 Binary evolution	19
1.4.1 Roche Lobe	20
1.4.2 Mass transfer	21
1.4.3 Common envelope phase	22
1.5 Binary mergers	24

1.5.1	Sk-69°202	25
1.5.2	RCB stars	26
1.6	Tools used in this thesis	28
1.7	This thesis	29
2	Binary merger evolutionary models for the progenitor of SN 1987A	35
2.1	Introduction	35
2.1.1	Aims and structure of this work	38
2.2	Methodology	38
2.2.1	The stellar evolution code: KEPLER	38
2.2.2	Effective-merger model	40
2.2.3	Initial parameters	42
2.3	Results	46
2.3.1	Progenitor models of SN 1987A	46
2.3.2	What factors affect the formation of BSGs?	50
	Surface N/C and N/O ratios	50
	Effective temperature, luminosity, and radius	53
	Lifetime of BSG model before explosion	55
2.4	Discussions and Conclusions	58
2.5	Appendix	61
3	Explosions of binary merger progenitors for peculiar Type II supernovae	67
3.1	Introduction	67
3.2	Methodology	72
3.2.1	Progenitor models used in this work	72
3.2.2	CRAB: The explosion code	74
3.3	Results	75
3.3.1	Comparison between binary merger and single star pre-supernova models	75
3.3.2	The light curve of SN 1987A	76
	Varying explosion parameters for SN 1987A	78
	Varying progenitor parameters	80
3.3.3	Other Type II-pec SNe: SN 1998A and SN 2006V	82

3.4	Discussions and Conclusions	89
3.5	Acknowledgements	91
4	Low-metallicity CO+He WD post-merger models for RCB stars and their connection to low-density graphite grains	93
4.1	Introduction	93
4.1.1	R Coronae Borealis stars	93
4.1.2	Pre-solar graphite grains	96
	Dust from supernovae	96
	Dust from RCB stars	98
4.2	Methodology	99
4.2.1	Initial setup	99
4.2.2	The four cases of this paper	102
4.2.3	Simulation algorithm	105
4.3	Results	105
4.3.1	Nucleosynthesis and mixing processes in the models	105
4.3.2	Elemental abundances and comparison with RCB stars	108
4.3.3	Comparison with pre-solar graphite grains	114
4.4	Discussions and Conclusions	119
5	Conclusions and Summary	123
	Bibliography	129

List of Figures

- 1 Nataraja as enshrined in the temple of Chidambaram. Artist: Athira Menon, Picture credit: Shripathy Hadigal. xiii
- 1.1 Evolutionary tracks of a $1 M_{\odot}$ star computed using MESA, a $16 M_{\odot}$ star with rotation, and without rotation, computed using KEPLER. The shaded grey box is the observed region for RCB stars (Clayton, 1996) and the orange box is where Sk-69°202 was observed to lie before it exploded as SN 1987A (Woosley, Pinto, and Weaver, 1988). 3
- 1.2 Cartoon depicting the final structure of a massive star, prior to core collapse. Image source: <https://courses.lumenlearning.com/astronomy/chapter/the-evolution-of-more-massive-stars/> 10
- 1.3 Comparing bolometric light curves of the Type II-P SNe, SN 1999em and SN 2003hn with that of SN 1987A. Day 0 refers to the first day of observation of the supernova. Figure from (Bersten and Hamuy, 2009). 11
- 1.4 SN 1987A located at the edge of the Tarantula Nebula in the Large Magellanic Cloud. Image credit: Anglo-Australian Observatory 13
- 1.5 Left: Image taken in H_{α} by Hubble space telescope (HST) in April 1994. Right: Simulated emission measured in H_{α} on day 2000 after the explosion from a binary merger model. Figure from Morris and Podsiadlowski (2009). 14
- 1.6 Different types of binary systems. Top panel: detached binary. Middle panel: semidetached binary. Bottom panel: contact binary. Image source: http://www.daviddarling.info/encyclopedia/C/close_binary.html 20
- 1.7 Evolutionary sequence for the binary system that led to the progenitor of SN 1987A. 31
- 1.8 Evolutionary sequence for the binary system that would lead to RCB stars. Figure edited from Solheim (2010). 32
- 1.9 Left: 1D evolutionary models (the coloured lines) of post CO+He WD mergers, constructed with solar metallicity in Menon et al. (2013). Shaded region is the observed position including error bars, of RCB stars. Right: $^{16}\text{O}/^{18}\text{O}$ ratios on surfaces of the models (coloured symbols) against observed values in RCB stars (black symbols; Clayton et al., 2007; García-Hernández et al., 2010). 33

2.1	Top panel, stage B in Fig. 2.4: Composition of the RSG model from a primary of $M_1 = 16 M_\odot$ consisting of a He core of $M_{\text{He},1} = 4.92 M_\odot$ just prior to the merger. Middle panel, stage C in Fig. 2.4: Composition at the end of the merger with $M_2 = 7 M_\odot$. The boundary of mixing m_b (dotted vertical line) is set for $f_c = 16.6\%$. At the end of the merger, the star has a smaller He core of mass $3.61 M_\odot$. Bottom panel, stage D in Fig. 2.4: Composition of the pre-SN model. The surface composition of the star does not change much from the one at the end of the merger.	40
2.2	Diagram (not according to scale) showing the equivalence of mass ejection from the CE phase to accreting lower secondary masses.	42
2.3	A schematic of the evolutionary sequence used in this work, illustrated for the binary system of $M_1 = 16 M_\odot$ and $M_2 = 7 M_\odot$. The primary is evolved until it becomes an RSG, over a period of 13.3 Myr, after which it is merged with the secondary over 100 yr. The post-merger model in this case is a BSG and it remains so for 49.2 kyr until its explosion. The He core mass is flat until ~ 25 yr from the start of the merger before it begins to shrink. This is because it takes ~ 25 yr for the boundary of the He core to recede due to dredge up of H-rich material from the envelope.	43
2.4	Evolutionary track of the merger of $M_1 = 16 M_\odot$ and $M_2 = 7 M_\odot$, with $f_c = 16.6\%$. Shaded orange region represents observational limits for Sk $-69^\circ 202$ by Woosley, Pinto, and Weaver (1988) for T_{eff} and $\log(L/L_\odot)$. A and B: from the zero-age main sequence of the primary to the required RSG model. B and C: merger with the secondary. C and D: evolution of the post-merger model until carbon ignition in the core. D and E: further evolution to the final model just before core collapse. The final model (E) satisfies conditions (i)–(iii) in Section 2.3.1.	47
2.5	Surface quantities of pre-SN models obtained from the merger of $M_1 = 15 M_\odot$ and $M_2 = 5 M_\odot$ with various dredge up fractions of the He core (f_c in %). <i>Left</i> : Number ratios, N/C and N/O. <i>Right</i> : Effective temperature (T_{eff}) and luminosity (L). Negative values of f_c represent the case for which the He core of the primary is penetrated and positive values show the case for which the mixing is restricted to above the He core of the primary. Also marked are the boundaries of the CO core, He core and the He shell of the primary. The shaded regions denote observational limits for Sk $-69^\circ 202$; the violet region limits are taken from Lundqvist and Fransson (1996) and the orange region from Woosley, Pinto, and Weaver (1988).	51

2.6	Distribution of number ratios, N/C and N/O of all final models for each of the primary masses, M_1 . These parameters are plotted in a column for each M_1 against the range of M_2 . The symbols stand for different values of f_{sh} . The bold blue symbols are progenitor models for SN 1987A that satisfy criteria 1-3 in Section 2.3.1. The shaded violet region denotes the observational limits as explained in Fig. 2.5.	52
2.7	Distribution of number ratios N/C vs. N/O at the surface of all 84 final models. The shaded violet region denotes the observational limits for Sk $-69^\circ 202$ as in Fig. 2.5. Yellow symbols are YSGs, blue symbols are BSGs and filled blue symbols are progenitor models for SN 1987A, which satisfy the conditions 1-3 in Section 2.3.1.	53
2.8	The evolutionary tracks of four cases computed for the merger of $M_1 = 16M_\odot$ and $M_2 = 6M_\odot$, with $f_{\text{sh}} = 10\%$, 50% , 90% , 100% . Stars denote the pre-SN models of individual evolutionary tracks. The shaded orange region denotes the observational limits as in Fig. 2.5.	54
2.9	The evolutionary tracks of four cases computed for the merger of $M_1 = 16M_\odot$ with $M_2 = 2M_\odot$, $4M_\odot$, $6M_\odot$, and $8M_\odot$, and $f_{\text{sh}} = 50\%$. Stars denote the pre-SN models of individual evolutionary tracks. The shaded orange region denotes the observational limits as in Fig. 2.5.	54
2.10	Distribution of effective temperature (T_{eff}), luminosity (L) and radius ($R_{\text{pre-SN}}$) of all 84 final models. Symbols are as in Fig. 2.6. The shaded orange region denotes the observational limits as in Fig. 2.5.	56
2.11	Distribution of all 84 final models in the HRD. Lines of constant surface radius (in R_\odot) are drawn. The shaded orange region denotes the observational limits as in Fig. 2.5. Symbols are as explained in Fig. 2.7.	57
3.1	Density profiles of Model 16-7b and single star pre-SN models used in Utrobin et al. (2015) as a function of mass coordinate (top) and radius (bottom).	77
3.2	Chemical composition of the original pre-SN models 16-7b (a) and 18-4d (b). Mass fraction of hydrogen (black line), helium (blue line), carbon (violet line), nitrogen (cyan line), oxygen (green line), neon (orange line), silicon (firebrick line), and iron (red line).	78

- 3.3 Dependence on the explosion energy. Bolometric light curves (panel a) and the photospheric velocity as a function of time (panel b) of Model 16-7b for the explosion energies of 1.7 B (blue line) and 2.5 B (magenta line) respectively. The computed curves are compared with the observed bolometric luminosity of SN 1987A obtained by Catchpole et al. (1987) and Catchpole et al. (1988b) (open circles) and Hamuy et al. (1988b) (open triangles), and with the velocity at the photosphere estimated by Phillips et al. (1988) with the absorption minimum of the $\text{Fe}_{\text{II}} \sim 5169 \text{ \AA}$ line (open circles). 79
- 3.4 Dependence on the boxcar mass width ΔM . Panel a: The chemical composition of the pre-SN models based on Model 16-7b after the boxcar averaging with the mass width $\Delta M = 2 M_{\odot}$ (green lines), $4 M_{\odot}$ (blue lines) and with no mixing, $\Delta M = 0 M_{\odot}$ (magenta lines). Mass fractions of hydrogen (thick line), helium (medium line), CNO elements (thin line), and Fe-peak elements (tiny line) are plotted. Panel b: The corresponding bolometric light curves are compared with the observations of SN 1987A obtained by Catchpole et al. (1987) and Catchpole et al. (1988b) (open circles) and Hamuy et al. (1988b) (open triangles). 80
- 3.5 Dependence on the extent of mixing of radioactive ^{56}Ni . Panel a: Mass fraction of radioactive ^{56}Ni as a function of velocity at day 50 for Model 16-7b. Panel b: The corresponding bolometric light curves compared with the observations of SN 1987A obtained by Catchpole et al. (1987) and Catchpole et al. (1988b) (open circles) and Hamuy et al. (1988b) (open triangles). 80
- 3.6 Variation in the fraction of the He-shell of the He core dredged up, f_{sh} : 10 % (red lines), 50 % (magenta lines), 90 % (green lines), and 100 % (blue lines) for $M_1 = 16 M_{\odot}$ and $M_2 = 6 M_{\odot}$. Panel a: density distributions as functions of interior mass for Models 16-6a, 16-6b, 16-6d, and 16-6c. Panel b: density distributions as functions of radius for the same models. Panel c: the chemical composition of the corresponding pre-SN models after the boxcar averaging with the mass width $\Delta M = 2 M_{\odot}$. Mass fractions of hydrogen (thick line), helium (medium line), CNO elements (thin line), and Fe-peak elements (tiny line) are plotted. Panel d: the calculated bolometric light curves are overplotted on the bolometric data of SN 1987A obtained by Catchpole et al. (1987) and Catchpole et al. (1988b) (open circles) and Hamuy et al. (1988b) (open triangles). 81
- 3.7 Variation in the secondary mass: $M_2 = 5 M_{\odot}$ (red lines), $6 M_{\odot}$ (magenta lines), $7 M_{\odot}$ (green lines), and $8 M_{\odot}$ (blue lines) for the primary mass $M_1 = 16 M_{\odot}$ and the fraction $f_{\text{sh}} = 10 \%$. See the legend of Figure 3.6 for details. 82

- 3.8 Pre-SN models for peculiar Type II-P supernovae. Panel a: density distributions as functions of interior mass for models 16-7b (magenta line) and 18-4d (blue line). Panel b: density distributions as functions of radius for the same models. Panel c: the chemical composition of the pre-SN model 16-7b after the boxcar averaging with the mass width $\Delta M = 2 M_{\odot}$. Mass fraction of hydrogen (black line), helium (blue line), CNO elements (green line), and Fe-peak elements (magenta line). Panel d: the same for the pre-SN model 18-4d. 84
- 3.9 Hydrodynamic model for SN 1987A. Panel a: the calculated bolometric light curve is compared with the observations of SN 1987A obtained by Catchpole et al. (1987) and Catchpole et al. (1988b) (open circles) and Hamuy et al. (1988b) (open triangles). Panel b: the calculated photospheric velocity is overplotted on the velocity at the photosphere estimated by Phillips et al. (1988) with the absorption minimum of the $\text{Fe}_{\text{II}} \sim 5169 \text{ \AA}$ line (open circles). Panel c: the mass fraction of radioactive ^{56}Ni as a function of velocity at day 50. 85
- 3.10 Hydrodynamic model for SN 1998A. Panel a: the calculated light curve is compared with the bolometric data of SN 1998A estimated by Lusk and Baron (2017) by means of direct integration (open circles). To fit the observations, the explosion date is suggested to be later by 10 days relative to that accepted by Pastorello et al. (2005). Panel b: the calculated photospheric velocity is overplotted on the velocity at the photosphere estimated by Pastorello et al. (2005) with the absorption minima of the $\text{Ba}_{\text{II}} \sim 6142 \text{ \AA}$ (open circles), $\text{Fe}_{\text{II}} \sim 5169 \text{ \AA}$ (filled circles), $\text{Sc}_{\text{II}} \sim 5527 \text{ \AA}$ (open triangles) lines. Panel c: the mass fraction of radioactive ^{56}Ni as a function of velocity at day 50. 86
- 3.11 Hydrodynamic model for SN 2006V. Panel a: the light curves calculated for different ^{56}Ni distributions (see panel c) are compared with the bolometric data of SN 2006V estimated by Taddia et al. (2012) (open circles) and by Lusk and Baron (2017) which used direct integration (filled circles). To fit the observations, the explosion date is suggested to be earlier by 3 days relative to that accepted by Taddia et al. (2012). Panel b: the calculated photospheric velocity is overplotted on the velocity at the photosphere estimated by Taddia et al. (2012) with the absorption minima of the $\text{Ba}_{\text{II}} \sim 6142 \text{ \AA}$ (open circles), $\text{Fe}_{\text{II}} \sim 5169 \text{ \AA}$ (filled circles) lines. Panel c: the mass fraction of radioactive ^{56}Ni as a function of velocity at day 50 for the ^{56}Ni distributions within sphere (magenta line) and spherical layer (blue line). 87
- 4.1 The four-zone profile of the initial post-merger model of Case 1 of this paper. . 100

- 4.2 The abundances and neutron densities of the hot SOFs of Cases 3 (left panel) and 4 (right panel), calculated at $T = 123$ MK and $\rho \approx 3 \times 10^4$ g/cm³. The dashed vertical line is when the $^{16}\text{O}/^{18}\text{O}$ drops to ≈ 2 , and the hot SOF abundances are taken at this point. 103
- 4.3 Snapshots of time for Case 1 from top to bottom: close to initial at $t=0.13$ Myr, $t=0.32$ Myr, $t=0.50$ Myr and at the termination of the evolution at $t=1.8$ Myr. Left: Mass fractions and diffusion coefficient ($\log D$) against mass coordinate. Right: Neutron density and number ratios of silicon isotopes against mass coordinate. Convection is shown as the grey shaded region. Since the mixing is restricted to the layers above the CO core, the mass range in this plot is restricted to $0.45 - 0.90 M_{\odot}$ 107
- 4.4 Snapshots of time for Cases 1 and 3, showing the evolution of the number fraction of Ca isotopes and neutron density. From top to bottom, Case 1 (Case 3): $t=0.13$ (0.11) Myr, $t=0.32$ (0.28) Myr, $t=0.34$ (0.31) Myr and $t=1.8$ (1.7) Myr. 110
- 4.5 Comparison of the surface abundance of the four cases in this work, with observed abundances of RCB stars. Square symbols are RCB minority stars and star symbols are RCB majority stars; the two filled square symbols have $^{16}\text{O}/^{18}\text{O}$ measured from García-Hernández et al. (2010). As a reference we also plot the abundances of Case 1 of Paper I as the + symbol. The prototype, R Coronae Borealis (RCrB) is the pink \star . **Case 1** and **Case 3** are plotted as filled green and orange \circ symbols respectively, and **Case 2** and **Case 4** as filled blue and purple \triangle symbols respectively. The grey \oplus symbol is the abundance from the initial $Z=0.0028$ alpha-enhanced composition. The teal-dashed line shows the scaled-solar composition. 112
- 4.6 Number ratios of $^{12}\text{C}/^{13}\text{C}$ (a) and $^{14}\text{N}/^{15}\text{N}$ (b) against $^{16}\text{O}/^{18}\text{O}$. The grain data are the grey stars along with error bars. Error bars for $^{16}\text{O}/^{18}\text{O}$ are within the symbol. Dilution lines connect points that represent different fractions of dilution with solar material; filled symbols are directly taken from the surface of the models (without any dilution) and empty symbols represent dilution with 0.1, 0.3, 0.5, 0.7, 0.9, 1.0 fraction of solar composition. The dashed cyan line is the value for the alpha-enhanced composition at $Z = 0.0028$ and dashed black line is the solar composition. The shaded region in (a) represents the observed limits for RCB stars; the lower bound for $^{12}\text{C}/^{13}\text{C}$ is set to 40 (Hema, Pandey, and Lambert, 2012) and $^{16}\text{O}/^{18}\text{O}$ is set to 1 – 25 (Clayton et al., 2007; García-Hernández et al., 2010). Note: The measurements for these two ratios were obtained independently and do not belong to the same stars. Symbols and lines of this figure are used in the following figures Fig. 4.7–4.8. 115

4.7	Number ratios of $^{16}\text{O}/^{17}\text{O}$ (a) and $^{26}\text{Al}/^{27}\text{Al}$ (c), and δ -values of $^{25}\text{Mg}/^{24}\text{Mg}$ number ratio (b), and of Ca isotopes (d), (e), (f) vs. $^{16}\text{O}/^{18}\text{O}$ for our models and the grains.	116
4.8	δ -values of Si isotopes (a) and (b), of Ti isotopes (c), (d), (e) and (f) vs. $^{16}\text{O}/^{18}\text{O}$ for our models and the grains.	117

List of Tables

2.1	Opacity tables with temperature and density regimes. $\log R = \log \rho - 3 (\log T - 6)$, where ρ and T are in cgs units.	38
2.2	Parameters of the primary RSG models selected for merging. M_1 is the main-sequence mass of primary; v/v_{crit} is the initial rotational velocity on the main sequence; Age is the age of RSG model; τ_{cc} is the time until core collapse; M_{RSG} is the mass of RSG model; $M_{\text{COc},1}$ and $M_{\text{He c},1}$ are the mass of the CO core and of the He core; $M_{\text{env},1}$ is the mass of the envelope, i.e., $M_{\text{RSG}} - M_{\text{He c},1}$; N/C, N/O, and He/H are surface number ratios.	45
2.3	Uniform isotopic composition for the accreted secondary model. Isotope is the isotopic species; X_f is the mass fraction of accreted isotopes; X_f/X_i is the change with respect to their initial values.	46
2.4	Parameters of the progenitor models of SN 1987A. M_1 and M_2 are the initial primary and secondary masses of the binary system; f_{sh} and f_{c} are percentage fractions of He-shell mass and helium core mass that were dredged up; m_{b} is the boundary of mixing. The following are the properties of the pre-SN models: $M_{\text{He c}}$, $M_{\text{Fe c}}$, M_{env} , and $M_{\text{pre-SN}}$ are He core mass, iron core mass, envelope mass and total mass ($M_{\text{c}} + M_{\text{env}}$); N/C, N/O, He/H are number ratios in the surface; T_{eff} , $\log(L)$, $R_{\text{pre-SN}}$ are the effective temperature, luminosity and radius; τ_{BSG} is the lifetime of the BSG before explosion. '-' under the column $M_{\text{Fe c}}$ are for those runs that crashed while at core-silicon burning (refer to text in Section 2.2).	49
2.5	Properties of different RSG models of $M_1 = 16 M_{\odot}$, $\omega/\omega_{\text{crit}} = 0.30$ and pre-SN models from their merger with $M_2 = 6 M_{\odot}$ and $f_{\text{sh}} = 50\%$. $X_{\text{He c}}$, ρ_{c} , T_{c} , R_{RSG} , and $M_{\text{He c},1}$ are central helium mass fraction, central density, central temperature, radius and He core mass of the RSG model; $\log(L)$, T_{eff} , $R_{\text{pre-SN}}$ are the luminosity, effective temperature and radius of the pre-SN model; N/C, N/O, He/H are number ratios in the surface of the pre-SN model; τ_{BSG} is the lifetime of BSG before explosion.	57
2.6	Parameters of BSG binary merger progenitors of Type II SNe ($T_{\text{eff}} \geq 12$ kK). Column headings are the same as in Table 2.4.	62

2.7	Parameters of YSG binary merger progenitors of Type II SNe ($4\text{kK} \leq T_{\text{eff}} < 12\text{kK}$). Column headings are same as Table 2.6.	65
3.1	Model denotes the name of the pre-SN model; M_1 and M_2 are the initial primary and secondary masses of the binary system; f_{sh} is the fraction of the He-shell mass dredged up; $M_{\text{He c}}$, $M_{\text{Fe c}}$, M_{env} , and $M_{\text{pre-SN}}$ are He core, iron core, envelope masses and mass of the pre-SN model ($M_{\text{c}} + M_{\text{env}}$); T_{eff} , $\log(L)$, $R_{\text{pre-SN}}$ are the effective temperature, luminosity, radius of pre-SN model, $\xi_{1.5}$ is the compactness parameters.	73
3.2	Predicted explosion and progenitor properties for five Type II-pec supernovae: Source: source of data, $^{56}\text{M}_{\text{ejecta}}$: ejecta mass, $R_{\text{pre-SN}}$: radius of progenitor, E : explosion energy, M_{Ni} : nickel mass from Lusk and Baron (2017). In parenthesis are the corresponding values of SN 1987A against which these parameters have been calibrated. The final column lists the method used for the calculations.	88
4.1	Isotopic mass fractions from the He WD models (limited to values $> 10^{-4}$) with different envelope masses: He WD(1): $M_{\text{env}} = 6.4 \times 10^{-3} M_{\odot}$, He WD(2): $M_{\text{env}} = 10^{-2} M_{\odot}$ and from the dredged-up region of the CO WD: CO WD (DUP).101	101
4.2	The four cases. Abundances in the last two columns are initial amounts in the SOF and envelope, and are listed in Table 4.3.	102
4.3	Isotopic mass fractions of the SOF and envelope regions for the initial post-merger models. The composition of the material dredged up from the CO WD is the same for all SOFs and envelopes as in Table 4.1. SOF(1): Cold, from He WD(1), SOF(2): Hot, $T_{\text{SOF}}=123$ MK, from He WD(1), SOF(3): Cold, from He WD(2), SOF(4): Hot, $T_{\text{SOF}}=123$ MK. Envelope(1): From He WD(1) and Envelope(2): From He WD(2).	102

Physical Constants

Mass of Sun	$M_{\odot} = 1.983 \times 10^{33} \text{ g}$
Radius of Sun	$R_{\odot} = 6.955 \times 10^{10} \text{ cm}$
Luminosity of Sun	$L_{\odot} = 3.826 \times 10^{33} \text{ ergs/s}$
Constant Name	<i>Symbol = Constant Value with units</i>

Chapter 1

Introduction

Pumbaa: “Timon, ever wonder what those sparkly dots are up there?”

Timon: “Pumbaa, I don’t wonder; I know.”

Pumbaa: “Oh. What are they?”

Timon: “They’re fireflies that got stuck up in that bluish-black thing”.

Pumbaa: “Oh, gee. I always thought they were balls of gas burning billions of miles away.”

Timon: “Pumbaa, with you, everything’s gas.”

The Lion King

Although this conversation seems to have swung toward the wrong conclusion (and a nasty snub at Pumba), we have all at least once, had a similar moment with the stars. An innate wonderment about what they are, where they came from and where we, came from.

Stars, like Pumba thought, are indeed hot balls of gas and plasma, the closest one being the Sun, about a hundred million kilometres away. Stars shine because of nuclear fusion occurring in their core, and the energy generated by nuclear reactions being transported to the surface by processes such as convection, conduction, and radiation. For most of their lifetime, stars fuse hydrogen into helium and are in hydrostatic equilibrium, i.e., the gravitational force from their mass acting downward is balanced by the pressure exerted by gas, radiation, and electrons acting upward (Kippenhahn, Weigert, and Weiss, 2012).

The Sun is a single star, i.e., it has no companion. This, however, is not the norm for other stars we observe in our Universe today. At least 50% of all stars are observed to have one or more companions (Poveda, Allen, and Parrao, 1982; Abt, 1983; Raghavan et al., 2010; Eggleton, 2011; Duchêne and Kraus, 2013). In fact, theory and observations of star formation indicate that most (maybe all) stars were born in wide binaries and multiple systems, including the Sun. Dynamic interactions during the early phase of their lives, may have ‘kicked’ one of the stars out of the system or brought the components closer into a tighter orbit (Marks et al., 2012; Reipurth et al., 2014; Sadavoy and Stahler, 2017). Currently, observational surveys indicate that the more massive a star is, the likelier it is to be found in a binary system (Sana et al., 2013; Moe and Di Stefano, 2015; De Marco and Izzard, 2017). Stars that are above 8 times the mass of the Sun ($8M_{\odot}$) have a 70% chance of being in a

binary system (Sana et al., 2012; Kiminki and Kobulnicky, 2012; Kobulnicky et al., 2014), while stars which are less than $8M_{\odot}$ have a 50% chance of being part of a binary system, and this number decreases as the mass of the star decreases (Lada, 2006; Raghavan et al., 2010; Duchêne and Kraus, 2013). Binary stars have far more interesting lives than single stars, much like it is with humans. One body gains mass while the other loses, some systems grow so distant that their individual components live like single stars, while others come closer and merge to create new stars.

Two simple characteristics of the surface of a star, its color and brightness, can give us insights into its age, radius, mass and the evolutionary stage of its life. Further information can be obtained through spectroscopic measurements, which tell us the chemical composition of the star and the effective gravity of its surface.

An astronomer uses a very simple nomenclature for the chemical makeup of a star; there is hydrogen, helium and every other element is called a metal. The abundance of an element in a star is typically defined by the fraction of its mass compared to the total mass of the star. The Sun had an initial hydrogen mass fraction, $X_{\text{H}} = 0.715$, a helium mass fraction, $X_{\text{He}} = 0.271$, and metallicity of $Z = 1 - (X_{\text{H}} + X_{\text{He}}) = 0.014$ (Asplund et al., 2009).

Knowing the initial metallicity Z and mass (M) of a star, one can predict its entire life cycle, provided the star lived as a single being. In the case of binaries, we need more information to predict the evolution of the individual components—their initial separation, how much mass was exchanged between them and how much was lost from the system. Due to mass exchange, the stars in a binary system can undergo a role reversal: low mass stars can gain mass to end up exploding as supernovae, whereas high mass stars can lose their mass to wither away quietly as white dwarfs. And in some cases, they can merge to form altogether new objects, with a rejuvenated life time and carry chemical imprints on their surface which are very different from what a single star of the same mass may have.

Some of the most exciting cosmic phenomena are only possible from the mergers of binary stars: Type Ia supernovae, some of which have been used as a standard candle to measure the rate of expansion of the Universe, come from mergers of carbon-oxygen white dwarfs (Iben and Tutukov, 1984; Solheim, 2010; Pakmor et al., 2012), the recent detection of gravitational waves by LIGO came from the merger of two black holes (Abbott et al., 2016; Belczynski et al., 2016), and one of the most massive stars ever discovered, η -Carinae of nearly $150M_{\odot}$, is speculated to have formed from the merger of two very massive stars in a triple system (Podsiadlowski, Morris, and Ivanova, 2006; Portegies Zwart and van den Heuvel, 2016). The objects studied in this thesis were also born out of binary mergers: the progenitor of the most well-observed celestial event of the telescopic era, Supernova 1987A (Arnett et al., 1989; Podsiadlowski, Joss, and Hsu, 1992; Smartt et al., 2009) and, R Coronae Borealis stars, a class of dust ejecting, hydrogen-deficient carbon stars with some of the lowest observed ratios of $^{16}\text{O}/^{18}\text{O}$ in any star (Clayton et al., 2007; García-Hernández et al.,

2010), amongst other chemical peculiarities.

1.1 The days of their lives

The initial mass of a single star largely determines its evolutionary path and its eventual death. In terms of mass, stars are classified as: low mass stars with $0.08 \lesssim M/M_{\odot} \lesssim 0.8$, intermediate stars with $1 \lesssim M/M_{\odot} \lesssim 8$ and massive stars with $M/M_{\odot} \gtrsim 8$. The structural and chemical evolution of a single star, from birth to death, is well-understood (Rose, 1998; Woosley, Heger, and Weaver, 2002; Ryan and Norton, 2010; Carroll and Ostlie, 2006; Kippenhahn, Weigert, and Weiss, 2012) and primarily depends on its initial mass. The most effective way to illustrate the life cycle of a star is the Hertzsprung Russel (HR) diagram (Fig. 1.1), which plots the surface luminosity ($\log L/L_{\odot}$) of a star as a function of its effective surface temperature (T_{eff}).

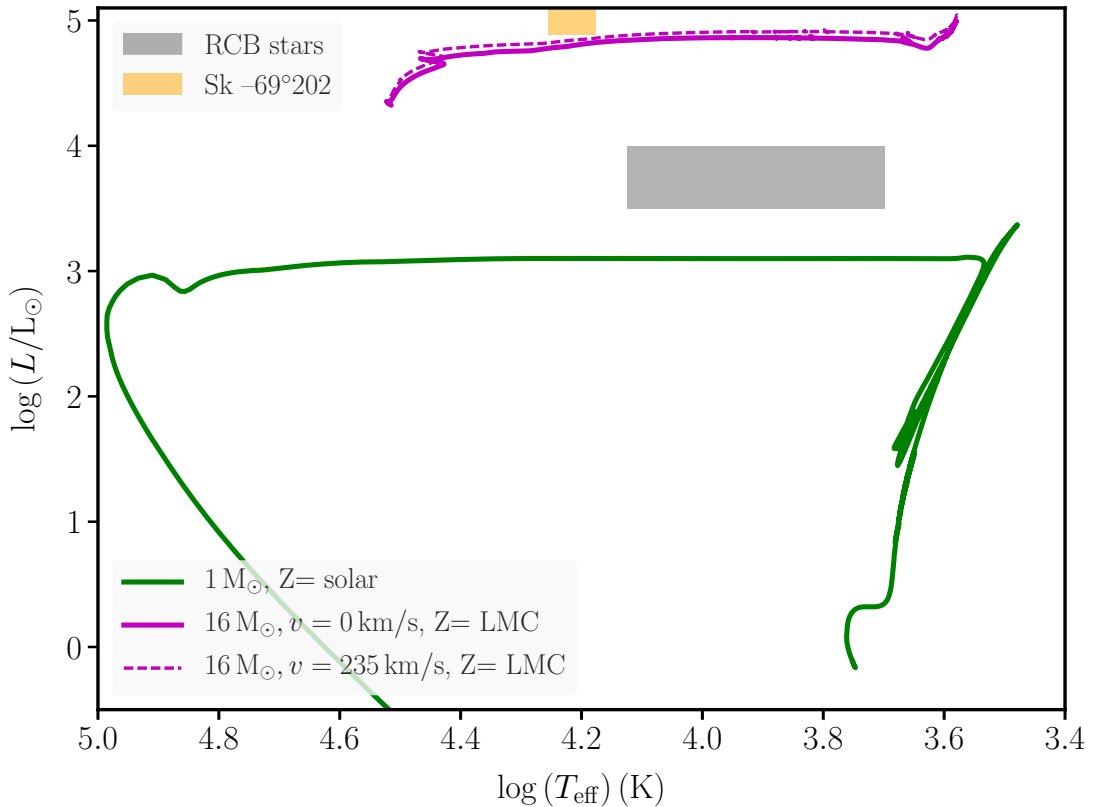


FIGURE 1.1: Evolutionary tracks of a $1 M_{\odot}$ star computed using MESA, a $16 M_{\odot}$ star with rotation, and without rotation, computed using KEPLER. The shaded grey box is the observed region for RCB stars (Clayton, 1996) and the orange box is where Sk $-69^{\circ}202$ was observed to lie before it exploded as SN 1987A (Woosley, Pinto, and Weaver, 1988).

Processes in a binary system can change the mass of a star. In this case, the future evolution of the individual stars depends on their current mass and not their initial mass. The following are the life cycles of single stars belonging to different mass categories.

1.1.1 Low mass stars $0.08 \lesssim M/M_{\odot} \lesssim 0.8$,

A star begins its life essentially when hydrogen nuclei (${}^1\text{H}$) start to fuse to helium (${}^4\text{He}$) in its core. This phase of its life is called the main-sequence (MS) phase and a star typically spends 90% of its life as an MS star. On the MS, stars with $0.08/M_{\odot} \lesssim 1.2$ have radiative cores and convective envelopes while stars more massive than $\sim 1.2M_{\odot}$ have convective cores and radiative envelopes (Kippenhahn, Weigert, and Weiss, 2012). H-fusion occurs dominantly through the proton-proton (pp) chain in stars of masses near that of the Sun or less, at core temperatures of $T \approx 18$ MK and in more massive stars H-fusion proceeds through the carbon-nitrogen-oxygen (CNO) cycle. Through the CNO cycle, the next major product of H-burning after ${}^4\text{He}$ is ${}^{14}\text{N}$.

When it exhausts all its hydrogen in the core, the star leaves the MS branch and expands to a cool, red luminous giant, which has a He core and a H-burning shell above it, and a convective envelope. Although it is not entirely clear how stars evolve to giants, it is believed that the energy from H-shell burning causes the star to inflate and ascend the Red Giant Branch (RGB). The He core of low mass stars is supported by electron degeneracy pressure (read also the next section for more details). H-shell burning in the red giant continues until the envelope is ejected by stellar winds and a helium white dwarf (He WD) is formed (more on stellar winds in Section 1.1.4). Low mass single stars will end their lives as He WDs, but since their evolutionary lifetime is longer than the age of the Universe, these He WDs have not formed yet. Those He WDs we observe in the Universe are a result of binary system interactions, which we shall discuss in later sections in this chapter.

1.1.2 Intermediate mass stars $0.8 \lesssim M/M_{\odot} \lesssim 8$

Intermediate mass stars will continue their evolution further from the RGB phase. In Fig. 1.1, the evolution of a $1 M_{\odot}$ star with solar metallicity is illustrated. As the star expands, the core contracts and the central temperature approaches He-fusion ($T \approx 10^8$ K). The nature of core He-burning depends on the initial mass of the star.

For stars with $M/M_{\odot} < 2.5$, He is ignited in the core under degenerate conditions (Kippenhahn, Weigert, and Weiss, 2012). This is because the He core grows in mass, due to the accumulation of the ashes of the H-burning shell above it. As the mass of the core increases, it contracts, thereby increasing its density until electron degeneracy sets in the core. As the core contracts, the temperature of the core grows but since electron degeneracy pressure is independent of temperature, the core only becomes hotter at constant pressure without expanding or contracting. When the central temperature is $T \approx 10^8$ K, He is ignited off-centre in the core due to energy losses through neutrinos in the preceding red giant phase. He burns via the triple-alpha chain reaction, wherein three ${}^4\text{He}$ particles are consumed to make one ${}^{12}\text{C}$. All the nuclear energy generated goes into the internal energy

of the star since the PdV work done on the core is zero. The rate of energy generation via the triple-alpha chain is proportional to $(T(K)/10^8) \times 10^{41}$ and is thus strongly dependent on temperature, leading to a thermonuclear runaway process in the core called the "core helium flash", where the local luminosity of the He core reaches $\approx 10^{11} L_{\odot}$ in a few seconds. The initial He-core burning is unstable, until degeneracy is lifted in the core due to increasing temperature at constant density. For a $1 M_{\odot}$ star, the material crosses the boundary from degenerate conditions to that of an ideal gas at $\sim 3 \times 10^8$ K. Thereafter, as pressure increases proportionally to temperature and the core expands as temperature increases, causing He-burning to proceed in a stable manner.

In the cores of more massive stars, i.e., with $M/M_{\odot} \geq 2.5$, He is ignited under non-degenerate conditions and is a stable process throughout. As temperature increases due to the contraction of the core, PdV work is done by the material of the core to expand it. After H-fusion, He-fusion is the next longest core-burning phase in any star. When enough ^{12}C becomes available through the triple-alpha reaction, ^{16}O is also formed by the capture of another ^4He nucleus by ^{12}C .

Once the ^4He is completely consumed, nuclear burning stops in the core and the star once again undergoes a period of gravitational compression, inflates to a giant, and ascends the Asymptotic Giant Branch (AGB), with a Carbon-Oxygen (CO) core, a He-burning shell and a convective envelope. The AGB phase is divided into two parts– the early-AGB phase and the thermal-pulsing AGB (TP-AGB) phase. In the E-AGB phase, the star continues to expand and becomes more luminous. At a certain point of its ascension on the AGB, a very thin H-shell is ignited just below the convective envelope. The structure at this point consists of the envelope, followed by a thin H-burning shell, a He-rich intershell region, a thin He-burning shell and a CO core. The episodic burning of the H and He shells result in thermal pulses on the surface. For detailed reviews on AGB stars, the reader is referred to Herwig (2005) and Karakas and Lattanzio (2014).

A characteristic feature of all giant phases of evolution of the star, are the mixing episodes due to convection called "dredge-ups", which result in the appearance of products of nuclear burning from within the star in the surface. The first dredge-up occurs in the RGB phase and the second dredge-up occurs in stars with $M > 3 M_{\odot}$, during the E-AGB phase. Both dredge-up episodes result in the surface to be enriched in ^4He , ^{13}C and ^{14}N and to be depleted in ^1H , ^{12}C , ^{15}N and ^{16}O . The third dredge-up occurs during the TP-AGB phase, during which the surface becomes enhanced in products of H-burning, He-burning and neutron-capture elements, particularly the *s*-process elements.

Mass loss is accelerated in the TP-AGB phase, until the star loses most of its envelope. The star leaves the AGB and moves across the HR diagram, as the star contracts to a CO white dwarf (CO WD). Since nuclear burning is dormant in the star, it begins to lose heat to its surroundings and descend the white dwarf cooling track. The WD finally coming into

thermal equilibrium with the cosmic microwave background radiation over the lifetime of the Universe.

The next stage of burning is C-ignition ($T=0.5-0.6$ GK), that creates O and neon (Ne) in the core. In the region where intermediate mass stars and massive stars intersect, between $6.5 - 10 M_{\odot}$, C is ignited off-centre under degenerate conditions, and at the end of C-burning in the core, the star evolves to a thermally pulsing super asymptotic giant (S-AGB) star (Doherty et al., 2015). In the lower end of this mass range, the star dies as an ONe WD, but on the higher end ($M > 8 M_{\odot}$) the star can explode as an electron-capture supernova (EC SN) (Doherty et al., 2017). Mass loss during the evolution of the star thus plays an important role in determining the final fate of an S-AGB star (see Section for more on mass loss).

1.1.3 Massive stars $M/M_{\odot} \gtrsim 8$

In massive stars, the core proceeds towards more advanced stages of nuclear burning. The evolution of a $16 M_{\odot}$ star with the metallicity of the Large Magellanic Cloud ($Z=0.0055$) is shown in Fig. 1.1. The following are the stages of core burning in massive stars (Iliadis, 2007; Woosley, Heger, and Weaver, 2002), along with temperatures of burning for a $20 M_{\odot}$ solar metallicity star as in (Heger et al., 2003) provided in parenthesis.

In stars more massive than $10 M_{\odot}$ (Woosley, Heger, and Weaver, 2002), fusion reactions continue in the core beyond carbon burning. At the end of C-burning, the core contains ^{16}O , ^{20}Ne , ^{23}Na and ^{24}Mg (Iliadis, 2007). The next stage of burning is that of the photodisintegration of Ne ($T=1.6$ GK), via $^{20}\text{Ne}(\gamma, \alpha)^{16}\text{O}$, through which α -particles are liberated. These α -particles are then used to synthesize ^{24}Mg and ^{28}Si .

After Ne is completely consumed, the next fusion process in the core is that of O-fusion ($T=2$ GK), whereby ^{16}O nuclei fuse to create ^{28}Si and ^{32}S . The next stage of core burning ($T=3.3$ GK) is not that of silicon (Si) fusion but that of photodisintegration reactions that result in the liberation of protons, neutrons and alpha-particles that create the heavier and more tightly-bound iron-peak nuclei (Iliadis, 2007). The dominant products of this stage of burning are ^{54}Fe , ^{56}Fe and ^{56}Ni along with smaller fractions of ^{57}Fe and isotopes of Ti, V and Cr (Woosley, Heger, and Weaver, 2002).

Iron nuclei have some of the highest binding energies per nucleon and the temperatures required for its fusion are not achievable during the contraction of the core. A single star at this stage is a red supergiant (RSG), which begins to collapse due to the lack of thermal pressure in its core. Depending on the initial mass of the star, the RSG can either explode as a supernova, leaving behind a neutron star or a black hole remnant, or directly collapse to form a black hole, or explode and leave no remnant behind (Woosley, Heger, and Weaver, 2002; Heger et al., 2003; Sukhbold et al., 2016).

1.1.4 Other factors affecting stellar evolution

Aside from mass, factors such as the initial metallicity, mixing processes, mass loss from the surface, and rotation play an important role in determining the evolutionary path of a star.

Metal-poor stars are more compact, hotter, more luminous and have longer evolutionary timescales than solar metallicity stars of the same mass (de Mink, Pols, and Yoon, 2008). Metallicity also affects the mass-loss rate of the star, as we shall see next.

- **Mass loss:** Stellar winds drive mass loss from the surface, at different stages of evolution for low/intermediate mass and high mass stars. These winds can result in the substantial decrease of a star's initial mass, thereby affecting its future evolution.

Cool, luminous red (super) giants which have $T_{\text{eff}} \approx 3000 - 4000$ K, are known to experience large mass loss from their surface through slow winds of 10-50 km/s (Willson, 2000). Although the actual physics of the mass loss is yet to be fully understood (Willson, 2000; Bennett, 2010), radiation pressure of photons on spectral lines of atoms, molecules and dust in the atmosphere is considered to be the main driver. The observed mass-loss rates of red (super) giants are found to decrease with metallicity, since there would be fewer molecules and dust to be driven by radiation pressure (Langer, 2012).

Stellar winds from red giants are the main mass loss drivers for low-mass stars, and occur during their RGB and AGB phase. During the thermal pulsing stage of AGBs, there is an increased mass loss from the surface, which results in the loss of the envelope and the star evolves to a hot WD (Herwig, 2005; Karakas and Lattanzio, 2014). In S-AGB stars, if mass loss is large enough and the core has grown enough, the end state of the star will be an ONe WD. On the other hand if the mass loss is low, the S-AGB star will explode as an EC SN (Doherty et al., 2015).

Mass loss from the surface of massive main-sequence stars, which have $T_{\text{eff}} > 10^4$ K, is driven by ultraviolet photons exerting radiation pressure on ions. These accelerated ions couple with other particles in the surface through scattering and electrostatic forces and drive a wind flow (Lucy and Solomon, 1970; Castor, Abbott, and Klein, 1975a; Kudritzki and Puls, 2000). Another type of mass loss for massive stars with $M > 60M_{\odot}$, is associated with the Eddington limit (Langer, 2012), where if the surface luminosity of the star exceeds the Eddington limit, radiation pressure can drive mass loss from the surface. The two types of winds described above, also affect the evolution of hot blue supergiants. Stellar pulsations, violent eruptions from the surface, and rotation at critical velocity can also result in mass loss.

In stellar evolution codes, empirical mass-loss rates based on observations are used for red giants and supergiants, the most commonly used ones being those of de Jager, Nieuwenhuijzen, and van der Hucht (1988) and Nieuwenhuijzen and de Jager (1990a).

For hotter stars, the empirical mass-loss rates of Hamann, Koesterke, and Wessolowski (1995) and Hamann, Gräfener, and Liermann (2006), along with analytic formulae derived from stellar wind models such as those of Vink, de Koter, and Lamers (2000), Vink, de Koter, and Lamers (2001), and Vink and de Koter (2005), are used. The reader is referred to the reviews of Willson (2000) for a review on winds of cool stars and Kudritzki and Puls (2000), Puls, Vink, and Najarro (2008), and Smith (2014) for winds of hot stars.

- **Mixing processes:** There are many types of mixing processes that can occur in a star. The most efficient one, is convective mixing which operates on the local dynamic timescale (Heger, Langer, and Woosley, 2000). Convective mixing smooths out compositional inhomogenities; the dredge-up episodes of giant stars mentioned earlier result in material from partially burnt layers in the inner regions of the star brought to the surface, and also bring down nuclear fuel from the outer layers of the star to the core, thus increasing their burning lifetime. The treatment of convection thus is very important in determining the chemical abundances of the surface of stars.

When the radiative temperature gradient in a region becomes larger than its adiabatic temperature gradient due to a large luminosity (such as in the cores of stars with $M > 1.2M_{\odot}$) or if the opacity is large (such as in the envelopes of red giants), the region cannot transport energy via radiation alone and convection sets in. The common description of convection used in stellar interiors, contains a free parameter called the mixing length. The ‘mixing length theory’ (MLT) describes convection through the rising of hot, buoyant bubbles and the sinking of cold, dense bubbles, which travel a characteristic mixing length before dissolving into its surroundings and depositing its energy there. This characteristic length of mixing is defined as $l = \alpha H_p$, where α is a coefficient determined by calibrating stellar models to the Sun ($\alpha=1.6$ for the Sun) and H_p is the pressure scale height (Kippenhahn, Weigert, and Weiss, 2012).

In addition to convection, there are other mixing processes at work in the star, such as semiconvection, overshooting, thermohaline mixing and mixing due to rotation and magnetic fields.

- **Rotation:** Every star rotates: high mass stars are faster rotators than their low-mass counterparts (Hunter et al., 2008a; Hunter et al., 2008b; Penny and Gies, 2009). Rotation can induce several changes in the star: centrifugal forces can cause the star to become more oblate and cause it to expand, which makes the star cooler and lowers its luminosity and effective gravity (Langer, 2012).

At the end of every burning phase in the core, the core contracts and spins faster while the envelope expands and spins slower, thereby seeding differential rotation in an initially rigidly rotating star. Convective mixing causes the movement of masses and redistributes angular momentum, which flattens the velocity gradient in those

zones that are differentially rotating. The transport of angular momentum from the core also prevents the rotating core from approaching critical velocity (Langer, 2012) which would otherwise result in an unstable stellar structure. The efficiency of angular momentum transport to the surface affects the spin rate of the envelope and the rotation of the iron core at the time of collapse, which in turn determines the spin rate of pulsars (Heger, Langer, and Woosley, 2000; Heger and Langer, 2000; Langer, 2012). Differential rotation can cause various types of instabilities, that mix material from the core to the envelope, such as: shear instability, Solberg-Hoiland instability, meridional (Eddington-Sweet) circulation and Goldreich-Schubert-Fricke instability. For details of these rotational instabilities, we refer the reader to the works of (Maeder, 1999; Heger, Langer, and Woosley, 2000; Maeder and Meynet, 2000).

Rotational mixing enriches the envelope of massive stars on the main-sequence with products of H-burning through the CNO cycle; we observe the surfaces of massive main-sequence stars to be rich in He and N (Hunter et al., 2008b). Since rotational mixing also increases the nuclear fuel supply of cores, rotating stars live longer than corresponding non-rotating models (Heger and Langer, 2000). The surface temperature and luminosity of rotating stellar evolution models are also higher than their non-rotating counterparts as shown in Fig. 1.1.

Differential rotation can also generate magnetic fields called dynamos, through magnetohydrodynamic mechanisms. These magnetic fields also induce mixing and exert torques on the core thereby reducing its spin rate (Spruit, 2004; Heger, Woosley, and Spruit, 2005). The overall transport of angular momentum is thus affected by various mixing processes and also by the torques exerted by magnetic fields.

Rotation can also cause mass-loss from the surface, when the equatorial velocity of the star approaches the break-up velocity causing it to shed mass and angular momentum latitudinally to maintain equilibrium (Friend and Abbott, 1986; Heger, Langer, and Woosley, 2000). What happens to the ejected mass after it is shed— whether it forms an accretion disk which falls back on to the star or if the disk will evaporate, is not very well-understood.

Low and intermediate mass stars will die as He, CO or ONe WDs. The majority of massive stars are likely to explode as core-collapse supernovae (Smartt et al., 2009), which we study in the next section.

1.2 The end of massive stars: core collapse supernovae

At the end of Si-burning in the core, the star has a degenerate Fe core surrounded by nuclear burning shells, resembling an onion-layered structure (Fig. 1.2). The iron core contracts

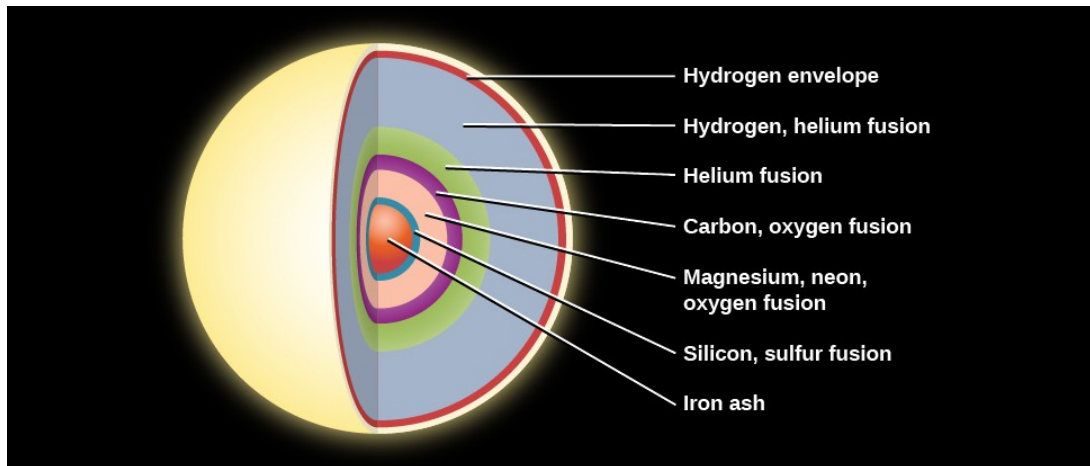


FIGURE 1.2: Cartoon depicting the final structure of a massive star, prior to core collapse. Image source: <https://courses.lumenlearning.com/astronomy/chapter/the-evolution-of-more-massive-stars/>

but does not reach temperatures required to fuse ^{56}Fe , which has the third highest binding energy per nucleon in nature. In the shell burning above the core, ashes of Si-burning increase the mass of the Fe core. When its mass reaches the Chandrasekhar limit of about $1.44 - 2M_{\odot}$, which is a function of the progenitor structure (Burrows, 2013), electron degeneracy pressure can no longer support the core and it begins to collapse. At temperatures around 10 GK, nuclear statistical equilibrium favours photodisintegration and electron capture reactions which together decrease the electron density in the core, thus accelerating its collapse (Janka et al., 2007; Janka, 2012). Neutrinos released by these reactions, interact with the surrounding matter. When the density of the core reaches nuclear densities ($\rho = 10^{14} - 10^{15} \text{ g/cc}$), repulsive short-range forces between nucleons abruptly stop the dynamical collapse of the core. The inner core bounces into the infalling layers and results in the propagation of a shockwave that explodes and unbinds the envelope of the star. Neutrinos carry away most of the gravitational energy released during the collapse ($\sim 10^{53}$ ergs) and only 1% of this energy is deposited at the bottom of the envelope, which transmits as the kinetic energy of the shockwave ($\sim 10^{51}$ ergs). The collapse of the core and its bounce, only take a fraction of a second, while the resulting supersonic shockwave travels through the envelope and emerges from the surface over a period of hours or days. Such explosions are called core-collapse supernovae (CCSNe) and they form the majority of all observed supernovae. For details on the explosion mechanism of CCSNe, please read the review articles of Janka et al. (2007), Janka (2012), Burrows (2013), and Müller (2017).

Supernovae are observationally classified based on the presence of H absorption lines in their spectra: Type II SNe have H-absorption lines while Type I SNe do not. The majority of CCSNe are Type II SNe, of which the most common type are Type II-Plateau (Type II-P) SNe, which are about 50 – 75% of all massive star supernovae (Smartt, 2009; Langer, 2012). Both models and observations indicate that the progenitors of Type II-P are massive

RSGs with radii of $\approx 500 - 100 R_{\odot}$ (Smartt, 2009; Hamuy, 2003; Dessart and Hillier, 2011). The distinct plateau phase of Type II-Ps are attributed to the large radius and mass of their RSG progenitors.

We next discuss the evolution of the light curve of Type II-P SNe. In Fig. 1.3, these are SN 1999em and SN 2003hn.

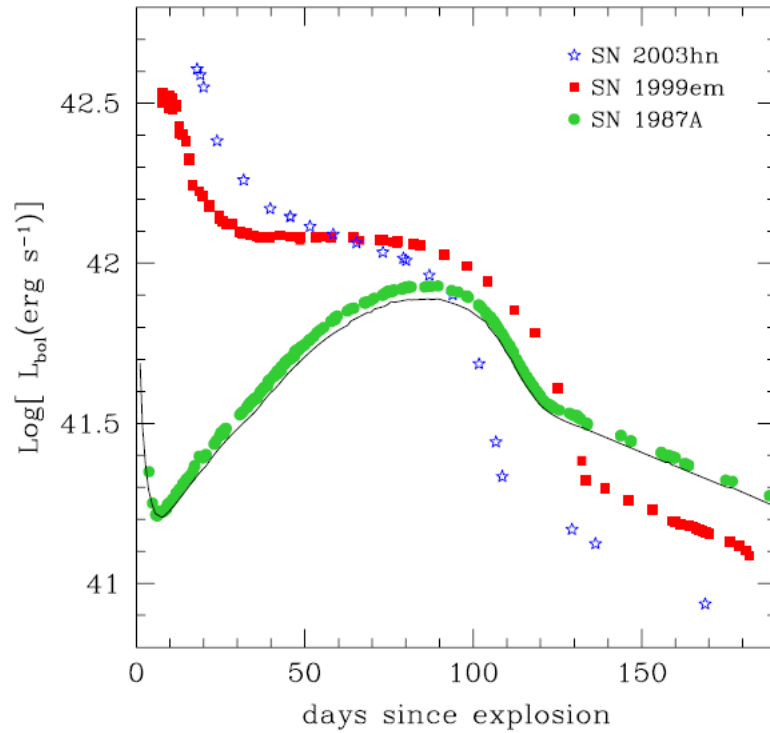


FIGURE 1.3: Comparing bolometric light curves of the Type II-P SNe, SN 1999em and SN 2003hn with that of SN 1987A. Day 0 refers to the first day of observation of the supernova. Figure from (Bersten and Hamuy, 2009).

After the collapse of the Fe core, a shockwave propagates outwards and most of its energy goes into adiabatically expanding the envelope to velocities greater than the local escape velocity while the rest of its energy heats the envelope and ionizes the surrounding gas (Utrobin, 1993). The passage of the shockwave heats the material in the outer core up to 5 GK within a fraction of a second causing the explosive burning of Si to nickel (Ni). The *shock breaks out* of the surface in a few hours-days and the luminosity surges to form a narrow peak in the soft X-ray/UV band (between $\sim 10^{44} - 10^{47}$ ergs/s). Due to its short duration, the early light curve phase has not been observed directly.

Due to adiabatic work done by the shockwave, the star expands by a factor of 30-100 (Woosley, 1988) and the ejecta begins to cool and consequently the bolometric luminosity drops rapidly. When the temperature of the outer layers drop to the recombination temperature of hydrogen, a photosphere forms at the shell where the hydrogen recombines,

and the ejecta becomes optically transparent (Hamuy, 2004). As the ejecta expands, a cooling and recombination wave (CRW) begins to travel inward in mass but stays at roughly the same radius and temperature, causing the inner layers of the star to become visible. The majority of the energy of the shockwave was used to adiabatically expand the star and only a small fraction of this energy is available as radiation (Woosley, 1988; Hamuy, 2004). When the CRW propagates inwards through the star, this trapped radiation diffuses outwards, causing the bolometric luminosity to rise. Although recombination does release energy, most of the visible bolometric luminosity is primarily the radiation energy left behind by the shock (Woosley, 1988). This is called the ‘*plateau phase*’, during which a well-defined photosphere travels inward and the bolometric luminosity is fairly flat. The properties of the plateau phase depend on the concentration of hydrogen and the radius of the expanded ejecta (Hamuy, 2004; Young, 2004), and it typically lasts for 100s of days. In this period, the outer envelope layers of the star (above the He core) are exposed.

The plateau phase ends when the CRW reaches the denser He-rich layers of the envelope, which expand at much slower velocities (Hamuy, 2004). The bolometric luminosity drops until the gamma-ray energy from the decay of ^{56}Ni to ^{56}Co trapped in the inner layers of the star (inside the He core), diffuses outward and powers the light curve. This is called the ‘*nebular phase*’ and is characterised by the exponentially declining luminosity tail, which follows the decay of ^{56}Ni (that has a half life of 6.1 days) to ^{56}Co (that has a half life of 77.1 days) which further decays to the stable ^{56}Fe . From the slope of the decay tail, we can estimate the mass of ^{56}Ni produced by the explosion (Smartt et al., 2009). Typically, $0.1 M_{\odot}$ of ^{56}Ni mass is produced in the explosion.

The type of remnant left behind after its explosion and its mass, depends on the initial mass of the progenitor, its metallicity and the ‘mass cut’ between the collapsing Fe core and the ejected envelope. These also determine the mass of nickel generated in the explosion and how much material falls back on the core after the explosion. The stellar evolution models of Heger et al. (2003) predict that single stars of initial mass $M = 8 - 40 M_{\odot}$ will end their lives as Type II-P SNe at all metallicities. The remnant is a neutron star for solar metallicity stars and for metal poor stars between $M = 8 - 25 M_{\odot}$, whereas for metal-poor stars between $M = 25 - 40 M_{\odot}$, the remnant is a black hole that is formed due to fallback from the ejecta of the supernova explosion. Observationally, however, Smartt (2009) find that progenitors of Type II-P SNe are most likely to have $M = 7 - 18 M_{\odot}$ which is lower than the theoretical progenitor mass of Heger et al. (2003). The more recent theoretical study of Sukhbold et al. (2016) demonstrated that the ‘explodability’ of a massive star cannot be taken for granted; they found that all stars between $M = 8 - 15 M_{\odot}$ will explode, but stars of masses between $M = 15 - 25 M_{\odot}$ and $M = 30 - 60 M_{\odot}$ rarely or never explode.

SN 1987A, the most well-studied supernova in literature, was a Type II SN, whose progenitor was a massive star with a H-rich envelope, but was not an RSG. Its light curve

hence, was not the typical plateau shaped light curve of Type II-P SNe.

1.2.1 Supernova 1987A



FIGURE 1.4: SN 1987A located at the edge of the Tarantula Nebula in the Large Magellanic Cloud. Image credit: Anglo-Australian Observatory

Until 1987, stellar evolution theory predicted that only red supergiant stars (RSGs) could explode as Type II SNe (Falk and Arnett, 1977; Woosley, Pinto, and Weaver, 1988; Arnett et al., 1989). In February 1987, the discovery of the closest supernova in 400 years turned tables on conventional stellar theory. SN 1987A (Fig. 1.4) which occurred in the Large Magellanic Cloud (LMC) became the most well-recorded celestial event of our time, data for which was collected from about 2 hours after the explosion took place (Menzies et al., 1987; Hamuy et al., 1988a), all the way until today (Catchpole et al., 1988a; Caldwell et al., 1993). H-absorption lines were visible in its early spectrum and it became classified as yet another Type II SN, whose progenitor was expected to be an RSG. The light curve of SN 1987A however, began to look distinctly different from Type II-P SNe (Fig. 1.3). At 10 days, the light curve slowly began rising to a maximum and its peak luminosity was lower than typical Type II SNe (Woosley, Pinto, and Weaver, 1988; Woosley, 1988). The overall dome shape of the light curve and the lack of a plateau feature, confirmed that the progenitor could not have been a radially extended giant, but a more compact one.

The progenitor, Sk $-69^{\circ}202$

Since SN 1987A had occurred in the nearby LMC, its progenitor was serendipitously recorded, the first direct progenitor detection ever made. The progenitor in the pre-explosion image was identified as Sanduleak $-69^{\circ}202$ (Sk $-69^{\circ}202$) – a hot, compact blue supergiant (BSG) of about $28\text{--}58R_{\odot}$ (Gilmozzi et al., 1987; Sonneborn, Altner, and Kirshner, 1987; Walborn et al., 1987; Woosley, Pinto, and Weaver, 1988). Neutrino burst events were detected preceding the optical detection of the supernova, which confirmed the neutrino driven core-collapse theory of supernovae explosions (Hirata et al., 1987; Bionta et al., 1987; Burrows and Lattimer, 1987).

A triple-ring nebula surrounding the supernova was discovered using the New Technology Telescope (NTT) of the European Space Observatory (ESO) (Fransson, 1988; Wampler et al., 1990). The nebula was observed to be an aspherical but assymmetric bipolar structure consisting of two outer rings, perpendicular to an equatorial inner ring, in the centre of which was the supernova. In April 1994, the high-resolution imaging of the nebula in H_{α} using the Hubble Space Telescope (HST) confirmed this structure and gave further details of its geometry and dimensions (Burrows et al., 1995). By measuring the velocity of the inner ring, it was determined that the nebula was ejected by the BSG at least 20 kyr before exploding (Burrows et al., 1995; Sugerman et al., 2005a; Sugerman et al., 2005b). The rings of the nebula, which reflected the surface composition of Sk $-69^{\circ}202$ at the time of ejection, were enriched in N/C, N/O and He/H (Fransson et al., 1989; Lundqvist and Fransson, 1996; France et al., 2011). All this information makes Sk $-69^{\circ}202$ the most well-recorded progenitor of any supernova yet.

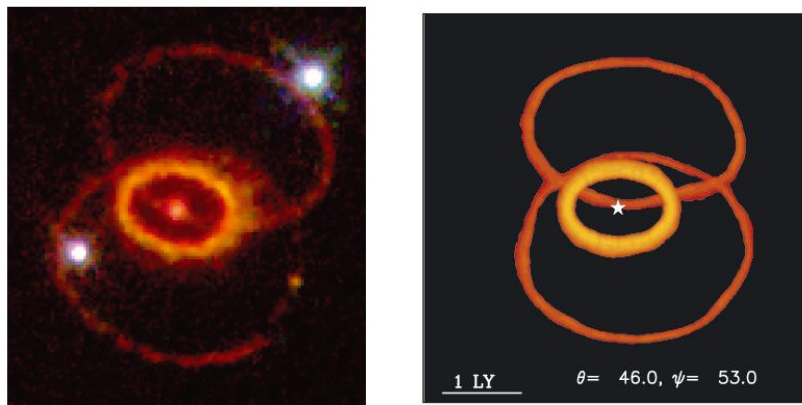


FIGURE 1.5: Left: Image taken in H_{α} by Hubble space telescope (HST) in April 1994. Right: Simulated emission measured in H_{α} on day 2000 after the explosion from a binary merger model. Figure from Morris and Podsiadlowski (2009).

The reason why the progenitor of SN 1987A was blue instead of red has been one of the biggest stellar evolution problems of the 20th century. The traditional approach was to investigate a stellar evolution problem, was to consider a single star model. These models,

however, had considerable difficulties in evolving to a BSG at the time of its explosion, without evoking extreme physics and delicate fine-tuning. For a review on single star models refer to Woosley, Pinto, and Weaver, (1988; Woosley, 1988; Arnett et al., 1989; Podsiadlowski, 1992 and references therein. The main issue with single star models was that they could not explain how a single star could rotate so rapidly as to gain enough angular momentum to eject mass in the form of the observed triple-ring nebula. The rotating single star models of Woosley et al. (1997), Heger and Langer (1998) and Chita et al. (2008), however, did undergo a red-blue loop during their evolution, which spun up the envelope and caused its ejection, but these models remained as RSGs till the end of their evolution.

The nebular structure was the key feature pointing toward a binary merger in the history of Sk $-69^{\circ}202$. The merger of a binary system can provide enough angular momentum to the envelope that would spin it up and cause its partial ejection (Podsiadlowski, 1992; Podsiadlowski, Morris, and Ivanova, 2006). The simulations of Morris and Podsiadlowski (2006) and Morris and Podsiadlowski (2009) that used binary merger models constructed from 3D hydrodynamic simulations, could reproduce the complex shape of the nebula (Fig. 1.5). Evolutionary calculations of Podsiadlowski, Joss, and Rappaport (1990) and Podsiadlowski, Joss, and Hsu (1992) showed that stars evolved from binary mergers could evolve and explode as BSGs. Details of the merger process and their possible post-merger evolution were studied by Ivanova and Podsiadlowski (2002b), Ivanova and Podsiadlowski (2002a), and Ivanova and Podsiadlowski (2003) and the hydrodynamic simulations of the merger process itself were performed by Ivanova, Podsiadlowski, and Spruit (2002) and Ivanova (2002). We review the binary evolution for Sk $-69^{\circ}202$ in Section 1.2.1.

Ring-shaped circumstellar nebulae have been found around other BSGs as well, such as MN18 (Gvaramadze et al., 2015), SBW1 (Smith, Bally, and Walawender, 2007; Smith et al., 2013), HD 168625 (Smith, 2007). An object that is considered a more luminous twin of Sk $-69^{\circ}202$ of luminosity $\log(L/L_{\odot}) = 5.78 - 5.90$ (Smartt et al., 2002; Melena et al., 2008) is Sher 25 located in the Milky Way. The nebula surrounding this BSG is enhanced in nitrogen (Smartt et al., 2002; Hendry et al., 2008) and has a similar hourglass morphology, mass and kinematics to the triple-ring nebula in of SN 1987A (Brandner et al., 1997b; Brandner et al., 1997a). This is also the case for the central star and circumstellar ring structure of SBW1 (Smith, Bally, and Walawender, 2007; Smith et al., 2013), suggesting that these stars may have undergone a similar evolution as Sk $-69^{\circ}202$.

The explosion

SN 1987A is classified as a peculiar Type II supernova (Type II-pec SN). Since its discovery, eleven other Type II-pec SNe have been discovered and hence are predicted to have had BSG progenitors (Pastorello et al., 2012; Taddia et al., 2013) with $R \leq 70 R_{\odot}$. The eleven other Type II-pec SNe also showed a similar light curve shape as SN 1987A and thus point toward

a similar BSG progenitor and evolutionary history. From observations of CCSNe it appears that Type II-pec SNe are rare events, forming only 3% of all CCSNe (Smartt, 2009). Binary population synthesis calculations expect, however, that 5-10% of all massive stars will undergo the merger that led to the formation of Sk -69°202 and thus explode as Type II-pec SNe (Podsiadlowski, Joss, and Rappaport, 1990; Podsiadlowski, Joss, and Hsu, 1992).

In Type II-pec SNe, most of the shock energy was used to adiabatically expand the compact progenitor compared to the extended red supergiant progenitor of Type II-P SNe, which hence led to a fainter peak luminosity than typical Type II-P SNe. For Type II-P SNe, the duration of the plateau phase is dependent on the concentration of hydrogen in the envelope and the mass of the envelope and ends when the photosphere enters the hydrogen poor layers of the star. In the case of a compact BSG progenitor however, it is the diffusion flux from the radioactive energy released by the decay of ^{56}Ni to ^{56}Co that determines the width of the plateau phase (Woosley, 1988; Blinnikov et al., 2000). Thus the dome-shaped light curves of Type-II pec SNe are powered by the radioactive decay of nickel from a very early stage (about 40 days for SN 1987A) (Woosley, 1988; Utrobin, 1993; Hamuy, 2004). From the luminosity of the Ni decay tail, it is estimated that $0.073 \pm 0.03 M_{\odot}$ of ^{56}Ni was created in the explosion of SN 1987A.

The smooth rise of the light curve (at day~ 8) and the broad dome shape, was predicted to have come from the large extent of mixing in the ejecta during the explosion (Woosley, Pinto, and Weaver, 1988; Shigeyama and Nomoto, 1990; Utrobin, 1993). Observations of the mixing of ^{56}Ni from the centre to the outer layers and that of ^1H mixed inward confirmed this prediction. Hydrogen was observed to mix down to layers moving at velocities of 500–600 km/s (Chugai, 1991; Kozma and Fransson, 1998), which explained the broad maximum of the light curve. The smooth rising of the light curve was explained by the large extent of mixing and clumping of ^{56}Ni (Fryxell, Arnett, and Mueller, 1991). On average ^{56}Ni clumps were observed to be mixed out to ≈ 3000 km/s (Erickson et al., 1988; Arnett, Fryxell, and Mueller, 1989), with even one clump found to be travelling at 4700 ± 500 km/s (Utrobin, Chugai, and Andronova, 1995).

3D hydrodynamic simulations that studied the explosion just after the core-collapse stage, using single star evolutionary progenitor models, could however, only obtain ^{56}Ni velocities upto 2200 km/s (Herant, Benz, and Colgate, 1992; Utrobin et al., 2015; Wongwathanarat, Müller, and Janka, 2015). Light curves calculated with a 1D radiation hydrodynamic code using these single star models also did not match the observed shape of SN 1987A very well either (Utrobin, 2005; Utrobin et al., 2015). Utrobin (2005) proposed that an optimal evolutionary model for SN 1987A, should have a radius $R = 35 R_{\odot}$ and an ejecta mass of $18 M_{\odot}$ and proposed that a binary merger evolutionary model may produce such an outcome.

In general, the astrophysics community agrees that a binary merger was responsible for the origin of Sk $-69^{\circ}202$ (Smartt et al., 2009). Since only single star pre-supernova models (i.e., models evolved until just prior to iron core collapse) for Sk $-69^{\circ}202$ are available in literature, explosion studies of SN 1987A are based on single star evolutionary models. As has been discussed in this section, these models cannot consistently explain all the observational characteristics of Sk $-69^{\circ}202$ and reproduce the explosion characteristics of SN 1987A.

What was missing from literature thus, were BSG pre-supernova (pre-SN) models built from binary mergers, that could consistently explain the observational features of the BSG progenitor of SN 1987A, namely, its position in the HRD, the N/C, N/O and He/H ratios observed in the nebula and its lifetime before explosion. The explosion of this pre-SN model should also match the light curve of SN 1987A. The work of this thesis, and the paper published thereof, Menon and Heger (2017), is the first to thoroughly and systematically investigated the evolution of mergers of massive binary systems in the context of SN 1987A and the outcomes of their explosion.

1.3 Born-again stars: R Coronae Borealis stars

R Coronae Borealis stars (RCBs) are a class of metal poor (Z is of the order of 0.001-0.0001), hydrogen-deficient carbon (HdC) stars. They are near-solar mass (Saio, 2008) F or G-type supergiants, with a surface luminosity of $3.5 \leq \log L/L_{\odot} \leq 4.0$ and temperature of $T_{\text{eff}} = 5000\text{K} - 8000\text{K}$ (Clayton, 1996; Alcock et al., 2001; Tisserand et al., 2008; Tisserand et al., 2013). They were first noticed due to their magnificent declines in brightness, by up to eight orders of magnitude in a few weeks at irregular intervals, and their slow recovery over months to years (Feast, 1979). These declines are attributed to the ejection of amorphous carbon dust from the surface of star (Feast et al., 1997; Feast, 1997).

Their surface chemical signatures are significantly different from typical metal-poor low-mass stars, thus indicating that these stars underwent an unusual evolutionary path. These surface chemical abundances are: nearly no hydrogen, 98% helium (Jeffery, 1996), $^{12}\text{C}/^{13}\text{C}$ ratios greater than solar (Rao, 2005; Hema, Pandey, and Lambert, 2012), enhancements in fluorine (Pandey, Lambert, and Kameswara Rao, 2008) and elements heavier than iron compared to solar (Rao and Lambert, 1996; Rao, 2005). The most unique of all nuclear signatures, is the number ratio of $^{16}\text{O}/^{18}\text{O}$ between 1 – 25 (Clayton et al., 2007; García-Hernández et al., 2010), which is much lower than the solar value of 500 and some of the lowest values measured in any star (a few HdC stars have $^{16}\text{O}/^{18}\text{O} \approx 0.1 - 0.3$; Clayton et al., 2007). These peculiar chemical signatures can only be explained by the burning and mixing processes occurring from the merger of a degenerate CO and He WD (Clayton et al., 2007; Longland et al., 2011; Staff et al., 2012; Menon et al., 2013). Other factors such as the lifetime

of the RCB phase and their observed numbers also indicate that a binary system was responsible for the origin of RCB stars. WD mergers are also expected to be the origin of other exotic objects such as Type Ia supernovae from CO + CO WD mergers (Han, 1998; Pakmor et al., 2012), helium subdwarfs (sdB stars) from He + He WD mergers (Saio and Jeffery, 2002) and also of close binary stars in planetary nebulae (De Marco, 2009).

Menon et al. (2013) demonstrated that the models built from CO+He WD mergers could evolve into RCB stars on the HR diagram, and reproduce the isotopic ratios and elemental abundances observed in RCB stars (Fig. 1.9). These were solar-metallicity models which were built from the library of stellar evolution tracks available at the time of that work. In order to confirm the validity of these models and directly compare them with the low-metallicity RCB stars, the same work needs to be done for CO+He WD merger models of the metallicity of RCB stars.

1.3.1 Pre-solar graphite grains

Observationally, nearly 100 RCBs have been recorded (Alcock et al., 2001; Tisserand et al., 2008; Tisserand et al., 2013). From the merger rate of CO+ He WD systems, these numbers can go up to 540 in our Galaxy (Karakas, Ruiter, and Hampel, 2015) and by extrapolating the observed numbers in the LMC population and with a higher WD merger rate, their number could even go up to 5700 (Clayton, 2012). Karakas, Ruiter, and Hampel (2015) identified that some pre-solar graphite grains, contain the low ratios of $^{16}\text{O}/^{18}\text{O}$ that are comparable to those found in RCB stars. Considering the expected number of RCB stars and their dust production rates, Karakas, Ruiter, and Hampel (2015) concluded that RCB stars could be viable sources of certain pre-solar grains.

Pre-solar grains are dust grains that condensed in the cool circumstellar environments of stars, which were then ejected into the interstellar medium via winds, novae, or supernovae explosions (Lugaro, 2005). At the time of the formation of the Solar System, some of these grains got trapped in asteroids and survived the destruction caused by gravitational heating when the protosolar molecular cloud collapsed (Lodders and Amari, 2005). Some of these asteroids were broken into smaller pieces due to impact with other rocks, and were deflected to enter the Earth's orbital path and hit its surface. The grains recovered from these meteorites, are nearly 4.5 Gyr old and were formed in the pristine conditions of the protosolar nebula. They thus give us insights into the conditions under which the Solar System formed (Zinner, 2014). Since each grain formed in the environment of a single star, studying their isotopic ratios can tell us the chemical composition of the gas surrounding the stars they originated from, and hence information about the nature of the parent star itself (Lugaro, 2005).

The current sample of pre-solar grains have been found in two meteorites: the Orgueil and Murchison meteorites, and they are broadly classified depending on their structure and

chemical composition into carbonaceous grains and oxide grains (Lodders and Amari, 2005; Lugaro, 2005). Relevant to this thesis, is the class of graphite grains (Amari et al., 1990), which are further divided as low density (LD) and high density (HD) grains. 22 of the LD grains contained the low $^{16}\text{O}/^{18}\text{O}$ ratios of RCBs.

In this thesis, we study the evolution of post CO+He WD merger models, computed with an initial metallicity comparable to that of RCB stars, using the methodology of Menon et al. (2013). We then compare their surface chemical abundances with those of RCB stars and also explore how viable RCB stars are as a source of certain pre-solar graphite grains.

1.4 Binary evolution

Most stars live in binary systems (Abt, 1983; Fischer and Marcy, 1992; Raghavan et al., 2010; Moe and Di Stefano, 2013). Binaries involving massive stars are observed to be more frequent than low mass binaries (Sana et al., 2013; Kobulnicky et al., 2014; Moe and Di Stefano, 2015). Like mass is to a single star, two main initial parameters of a binary system define the course of its evolution. They are the mass ratio between the components, $q = M_2/M_1$, where M_1 is the mass of the initially more massive component called the primary and M_2 is the mass of the secondary, and the initial separation between them (A).

Broadly, binary systems are categorized as interacting and non-interacting binaries. Stars in a binary system with a wide orbital separation, also called a **detached binary** (top panel in Fig. 1.6), do not interact with each other and are called non-interacting binaries. They may either be born as a detached binary or have undergone interactions during their evolution to become too widely separated to interact in the future. Stars in detached binary systems evolve as isolated single stars (Eggleton, 2011; Izzard et al., 2012).

Of interest to us are the interacting binary systems, in which mass is transferred from one companion to the other through various means (Webbink, 1984; Iben and Tutukov, 1984; Iben and Tutukov, 1987; Podsiadlowski, 2001; Ivanova et al., 2013). 30 – 50% of all stars (Podsiadlowski, 2001) and 70% of all massive stars are in interacting binaries (Sana et al., 2012). Many processes occur during the evolution of these systems, such as mass transfer, common envelope interactions, gravitational wave radiation, magnetic stellar winds, magnetic braking and tidal interactions. Mass exchange during a binary evolution changes the separation between the two stars and their individual structures as well. Prior to discussing interacting binaries, we need to understand two concepts: Roche lobe overflow and different types of mass transfer.

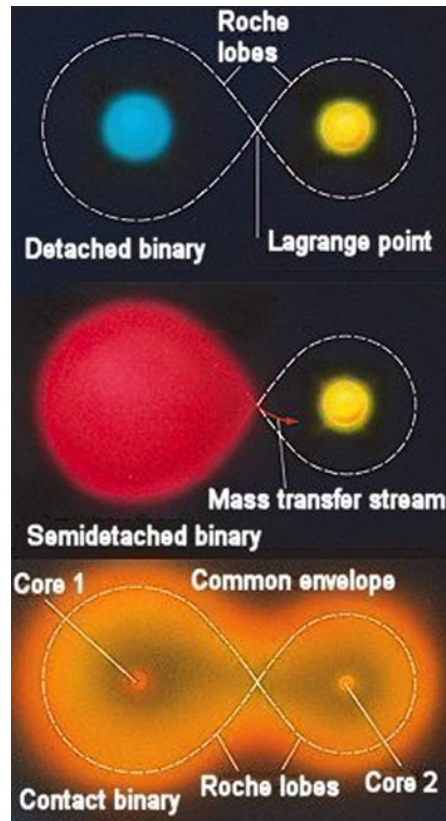


FIGURE 1.6: Different types of binary systems. Top panel: detached binary. Middle panel: semidetached binary. Bottom panel: contact binary. Image source: http://www.daviddarling.info/encyclopedia/C/close_binary.html

1.4.1 Roche Lobe

Mass is transferred from one star to another either via a stellar wind or via the more efficient way of a Roche-lobe overflow (RLOF) from one star to another.

Consider a system in which a massless test particle is in motion in the gravitational field of two stars of masses M_1 and M_2 , that have been brought to synchronised corotation by tidal forces. The equipotential in the corotating frame is determined by considering the gravitational potential of the stars and the centrifugal and coriolis forces on the particle (van den Heuvel, 2002). The equipotential surface is figure-of-eight shaped and the neutral point where this equipotential crosses itself is called the ‘inner Lagrangian point’, L_1 (Eggleton, 2011). Thus there are two teardrop-shaped surfaces surrounding each star— each of which is called the ‘Roche lobe’ and it is the volume within which material is gravitationally bound to the respective stars (Vanbeveren, De Loore, and Van Rensbergen, 1998; Eggleton, 2011). The Roche lobe radius (R_L) is only a function of q and the initial separation (A) between the two stars (Eggleton, 1983). For the primary R_L is calculated with $q = M_1 / M_2$ using:

$$R_L(A) = 0.49q^{2/3} / (0.6q^{2/3} + \ln(1 + q^{1/3})) \quad (1.1)$$

For the secondary, R_L is calculated by eq. 1.1 with $q = M_2/M_1$.

When a star expands and exceeds the radius of its Roche lobe, mass is transferred through L_1 to its companion. This mechanism of mass transfer is called the Roche-lobe overflow (RLOF) and occurs when the initial orbital period of the system is ≤ 1000 days (Podsiadlowski, 2008a; Eggleton, 2011), and also depends on the maximum radius of the stars and the amount of mass lost during the evolution.

A star can undergo a RLOF through a few ways (Iben and Livio, 1993)–when it evolves to a giant, as its radius expands about 1-3 orders of magnitude than its radius on the main sequence branch, thus exceeds its R_L . Under special conditions, a star on the main sequence can also overflow its Roche Lobe, and requires small orbital periods between 0.65-1.5 days (Paczynski, 1971). RLOF can also occur due to the orbital shrinkage, due to the loss of angular momentum through gravitational wave radiation (GRW) or magnetic stellar wind (MSW). Other reasons to trigger an RLOF from a star include the companion star being captured into its envelope due to tidal forces or, due to collisions with other stars in globular clusters.

1.4.2 Mass transfer

Mass transfer from one star to its companion can be a conservative process, i.e., no mass is lost from the binary system or, a non-conservative process, i.e., only a fraction of the mass is dumped on the companion and the rest is lost from the system. Mass transfer efficiency is thus an important parameter in the course of binary evolution. The star that transfers mass is called the ‘donor’ and the one that accretes mass is called the ‘accretor.’ As the primary is the initially more massive component of a binary system, it evolves faster to the giant phase and becomes a donor first. Mass transfers are further classified depending on what stage of evolution the primary fills up its Roche lobe. Orbital periods for a system with $M_1 = 5 M_\odot$, $M_1/M_2 = 2$ from Paczynski (1971) are given in parenthesis:

Case A: When RLOF from the primary occurs on the main sequence ($P_{\text{orbit}} = 0.65 - 1.5$ d).

Case B: When RLOF happens after hydrogen exhaustion in the core (on the Hertzsprung gap), but before the beginning of He fusion ($P_{\text{orbit}} = 1.5 - 87$ d).

Case C: When RLOF occurs after the ignition of helium in the core ($P_{\text{orbit}} = 87 - 4300$ d).

Early Case C mass transfer is said to occur during the He-shell burning phase in the AGB and late Case C mass transfer occurs after the end of He fusion and the primary has a CO core.

Depending on whether mass is transferred on a dynamically-stable or unstable timescale of the donor, there can be two types of interacting binary systems (Podsiadlowski, 2008b; Eggleton, 2011):

Semidetached binaries: A semidetached binary (middle panel in Fig. 1.6) is formed when the donor overflows its Roche lobe and transfers mass on a dynamically stable timescale to the companion star. The donor responds to the mass transfer by readjusting its structure and staying within its Roche lobe radius. Mass transfer occurs on a timescale larger than the thermal timescale of the accretor, hence it can accommodate the newly added mass. In order to conserve angular momentum (assuming no mass is lost from the system), the orbital distance of the system is widened. Mass transfer occurs until the donor loses most of its H-rich envelope and its final structure is that of a helium star with a thin H envelope. If the accretor was on the main sequence during the mass transfer, it becomes a more massive main sequence star. On the other hand, if it was a red giant, the added mass could lead to the formation of a more massive BSG (Podsiadlowski and Joss, 1989).

Contact binaries: A contact binary system is one in which the outer layers of the donor and the accretor touch each other. Often this happens when the accretor is immersed in the envelope of the donor (bottom panel in Fig. 1.6). Consider a donor giant star with a convective envelope, that expands and its radius exceeds its Roche Lobe. When this donor loses mass, it expands even further (although this may not be true for all giants with convective envelopes; Passy et al., 2011). The Roche Lobe radius of the donor shrinks according to Eq. 1.1, as $q = M_1 / M_2$ decreases with the decreasing mass of the primary. As the donor expands and the Roche Lobe radius shrinks simultaneously, a runaway mass transfer ensues from the donor on a dynamically unstable timescale. The accretor is engulfed in the envelope of the donor resulting in a ‘common envelope’ (CE) phase (Paczynski, 1976; Iben and Livio, 1993; Ivanova et al., 2013). A CE phase can also occur when material is transferred to the secondary faster than its thermal timescale. The secondary hence cannot accrete all the material deposited on it and overflows its Roche Lobe, leading to a CE episode (Ivanova et al., 2013). Such a system is called a ‘contact binary’ where both components are in physical contact.

1.4.3 Common envelope phase

The CE phase is one of the least understood phases of binary evolution (Iben and Livio, 1993; Ivanova et al., 2013). In a binary population synthesis code, mass transfer is considered dynamically unstable and leading to a CE episode, when the donor (of mass M_2) has a convective envelope and the mass ratio $q = M_1 / M_2 > q_{\text{crit}} = 0.67$ (Paczynski, 1976). The condition is not quite simple however for dynamical mass transfer to set in—detailed binary evolution calculations show, that mass transfer is dynamically unstable when $q > 0.83$ (Han et al., 2002). Some systems have been detected which have experienced late Case B/ Case C mass transfer, but still have relatively long orbital periods, suggesting that they did not

experience the dramatic orbital shrinkage that is the usual outcome of a CE phase (Eggleton and Tout, 1989; Podsiadlowski, Joss, and Hsu, 1992).

At the onset of the CE phase, the companion and the donor are in corotation with the envelope due to tidal forces. Due to dynamic friction with the envelope, the core and the companion begin spiralling in toward each other (Podsiadlowski, 2001; Ivanova et al., 2013), leading to the loss of orbital energy to the surface which drives the expansion of the envelope (Podsiadlowski, Morris, and Ivanova, 2006). As the envelope expands, tidal forces cannot synchronize the rotation of the envelope with that of the in-spiralling binary, leading to the loss of corotation (Podsiadlowski, 2001). The loss of corotation accelerates the spiral-in of the binary and the energy lost by orbital decay drives the further expansion of the envelope.

Depending on how much energy is transferred to the envelope, one of two things can happen: a) energy lost from the binary system is greater than the binding energy of the envelope, causing it to be entirely ejected, b) only a partial amount of the expanded envelope is ejected.

If it is case a), then the two components come closer and end up in a stable configuration, called a ‘close binary’, with an orbital period of a few hours to days (Paczynski, 1976; Eggleton, 2011). Double degenerate white dwarf binaries and cataclysmic variables are results of such a complete ejection of the common envelope (Schreiber et al., 2009). Further evolution of the close binary is driven by gravitational wave radiation and magnetic wind braking, which further shrink the orbital separation. This can ultimately lead to the merging of the two components.

If it is case b), the inspiral of the companion slows down as it reaches the denser layers of the envelope. The spiral-in of the companion continues until either the envelope is ejected due to the orbital energy radiated to the surface or when the companion overflows its Roche Lobe (Ivanova and Podsiadlowski, 2002b; Ivanova et al., 2013). The latter case leads to what is characterised as a ‘slow merger’ of the core of the primary and the secondary, which occurs over a period of ~ 100 years (Ivanova and Podsiadlowski, 2003; Podsiadlowski, Morris, and Ivanova, 2006).

A simple approximation to calculate how much mass is lost from the envelope, is to compare the orbital energy lost (ΔE_{orb}), i.e, the energy difference before and after the CE phase, with the gravitational binding energy of the envelope (E_{bind} ; Webbink, 1984; Iben and Livio, 1993). As not all of the orbital energy goes into driving envelope ejection during the CE event, an efficiency parameter called α_{CE} , such that $\alpha_{\text{CE}} = \Delta E_{\text{orb}} / \Delta E_{\text{bind}}$, is used to determine if the envelope will be ejected. If α_{CE} is greater than a particular value, then the envelope is expected to be ejected from the system.

The α -formalism for energy transferred to the CE, was developed further to include

the internal energy of the primary to calculate E_{bind} (de Kool, 1990), via a λ parameter. Using this prescription of the α -formalism, De Marco et al. (2011) found that systems with low values of the mass ratio $q = M_2/M_1$ have higher values of α , which means less massive companion stars are more efficient in ejecting the envelope. These systems with low values of q are hence more represented in the population of post-CE binaries.

The α -formalism described above can only be applied when the CE phase occurs on a dynamic timescale, i.e., within a closed system where there are no other sources of energy other than initial internal energy of the envelope and the orbital energy of the binary system (Ivanova et al., 2013). If the CE occurs on a longer timescale, such as the thermal or nuclear timescale of the envelope, other sources of energy also have to be considered, such as the accretion energy, recombination energy, tidal heating and nuclear energy (Ivanova and Podsiadlowski, 2002b; Ivanova et al., 2013).

Instead of considering the energy budget of the binary system to determine the result of the CE episode, one can also consider the angular momentum budget of the system. This method called the γ -formalism, examines the angular momentum lost from the system. The observational evidence which motivated this formalism came from close double-white dwarf binary systems, in which angular momentum had been lost through gravitational wave radiation (Nelemans et al., 2000; Nelemans and Tout, 2005). Overall, the γ -formalism is less commonly adopted in CE studies than the α -formalism method (Schreiber et al., 2009; Willems and Kolb, 2004; Ivanova et al., 2013).

We can thus conclude that the CE phase in a binary system's evolution is complex and its details are still uncertain. The general outcome of the CE phase for most binary systems, is to bring its components closer, and potentially lead to their merger to a single star, which we discuss in the next section.

1.5 Binary mergers

Ten percent of all stars are expected to merge (Podsiadlowski, Joss, and Hsu, 1992; Podsiadlowski, Morris, and Ivanova, 2006) while one in three of all massive star binary systems are expected to merge (Sana, Gosset, and Evans, 2009; Sana et al., 2012). Mergers are considered to be responsible for the origin of many interesting objects. Massive star mergers may have led to the formation of FK Com, V Hyd, η -Carinae, V838 Mon, the progenitor of SN 1987A, Sk -69°202 and other blue supergiants such as Sher 25, B[e] supergiants and HD 168625 (Podsiadlowski, Morris, and Ivanova, 2007). WD mergers may result in Type Ia Supernovae, R Coronae Borealis (RCB) stars and helium subdwarfs (sdB). Mergers also occur in neutron star binaries and black hole binaries. The merger process itself, however, is poorly understood and one of the least modelled phases of binary evolution (Ivanova et al., 2013).

We describe the likely binary evolutionary sequence for the two objects studied in this thesis: Sk $-69^{\circ}202$ and RCB stars.

1.5.1 Sk $-69^{\circ}202$

Chevalier and Soker (1989) were the first to suggest that Sk $-69^{\circ}202$ may have formed through binary interactions, by considering the aspherical expansion of the envelope of the supernova. The first studies to investigate merger models for Sk $-69^{\circ}202$ are those of Hillebrandt and Meyer (1989), Podsiadlowski, Joss, and Rappaport (1990), and Podsiadlowski, Joss, and Hsu (1992). The scenario consists of the companion star merging with the primary RSG, via a case B/C mass transfer after which the secondary star is completely dissolved in the primary's envelope. A BSG model is formed either due to the enrichment of He in the envelope through dredge-up, which lowers the opacity of the surface (Hillebrandt and Meyer, 1989) or due to the secondary being dumped on the primary, which increases the latter's envelope mass (Podsiadlowski and Joss, 1989; Podsiadlowski, Joss, and Rappaport, 1990).

The merger model of Podsiadlowski, Joss, and Hsu (1992) involves a common envelope phase, wherein the cores of the primary and secondary stars are embedded in the envelope of the primary. Angular momentum transferred to the envelope from the winding orbital motion of the cores, leading to its spin-up and subsequent mass ejection. This is the first complete progenitor model that showed promise in explaining nearly all the observational aspects of SN 1987A (Podsiadlowski, 1992). The position of the final models in two evolutionary tracks published by these authors, lie where Sk $-69^{\circ}202$ was found before it exploded (Fig. 13 in Podsiadlowski, Joss, and Hsu 1992). This model was further developed via hydrodynamic simulation studies of the merger (Ivanova, Podsiadlowski, and Spruit, 2002; Ivanova, 2002) and the behaviour of the post-merger model (Ivanova and Podsiadlowski, 2002b), and the formation of the triple-ring nebula from the merger (Morris and Podsiadlowski, 2007; Morris and Podsiadlowski, 2009).

Fig. 1.7 describes the sequence of events characterising the binary evolution for Sk $-69^{\circ}202$, based on the evolutionary model of Podsiadlowski, Joss, and Hsu (1992) and Podsiadlowski, Morris, and Ivanova (2007). The binary system in these works initially consists of a primary star ($M_1 = 15 M_{\odot} - 20 M_{\odot}$) and a secondary ($M_2 = 1 M_{\odot} - 5 M_{\odot}$) companion star, both on the main sequence, orbiting with an initial period greater than 10 yr. As the primary approaches core He-depletion, it expands to an RSG which consists of a He core (consisting of a CO core + He shell) and convective envelope. It then overflows its Roche lobe and a dynamically unstable case C mass transfer from the primary to the secondary initiates a common envelope (CE) episode that engulfs the secondary. The system now consists of the He core of the primary and the main-sequence secondary inside the convective envelope. Due to viscous drag forces, the secondary spirals in rapidly towards the core and a fraction of the energy released during the orbital decay is transferred to the outer layers of the CE,

spinning it up. When the total orbital energy deposited in the envelope becomes comparable to the envelope binding energy, the envelope expands and ejects some of its mass. The outer rings of the nebula may have formed from the mass ejected during this CE phase.

The in-spiral phase ends when the secondary overflows its own Roche lobe (at a separation of about $10R_{\odot}$) and starts stable mass transfer to the core of the primary, driven by the friction with the envelope in a period of the order of ~ 100 yr. H-rich material from the secondary forms a stream during the accretion and penetrates the He core. This causes the dredge-up of He to the envelope and hence the He core shrinks in mass. As the secondary mass accretes on the He core, it also gets mixed in the convective envelope of the primary. A fraction of the H-rich secondary mass also penetrates the He core while an equivalent fraction of the He core is dredged up. The region just below the boundary of the He core is hot enough for the CNO cycle to operate and this burns the fresh fuel of hydrogen to helium and nitrogen. The He core mass that is dredged up to the surface is thus enriched in helium and nitrogen. Mass continues to be transferred from the secondary until it finally gets dynamically disrupted and dissolved in the envelope of the primary.

At the end of the merger, the structure of the star consists of a smaller He core, surrounded by an envelope of homogeneous chemical abundances which comprises of the envelope of the RSG primary, mixed with the mass of the secondary star and the material dredged-up from the core. Such a merger, occurring over a timescale of ~ 100 yr, is classified as a ‘moderate’ merger. The remnant will immediately appear as an RSG out of thermal equilibrium, then contracts continuously towards hotter temperatures and higher luminosities in the HRD. The star thus transitions from the red to the blue part of the HRD and appears as a near-critically rotating BSG, which sheds mass to form the inner ring of the nebula. It is expected that the post-merger star would live as a BSG for about 15 – 20 kyr until its explosion (Podsiadlowski, Morris, and Ivanova, 2006; Heger and Langer, 1998).

The best-fit hydrodynamic model of Morris and Podsiadlowski (2007) constructed on the basis of the above merger scenario, can successfully reproduce the triple-ring structure of the nebula, with a chosen inner ring mass of $\sim 0.4M_{\odot}$ and an outer ring mass obtained from the merger itself, of $\sim 0.02M_{\odot}$ each. The ring mass has not been rigorously constrained and could be higher than current estimates, depending on how much angular momentum is lost from the spiral-in of the secondary (Phillip Podsiadlowski, private comm.).

1.5.2 RCB stars

Two evolutionary channels have been proposed to explain the origin of RCBs: post-AGB stars that underwent a late He-shell flash while transiting to the WD track on the Hertzsprung Russell diagram (HRD), referred to as the final flash (FF) model (Renzini, 1990) and, the mergers of degenerate carbon-oxygen (CO) and helium (He) white dwarfs (WDs), referred

to as the double degenerate (DD) model (Webbink, 1984; Iben, Tutukov, and Yungelson, 1996). Two observational deductions favour the DD scenario over the FF scenario. One is the presence of high amounts of ^{18}O and ^{19}F in the atmosphere of the star; if RCBs originated from an FF, then they should not show excesses in these isotopic ratios as the He-burning temperatures in FF models can completely destroy the ^{18}O and ^{19}F to ^{22}Ne (Clayton et al., 2007; Werner and Herwig, 2006; Herwig et al., 2011). Sakurai's object which originated from a FF has a low ratio of $\sim 1.5 - 5$ (Asplund et al., 1997) whereas most RCBs have high values of this ratio, greater than 40. The second reason in favour of the DD scenario is the mass estimated of RCBs, between $0.8 - 0.9 M_{\odot}$, inferred from their pulsation periods (Saio, 2008). Single WDs have masses typically between $0.5 - 0.7 M_{\odot}$ (Bergeron, Gianninas, and Boudreault, 2007; Tremblay et al., 2016) and hence cannot explain the mass of RCBs. Overall, the DD evolutionary channel appears to be the main channel of formation for RCBs and have been studied by a number of works such as Saio and Jeffery (2002), Clayton et al. (2007), Lorén-Aguilar, Isern, and García-Berro (2009), Jeffery, Karakas, and Saio (2011), Longland et al. (2011), Staff et al. (2012), Menon et al. (2013), and Zhang et al. (2014). The evolutionary sequence for the DD scenario for RCB stars is shown in Fig. 1.8. The post-merger models of Menon et al. (2013) had a lifetime of $0.97 - 2.75 \times 10^5$ yr as RCB stars and agree with the expected lifetime of RCB stars of 10^5 yr (Clayton et al., 2011; Clayton, 2012).

Mergers of double degenerate WDs are calculated to occur at a rate of 0.0018-0.018/ yr (Han, 1998; Karakas, Ruiter, and Hampel, 2015). The following is the evolution sequence described in Webbink (1984), Iben, Tutukov, and Yungelson (1996), and Solheim (2010). Consider a close-binary system of low-intermediate mass main-sequence (MS) stars, for example, with $M_1 = 3 M_{\odot}$ for the primary and $M_2 = 1 M_{\odot}$ for the secondary. When the primary evolves to the AGB with a degenerate CO core, it overflows its Roche lobe and an unstable mass-transfer begins to the secondary. This leads to the first CE event, in which the CO core of the primary and the main-sequence secondary are engulfed by the envelope of the primary. Due to energy lost by the in-spiral of the two components, the CE is entirely ejected, leaving behind a CO WD and the nearly unchanged MS star, brought closer in a tight orbit. The secondary then evolves into a giant with a degenerate He core, overflows its Roche lobe and transfers mass on a dynamically-unstable timescale to the CO WD. This leads to a second CE event. Energy is lost to the surface as frictional and tidal forces act on the CO and He WD, with a subsequent decaying of their orbit. Once again, nearly the entire CE is ejected, and we are left with a CO and He WD orbiting around a common centre of mass in a common envelope. As they lose energy to the surface due to frictional forces, the two WDs come closer and the energy released to the surface causes the entire common envelope to be shed. The WD system now has an orbital period of a few hours. Due to gravitational wave radiation and magnetic braking, the two WDs come closer and the He WD begins to get tidally disrupted by the more massive and compact CO WD. We further describe the DD scenario in Chapter 4.

Hydrodynamic simulations of the merger show that the merging phase lasts for 100-1000 seconds with the He WD material settled over the CO WD (Lorén-Aguilar, Isern, and García-Berro, 2009; Staff et al., 2012). In the long term, this post-merger structure may evolve into a He-rich supergiant with solid-body rotation (Shen et al., 2012; Schwab et al., 2012), which could have the properties of an RCB star.

The work of Menon et al. (2013) is a prelude to the work done in this thesis on the evolution of RCB stars. Menon et al. (2013) constructed spherically symmetric 1D models of merged CO+He WDs based on the hydrodynamic simulations of Staff et al. (2012). The evolution of the post-merger structure was followed into the domain of the HR diagram where RCBs are observed to lie and the surface abundances of the models were compared with the observations of RCB stars. Along with convective mixing, these models also included an artificial mixing profile, motivated by the rotating envelope of the post-merger object. The models of Menon et al. (2013) could consistently obtain the low $^{16}\text{O}/^{18}\text{O}$ ratios of RCB stars, along with their other isotopic signatures and their position in the HR diagram (Fig 1.9), thus further strengthening the hypothesis that RCB stars originated from CO+He WD mergers.

1.6 Tools used in this thesis

The following is a description of the computational tools used in this thesis.

KEPLER: For the study on SN 1987A, the 1D hydrodynamic stellar evolution code KEPLER (Weaver, Zimmerman, and Woosley, 1978; Heger et al., 2003; Heger, Woosley, and Spruit, 2005; Sukhbold et al., 2016) was used. KEPLER includes angular momentum transport due to rotation, mixing induced by rotational instabilities (as mentioned under the ‘Rotation’ subsection of Section 1.1.4), nucleosynthesis and follows the evolution of the star until just prior to the onset of core collapse. Evolutionary calculations are computed with a 19-isotope network that follows energy generation until the exhaustion of oxygen in the core (Weaver, Zimmerman, and Woosley, 1978) and thereafter follows the evolution using a 128 species quasi-equilibrium network (Rauscher et al., 2002). The code also assumes that zones that are convectively unstable do not have a gradient in the velocity, i.e., these zones rotate with a uniform velocity. Further details of the code are presented in Chapter 2.

Opacity tables in the code were updated for the purpose of this project. Previously KEPLER only contained Type I OPAL tables (Iglesias and Rogers, 1996). We would like to acknowledge Dr. Thomas Constantino for extending the opacity tables of KEPLER, by providing his opacity interpolation routines and helping integrating them into KEPLER. The opacity tables now include Type II CO-enhanced OPAL tables, conductive opacities (Potekhin et al., 2006) and molecular opacities (Ferguson et al., 2005), taking

special care to treat temperatures lower than 10^4 K (Constantino et al., 2014). Previous versions of KEPLER did not finely resolve the surface zones of a model, which led to incorrect computations of the surface luminosity and temperature. We modified the code to compute finer zones between an optical depth of zero and $2/3$, where the photosphere is defined.

MESA: For the study on RCB stars, the open-source stellar evolution code MESA, v.6794 (Modules for experiments in stellar astrophysics; Paxton et al., 2015) was used. Chapter 4 includes details of how MESA was used in the project on RCB stars. For mass loss, we use the Blocker’s wind formula with a coefficient of $\eta = 0.05$ during the RCB phase, which was used in the AGB simulations by the NuGrid team (Pignatari et al., 2016) and Type I OPAL tables are used for calculating opacities.

NUGRID: Using the multi zone post processing network (MPPNP) frame of the Nucleosynthesis Grid (NuGrid) project (Herwig et al., 2008; Pignatari et al., 2016; Ritter, *in press*), each evolutionary track computed with MESA was post-processed. The code consists of a nuclear network spanning over 1000 isotopes and their corresponding nuclear reactions. At every cycle of the evolution, each radial zone of the star, which contains information such as its temperature, density, mixing, energy generated by nuclear burning, etc., is read in by the code to give a radial distribution of the chemical abundances of the star. The composition at the surface of the model is then compared with observations. The single zone frame of NuGrid was also used to compute chemical abundances at constant temperature and density conditions.

PYTHON: The open-source code Python was used to make all plots in this work (Hunter, 2007).

1.7 This thesis

This thesis is the summation of three projects. The research question in each project is as follows:

Chapter 2: The binary merger models for the progenitor of SN 1987A: Can binary mergers produce blue supergiants? What are the conditions under which they do? Would these match the observations of Sk –69°202 ? Published: Menon& Heger, MNRAS, May 2017 (Menon and Heger, 2017)

Chapter 3: Explosions of binary merger progenitors for peculiar Type II supernovae: Do the explosions of blue supergiant models from binary mergers match the light curve and other constraints of SN 1987A? How do they fare for other Type II-pec SNe? In preparation: Menon, Utrobin & Heger

Chapter 4: RCB stars and pre-solar grains: Can low-metallicity CO+He WD merger models match the observations of RCB stars? Could RCB stars be the origin of certain pre-solar graphite grains? Submitted to MNRAS: Menon, Karakas, Lugaro, Doherty & Ritter, October 2017

Chapter 5: Discussions & Conclusions: The main results of the thesis are summarized along with discussions about future work.

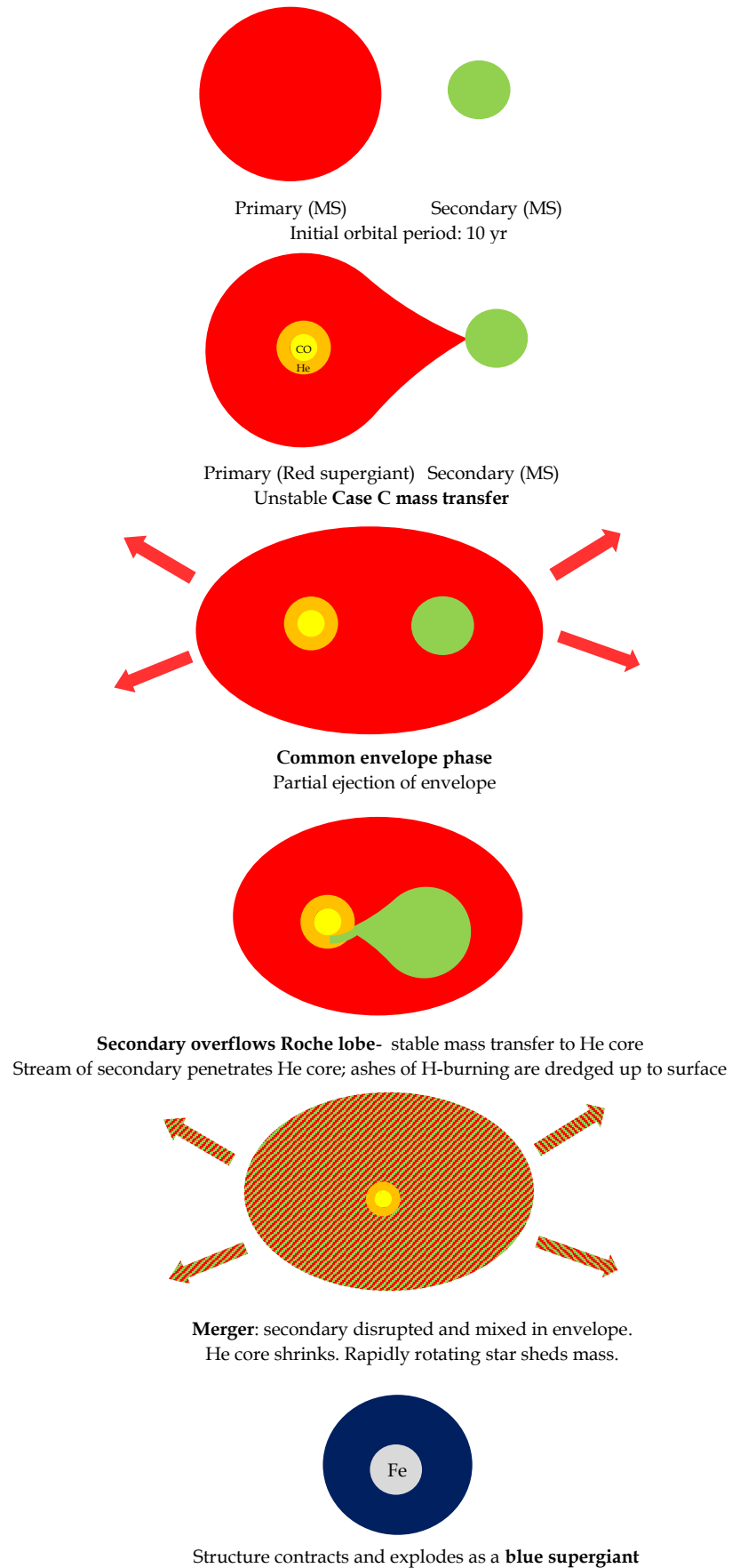


FIGURE 1.7: Evolutionary sequence for the binary system that led to the progenitor of SN 1987A.

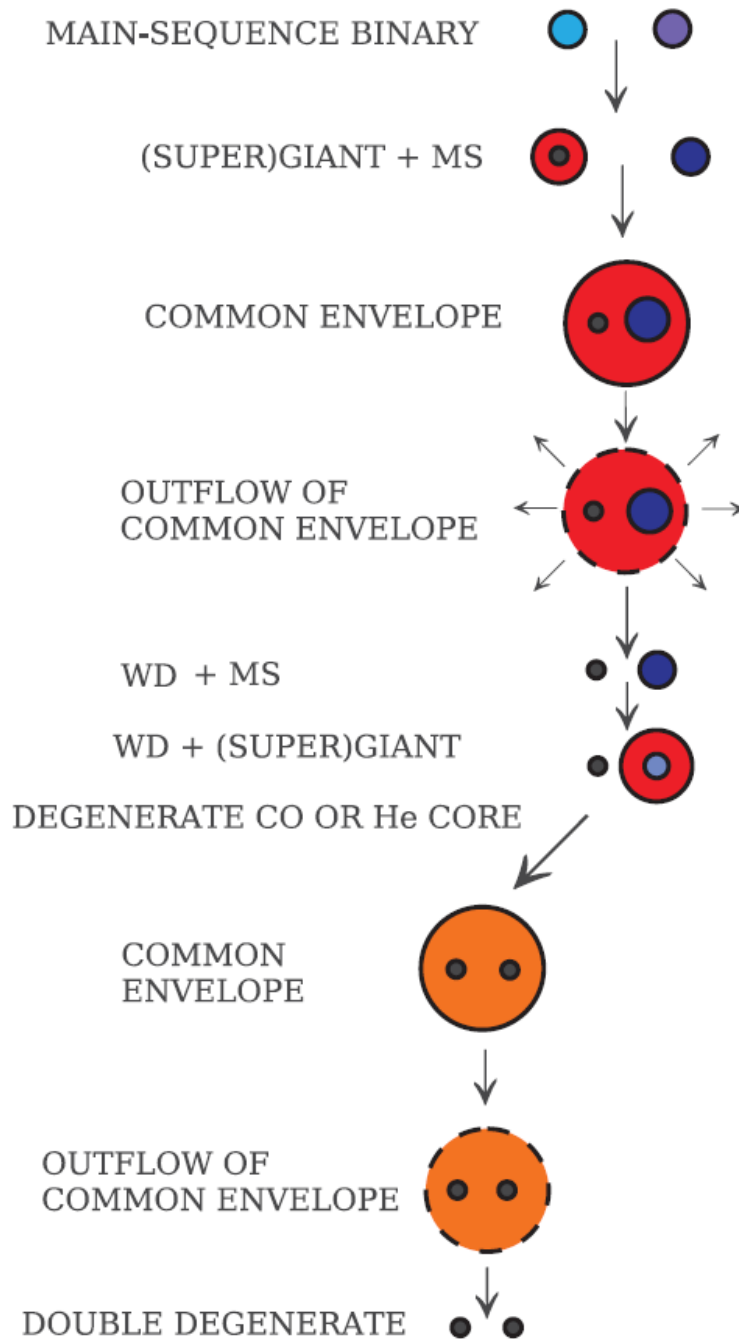


FIGURE 1.8: Evolutionary sequence for the binary system that would lead to RCB stars. Figure edited from Solheim (2010).

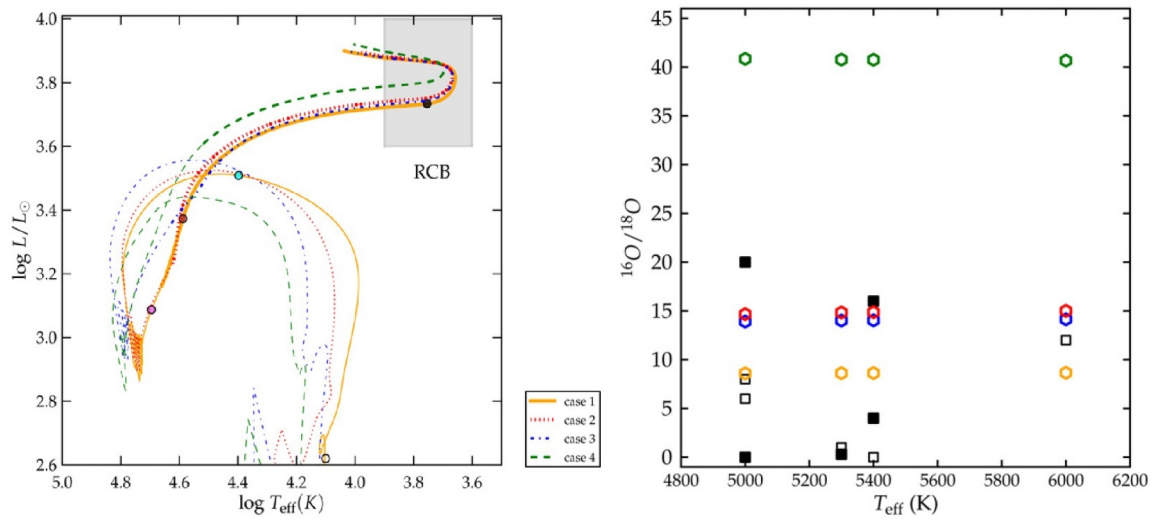


FIGURE 1.9: Left: 1D evolutionary models (the coloured lines) of post CO+He WD mergers, constructed with solar metallicity in Menon et al. (2013). Shaded region is the observed position including error bars, of RCB stars. Right: $^{16}\text{O}/^{18}\text{O}$ ratios on surfaces of the models (coloured symbols) against observed values in RCB stars (black symbols; Clayton et al., 2007; García-Hernández et al., 2010).

Chapter 2

Binary merger evolutionary models for the progenitor of SN 1987A

2.1 Introduction

In this chapter, we present the results of the binary merger models for the progenitor of SN 1987A, Sk $-69^{\circ}202$. We know the following characteristics of the progenitor:

Position in the HRD: From its absolute magnitude measurements and by calibrating it against other B3 supergiants in the LMC, the luminosity of Sk $-69^{\circ}202$ was deduced to be $\log(L/L_{\odot}) = 5.15 - 5.45$, with an effective temperature, $T_{\text{eff}} = 15\text{kK} - 18\text{kK}$ (Woosley, Pinto, and Weaver, 1988; Woosley, 1988; Arnett et al., 1989; Walborn et al., 1989). The radius of the star was thus calculated to be $R = (3 \pm 1) \times 10^{12} \text{ cm}$ ($\approx 28R_{\odot} - 58R_{\odot}$). Barkat and Wheeler (1989b) deduce a slightly less luminous and possibly cooler progenitor, with $\log L/L_{\odot} = 4.90 - 5.11$ and $T_{\text{eff}} = 12\text{kK} - 19\text{kK}$.

Surface chemical composition: The enhancements of helium and nitrogen in the nebular material, which was ejected from the envelope of Sk $-69^{\circ}202$ before its explosion, indicate that the star underwent H-burning through the CNO cycle during its evolution (Saio, Nomoto, and Kato, 1988; Fransson et al., 1989; Sonneborn et al., 1997; France et al., 2011). Fransson et al. (1989) and Lundqvist and Fransson (1996) measured $\text{He}/\text{H} = 0.25 \pm 0.05$ (ratio by number of atoms), in the nebular material but more recent estimates have lowered this value to $\text{He}/\text{H} = 0.17 \pm 0.06$ (Mattila et al., 2010) and $\text{He}/\text{H} = 0.14 \pm 0.06$ (France et al., 2011). Nitrogen is also enhanced in the nebula relative to carbon and oxygen; Lundqvist and Fransson (1996) estimated values of $\text{N}/\text{C} \sim 5 \pm 2$ and $\text{N}/\text{O} \sim 1.1 \pm 0.4$ while Mattila et al. (2010) reported $\text{N}/\text{O} \sim 1.5 \pm 0.7$. Older estimates for these ratios are $\text{N}/\text{C} \sim 8 \pm 4$ and $\text{N}/\text{O} \sim 1.6 \pm 0.8$ (Arnett et al., 1989).

Panagia et al. (1996) found that the outer rings are less enriched in N/C and N/O , by a

factor of ~ 3 than the corresponding values measured in the inner ring, thus concluding that the outer rings may have been ejected 10 kyr before the inner ring. These results were contested by Crotts and Heathcote (2000), who through a kinematic study, deduced that all three rings were expelled ~ 20 kyr before the supernova explosion. Maran et al. (2000) further supported this result, through long-slit optical spectroscopic measurements of the CNO abundances of the rings and found no discrepancies between the inner and outer rings, stating that Panagia et al. (1996) may not have taken time-dependent line emissions from the outer rings into account while measuring these abundances.

Possible enhancements in *s*-process elements, Ba and Sr, were also detected in the spectrum during the recombination phase (Mazzali, Lucy, and Butler, 1992; Mazzali and Chugai, 1995).

Duration of the BSG phase: The dynamical age of the blue supergiant (BSG), measured from the expansion velocity of the inner ring of the nebula, is estimated to be about 15 kyr–20 kyr before explosion (Burrows et al., 1995; Smith et al., 1998; Crotts and Heathcote, 2000).

Most of the mass of the nebula resides in the inner ring; the outer rings each weigh $\sim 0.045M_{\odot}$ (Lundqvist and Fransson, 1996). The total mass of the nebula is however, uncertain, although estimates range between $0.34M_{\odot}$ (Crotts and Kunkel, 1991) and $1.7M_{\odot}$ (Burrows et al., 1995; Sugerman et al., 2005a; Sugerman et al., 2005b). It should be borne in mind however, that these estimates are based on an hour glass model while the circumstellar nebula of SN 1987A is in the form of a triple-ring structure (Phillip Podsiadlowski, private comm.).

The current pre-SN models in literature are from single stars. Single star models include those of low-metallicity (Arnett et al., 1989), extreme mass-loss (Maeder, 1987; Wood, 1988), restricted-convection (Woosley et al., 1997; Langer, 1991), helium-enrichment (Saio, Nomoto, and Kato, 1988) and rapid-rotation (Weiss, Hillebrandt, and Truran, 1988; Hirschi, Meynet, and Maeder, 2004) (see (Arnett et al., 1989; Podsiadlowski, 1992; Smartt, 2009) for a full review). Barkat and Wheeler (1989a) performed a parameterised study which showed that the penetration of the convective envelope in the He core (i.e., the H-free core) shrinks the core and dredges up He and N to the surface. Furthermore, the smaller He core relative to the total mass favours a blue solution for the final model. A similar parameterised study by Petermann et al. (2015) for rotating massive stars, demonstrated that models with small He cores could evolve to BSGs.

From the luminosity of Sk -69°202 and by fitting light curves from explosions of single star models, the He core mass and envelope mass were estimated to be $M_{\text{He core}} \approx 4M_{\odot} - 7M_{\odot}$, and $M_{\text{env}} \approx 5M_{\odot} - 10M_{\odot}$ respectively (Woosley, 1988; Nomoto et al., 1988;

Woosley et al., 1997). These implied progenitor single stars of main-sequence mass between $14M_{\odot} - 20M_{\odot}$ (ignoring mass loss, rotation and overshoot mixing) (Woosley, Pinto, and Weaver, 1988; Saio, Nomoto, and Kato, 1988; Arnett et al., 1989; Smartt et al., 2009). As discussed in Section 1.2.1, these models however required extreme fine-tuning of parameters to obtain the transition from red to blue in the HR diagram (HRD) and to reproduce the unusual composition of the circumstellar material. Moreover they could not simultaneously explain how the triple-ring nebula was ejected prior to the explosion and how the model exploded as a BSG.

The drawbacks of the single star models can be explained by evoking a binary merger scenario. In this work, we use the merger model proposed by Podsiadlowski, Joss, and Hsu (1992) and Podsiadlowski, Morris, and Ivanova (2007). It begins with a wide binary system of a $15M_{\odot} - 20M_{\odot}$ primary and a $1M_{\odot} - 5M_{\odot}$ secondary, with an initial orbital period of greater than 10 yr. When the primary evolves to an RSG with a He-depleted core, it transfers mass on a dynamically unstable timescale on the secondary main-sequence star leading to a common envelope (CE) episode, during which the envelope is partially ejected. The secondary star is engulfed by the envelope of the primary and eventually undergoes a merger over ~ 100 yr (Ivanova, Podsiadlowski, and Spruit, 2002; Ivanova and Podsiadlowski, 2003). After thermally adjusting to its structure, the merged star is expected to contract to a rapidly-rotating BSG which sheds additional mass and finally explodes as a Type II-pec SN. The hot and fast wind of the BSG sweeps up the circumstellar material and shapes it to the triple-ring nebular structure we currently observe (Chevalier and Dwarkadas, 1995; Podsiadlowski, Morris, and Ivanova, 2007; Morris and Podsiadlowski, 2007; Morris and Podsiadlowski, 2009). The details of the entire binary evolution sequence are provided in Section 1.5.1.

In this work, we independently construct our evolutionary model based on the above merger scenario and the results of the hydrodynamic simulations and studies thereof by Ivanova and Podsiadlowski (2002b), Ivanova and Podsiadlowski (2002a), Ivanova, Podsiadlowski, and Spruit (2002), and Ivanova and Podsiadlowski (2003).

Of particular insight and relevance to our study are the predictions of Barkat and Wheeler (1989a). In their parameterised study of single star models between $18M_{\odot} - 25M_{\odot}$, they showed that if the He core is penetrated by the H-rich envelope, the star would have a smaller He core to total mass ratio. This in turn could influence the star to turn from red to blue during its evolution. The core penetration would also lead to the dredge up of CNO-cycle processed material, thus enriching the surface of the star with He and N. Through a similar parameterised study applied to rotating single massive stars, Petermann et al. (2015) also demonstrated that models with smaller He cores than their initial values, could favour blue solutions. Barkat and Wheeler (1989a) mentioned another solution to obtain a small He core to total mass ratio— one where the primary star accretes mass from its companion

in a binary system.

We study the evolution of 84 initial systems, through the merger phase and until just before the onset of iron-core collapse. Of these, six pre-SN models successfully reproduce the three signatures of Sk $-69^{\circ}202$: its position as a BSG in the HRD, its lifetime as a BSG before explosion and the high N/C, N/O and He/H ratios in its surface. These are the first pre-SN models in refereed literature to have obtained all the major characteristics of Sk $-69^{\circ}202$.

2.1.1 Aims and structure of this work

We build an ‘effective-merger’ model and follow the progress of the post-merger star until the onset of core collapse, using the stellar evolution code KEPLER.

Our aims are to:

1. Run simulations over a grid of initial parameter space consisting of primary and secondary masses and the boundary of mixing in the He core during the merger. These are the three major aspects that control the outcome of the merger.
2. Analyse the distribution of pre-SN models in the HRD and the number ratios N/C, N/O and He/H in the surface; determine how the choice of initial parameters affect the pre-SN models.
3. Identify progenitor candidates of SN 1987A that match the observed characteristics of Sk $-69^{\circ}202$.

We describe the code employed, the construction of our effective-merger model, the initial parameters and models in Section 2.2. We present the pre-SN models and how the choice of initial parameters affect them in Section 2.3. Finally we discuss our results and enlist the conclusions of our study in Section 2.4.

2.2 Methodology

2.2.1 The stellar evolution code: KEPLER

TABLE 2.1: Opacity tables with temperature and density regimes. $\log R = \log \rho - 3 (\log T - 6)$, where ρ and T are in cgs units.

Opacity tables	$\log \rho$ (gcm^{-3})	$\log T$ (K)
OPAL 1995	$-8.0 - 1.0$	$3.75 - 8.70$
Conductive opacities	$0.0 - 7.0$	$3 - 9$
Low-temperature opacities	$-8.0 - 1.0$	≤ 4

Based on the binary merger scenario in Section 1.5.1, we use KEPLER, an implicit one-dimensional hydrodynamics code that can compute stellar evolution models with rotation and nucleosynthesis (Heger, Langer, and Woosley, 2000; Heger, Woosley, and Spruit, 2005; Woosley, Heger, and Weaver, 2002; Woosley and Heger, 2007). The code uses the Ledoux criterion for convection. Energy generation follows a 19 isotope nuclear reaction network prior to oxygen depletion and a 128 isotope quasi-equilibrium network thereafter. A detailed description of the nuclear reaction rates used for energy generation can be found in Rauscher et al. (2002) and Heger et al. (2002). The physics of rotation in the stellar interior includes angular momentum transport, time-dependent mixing from various rotational instabilities, along with magnetic torques, turbulent viscosities and diffusivities from the dynamo model (please refer to Heger, Langer, and Woosley, 2000, Heger and Langer, 2000 and Heger, Woosley, and Spruit, 2005 for more details). Mass loss in the models arise from rotationally modulated winds (Heger, Langer, and Woosley, 2000) and mass-loss prescriptions, as described in Nieuwenhuijzen and de Jager (1990b). The evolution of the model is terminated at the onset of iron-core collapse which is considered to occur when the infall velocity approaches 9×10^7 cm/s. Due to convergence problems during the simulations, some of the models crash in the last few time-steps during core-silicon burning, before reaching the pre-SN stage. We cannot hence provide an estimate of their iron core mass ($M_{\text{Fe,c}}$). The surface quantities of these models however, do not change over such small time-steps of the order of hours. Therefore the radius, effective temperature, luminosity and chemical abundances of these models will be the same as those expected from their pre-SN models.

We recently updated the opacity tables in KEPLER which previously consisted only of Type I OPAL tables (Iglesias and Rogers, 1996 and Achim Weiss, private communication). KEPLER now includes alpha-enhanced Type I OPAL tables, Type II CO-enhanced OPAL tables and conductive opacities from Potekhin et al. (2006). The opacities (Table 2.1) and the routines for interpolating them in metallicity, temperature, density, hydrogen mass fractions and enhancements in C, N, O, and Ne were obtained from Boothroyd's homepage (<http://www.cita.utoronto.ca/~boothroyd/kappa.html>). Routines which vary opacity from changes in CNO abundances due to nuclear burning were also included. For temperatures lower than 10^4 K, composition-dependent low-temperature Rosseland mean opacities were computed with AESOPUS (Marigo and Aringer, 2009) which includes various sources of atomic, molecular and collision-induced opacities. The routine to interpolate these opacities was provided by Dr. Thomas Constantino (Constantino et al., 2014).

The new opacities are smaller compared to the values obtained from the old tables. The overall effective temperature and luminosity of the pre-SN models increase significantly with these smaller opacities. The role of correct opacities is thus crucial in determining the evolutionary path of the star.

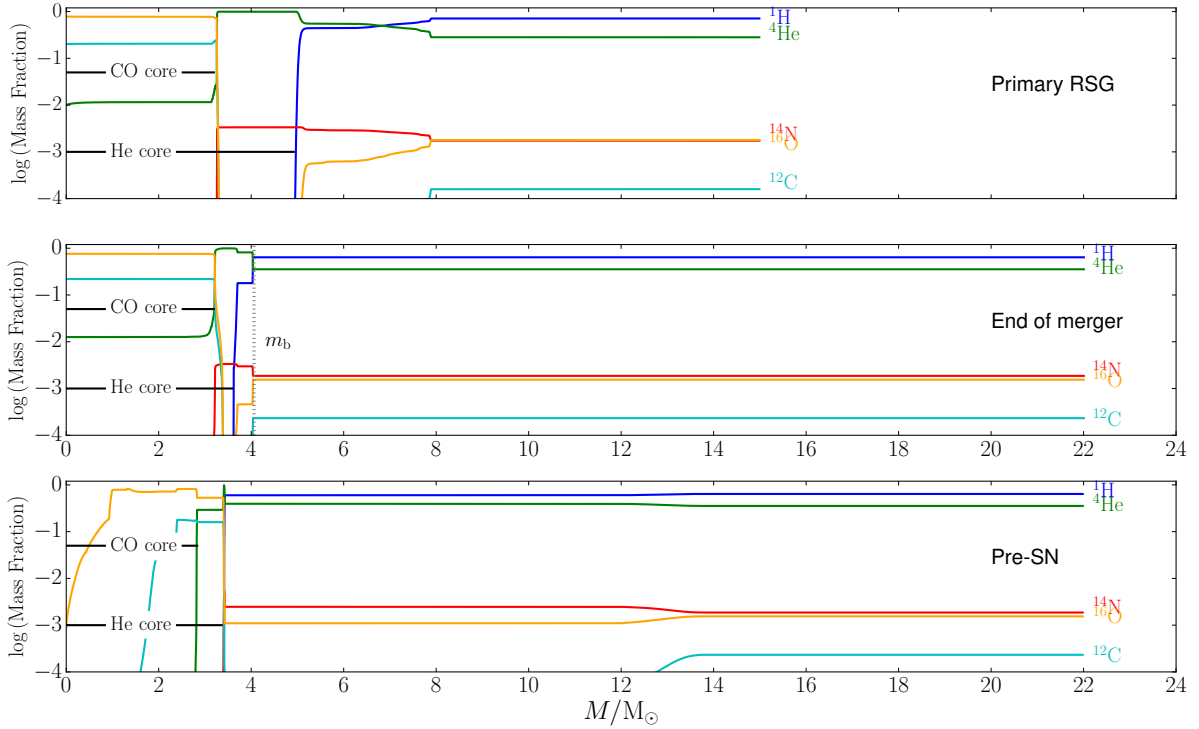


FIGURE 2.1: Top panel, stage B in Fig. 2.4: Composition of the RSG model from a primary of $M_1 = 16 M_\odot$ consisting of a He core of $M_{\text{HeC},1} = 4.92 M_\odot$ just prior to the merger. Middle panel, stage C in Fig. 2.4: Composition at the end of the merger with $M_2 = 7 M_\odot$. The boundary of mixing m_b (dotted vertical line) is set for $f_c = 16.6\%$. At the end of the merger, the star has a smaller He core of mass $3.61 M_\odot$. Bottom panel, stage D in Fig. 2.4: Composition of the pre-SN model. The surface composition of the star does not change much from the one at the end of the merger.

2.2.2 Effective-merger model

Our 1D effective-merger model is based on the processes outlined in Section 1.5.1. The merging phenomenon is characterised by the simultaneous accretion and mixing of the secondary star in the envelope of the primary.

In this model, we assume merging immediately follows after the primary of main-sequence mass M_1 evolves to become the required pre-merger RSG model (as will be described in Section 2.2.3) whose mass is M_{RSG} and consists of a He core of mass $M_{\text{HeC},1}$. M_{RSG} is slightly smaller than M_1 by $\approx 0.01 M_\odot$ due to mass loss through winds. From the hydrodynamic simulations described in Section 1.5.1, the merging phase is of the order of 100 yr, so in our scenario we choose a fixed merging period of 100 yr. This merging timescale is much shorter than the thermal time scale of the envelope, some 1000 yr, yet the thermal time scale is short compared to the lifetime of the post-merger star before its explosion (of the order of 10^4 yr– 10^5 yr), hence varying the merging period within an order of 100 yr does not affect the post-merger evolution in any significant way. The rate of accretion is $M_2/100$ yr, and for the range of M_2 we choose, this leads to accretion rates of $\dot{M}_{\text{acc}} = 0.02 M_\odot/\text{yr} - 0.08 M_\odot/\text{yr}$. M_2 is accreted with the same entropy and angular momentum as that of the surface of the

primary.

From the merger scenario, we know that the secondary star is entirely disrupted and mixed in the convective envelope of the primary by the end of the merger (Ivanova and Podsiadlowski, 2002b; Ivanova and Podsiadlowski, 2002a; Ivanova and Podsiadlowski, 2003). We implement this merging in our models by accreting a secondary star of uniform chemical composition on the primary RSG. In order to obtain this composition, the secondary main-sequence star is evolved to the same age as that of the RSG and then the total masses of individual isotopes are averaged over M_2 .

As M_2 gets accreted on the primary, it is also simultaneously mixed throughout its envelope. This mixing phenomenon is implemented through a Lagrangian mixing recipe, wherein each unit of M_2 accreted per timestep of the code ($\dot{M}_{\text{acc}} \times dt$) is mixed down progressively in mass to a boundary we specify, m_b , inside $M_{\text{He c}, 1}$. The He core mass is defined as the mass within which the hydrogen mass fraction drops to below $\sim 10^{-2}$. As a fraction of M_2 penetrates the He core of the primary, it brings down H-rich material and thus shrinks the mass of the He core, while an equivalent fraction (f_c) of $M_{\text{He c}, 1}$ is dredged up and mixed uniformly in the envelope. The boundary of penetration or mixing, m_b , of the secondary is thus set by f_c ; $m_b = M_{\text{He c}, 1} - f_c \times M_{\text{He c}, 1}$. Effectively, m_b determines the boundary of the He core of the merged star. Since, however, a convection zone forms during the merger at m_b , an additional amount of H-rich material is mixed down from the envelope resulting in a He core boundary that is smaller by 7% – 22% of m_b .

In this manner, by the end of the merger we have a star that consists of a He core whose mass is smaller by a fraction $\sim f_c$, and a massive homogenous envelope mixed with M_2 and $f_c \times M_{\text{He c}, 1}$ (Fig. 2.1). The total mass of the post-merger star is $\approx M_{\text{RSG}} + M_2$.

In this first study, the effective-merger we implement is a simplified model. We do not include any heating of the mass dumped by accretion, nor do we track its angular momentum. We also do not compute the angular momentum loss post the CE phase and consequently there is no additional momentum in the envelope or associated mass loss in our models. Our BSG models do not reach break-up velocities after the RSG contracts, hence no mass is shed from the system (aside from the $< 0.1M_{\odot}$ through RSG winds) and we cannot provide predictions for the BSG wind. These processes require detailed hydrodynamic simulations and have been investigated in other works mentioned in Section 1.5.1.

Mass-loss is, however, an important effect and it does play a significant role in the evolution of a star. Unfortunately an analytical prescription to calculate the mass ejected after the merger there does not exist (Morris and Podsiadlowski, 2009; Vanbeveren et al., 2013). The mass of the circumstellar nebula ejected by the progenitor, is currently estimated as $1.7M_{\odot}$ (Burrows et al., 1995). Thus the resultant mass of the post-merger star would be smaller by $1.7M_{\odot}$ than the sum of its components $M_{\text{RSG}} + M_2$.

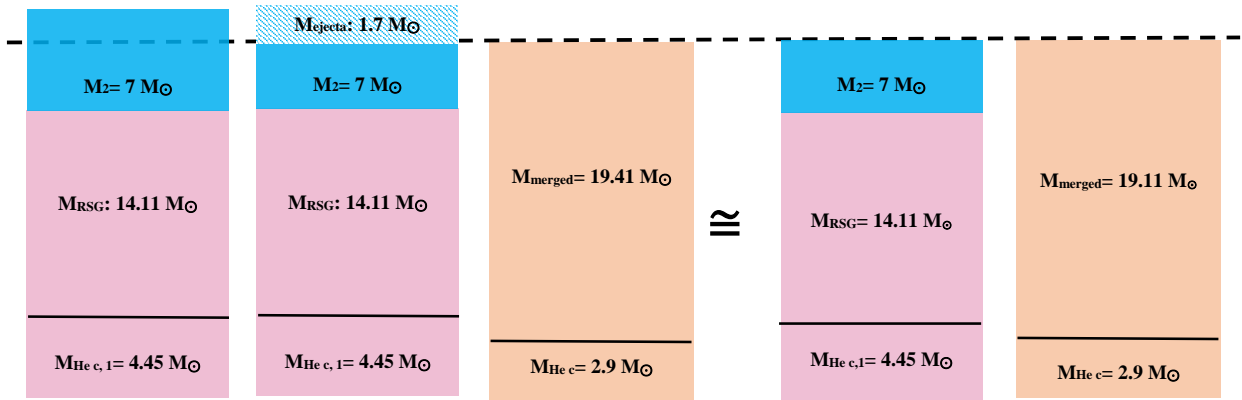


FIGURE 2.2: Diagram (not according to scale) showing the equivalence of mass ejection from the CE phase to accreting lower secondary masses.

We account for the mass-ejection phenomenon indirectly—by accreting different values of M_2 on a particular RSG model. For example, let us take the merger of a system of $M_1 = 15 M_\odot$ ($M_{\text{RSG}} = 14.11 M_\odot$) and $M_2 = 7 M_\odot$, which will result in a star of $21.11 M_\odot$. If $1.7 M_\odot$ is ejected from the merger, this would reduce the total mass to $\approx 19.41 M_\odot$. Equivalently, we can merge a system of $M_1 = 15 M_\odot$ ($M_{\text{RSG}} = 14.11 M_\odot$) and $M_2 = 5 M_\odot$ which would result in a star of $19.11 M_\odot$, close to the mass obtained from the previous system (Fig. 2.2). The two systems will also have the same surface composition in the post-merger star. Thus the post-merger evolutionary tracks obtained from both scenarios, the one with mass ejection and the one with a lower M_2 , will be the same.

Fig. 2.3 outlines the evolutionary sequence for every system— we begin with the evolution of the primary star from the main sequence, merge it with a secondary main-sequence star, and follow the evolution until just prior to iron-core collapse, i.e., the pre-SN model. In the next section we quantify the initial parameters chosen for our study.

2.2.3 Initial parameters

The primary and secondary stars are evolved from the zero age main sequence (ZAMS) with a solar-scaled composition of the LMC: $X_{\text{H}} = 0.739$, $X_{\text{He}} = 0.255$ and $Z = 0.0055$, which is 0.4 dex of the Asplund et al. (2009) solar metallicity, $Z_\odot = 0.014$. This metallicity is the value used by Brott et al. (2011), measured from observations of young massive stars in the H-II regions of the LMC, although they use initial C, N, O values that are enhanced over solar. As we shall discuss later, the metallicity is not the primary reason for stars becoming blue from

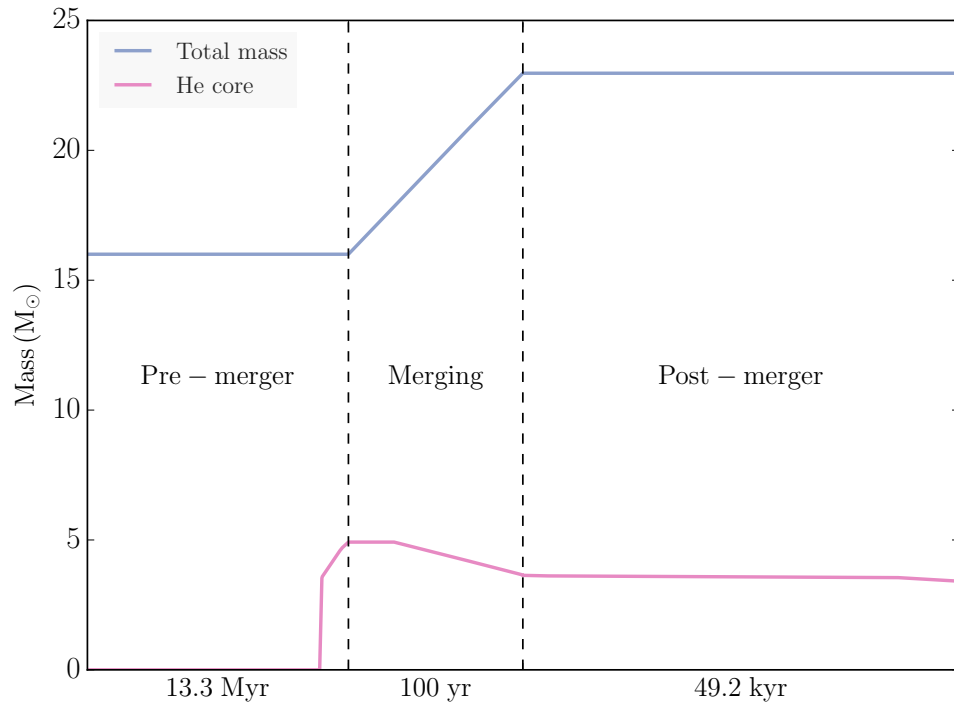


FIGURE 2.3: A schematic of the evolutionary sequence used in this work, illustrated for the binary system of $M_1 = 16M_{\odot}$ and $M_2 = 7M_{\odot}$. The primary is evolved until it becomes an RSG, over a period of 13.3 Myr, after which it is merged with the secondary over 100 yr. The post-merger model in this case is a BSG and it remains so for 49.2 kyr until its explosion. The He core mass is flat until ~ 25 yr from the start of the merger before it begins to shrink. This is because it takes ~ 25 yr for the boundary of the He core to recede due to dredge up of H-rich material from the envelope.

mergers.

Our choice of main-sequence masses for the binary components is motivated by the mass predicted by single star models for Sk -69°202 and the merger scenario outlined by Podsiadlowski, Morris, and Ivanova (2007), i.e, $M_1 + M_2 = 18M_\odot - 22M_\odot$. The primary RSG model chosen for the merger consists of a convective envelope and a He core with a central helium mass fraction of $X_{\text{He},c,1} \sim 10^{-2}$ (Fig. 2.1). The primary main-sequence star has an initial rotational velocity at the equator of $\omega/\omega_{\text{crit}} = 0.30$ ($v_{\text{eq}} \sim 216$ km/s). When it arrives on the RSG, its surface is enriched with the ashes of CNO-burning dredged up from the core to the envelope by rotational mixing. Thus the surface of the primary RSG model has high N/C and N/O ratios. Properties of the primary models studied in this work are listed in Table 2.2.

The main-sequence masses of the secondary considered in this study are between $M_2 = 2M_\odot - 8M_\odot$. Within the age of the primary RSG models (12.3 Myr – 14.3 Myr, Table 2.2), the average isotopic abundances of the secondary masses vary only by a few percent; X_{H} decreases (X_{He} increases) by 8% between $M_2 = 5M_\odot$ and $10M_\odot$. This does not significantly impact the evolution of the post-merger star or its abundances. Hence we choose a ‘standard’ uniform isotopic composition for the accretion of secondary masses– that of a $5M_\odot$ main-sequence star evolved until 14.3 Myr (Table 2.3).

TABLE 2.2: Parameters of the primary RSG models selected for merging. M_1 is the main-sequence mass of primary; ν/ν_{crit} is the initial rotational velocity on the main sequence; Age is the age of RSG model; τ_{cc} is the time until core collapse; M_{RSG} is the mass of RSG model; $M_{\text{CO c,1}}$ and $M_{\text{He c,1}}$ are the mass of the CO core and of the He core; $M_{\text{env,1}}$ is the mass of the envelope, i.e., $M_{\text{RSG}} - M_{\text{He c,1}}$; N/C, N/O, and He/H are surface number ratios.

M_1 (M_{\odot})	ν/ν_{crit}	Age (Myr)	τ_{cc} (kyr)	M_{RSG} (M_{\odot})	$M_{\text{CO c,1}}$ (M_{\odot})	$M_{\text{He c,1}}$ (M_{\odot})	$M_{\text{env,1}}$ (M_{\odot})	N/C	N/O	He/H
15	0.30	14.35	20.2	14.11	2.89	4.45	9.66	10.1	1.09	0.10
16	0.30	13.28	21.2	15.04	3.25	4.87	10.17	9.2	1.12	0.10
17	0.30	12.33	37.8	15.87	3.62	5.26	10.61	9.5	0.75	0.10

TABLE 2.3: Uniform isotopic composition for the accreted secondary model. Isotope is the isotopic species; X_f is the mass fraction of accreted isotopes; X_f/X_i is the change with respect to their initial values.

Isotope	X_f	X_f/X_i
^1H	7.22×10^{-1}	0.98
^4He	2.72×10^{-1}	1.08
^{12}C	4.91×10^{-4}	0.50
^{14}N	1.28×10^{-4}	4.48
^{16}O	1.87×10^{-3}	0.80

The initial parameters that we vary are:

1. Primary star mass (M_1): Models of the primary on the main sequence of mass $M_1 = 15M_\odot, 16M_\odot, 17M_\odot$, with an initial rotational velocity of $\omega/\omega_{\text{crit}} = 0.30$, which are evolved to the required RSG model (see text above) for the merger.
2. Secondary star mass (M_2): Main-sequence star of a mass between $M_2 = 2M_\odot - 8M_\odot$ is merged with each primary RSG model. The initial mass ratio (M_2/M_1) thus spans a range of 0.12 – 0.53.
3. Fraction of He core of the primary dredged up (f_c): For each combination of M_1 and M_2 , we set the boundary of mixing m_b for M_2 by specifying f_c . Increasing f_c results in larger fractions of the He core dredged up to the surface and smaller He cores for the post-merger star. It becomes instructive to use f_{sh} , the fraction of He-shell of the He core dredged up, in place of f_c , as we shall see in Section 2.3.

Thus for every model, we choose a value of M_1 and M_2 and then choose a value for f_c , which determines m_b . By varying these three parameters, we establish a grid of 84 initial systems to study. In the next section, we explain the results of their evolution.

2.3 Results

2.3.1 Progenitor models of SN 1987A

A successful SN 1987A progenitor model is one that satisfies the following criteria:

1. The location of Sk-69°202 in the HRD: $\log(L/L_\odot) = 5.15 - 5.45$, $T_{\text{eff}} = 15\text{ kK} - 18\text{ kK}$ and $R/R_\odot = 28 - 58$ (Woosley, Pinto, and Weaver, 1988).
2. Surface number ratios match those of the triple-ring nebula; $\text{N/C} \sim 5 \pm 2$, $\text{N/O} \sim 1.1 \pm 0.4$ (Lundqvist and Fransson, 1996) and $\text{He/H} = 0.14 \pm 0.06$ (France et al., 2011).
3. Lifetime of the BSG phase after the merger until the explosion is at least 15kyr.

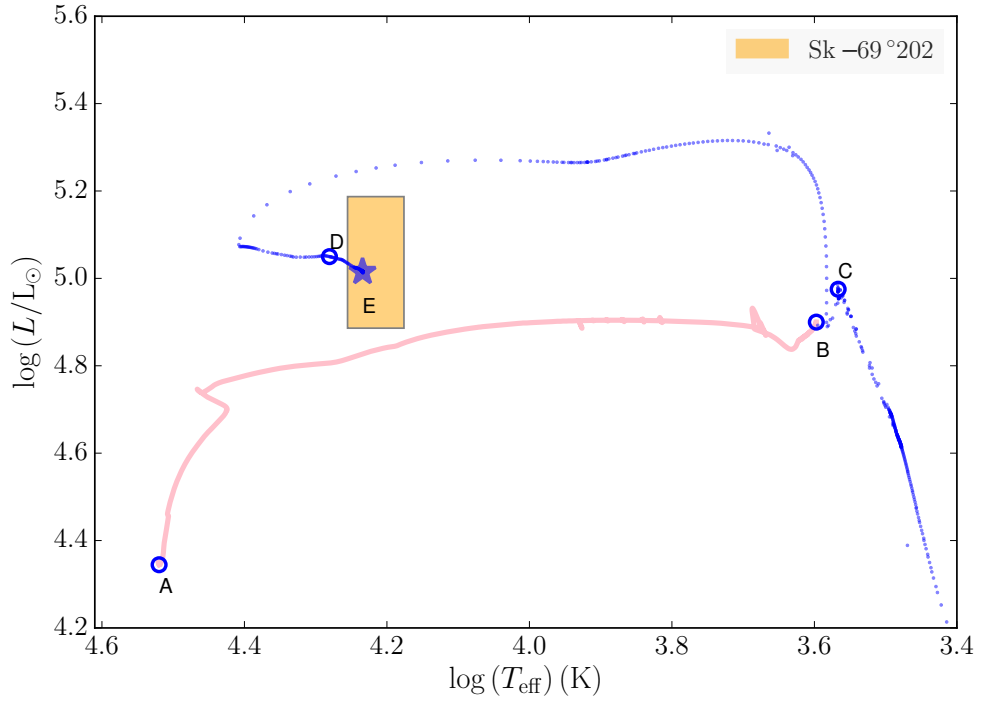


FIGURE 2.4: Evolutionary track of the merger of $M_1 = 16M_\odot$ and $M_2 = 7M_\odot$, with $f_c = 16.6\%$. Shaded orange region represents observational limits for Sk $-69^\circ 202$ by Woosley, Pinto, and Weaver (1988) for T_{eff} and $\log(L/L_\odot)$. A and B: from the zero-age main sequence of the primary to the required RSG model. B and C: merger with the secondary. C and D: evolution of the post-merger model until carbon ignition in the core. D and E: further evolution to the final model just before core collapse. The final model (E) satisfies conditions (i)–(iii) in Section 2.3.1.

We classify our pre-SN models as Blue supergiants (BSGs), Yellow supergiants (YSGs), Red supergiants (RSGs), based on their T_{eff} as follows:

1. **BSG:** $T_{\text{eff}} \geq 12 \text{ kK}$
2. **YSG:** $12 \text{ kK} < T_{\text{eff}} \leq 4 \text{ kK}$
3. **RSG:** $T_{\text{eff}} < 4 \text{ kK}$

The evolution of one of the models that resembles the progenitor of SN 1987A ($M_1 = 16M_\odot$, $M_2 = 7M_\odot$ and $f_c = 16.6\%$, see Table 2.4) is shown in the HRD in Fig. 2.4 and in the schematic Fig. 2.3. Beginning from the ZAMS model (A), the primary inflates to an RSG with a He-depleted core over a period of 13.3 Myr (B). At stage B, the time until core collapse is 21.1 kyr. The merger is initiated immediately at point B and the secondary is accreted and mixed with the envelope of the primary until point C over 100 yr. During the merging process, the star goes out of thermal equilibrium and the code takes small timesteps to evolve the model, resulting in a noisy phase on the HRD (the extended dotted blue line in Fig. 2.4). Due to the penetration of H-rich material, the He core mass shrinks, thereby increasing the

lifespan of the post-merger star (by nearly 28 kyr) before it explodes. The H-fuel deposited increases the mass of the H-burning shell and its resulting higher luminosity pushes the convective envelope outward, causing the star to inflate after the merger. When the convective envelope stops expanding and begins to recede, the star contracts and evolves towards the blue part of the HRD. At a certain point in its evolution, the convective envelope stops receding and begins to expand again causing the star to loop back to the red. It then undergoes carbon ignition in the core (D) and subsequent stages of nuclear burning and the evolution is terminated until just before the onset of iron-core collapse (E). The lifespan of this BSG model is 49.2 kyr before core collapse.

TABLE 2.4: Parameters of the progenitor models of SN 1987A. M_1 and M_2 are the initial primary and secondary masses of the binary system; f_{sh} and f_c are percentage fractions of He-shell mass and helium core mass that were dredged up; m_b is the boundary of mixing. The following are the properties of the pre-SN models: $M_{\text{He c}}$, $M_{\text{Fe c}}$, M_{env} , and $M_{\text{pre-SN}}$ are He core mass, iron core mass, envelope mass and total mass ($M_c + M_{\text{env}}$); N/C, N/O, He/H are number ratios in the surface; T_{eff} , $\log(L)$, $R_{\text{pre-SN}}$ are the effective temperature, luminosity and radius; τ_{BSG} is the lifetime of the BSG before explosion. ‘-’ under the column $M_{\text{Fe c}}$ are for those runs that crashed while at core-silicon burning (refer to text in Section 2.2).

M_1 (M_{\odot})	M_2 (M_{\odot})	f_{sh} %	f_c %	m_b (M_{\odot})	$M_{\text{He c}}$ (M_{\odot})	M_{env} (M_{\odot})	$M_{\text{pre-SN}}$ (M_{\odot})	T_{eff} (kK)	$\log(L)$ (L_{\odot})	$R_{\text{pre-SN}}$ (R_{\odot})	$M_{\text{Fe c}}$ (M_{\odot})	N/C	N/O	He/H	τ_{BSG} (kyr)
15	7	50	17.5	3.67	2.90	18.16	21.06	16.0	4.89	36.7	1.46	6.5	1.3	0.13	82
15	8	50	17.5	3.67	2.95	19.10	22.05	17.8	4.95	31.8	1.39	5.8	1.3	0.13	83
16	4	10	3.30	4.71	4.11	14.89	19.00	16.8	4.95	35.4	1.65	6.6	1.4	0.13	41
16	7	50	16.6	4.06	3.41	18.57	21.98	17.1	5.02	36.8	-	6.9	1.4	0.14	49
17	7	10	15.6	4.44	3.86	18.95	22.81	16.2	5.02	34.5	1.65	7.0	1.4	0.14	41
17	8	10	15.6	4.44	3.83	19.98	23.81	17.1	5.06	33.4	-	6.4	1.4	0.14	41

2.3.2 What factors affect the formation of BSGs?

Of the 84 models computed, 59 are BSGs and 25 are YSGs. Six of the BSGs qualify as progenitor models of SN 1987A, in accordance with criteria 1-3 in Section 2.3.1 (Fig. 2.11, Fig. 2.7) and are summarized in Table. 2.4. We find that RSG pre-SN models result from mergers only if dredge-up occurs from the envelope, i.e., the He core is not penetrated, as will be discussed in the following sections.

We shall now investigate how the choice of initial parameters affects the observed quantities of Sk-69°202.

Surface N/C and N/O ratios

The envelope of the RSG primary model at the time of merger is already enhanced in nitrogen at the surface due to rotational mixing, as explained in Section 2.2.3 (also see Fig. 2.1, top panel). Depending on the values of M_2 and f_c , the N/C and N/O in the envelope will change as explained below.

Our choice for the mixing boundary m_b being set inside the He core is motivated by two factors— first, we know from hydrodynamic simulations that the He core is penetrated by a fraction of the secondary mass and second, from our models we find that the surface ratios of N/C and N/O are sensitive to the position of m_b . In Fig. 2.5 we demonstrate this for the case of $M_1 = 15 M_\odot$ and $M_2 = 5 M_\odot$ with varying amounts of f_c . The larger f_c is, the deeper m_b is set inside the He core, resulting in larger amounts of $M_{\text{He},c,1}$ being mixed in the envelope. This is because the He shell, between the boundary of the CO core and He core, is nitrogen rich (Fig. 2.1). Thus in order to obtain high N/C and N/O ratios at the surface of the merged star, the boundary of dredge up during the merger must be set within the He-shell region. If this boundary is set inside the CO core, the mass dredged up to the surface will be rich in carbon and oxygen, thereby reducing N/C and N/O. Since we restrict mixing only inside the He shell, it would be more instructive to use f_{sh} , the fraction of He-shell mass dredged up, to set m_b .

Two models are also computed for the case where m_b is set outside the He core of the primary, i.e., the envelope does not penetrate the core. For this case, since mass is dredged up only from the homogeneously mixed envelope, the surface values of N/C and N/O are unchanged from their initial amounts.

We now demonstrate how these quantities vary for all the binary systems studied in this work, spanning the entire initial parameter space of M_1 , M_2 and $f_{\text{sh}} = 10, 50, 90$ and 100 % (Fig. 2.6). A table containing details of all the pre-SN models computed in this work is provided in Appendix A. As M_2 increases for a fixed f_{sh} , N/C and N/O decrease again. This is because the envelope mass increases as M_2 increases, causing the amount of nitrogen dredged up to be diluted in the envelope, thereby decreasing its mass fraction at the surface.

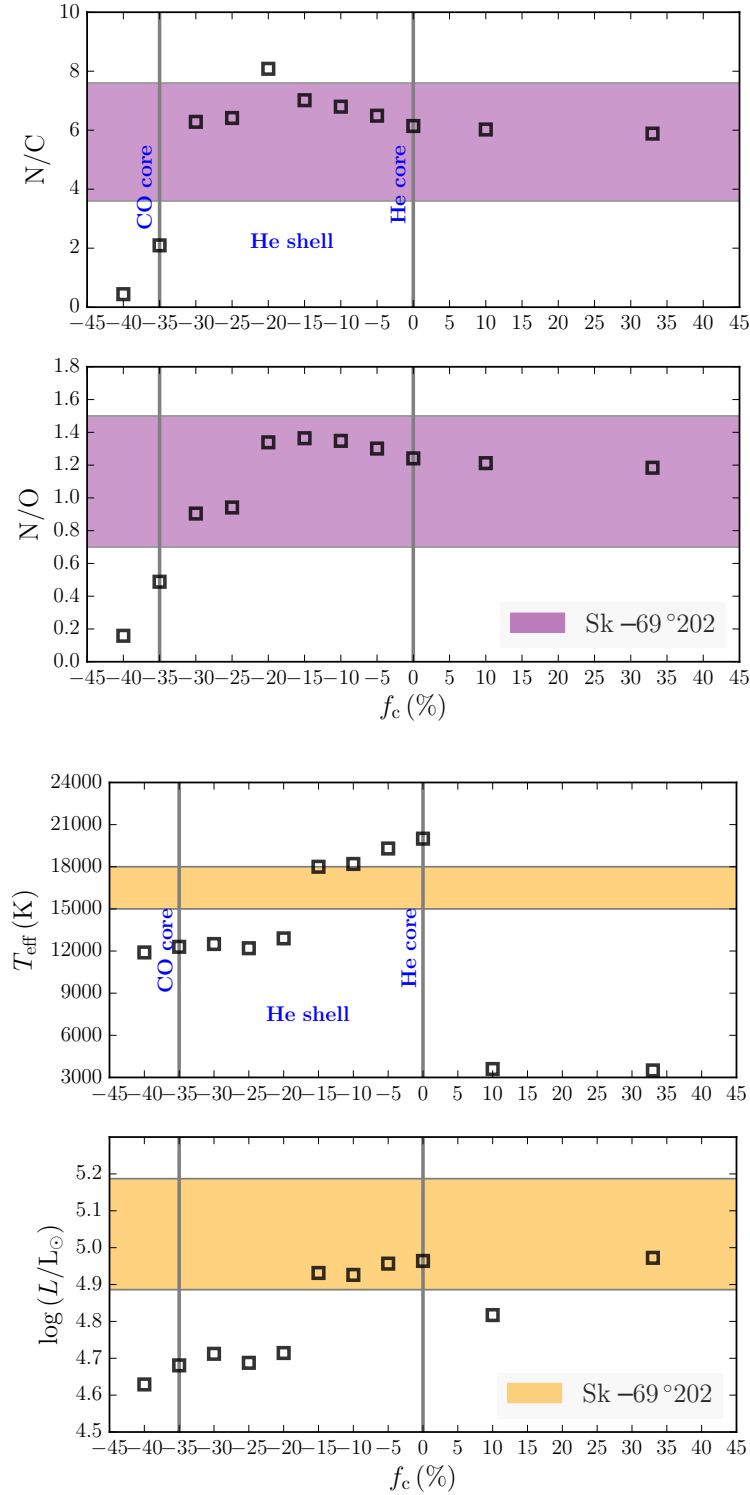


FIGURE 2.5: Surface quantities of pre-SN models obtained from the merger of $M_1 = 15 M_{\odot}$ and $M_2 = 5 M_{\odot}$ with various dredge up fractions of the He core (f_c in %). *Left:* Number ratios, N/C and N/O . *Right:* Effective temperature (T_{eff}) and luminosity (L). Negative values of f_c represent the case for which the He core of the primary is penetrated and positive values show the case for which the mixing is restricted to above the He core of the primary. Also marked are the boundaries of the CO core, He core and the He shell of the primary. The shaded regions denote observational limits for Sk -69°202; the violet region limits are taken from Lundqvist and Fransson (1996) and the orange region from Woosley, Pinto, and Weaver (1988).

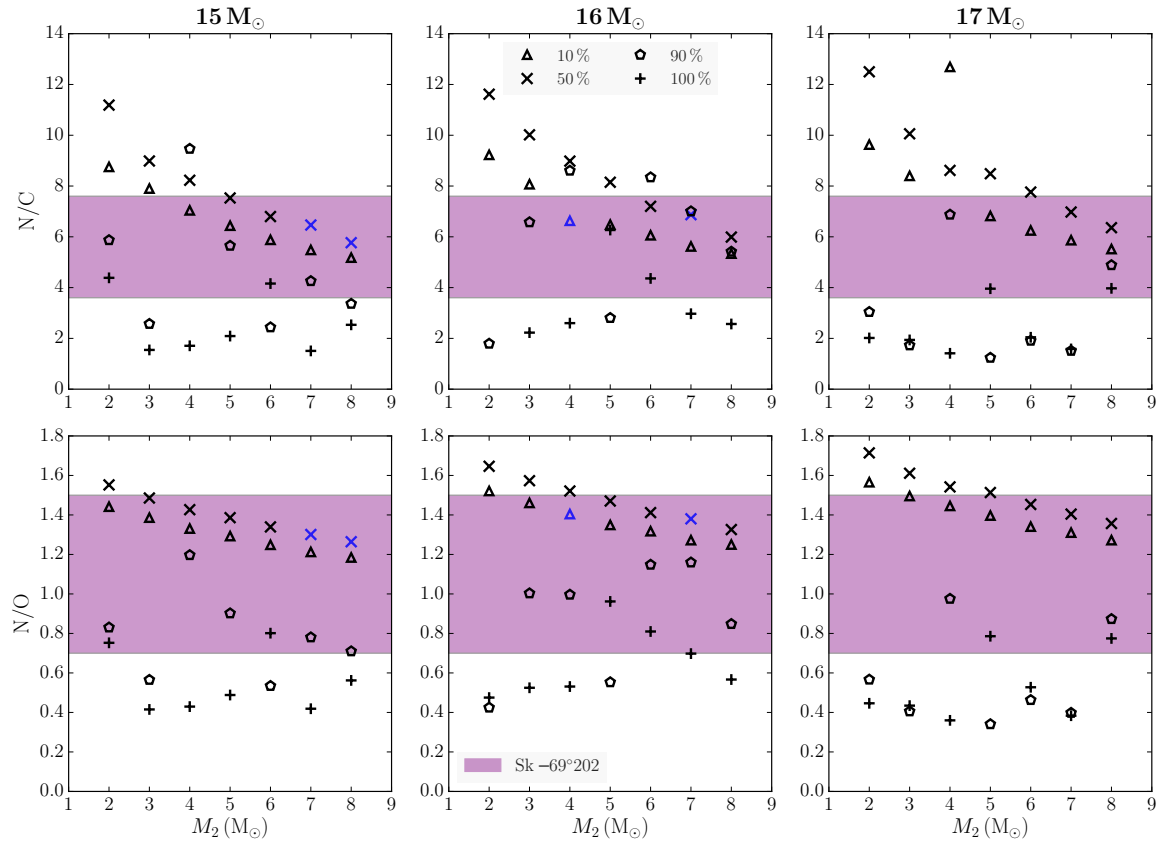


FIGURE 2.6: Distribution of number ratios, N/C and N/O of all final models for each of the primary masses, M_1 . These parameters are plotted in a column for each M_1 against the range of M_2 . The symbols stand for different values of f_{sh} . The bold blue symbols are progenitor models for SN 1987A that satisfy criteria 1-3 in Section 2.3.1. The shaded violet region denotes the observational limits as explained in Fig. 2.5.

As M_1 increases, the RSG models are increasingly enhanced in N/C and N/O at the surface (Table 2.2). Therefore for a given M_2 and f_{sh} , the values of N/C and N/O at the surface after the merger also increase in proportion to M_1 .

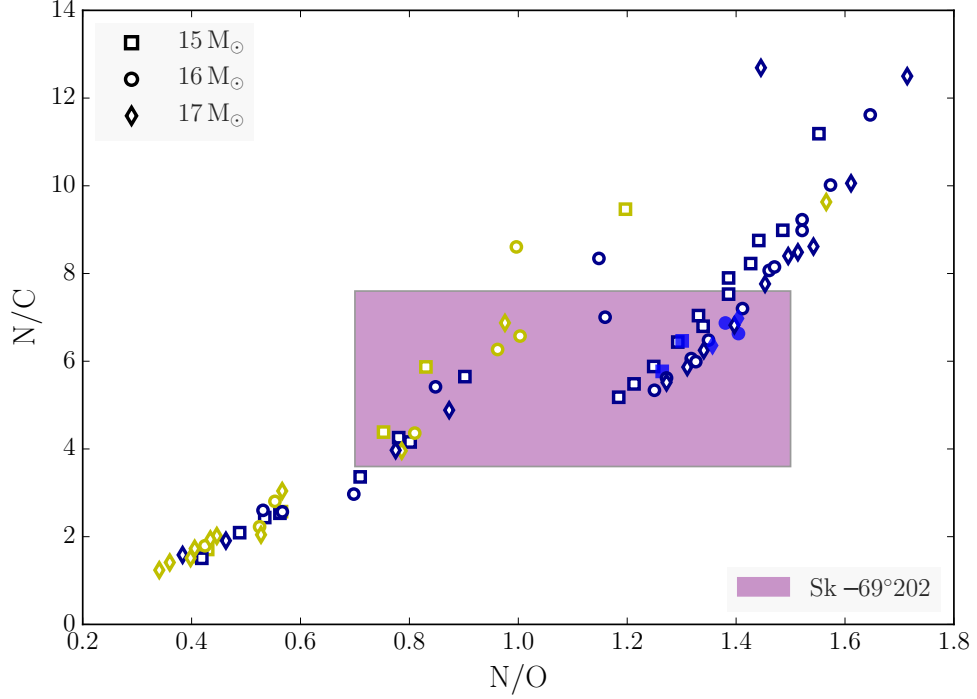


FIGURE 2.7: Distribution of number ratios N/C vs. N/O at the surface of all 84 final models. The shaded violet region denotes the observational limits for Sk $-69^{\circ}202$ as in Fig. 2.5. Yellow symbols are YSGs, blue symbols are BSGs and filled blue symbols are progenitor models for SN 1987A, which satisfy the conditions 1-3 in Section 2.3.1.

From Fig. 2.7, the BSG pre-SN models from our simulations span a large range in surface ratios of N/C and N/O, indicating that there is no correlation between being a BSG and having high values of N/C and N/O at the surface, i.e., these parameters are independent of each other. The YSG pre-SN models (except for two) are somewhat more constrained, since they are less enriched in N/C and N/O at the surface than BSGs ($N/O < 1.0$, $N/C < 9.7$). The ratio of He/H at the surface does not vary significantly within the parameter range we use, and is between 0.13-0.17 for all the pre-SN models.

Effective temperature, luminosity, and radius

Varying f_c affects the effective temperature, T_{eff} , and luminosity, L , of the pre-SN model (Fig. 2.5). For a fixed primary and secondary mass, increasing f_c (or f_{sh}) decreases the He core mass and causes T_{eff} and L to also decrease. For the particular merger model demonstrated in Fig. 2.5, dredging up more than 15% of $M_{\text{He},1}$ (50% of the He-shell mass), brings down T_{eff} from 18 kK to nearly 12 kK. T_{eff} does not drop much below 12 kK for larger values of f_c .

It is interesting to note that when m_b is set on the boundary of the CO core (i.e., $f_c = 0$), the pre-SN model also becomes a BSG ($T_{\text{eff}} \approx 20\text{kK}$). In the two models where m_b is set above the He core, the post-merger star ends its life as a cool RSG with $T_{\text{eff}} = 3\text{kK}$.

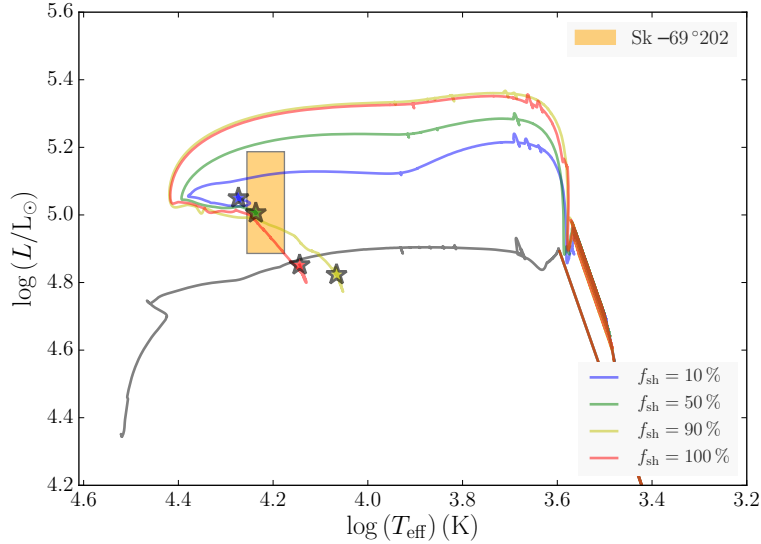


FIGURE 2.8: The evolutionary tracks of four cases computed for the merger of $M_1 = 16M_{\odot}$ and $M_2 = 6M_{\odot}$, with $f_{\text{sh}} = 10\%$, 50% , 90% , 100% . Stars denote the pre-SN models of individual evolutionary tracks. The shaded orange region denotes the observational limits as in Fig. 2.5.

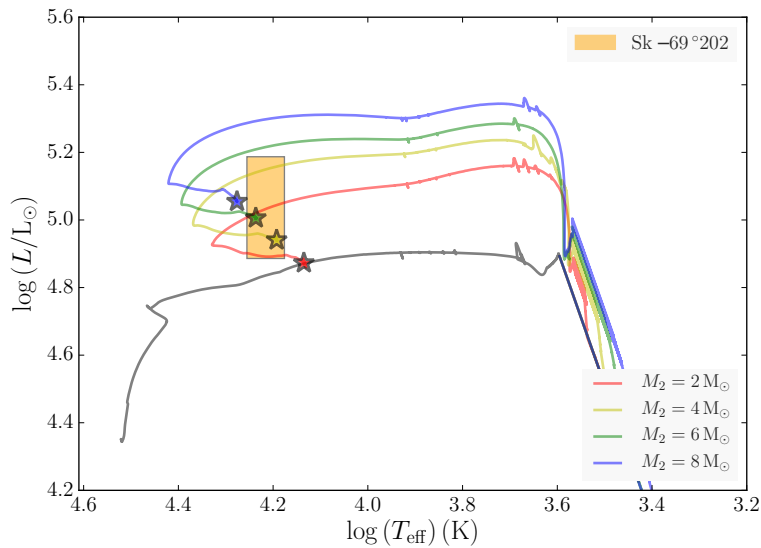


FIGURE 2.9: The evolutionary tracks of four cases computed for the merger of $M_1 = 16M_{\odot}$ with $M_2 = 2M_{\odot}$, $4M_{\odot}$, $6M_{\odot}$, and $8M_{\odot}$, and $f_{\text{sh}} = 50\%$. Stars denote the pre-SN models of individual evolutionary tracks. The shaded orange region denotes the observational limits as in Fig. 2.5.

By increasing f_{sh} (Fig. 2.8), the secondary star mixes deeper inside the He core and the stars become brighter and hotter after the merger but evolve further from the bluest point of their evolution to the cooler and less luminous regions of the HRD. Thus, reducing

the He core mass for a given M_1 and M_2 causes the pre-SN model to become redder. On the other hand, for a fixed value of f_{sh} and primary mass, increasing M_2 (Fig. 2.9) causes the envelope mass to increase. As the envelope-to-core mass ratio increases, the post-merger stars appear hotter and more luminous throughout their evolution.

We arrive at two results at this point. Firstly, in order to obtain high values of N/C and N/O at the surface and high values of T_{eff} and luminosity required for the progenitor of SN 1987A, we need to restrict the mixing boundary m_b to be inside the He shell or on the He core boundary. Secondly, without He core penetration during the merger, the post-merger stars evolve as cool RSGs until they explode. Thus accretion alone does not suffice to make blue stars. Let us now understand how varying f_{sh} and M_2 for a particular M_1 affects the evolution of the post-merger star.

From Fig. 2.9, we see that for a fixed combination of M_1 and M_2 , increasing f_{sh} makes the pre-SN model cooler. On the other hand, for a fixed value of f_{sh} , increasing M_2 increases the envelope mass and makes the final model hotter and also more luminous.

We now arrive at our next set of conclusions. A merged star is most likely to end its life as a BSG and have high values of N/C and N/O in the surface across all values of M_1 and M_2 used in this study, if f_{sh} is between 10 and 50 %. The frequency of cooler stars ($T_{\text{eff}} < 12$ kK) increases as M_1 and f_{sh} increase and M_2 decreases. The most crucial initial parameter that affects T_{eff} of the pre-SN model is f_{sh} , which determines the He core mass, followed by M_2 , which determines the envelope mass and, finally, M_1 . This suggests that there must exist an underlying connection between T_{eff} and envelope-to-core mass ratio of the post-merger star.

The majority of our pre-SN models are BSGs while the rest are YSGs (Fig 2.11).

Lifetime of BSG model before explosion

We address the final quantity measured for Sk $-69^\circ 202$, the duration of the BSG phase of the post-merger model, τ_{BSG} . We calculate τ_{BSG} as the period from when the post-merger star attains $T_{\text{eff}} = 12$ kK until the time of its explosion. From Table 2.4, our BSG progenitors for SN 1987A lifetimes that are larger than 15–20 kyr expected from observations (and is the case for all the BSG pre-SN models obtained in this study, see Appendix 2.5). This parameter, however, does not depend on the three initial parameters we varied, but, in fact, on the age of the primary RSG model just before the merger begins. The younger the RSG model is (the earlier along the giant branch it is), the longer the post-merger remnant lives as a BSG. The further along the giant branch the primary RSG is, the closer the core gets to carbon ignition. A proxy for the age of the RSG model is the mass fraction of helium at the centre ($X_{\text{He},c,1}$), which decreases as the RSG model grows older. The RSG primary models in this study were chosen when $X_{\text{He},c,1} \sim 10^{-2}$. We compute pre-SN models from a particular initial

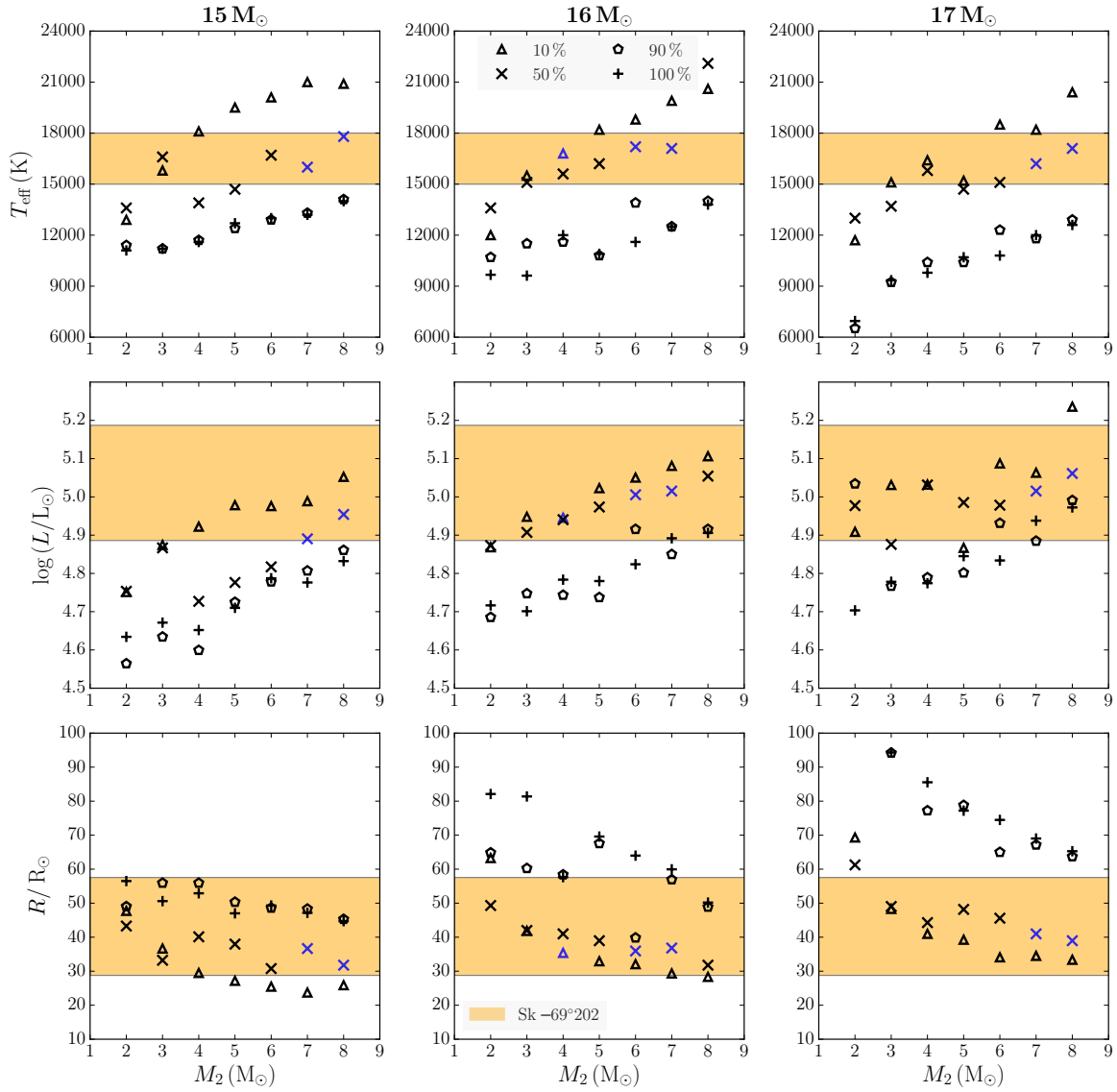


FIGURE 2.10: Distribution of effective temperature (T_{eff}), luminosity (L) and radius ($R_{\text{pre-SN}}$) of all 84 final models. Symbols are as in Fig. 2.6. The shaded orange region denotes the observational limits as in Fig. 2.5.

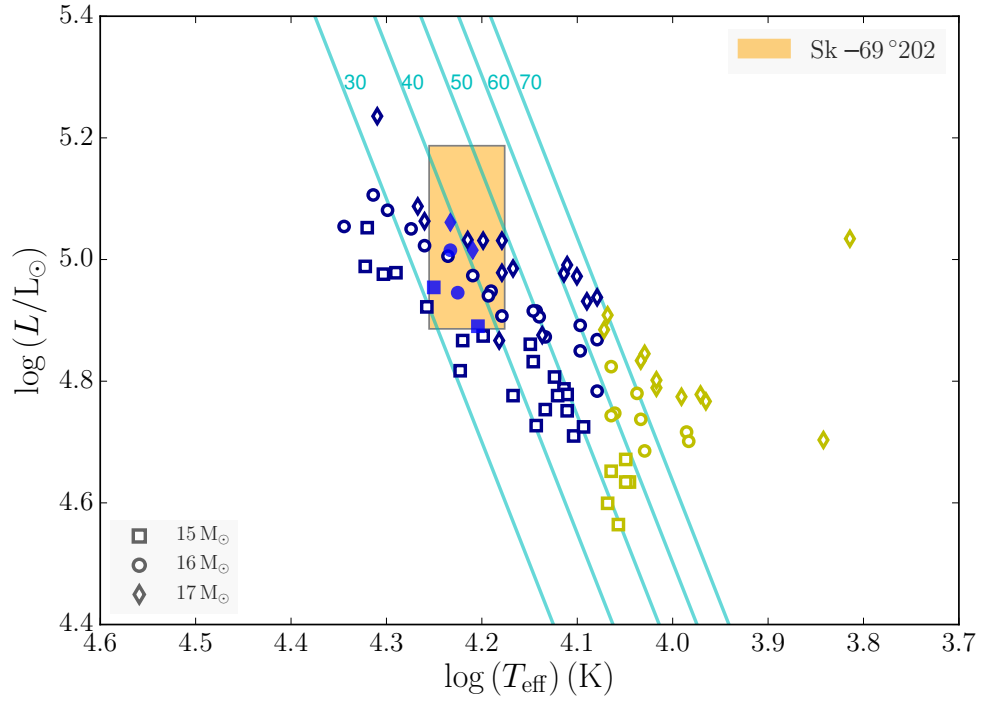


FIGURE 2.11: Distribution of all 84 final models in the HRD. Lines of constant surface radius (in R_{\odot}) are drawn. The shaded orange region denotes the observational limits as in Fig. 2.5. Symbols are as explained in Fig. 2.7.

system of $M_1 = 16M_{\odot}$, $M_2 = 6M_{\odot}$ and $f_{\text{sh}} = 50$ percent, by choosing primary RSG models with decreasing values of $X_{\text{He},c,1}$. From Table 2.5, we see that for $X_{\text{He},c,1} \leq 10^{-4}$, the lifetime of the BSG model after the merger is 17.1 kyr – 18.3 kyr. The other parameters of the pre-SN model are largely unaffected.

We have thus demonstrated that it is possible to obtain BSG progenitors for Type II SNe, with a range of luminosities, effective temperatures, envelope compositions and lifetimes, from various combinations of initial parameters for binary mergers. We summarize our results and discuss their implications in Section 2.4.

TABLE 2.5: Properties of different RSG models of $M_1 = 16M_{\odot}$, $\omega/\omega_{\text{crit}} = 0.30$ and pre-SN models from their merger with $M_2 = 6M_{\odot}$ and $f_{\text{sh}} = 50\%$. $X_{\text{He},c}$, ρ_c , T_c , R_{RSG} , and $M_{\text{He},c,1}$ are central helium mass fraction, central density, central temperature, radius and He core mass of the RSG model; $\log(L)$, T_{eff} , $R_{\text{pre-SN}}$ are the luminosity, effective temperature and radius of the pre-SN model; N/C, N/O, He/H are number ratios in the surface of the pre-SN model; τ_{BSG} is the lifetime of BSG before explosion.

$X_{\text{He},c}$	ρ_c (10^3 g/cc)	T_c (10^8 K)	R_{RSG} (R_{\odot})	$M_{\text{He},c,1}$ (M_{\odot})	$\log(L)$ (L_{\odot})	T_{eff} (kK)	$R_{\text{pre-SN}}$ (R_{\odot})	N/C	N/O	He/H	τ_{BSG} (kyr)
10^{-2}	2.5	2.6	607	4.92	4.97	16.7	43.1	8.1	1.5	0.15	48.0
10^{-4}	4.4	3.1	773	4.94	4.94	16.6	36.5	7.6	1.42	0.14	18.3
10^{-6}	5.5	3.3	778	4.94	5.07	16.7	41.4	8.0	1.43	0.14	17.2
10^{-8}	5.5	3.4	824	4.94	5.02	16.3	41.4	8.2	1.43	0.14	17.1

2.4 Discussions and Conclusions

In this paper, we present Type II SN progenitors from the first detailed stellar evolution study of binary mergers of massive stars. Our pre-SN models span a large range of N/C and N/O ratios at the surface, demonstrating that chemical abundances and the position in the HRD of the progenitor are independent constraints. We can simultaneously reproduce the three key signatures of Sk $-69^{\circ}202$ in our pre-SN models- the position of Sk $-69^{\circ}202$ in the HRD, its surface number ratios and its lifetime before exploding as SN 1987A.

We provide details of the 84 models computed in Appendix 2.5. These merger models were evolved until prior to the collapse of the iron core, from a parameter space consisting of the primary mass $M_1 = 15\text{--}17M_{\odot}$, the secondary mass $M_2 = 2\text{--}8M_{\odot}$ and the fraction of He shell dredged up from the He core, $f_{\text{sh}} = 10, 50, 90$ and 100% . Within the evolutionary scenario and parameter space explored, we find that Sk $-69^{\circ}202$ can be reproduced with different combinations of the above three parameters. The nature of the pre-SN models rely only on the choice of these three parameters and no additional fine-tuning is required during the evolution of the star to produce BSGs. The majority of the final models are BSGs (59 out of 84) while the rest are YSGs. This leads us to conclude that the progenitors of Type II-pec SNe are highly favoured outcomes from a binary merger.

We draw the following inferences from our results:

1. The parameter of paramount influence on the surface temperature of the pre-SN model, is f_{sh} , which determines the boundary of mixing during the merger and the He core mass of the post-merger model. Across the range of primary and secondary masses chosen, BSG pre-SN models with $T_{\text{eff}} \geq 12\text{ kK}$ are produced when $f_{\text{sh}} \leq 50\%$. Since dredge-up is restricted to the nitrogen-rich region of the He shell, these values of f_{sh} also result in high values of N/C and N/O in the surface.
2. The second parameter of importance is the mass of the secondary star, M_2 . Increasing M_2 for a fixed value of f_{sh} (which determines the post-merger He core mass) increases the T_{eff} of the pre-SN star but decreases N/C and N/O in the surface. The second parameter of importance is the mass of the secondary star, M_2 . Increasing M_2 for a fixed value of f_{sh} (which determines the post-merger He core mass) increases the T_{eff} of the pre-SN star but decreases N/C and N/O in the surface.
3. Finally, the parameter that affects the lifetime of the BSG star before its explosion is the age of the primary RSG model at the time of the merger. For a given M_1 , older the RSG model is at the time of the merger, shorter the lifetime of the BSG after the merger. Thus for any initial system, the lifetime of the BSG models can be reduced to 15 – 20 kyr as expected for Sk $-69^{\circ}202$, by choosing older RSG models. This choice

of the RSG model, does not significantly affect the surface quantities of the pre-SN model.

4. YSG progenitors are produced when either $M_2 = 2 M_\odot$ or for small He cores, i.e. when $f_{\text{sh}} > 50$ percent. These models increase in number as M_1 increases. The only condition under which RSG progenitors are produced is when the mixing boundary is set above the He core, i.e. the He core is not penetrated in the merger.
5. The only conditions under which RSG progenitors are produced in our merger scenario, is when the mixing boundary is set above the He core, i.e., the He core is not penetrated in the merger. Thus accretion alone does not result in hot, compact progenitors.
6. The pre-SN models that match Sk-69°202 are from the following systems: $M_1 + M_2$ (f_{sh}) = $15 + 7M_\odot$ (50%), $15 + 8M_\odot$ (50%), $16 + 4M_\odot$ (10%), $16 + 7M_\odot$ (50%), $17 + 7M_\odot$ (50%), $17 + 8M_\odot$ (10%).
7. BSGs are found to span a large range of N/C and N/O values in the surface (N/C = 1.8–13, N/O = 0.4–1.8), whereas YSGs are found almost entirely within N/C = 1–9.7 and N/O = 0.4–1.0. He/H in the surface is between 0.13–0.17 in all models.

Previous works such as those of Barkat and Wheeler (1989a), Podsiadlowski, Joss, and Hsu (1992), Woosley et al. (1997), Vanbeveren et al. (2013) and Petermann et al. (2015), have shown that small He cores and large envelope masses can make stars blue. These works find that reducing the He core to total mass ratio is alone sufficient to make BSGs. Podsiadlowski, Joss, and Hsu, 1992 found that increasing the accreted secondary mass for a particular He core mass of the primary, increases the T_{eff} of pre-SN models monotonically. They were hence able to determine a critical value for the He core to total mass ratio, below which pre-SN BSGs were possible.

In our study however, we find that with accretion alone, the post-merger stars remain red until the end of their evolution. A necessary condition is the penetration of the He core by the envelope, during the merging process. In fact, for a fixed secondary and primary mass, the T_{eff} of the pre-SN model decreases as the mass of the He core decreases with deeper penetration by the envelope. Increasing the secondary mass for a fixed primary mass and penetration depth however, does increase the T_{eff} of the pre-SN models. In our study thus, the final T_{eff} is tied in with two parameters- the fractional decrease of the He core after the merger and the envelope to core mass ratio. This is why we do not obtain a monotonic relationship between T_{eff} and the core-to-envelope mass ratio.

There maybe other reasons as to why BSGs to form– Ivanova (2002) and Vanbeveren et al. (2013) mention that the sharp rise in the hydrogen profile between the He core and the envelope after the merger or the additional fuel supplied to the H-burning shell may also be

causes. We hope that our findings will contribute to the quest of understanding why stars end up becoming BSGs or for that matter, RSGs.

Using higher-mass mergers, we can obtain larger N/O ratios and luminosity, comparable to that of Sher 25, which has $\log(L/L_{\odot}) > 5.78 - 5.90$ (Smartt et al., 2002; Melena et al., 2008) and $N/O \sim 1.7 - 2.1$ (Hendry et al., 2008). In the same vein, we can compare our models with the circumstellar abundances and HRD positions of other BSGs that have ring nebulae around them to confirm their origin from binary mergers.

The majority of Type II-pec SNe found so far have been in low-metallicity galaxies and hence Pastorello et al. (2012) and Taddia et al. (2013) suggest that low metallicities may play a role in forming BSG progenitors. There maybe an influence of metallicity on the interactions of binary systems— de Mink, Pols, and Yoon (2008) found that case C mass transfers from massive stars are more likely in low-metallicity environments than in those of solar metallicity. Eggenberger, Meynet, and Maeder (2002) find that the red-to-blue supergiant ratio decreases with metallicity. In order to pursue the question of how likely these mergers are in low-metallicity environments, we need to perform a population synthesis study.

The abundances of Ba and Sr in the surface of our pre-SN models are unchanged from their initial amounts and hence do not exhibit the s-process overabundance detected by Mazzali, Lucy, and Butler (1992) and Mazzali and Chugai (1995). More recent studies, such as those by Utrobin (2005) and Dessart and Hillier (2008), have shown the importance of time-dependent hydrogen ionization in the evolution of Type II SN spectra. From the time-dependent ionization models for SN 1987A, Utrobin (2005) concluded that the barium abundance in its atmosphere matched the LMC value and was not in fact enhanced.

The N/C and N/O ratios in the surface do not vary much from the end of the merger to core collapse. This may suggest that the outer rings likely formed from material ejected by the wind after the merger, but we cannot provide a more detailed dating based on abundance patterns.

We do not include the spin-up of the common envelope, or the heating of accreted material in our model, which we intend to look into as part of future work. These effects may affect the evolutionary path of the stars and also help gauge how fast the core will be rotating at the time of explosion.

Mass ejection from the CE phase is not explicitly modelled in this study. Since no circumstellar disk has been found around the remnant, we assume that the material ejected from the CE is in the nebula alone. The effect of mass loss from the merger is to cause the envelope mass to reduce and thereby increase the core-to-envelope mass ratio of the post-merger model. We indirectly explore the effect of mass ejection, by accreting a wide range of secondary masses for every primary RSG model which changes the core-to-envelope mass ratio. Within the range of secondary masses and the age of the primary model at the time of

merger, helium is enhanced by a maximum of 9 percent in the post-merger envelope compared to its initial value. This level of enhancement in helium does not by itself significantly impact the evolutionary path of the post-merger models. We thus rule out the role of helium in obtaining BSGs from mergers.

Overall, our BSG pre-SN models are more massive than the current single star progenitor models for SN 1987A. With single star models, the progenitor mass is determined by first comparing the surface luminosity with the mass of the evolved He core and then determining the initial mass of the progenitor (Woosley, 1988; Smartt et al., 2009; Dessart, Livne, and Waldman, 2010). The reason the He core mass is strongly correlated to the ZAMS mass of the star is because, in single star models the mass loss from the surface has little effect on the He core mass (Dessart, Livne, and Waldman, 2010). The He core mass thus determined for the luminosity of Sk -69°202 is $M_{\text{He c}} = 4 M_{\odot} - 7 M_{\odot}$, which would originate from a ZAMS star of mass, $M_{\text{ZAMS}} = 14 M_{\odot} - 20 M_{\odot}$ (Arnett et al., 1989; Smartt, 2009; Smartt et al., 2009). In the case of our merger models, the pre-SN He core mass depends on M_1 and the boundary of mixing during the merger, while the initial mass is the sum of M_1 and M_2 . Hence, a given He core mass could belong to any number of initial masses depending on the accreted value of M_2 .

Consequently these merger models will impact the parameterised studies of SN explosion properties that are calibrated against SN 1987A, such as those of Kleiser et al. (2011). Typical single star models used for SN 1987A are those from Woosley, Pinto, and Weaver (1988) and Woosley (1988), $M_{\text{ZAMS}} = 15 - 20 M_{\odot}$, $M_{\text{He c}} = 4.1 - 6.2 M_{\odot}$ and $M_{\text{env}} = 5 - 10 M_{\odot}$ (Arnett et al., 1989; Dessart and Hillier, 2010; Utrobin et al., 2015) or the He-enriched models of Nomoto et al. (1988) and Saio, Nomoto, and Kato (1988), $M_{\text{ZAMS}} = 23 M_{\odot}$, $M_{\text{He c}} = 6 M_{\odot}$ and $M_{\text{env}} = 10.3 M_{\odot}$ (Blinnikov et al., 2000; Kleiser et al., 2011; Ugliano et al., 2012). In contrast to the above single star models, Utrobin (2004) and Utrobin (2005) found that a compact, more massive pre-SN model, of $35 R_{\odot}$ and $M_{\text{env}} = 18 M_{\odot}$, fits both the bolometric light curve as well as the H-alpha profile of SN 1987A, with large amounts of mixing of ^{56}Ni .

Our BSG pre-SN models have lower He core masses, $M_{\text{He c}} = 2.4 - 4.5 M_{\odot}$, and much larger envelope masses $M_{\text{env}} = 12.3 - 20.5 M_{\odot}$. It is therefore imperative to determine the explosion properties of SN 1987A with these models. In a subsequent paper, we will present the light curves and spectra from the explosions of these models and compare them to SN 1987A and other Type II-pec SNe.

2.5 Appendix

This section contains the properties of all the pre-SN models computed in this study.

TABLE 2.6: Parameters of **BSG** binary merger progenitors of Type II SNe ($T_{\text{eff}} \geq 12$ kK). Column headings are the same as in Table 2.4.

M_1 (M_{\odot})	M_2 (M_{\odot})	f_{sh} %	f_c %	m_b (M_{\odot})	$M_{\text{He c}}$ (M_{\odot})	M_{env} (M_{\odot})	$M_{\text{pre-SN}}$ (M_{\odot})	T_{eff} (kK)	$\log(L)$ (L_{\odot})	$R_{\text{pre-SN}}$ (R_{\odot})	$M_{\text{Fe c}}$ (M_{\odot})	N/C	N/O	He/H	τ_{BSG} (kyr)
15	2	10	3.5	4.29	3.75	12.33	16.08	12.9	4.75	47.8	1.49	8.8	1.4	0.14	85
15	2	50	17.5	3.67	3.40	12.71	16.09	13.6	4.75	43.3	-	11.2	1.6	0.15	76
15	3	10	3.5	4.29	3.67	13.41	17.08	15.8	4.87	36.7	1.51	7.9	1.4	0.13	65
15	3	50	17.5	3.67	3.40	13.68	17.08	16.6	4.87	33.2	-	9.0	1.5	0.15	78
15	4	10	3.5	4.29	3.65	14.43	18.08	18.1	4.92	29.5	-	7.0	1.3	0.13	66
15	4	50	17.5	3.67	2.85	15.22	18.07	13.9	4.73	40.1	-	8.2	1.4	0.14	101
15	5	10	3.5	4.29	3.51	15.56	19.07	19.5	4.98	27.2	-	6.4	1.3	0.13	71
15	5	50	17.5	3.67	2.86	16.21	19.07	14.7	4.78	38.0	1.42	7.5	1.4	0.14	105
15	5	100	35.0	2.89	2.35	16.70	19.05	12.7	4.71	47.1	-	2.1	0.5	0.15	149
15	5	90	31.5	3.05	2.59	16.47	19.06	12.4	4.72	50.4	-	5.6	0.9	0.15	104
15	6	10	3.5	4.29	3.57	16.50	20.07	20.1	4.98	25.5	-	5.9	1.2	0.12	71
15	6	50	17.5	3.67	3.00	17.07	20.07	16.7	4.82	30.8	1.43	6.8	1.3	0.14	77
15	6	100	35.0	2.89	2.65	17.40	20.05	13.0	4.79	49.4	-	4.2	0.8	0.15	95
15	6	90	31.5	3.05	2.44	17.61	20.05	12.9	4.78	48.6	-	2.4	0.5	0.15	133
15	7	10	3.5	4.29	3.57	17.49	21.06	21.0	4.99	23.7	1.44	5.5	1.2	0.07	82
15	7	50	17.5	3.67	2.90	18.16	21.06	16.0	4.89	36.7	1.50	6.5	1.3	0.13	82
15	7	100	35.0	2.89	2.40	18.63	21.03	13.2	4.78	47.2	-	1.5	0.4	0.15	132
15	7	90	31.5	3.05	2.50	18.55	21.05	13.3	4.81	48.3	-	4.3	0.8	0.14	126
15	8	10	3.5	4.29	3.32	18.73	22.05	20.9	5.05	25.9	-	5.2	1.2	0.12	69
15	8	50	17.5	3.67	2.95	19.10	22.05	17.8	4.95	31.8	1.45	5.8	1.3	0.13	83

15	8	100	35.0	2.89	2.35	19.68	22.03	14.0	4.83	44.7	-	2.5	0.6	0.14	133
15	8	90	31.5	3.05	2.56	19.48	22.04	14.1	4.86	45.3	-	3.4	0.7	0.14	102
16	2	10	3.3	4.71	4.16	12.85	17.01	12.0	4.87	63.3	-	9.2	1.5	0.14	38
16	2	50	16.6	4.06	3.73	13.28	17.01	13.6	4.87	49.4	-	11.6	1.6	0.16	62
16	3	10	3.3	4.71	4.15	13.85	18.00	15.5	4.95	41.9	1.59	8.1	1.5	0.14	66
16	3	50	16.6	4.06	3.60	14.40	18.00	15.1	4.91	42.0	1.44	10.0	1.6	0.15	68
16	4	10	3.3	4.71	4.11	14.89	19.00	16.8	4.95	35.4	1.58	6.6	1.4	0.13	41
16	4	50	16.6	4.06	3.63	15.37	19.00	15.6	4.94	41.0	1.50	9.0	1.5	0.15	48
16	4	100	33.2	3.25	2.86	16.12	18.98	12.0	4.78	57.7	-	2.6	0.5	0.17	106
16	5	10	3.3	4.71	4.05	15.94	19.99	18.2	5.02	32.9	1.51	6.5	1.3	0.13	51
16	5	50	16.6	4.06	3.65	16.34	19.99	16.2	4.97	39.0	1.50	8.1	1.5	0.15	47
16	6	10	3.3	4.71	3.97	17.02	20.99	18.8	5.05	32.1	1.36	6.1	1.3	0.13	55
16	6	50	16.6	4.06	3.61	17.38	20.99	17.2	5.01	36.0	1.46	7.2	1.4	0.14	48
16	6	90	30.0	3.41	3.09	17.89	20.98	13.9	4.92	39.9	1.37	8.3	1.1	0.15	74
16	7	10	3.3	4.71	3.85	18.14	21.99	19.9	5.08	29.4	1.53	5.6	1.3	0.13	41
16	7	50	16.6	4.06	3.41	18.57	21.98	17.1	5.02	36.8	-	6.9	1.4	0.14	49
16	7	100	33.2	3.25	2.98	18.99	21.97	12.5	4.89	60.0	-	3.0	0.7	0.15	63
16	7	90	30.0	3.41	2.82	19.15	21.97	12.5	4.85	57.0	1.53	7.0	1.2	0.15	67
16	8	10	3.3	4.71	3.84	19.14	22.98	20.6	5.11	28.3	-	5.3	1.2	0.13	42
16	8	50	16.6	4.06	3.52	19.45	22.97	22.1	5.05	31.8	-	6.0	1.3	0.13	60
16	8	100	33.2	3.25	2.91	20.04	22.95	13.8	4.91	50.2	-	2.6	0.6	0.15	87
16	8	90	30.0	3.41	2.93	20.03	22.96	14.0	4.92	48.9	1.49	5.4	0.8	0.15	89
17	2	50	15.6	4.44	4.07	13.77	17.84	13.0	4.98	61.3	1.62	12.5	1.7	0.17	40

17	3	10	3.1	5.10	4.62	14.22	18.84	15.1	5.03	48.3	-	8.4	1.5	0.14	34
17	3	50	15.6	4.44	4.24	14.59	18.84	13.7	4.88	49.1	1.53 10.1	1.6	0.16	39	
17	4	10	3.1	5.10	4.49	15.35	19.84	16.4	5.03	41.0	-	12.7	1.4	0.14	36
17	4	50	15.6	4.44	4.30	15.53	19.83	15.8	5.03	44.3	1.55 8.6	1.5	0.15	37	
17	5	10	3.1	5.10	4.48	16.35	20.83	15.2	4.87	39.3	1.55 6.8	1.4	0.14	39	
17	5	50	15.6	4.44	3.93	16.90	20.83	14.7	4.99	48.2	1.52 8.5	1.5	0.15	41	
17	6	10	3.1	5.10	4.34	17.48	21.82	18.5	5.09	34.1	-	6.2	1.3	0.13	35
17	6	50	15.6	4.44	3.88	17.94	21.82	15.1	4.98	45.6	1.52 7.8	1.5	0.14	41	
17	6	90	28.1	3.78	3.29	18.51	21.80	12.3	4.93	65.0	- 1.9	0.5	0.16	57	
17	7	10	3.1	5.10	4.25	18.57	22.82	18.2	5.06	34.5	1.62 5.9	1.3	0.13	39	
17	7	50	15.6	4.44	3.86	18.95	22.81	16.2	5.02	41.0	1.53 7.0	1.4	0.14	41	
17	7	100	31.2	3.62	3.21	19.60	22.79	12.0	4.94	69.1	1.48 1.6	0.4	0.16	54	
17	8	10	3.1	5.10	4.24	19.57	23.81	20.4	5.24	33.4	- 5.5	1.3	0.13	40	
17	8	50	15.6	4.44	3.83	19.98	23.81	17.1	5.06	39.0	1.67 6.4	1.4	0.14	41	
17	8	100	31.2	3.62	3.32	20.47	23.79	12.6	4.97	65.3	1.48 4.0	0.8	0.15	50	
17	8	90	28.1	3.78	3.35	20.44	23.79	12.9	4.99	63.7	1.49 4.9	0.9	0.15	54	

TABLE 2.7: Parameters of **YSG** binary merger progenitors of Type II SNe ($4\text{ kK} \leq T_{\text{eff}} < 12\text{ kK}$). Column headings are same as Table 2.6.

M_1 (M_{\odot})	M_2 (M_{\odot})	f_{sh} %	f_c %	m_b (M_{\odot})	$M_{\text{He c}}$ (M_{\odot})	M_{env} (M_{\odot})	$M_{\text{pre-SN}}$ (M_{\odot})	T_{eff} (kK)	$\log(L)$ (L_{\odot})	$R_{\text{pre-SN}}$ (R_{\odot})	$M_{\text{Fe c}}$ (M_{\odot})	N/C	N/O	He/H	τ_{BSG} (kyr)	
15	2	100	35.0	2.89	2.68	13.40	16.08	11.1	4.63	56.5	1.41	4.4	0.8	0.17	0.0	
15	2	90	31.5	3.05	2.67	14.13	16.80	11.4	4.56	49.1	-	-	5.9	0.8	0.17	0.0
15	3	100	35.0	2.89	2.51	14.55	17.06	11.2	4.67	50.6	-	-	1.5	0.4	0.17	0.0
15	3	90	31.5	3.05	2.67	14.40	17.07	11.2	4.63	56.0	-	-	2.6	0.6	0.17	0.0
15	4	100	35.0	2.89	2.46	15.60	18.06	11.6	4.65	52.9	1.41	1.7	0.4	0.16	0.0	
15	4	90	31.5	3.05	2.74	15.33	18.07	11.7	4.60	56.0	-	-	9.5	1.2	0.16	0.0
16	2	100	33.2	3.25	3.14	13.86	17.00	9.67	4.72	82.2	-20.4	-	0.5	0.18	0.0	
16	2	90	30.0	3.41	3.05	13.95	17.00	10.7	4.69	64.9	-1.8	-	0.4	0.18	0.0	
16	3	100	33.2	3.25	3.05	14.94	17.99	9.62	4.70	81.4	-2.2	-	0.5	0.17	0.0	
16	3	90	30.0	3.41	3.10	14.90	18.00	11.5	4.75	60.3	-6.6	-	1.0	0.17	0.0	
16	4	90	30.0	3.41	3.04	15.96	19.00	11.6	4.74	58.4	-8.6	-	1.0	0.16	0.0	
16	5	100	33.2	3.25	3.06	16.93	19.99	10.9	4.78	69.6	-6.3	-	1.0	0.16	0.0	
16	5	90	30.0	3.41	3.00	16.98	19.98	10.8	4.74	67.6	1.34	2.8	0.6	0.16	0.0	
16	6	100	33.2	3.25	3.06	17.92	20.98	11.6	4.82	64.0	1.38	4.4	0.8	0.16	0.0	
17	2	10	3.1	5.10	4.63	13.21	17.84	11.7	4.91	69.4	1.67	9.6	1.6	0.15	0.0	
17	2	90	28.1	3.78	3.46	14.37	17.83	6.52	5.03	177.0	1.51	3.0	0.6	0.19	0.0	
17	2	100	31.2	3.62	3.44	14.39	17.83	6.95	4.70	156.8	1.48	2.0	0.4	0.19	0.0	
17	3	100	31.2	3.62	3.39	15.43	18.82	9.35	4.78	94.4	1.49	1.9	0.4	0.18	0.0	
17	3	90	28.1	3.78	3.37	15.45	18.82	9.23	4.77	94.2	1.44	1.7	0.4	0.18	0.0	
17	4	100	31.2	3.62	3.30	16.51	19.81	9.79	4.77	85.6	1.47	1.4	0.4	0.17	0.0	

17	4	90	28.1	3.78	3.41	16.41	19.82	10.4	4.79	77.3	1.49	6.9	1.0	0.17	0.0
17	5	100	31.2	3.62	3.39	17.42	20.81	10.7	4.85	77.3	1.50	4.0	0.8	0.17	0.0
17	5	90	28.1	3.78	3.17	17.64	20.81	10.4	4.80	78.8	1.45	1.2	0.3	0.17	0.0
17	6	100	31.2	3.62	3.35	18.45	21.80	10.8	4.83	74.5	1.49	2.0	0.5	0.16	0.0
17	7	90	28.1	3.78	3.22	19.57	22.79	11.8	4.88	67.2	1.47	1.5	0.4	0.16	0.0

Chapter 3

Explosions of binary merger progenitors for peculiar Type II supernovae

3.1 Introduction

In this chapter we investigate the explosions of our binary merger models from Chapter 2 for SN 1987A and two other peculiar Type II (Type II-pec) SNe, SN 1998A and SN 2006V.

Along with the unusual progenitor characteristics and the light curve shape, there was another surprising aspect about SN 1987A. This was the extent of mixing of Ni out into the envelope where it could not have been produced by thermonuclear reactions, along with the mixing of H and other chemical species into the He core, both of which were required to explain the smooth rise and the broad dome of the light curve (Woosley, 1988; Utrobin, 2004; Blinnikov et al., 2000). The fast and smooth rise of the light curve and its broad dome shape indicated a large extent of mixing of ^{56}Ni out into the envelope where it could not have been produced by thermonuclear reactions, along with the mixing of H and other chemical species into the He core (Woosley, 1988; Shigeyama and Nomoto, 1990; Blinnikov et al., 2000; Utrobin, 2004). Spectral observations between 20 – 100 days showed an unusual phenomenon called the ‘Bochum event’, wherein fine structures were observed in the H_α line profile (Hanuschik and Dachs, 1987; Phillips and Heathcote, 1989). In addition, the net flux of the H_α line dropped to zero at day 20 but was greater than zero before and after that, which indicated that an additional heating source powered the H_α line after its drop at day 20 (Phillips and Heathcote, 1989; Thimm, Hanuschik, and Schmidt-Kaler, 1989). This heating source was attributed to the emission of γ -rays from the decay of ^{56}Ni and ^{56}Co clumps or fingers, which were mixed from the explosion engine to the outer layers of the ejecta where H was present (Woosley, 2012). The mixing is expected to occur when the shockwave from the explosion gets decelerated at the the (C+O)/He and He/H composition interfaces. The formation of Rayleigh-Taylor (RT) instabilities at these interfaces causes outward mixing of ^{56}Ni into the hydrogen envelope, while inward mixing of hydrogen into

the helium core of the progenitor star only depends on the strength of RT instabilities at the He/H composition interface (see e.g., Arnett et al., 1989; Shigeyama and Nomoto, 1990; Kifonidis et al., 2003; Kifonidis et al., 2006; Wongwathanarat, Müller, and Janka, 2015).

Observations of the ejecta between 20 – 100 days showed an unusual feature called the ‘Bochum event’, wherein fine structures were observed in the velocity distribution of the H_α line profile (Hanuschik and Dachs, 1987; Phillips and Heathcote, 1989). In addition, the net flux of the H_α line dropped to zero at day 20 but was greater than zero before and after that, which indicated that an additional heating source powered the H_α line after its drop at day 20 (Phillips and Heathcote, 1989; Thimm, Hanuschik, and Schmidt-Kaler, 1989). This heating source was attributed to the deep mixing of ^{56}Ni and ^{56}Co clumps or fingers from the iron core to the outer layers of the ejecta where H was present and their subsequent radioactive decay (Woosley, 2012). Observations also supported the requirement of strong mixing in the ejecta: the bulk of the Ni and Fe mass in the ejecta was observed to mix out to regions travelling at 3000 km/s (Colgan et al., 1994). Utrobin, Chugai, and Andronova (1995) could reproduce the Bochum event by accounting for the fast, outward mixing of Ni clumps with one clump of Ni found to be travelling as fast as 4700 km/s. The later evolution (> 200 days) of velocity estimated from the H_α line profile in the ejecta showed that H was distributed down to regions within the He core, where the ejecta had velocities of 500 – 700 km/s (Chugai, 1991; Kozma and Fransson, 1998). Observations of the 3D distribution of the ejecta by Larsson et al. (2016) found H_α line emission in the ejecta down to velocities of 450 km/s.

The light curve of SN 1987A can be classified into two parts. The early light curve, up to 20 – 30 days, was powered by the release of the internal energy left behind by the shock wave after propelling the expansion of the ejecta. The later part of the light curve was entirely powered by the radioactive decay energy of ^{56}Ni to ^{56}Co and thereafter, the later part of the light curve > 100 days, by the decay of ^{56}Co to ^{56}Fe (Woosley, 1988; Shigeyama and Nomoto, 1990; Utrobin, 2004). These features of the light curve of SN 1987A make it significantly different from those of typical Type IIP SNe (Woosley, 1988; Arnett et al., 1989; Hamuy, 2003).

There are two methods to approach modelling the light curve of supernovae: using evolutionary models or using artificially constructed non-evolutionary models. The first method uses a progenitor model obtained from stellar evolution calculations and then varies the explosion parameters to produce a match with the observations. The second one is a reverse-engineering process in which one constructs an ‘optimal’ stellar model by assuming a homologous relation between mass and radius. In this method, individual parameters such as the radius, ejecta mass, explosion energy, mixing are varied to obtain the

best parameter set to reproduce the light curve. For the rest of this chapter we use the following notation for the above parameters: $R_{\text{pre-SN}}$ is the radius of the progenitor (or pre-SN) model and $M_{\text{pre-SN}}$ is the mass of the pre-SN model. M_{ej} is the ejecta mass given by $M_{\text{ej}} = M_{\text{pre-SN}} - \text{mass cut} = M_{\text{pre-SN}} - 1.4M_{\odot}$, where the mass cut is the boundary of the neutron star and is not included in the explosion (see Section 3.2.2). E is the explosion energy applied at the mass cut, in units of Bethe (B) where $1\text{B} = 10^{51}$ ergs; it is the excess above the total energy of the envelope beyond the mass cut and hence is essentially the kinetic energy of the ejected mass. The Ni mass in the ejecta is denoted as M_{Ni} and the velocity of the ejected nickel mass is denoted as v_{Ni} .

All explosion studies for SN 1987A so far have used single star pre-SN models. These models were derived by fine-tuning specific aspects of the evolutionary path to force the star to explode as a BSG, such as rotation (Weiss, Hillebrandt, and Truran, 1988), reducing the helium core mass (Barkat and Wheeler, 1989a), decreasing the envelope metallicity (Arnett et al., 1989), increasing the He abundance in the envelope and increasing mass loss (Saio, Nomoto, and Kato, 1988; Shigeyama and Nomoto, 1990), restricting convection (Woosley, Pinto, and Weaver, 1988) or inducing rotation and restricting semi-convection (Woosley et al., 1997). The He core mass is denoted as M_{HeC} and the envelope mass is M_{env} , given by $M_{\text{pre-SN}} - M_{\text{HeC}}$.

Explosion studies that have used these single star evolutionary models have been done by e.g., Woosley (1988), Nomoto et al. (1988), Saio, Nomoto, and Kato (1988), Arnett et al. (1989), Shigeyama and Nomoto (1990), Blinnikov et al. (2000), and Utrobin (2004), using 1D radiation hydrodynamic codes. These models have a radius of $R_{\text{pre-SN}} = 30 - 70 R_{\odot}$, He core mass of $M_{\text{HeC}} = 4 - 7.4 M_{\odot}$ and an envelope mass of $M_{\text{env}} = 9 - 14 M_{\odot}$. With a choice of explosion parameters that include $E = 0.6 - 1.65 \text{ B}$, $M_{\text{Ni}} \approx 0.07$ which was determined from the luminosity of the Ni-decay tail of the light curve, and a ‘strong’ nickel mixing velocity compared to the observed value of 3000 km/s of $v_{\text{Ni}} = 4000 \text{ km/s}$, produced reasonably good fits with the light curve shape. Dessart and Hillier (2010) used a more sophisticated 1D time-dependent radiative transfer code to study the first 20 days of the spectral and light curve evolution, with an $18 M_{\odot}$ progenitor model which had $M_{\text{ej}} = 15.4 M_{\odot}$ and $R_{\text{pre-SN}} = 47 R_{\odot}$. The results from the explosion of this model also matched the observations in this period very well.

Non-evolutionary explosion calculations carried out by Utrobin (1993), Utrobin (2004), and Utrobin (2005) predicted different results for the progenitor than the above evolutionary calculations. Utrobin (1993) demonstrated that a progenitor model with $M_{\text{ej}} = 15 - 19 M_{\odot}$ and a density structure with a polytropic index of $n=3$ when exploded with $E = 1.25 - 1.65 \text{ B}$ can fit the light curve. Utrobin (2004) scaled an evolutionary model which had $M_{\text{ej}} = 17.8 M_{\odot}$ and $R_{\text{pre-SN}} = 64.2 R_{\odot}$ to one with $M_{\text{ej}} = 18 M_{\odot}$ and $R_{\text{pre-SN}} = 46.8 R_{\odot}$. By using an explosion energy of 1 B and a nickel mass of $0.073 M_{\odot}$ with this scaled model, Utrobin (2004) could

produce an excellent fit with the light curve data, but again with a strong nickel mixing velocity of 4000 km/s. On the other hand, an artificially constructed progenitor model which had $M_{\text{ej}} = 18 M_{\odot}$, $R_{\text{pre-SN}} = 46.8 R_{\odot}$ and a modified density distribution than the above evolutionary model, could reproduce the observed light curve with a ‘moderate’ nickel mixing velocity of 2500 km/s which is closer to the observed value.

Except for Dessart and Hillier (2010), all the above studies, both evolutionary and non-evolutionary, used only the photometric data of SN 1987A to constrain the progenitor model and did not study the evolution of the spectral lines in the ejecta. Utrobin (2005) were the first to simultaneously constrain a progenitor model by including both the photometric and spectroscopic observations of SN 1987A, using a non-evolutionary model of Utrobin (2004). Based on this study, Utrobin (2005) predicted that the ideal progenitor model whose explosion can match the bolometric light curve, the kinetics of spectral lines and the Ni mixing velocity of $v_{\text{Ni}} = 3000$ km/s required from observations, has $R_{\text{pre-SN}} = 35 \pm 5 R_{\odot}$, $M_{\text{ej}} = 18 \pm 1.5 M_{\odot}$, and an explosion energy to ejecta mass ratio of $E/M_{\text{ej}} = 0.83 \times 10^{50}$ ergs/ M_{\odot} , which gives $E = 1.5 \pm 0.12$ B for this model.

The most detailed work on the explosion properties of SN 1987A so far, is that of Utrobin et al. (2015), where they modelled the evolution of the supernova ejecta from the early explosion phase until the late nebular phase. Using specific single star BSG progenitor models, they performed 3D neutrino-driven explosion simulations (Wongwathanarat, Müller, and Janka, 2015) to study the evolution of hydrodynamic and chemical composition quantities until shock breakout and thereafter mapped these quantities to a 1D spherically symmetric model. None of the single star evolutionary models used in the study could correctly reproduce the light curve shape or spectral observations of SN 1987A, except for the optimal model of Utrobin (2005). The required value of $v_{\text{Ni}} = 3000$ km/s was found only in the 3D explosion simulation of one of the evolutionary models (B15), which had $M_{\text{ej}} = 15 M_{\odot}$ and $R_{\text{pre-SN}} = 56.1 R_{\odot}$, while the explosions of the other evolutionary models could only obtain $v_{\text{Ni}} \leq 2000$ km/s. Hydrogen was found to be mixed inward upto velocities of 100 km/s in all models, which is in agreement with observations.

Previous 3D hydrodynamic simulations of the explosion also obtained similar low values of the Ni mixing velocity of $v_{\text{Ni}} \approx 2000$ km/s (Yamada and Sato, 1991; Nagataki, Shimizu, and Sato, 1998; Hungerford, Fryer, and Warren, 2003; Ellinger et al., 2012). Nickel mixing in the ejecta is calculated in 3D explosion simulations by studying the growth of Rayleigh Taylor (RT) instabilities following the passage of the shockwave. The first simulations to report the development of RT mushrooms (also called RT fingers) after the shock passes through the outer layers of the star, seeded by the initial asymmetries in the supernova core, were of Kifonidis et al. (2003) in 2D. These RT mushrooms were found to penetrate the CO/O and He/H interfaces and carry nickel outward into the He shell and hydrogen inward from the envelope into the He core. Later, 3D explosion simulations also reported such mixing due to

RT mushrooms (Hammer, Janka, and Müller, 2010; Ellinger et al., 2012; Müller, Janka, and Heger, 2012; Wongwathanarat, Müller, and Janka, 2015).

The 3D simulations of Wongwathanarat, Müller, and Janka (2015) whose results were included in the work of Utrobin et al. (2015), demonstrated that the extent of mixing in the supernova explosion depends heavily on the overall progenitor density structure particularly the density gradient at the He/H interface, the compactness of the CO core and the location of the composition interfaces. It was found that Ni fingers penetrate deeper in the RSG models, into regions travelling at 4000 – 5000 km/s of the H-rich envelope, than in BSG models where the fingers penetrated out only up to velocities of 2200 km/s, except in model B15 where Ni fingers mixed out to a maximum velocity of 3500 km/s. The reason for this difference in v_{Ni} between RSG and BSG models, is that the growth rate of RT instabilities depends on the location where they are formed. This location is connected to the density structure of the He core and the time at which the reverse shock forms due to the deceleration of the outward propagating shockwave when it encounters the He/H interface (Herant and Benz, 1991). In the case of the single star BSG models used, Ni fingers in the He core do not have sufficient time to grow and penetrate the envelope before being stalled by the reverse shock (Herant, Benz, and Colgate, 1992). In order to allow the growth of Ni fingers, a steeper density gradient at the He/H interface similar to what is found in RSGs, is required in the BSG models as well (Herant, Benz, and Colgate, 1992; Wongwathanarat, Müller, and Janka, 2015).

There are thus two reasons why we need new pre-SN models for SN 1987A. Despite strong proof that the progenitor of SN 1987A evolved from a binary merger, there are no pre-SN models in published literature based on the binary merger scenario that can satisfactorily match both, the observed signatures of Sk –69°202 and whose explosions also match the light curve and spectral features of the supernova. Second, there is a need for an evolutionary model whose 3D-neutrino driven explosion can reproduce the required penetration of Ni and H fingers which agree with the observed mixing velocities and thereafter fit the light curve as well. Utrobin et al. (2015) also hinted that a progenitor from a binary merger can have larger envelope masses and may be more favourable to match the overall light curve shape of SN 1987A.

Menon and Heger (2017), Chapter 2, conducted the first systematic and detailed investigation of binary merger evolutionary models which were evolved until the pre-SN stage, i.e., until just prior to the onset of iron-core collapse. The majority of the 84 pre-SN models were blue and six of them matched the observational criteria for Sk –69°202 . The study included a large range of initial parameters, including the primary and secondary masses and mixing boundary during the merging. We shall provide an overview of this work in the next section.

Our first aim in this chapter, is to study the explosions of the progenitor models from

Chapter 2 and compare their light curves with that of SN 1987A. We broaden our study to investigate the viability of our progenitor models for two other Type-II pec SNe: SN 1998A and SN 2006V.

The merger pre-SN models have been computed using the stellar evolution code KEPLER and the light curves were calculated using the 1D radiation-hydrodynamic code CRAB, as explained in Section 3.2. In Section 3.3 we give an overview of the binary merger pre-SN models and their structural differences from single star models, the role of different parameters affecting the shape of the light curve, how they compare with earlier single star models and the best fit model for SN 1987A, along with SN 1998A and SN 2006V.

3.2 Methodology

3.2.1 Progenitor models used in this work

In Chapter 2, we constructed post-merger models using the implicit hydrodynamic stellar evolution code KEPLER based on the binary merger scenario outlined in Podsiadlowski, Joss, and Hsu (1992) and Podsiadlowski, Morris, and Ivanova (2007), and incorporating results from merger simulations of Ivanova and Podsiadlowski (2002b) and from 1D post-merger simulations of Ivanova and Podsiadlowski (2003). Evolutionary models were constructed by considering three initial parameters: the primary mass, M_1 , the secondary mass, M_2 and the fraction of the He shell of the primary's He core dredged up, f_{sh} . The range of these parameters were: $M_1 = 15, 16, 17 M_{\odot}$, $M_2 = 2, 3, \dots, 8 M_{\odot}$ and $f_{\text{sh}} = 10, 50, 90, 100\%$ (where 100% was the boundary of the CO core).

The evolution was followed from the zero age main sequence of the rotating primary star ($v/v_{\text{crit}} = 0.30$), until the central helium abundance dropped to $\sim 10^{-2}$, i.e., until the end of core He-burning. At this stage the primary star is a RSG with a He-depleted core and is merged with the secondary main-sequence star. A simple 1D merging prescription based on the merger simulations of Ivanova, Podsiadlowski, and Spruit (2002) and Ivanova and Podsiadlowski (2002a) and Ivanova and Podsiadlowski (2003) was used and is described in Section 2.2.2 in Chapter 2. At the end of the merger, the He core mass of the primary reduces depending on the mixing boundary set by f_{sh} , and the envelope mass increases depending on the value of M_2 . The models are evolved all the way until the pre-SN stage, i.e., when the infall velocity in any part of the star was $\sim 10^9$ cm/s, after the model attains an iron core.

Two factors were found to be important to determine the final position of the post-merger star in the HR diagram: first, the value of f_{sh} and next, the value of M_2 . In general, increasing f_{sh} for a given value M_1 and M_2 led to smaller He-cores and resulted in the pre-SN model becoming cooler, whereas increasing M_2 for a given M_1 and f_{sh} caused the pre-SN model to become hotter. For the parameter space we considered, BSG pre-SN models (with

TABLE 3.1: Model denotes the name of the pre-SN model; M_1 and M_2 are the initial primary and secondary masses of the binary system; f_{sh} is the fraction of the He-shell mass dredged up; $M_{\text{He c}}$, $M_{\text{Fe c}}$, M_{env} , and $M_{\text{pre-SN}}$ are He core, iron core, envelope masses and mass of the pre-SN model ($M_{\text{c}} + M_{\text{env}}$); T_{eff} , $\log(L)$, $R_{\text{pre-SN}}$ are the effective temperature, luminosity, radius of pre-SN model, $\xi_{1.5}$ is the compactness parameters.

Model	M_1 (M_{\odot})	M_2 (M_{\odot})	f_{sh} %	$M_{\text{He c}}$ (M_{\odot})	M_{env} (M_{\odot})	$M_{\text{pre-SN}}$ (M_{\odot})	$M_{\text{Fe c}}$ (M_{\odot})	T_{eff} (kK)	$\log(L)$ (L_{\odot})	$R_{\text{pre-SN}}$ (R_{\odot})	$\xi_{1.5}$
SN 1987A											
16-6a	16	6	10	4.0	16.0	20.0	1.52	16.8	4.9	32.8	0.008
16-6b	16	6	50	3.6	17.4	21.0	1.50	16.9	4.9	35.7	0.009
16-6d	16	6	90	3.1	17.9	21.0	1.40	12.8	4.7	46.0	0.006
16-6c	16	6	100	3.1	17.9	21.0	1.38	11.0	4.8	64.3	0.008
16-5a	16	5	10	4.0	16.0	20.0	1.52	16.8	4.9	32.8	0.011
16-7a	16	7	10	3.8	18.2	22.0	1.53	16.9	4.9	30.8	0.009
16-8a	16	8	10	3.8	19.2	22.0	1.53	18.8	5.0	28.8	0.009
16-7b	16	7	50	3.4	18.8	22.0	1.38	15.8	4.9	37.4	0.009
SN 1998A											
16-7b	16	7	50	3.4	18.8	22.0	1.38	15.8	4.9	37.4	0.009
SN 2006V											
18-4d	18	4	90	3.8	16.7	20.5	1.50	7.5	4.8	150.3	0.009

$T_{\text{eff}} \geq 12\text{kK}$) formed for the range of M_1 values, when $f_{\text{sh}} = 10 - 50\%$ and $M_2 \geq 4 M_{\odot}$. Fifty-nine of the 84 pre-SN models computed were BSGs while the rest were yellow supergiants (YSGs, with $7 \leq T_{\text{eff}} < 12\text{kK}$).

Although eleven Type II-pec SNe are known (Pastorello et al., 2012), only five of these have reasonably good observational data (Lusk and Baron, 2017) aside from SN 1987A. These are: SN 1998A, SN 2000cb, SN 2006au, SN 2006V and SN 2009e. SN 2000cb was studied by Utrobin and Chugai (2011) and its progenitor was predicted to have $R_{\text{pre-SN}} = 35 \pm 14 R_{\odot}$ and $M_{\text{ej}} = 22.3 \pm 1 M_{\odot}$. For the present work, we attempted to make more massive merger models with the above ejecta mass of $22.3 \pm 1 M_{\odot}$ than the ones in Section 2.5, however the radius of these models was much larger than $35 \pm 14 R_{\odot}$. Hence we could not study SN 2000cb in this work. For SN 2006au, there were no data points for the nickel decay tail luminosity in the bolometric light curve and therefore we could not investigate this supernova in this study. In the case of SN 2009e, there were not enough data points in the bolometric light curve for $t < 100$ days (Pastorello et al., 2012), without which it was not possible to perform a progenitor analysis. Hence SN 2009E was also omitted from our study.

In this work, we used the pre-SN models of Chapter 2 for SN 1987A and SN 1998A and computed additional models for SN 2006V. While the progenitor models for SN 1987A listed in Table 2.4 of Chapter 2 are those that satisfy all the observational criteria of Sk – 69°202, we also study the impact of changing the initial progenitor parameters, f_{sh} and M_2 , and hence include other BSG pre-SN models as well. In Table 3.1 we list all the progenitor models discussed in this chapter.

3.2.2 CRAB: The explosion code

The implicit Lagrangian radiation hydrodynamics code CRAB (Utrobín, 2004; Utrobín, 2007) integrates the spherically symmetric equations. It solves the set of hydrodynamic equations including self-gravity, and a radiation transfer equation. The latter is treated in the one-group (gray) approximation in the outer, optically transparent or semitransparent layers of the SN ejecta and is described as the diffusion of equilibrium radiation in the approximation of radiative heat conduction in the inner, optically thick layers, where thermalization of radiation takes place (e.g., Mihalas and Mihalas, 1984). The pre-SN models provided by the evolutionary simulations of binary mergers are used as the initial data in our hydrodynamic modeling of the SN outburst. The SN explosion is initiated by a supersonic piston applied to the bottom of the stellar envelope at the boundary of the $\sim 1.4 M_{\odot}$ central core, which is removed from the computational mass domain and assumed to collapse becoming a neutron star.

The time-dependent radiative transfer equation, written in a comoving frame of reference to accuracy of order v/c (v is the fluid velocity, c is the speed of light), is solved as a system of equations for the zeroth and first angular moments of the non-equilibrium radiation intensity. To close this system of moment equations, a variable Eddington factor is calculated, directly taking the scattering of radiation in the ejecta into account. The total set of equations is discretized spatially using the method of lines (e.g., Hairer, Norsett, and Wanner, 1993; Hairer and Wanner, 1996). The resultant system of ordinary differential equations is integrated by the implicit method of Gear (1971) with an automatic choice of both the time integration step and the order of accuracy of the method. Shock waves are automatically captured by means of the linear and nonlinear artificial viscosity of Caramana, Shashkov, and Whalen (1998). The radiation hydrodynamic equations include additional Compton cooling and heating according to Weymann (1966). The bolometric luminosity of the SN is calculated by including retardation and limb-darkening effects.

Energy deposition of gamma rays from the decay chain $^{56}\text{Ni} \rightarrow ^{56}\text{Co} \rightarrow ^{56}\text{Fe}$ is calculated by solving the gamma-ray transport with the approximation of an effective absorption opacity of $0.06 Y_e \text{ cm}^2 \text{ g}^{-1}$, while positrons are assumed to deposit their energy locally. The Compton electrons, occurring in scattering of gamma rays, lose their energy through Coulomb heating of free electrons, and ionization and excitation of atoms and ions. The rates of non-thermal heating, excitation, and ionization of atoms and ions are taken from Kozma and Fransson (1992).

A non-equilibrium radiation field and a non-thermal excitation and ionization require solving the general problem of the level populations and the ionization balance instead of using the Boltzmann formulae and the Saha equations under the LTE conditions. Multiple calculations of the corresponding equation of state in hydrodynamic modeling are possible by neglecting the excited atomic and ionic levels, i.e. by considering only the

atomic and ionic ground states and their ionization balance. The non-LTE ionization balance includes the elements H, He, C, N, O, Ne, Na, Mg, Si, S, Ar, Ca, Fe, and the negative hydrogen ion H^- , and is controlled by the following elementary processes: photoionization and radiative recombination, electron ionization and three-particle recombination, and non-thermal ionization. The partition functions are calculated with the polynomial approximation fit obtained by Irwin (1981). The photoionization cross sections of atoms and ions are evaluated with data of Verner and Yakovlev (1995), and Verner et al. (1996). The electron collisional ionization rates for atoms and ions are computed using the approximate formulae of Voronov (1997). The photoionization cross section data for the negative hydrogen ion are taken from Wishart (1979), and the rate coefficient of the electron collisional detachment reaction for the negative hydrogen ion from Janev, Langer, and Evans (1987).

Non-LTE effects are adequately taken into account when determining the mean opacities, the thermal emission coefficient, and the contribution of lines to the opacity. The mean opacities have contributions from photoionization, free-free absorption, Thomson scattering on free electrons, and Rayleigh scattering on neutral hydrogen. Line opacities are treated by the Sobolev approximation and also as scattering. The free-free absorption coefficient is calculated with the effective nuclear charge including screening effects (Sutherland and Dopita, 1993) and the temperature-averaged free-free Gaunt factor from Sutherland (1998). The free-free absorption coefficient of negative hydrogen ions was computed by Bell and Berrington (1987). The Rayleigh scattering by hydrogen atoms is calculated using the cross-section of Gavrilin (1967) and the exact static dipole polarizability of hydrogen from Teachout and Pack (1971).

In expanding SN ejecta with a velocity gradient, the contribution of spectral lines to the opacity is essential and estimated by the generalized formula of Castor, Abbott, and Klein (1975b). In these outer, semitransparent and transparent layers, the ground state populations are calculated in non-LTE for the equation of state and for continuum opacity. The expansion line opacities are determined by atomic and ionic level populations with the Boltzmann formulae and the Saha equations for a mixture of all elements from H to Zn with the local non-equilibrium radiation temperature. Oscillator strengths of lines are taken from the line database of Kurucz (2002) which contains nearly 530 000 lines. The corresponding energy level data are from the atomic spectra database of the National Institute of Standards and Technology.

3.3 Results

3.3.1 Comparison between binary merger and single star pre-supernova models

The binary merger BSG models in Table 3.1 are structurally different from single star models of earlier studies. In Fig. 3.1, we compare the density profiles of the pre-SN model 16-7b

which has a total mass of $22 M_{\odot}$ and single star pre-SN models used in Utrobin et al. (2015), with main-sequence masses of $15 - 20 M_{\odot}$.

In general, our merger models have smaller He cores than single star models ($3 - 4 M_{\odot}$ compared to $4 - 7.2 M_{\odot}$), more massive envelopes ($16 - 19.2 M_{\odot}$ compared to $11 - 14.5 M_{\odot}$) and have smaller radii as well ($29 - 64 R_{\odot}$ compared to $47 - 64 R_{\odot}$). The density profile of the binary merger model is steeper at the He core/envelope interface in the binary merger model than the single star model and have denser envelopes as well. The compactness parameter in this study is calculated as $\xi_{1.5} = (M/M_{\odot})/(R(M)/1000 \text{ km})$ for $M = 1.5 M_{\odot}$ as in Utrobin et al. (2015). Our models have a smaller compactness parameter between $0.006 - 0.011$ compared to single star models which have a compactness parameter of $0.24 - 0.78$. The Fe core masses of the merger pre-SN models are between $1.4 - 1.5 M_{\odot}$ while those of the single star models are between $1.2 - 1.5 M_{\odot}$.

The ‘optimal’ non-evolutionary model computed by Utrobin (2005) whose explosion matched the light curve and H-line photospheric velocity profile, had an ejecta mass of $18 M_{\odot}$ and a radius of $35 R_{\odot}$. The single star evolutionary models in Fig. 3.1 thus have larger radii and smaller ejecta masses than this optimal model, whereas some of our binary merger models from Table 3.1 do fit these ideal progenitor characteristics.

3.3.2 The light curve of SN 1987A

The light curve of Type II SNe are powered by two sources: the deposited shock energy from the explosion and the energy from the radioactive decay of ^{56}Ni to ^{56}Co and later ^{56}Co to ^{56}Fe . In the case of compact progenitors, most of the shock energy is expended to adiabatically expand the star and hence the light curve is predominantly powered by gamma-ray energy (Woosley, 1988; Blinnikov et al., 2000; Utrobin, 2004). If there were no ^{56}Ni in the star, the light curve would begin to descend after 40 days after radiating away the fraction of shock energy deposited (Utrobin, 2004).

Subsequent to the triggering of the explosion, the passage of the shockwave heats up the outer layers of the star and causes it to expand. After the shock breaks out of the surface, the luminosity surges to a peak between $10^{44} - 10^{45} \text{ erg/s}$ (Woosley, 1988; Blinnikov et al., 2000). As the star expands and cools, the luminosity decreases until about ~ 8 days at which point the temperature at some layer in the star approaches that of hydrogen recombination, and a photosphere forms at this shell, because gas outside of this shell becomes transparent. A cooling and recombination wave (CRW) travels inward, with the photosphere in it, and the internal energy of the star begins to radiate outward (Hamuy, 2003). The period of time $t < 40$ days is referred to as the early light curve. After about 40 days until 120 days, referred to as the middle light curve, the energy diffused outward increasingly becomes dominated by the gamma-ray radioactive energy (Young, 2004). When the CRW reaches the H-poor layers

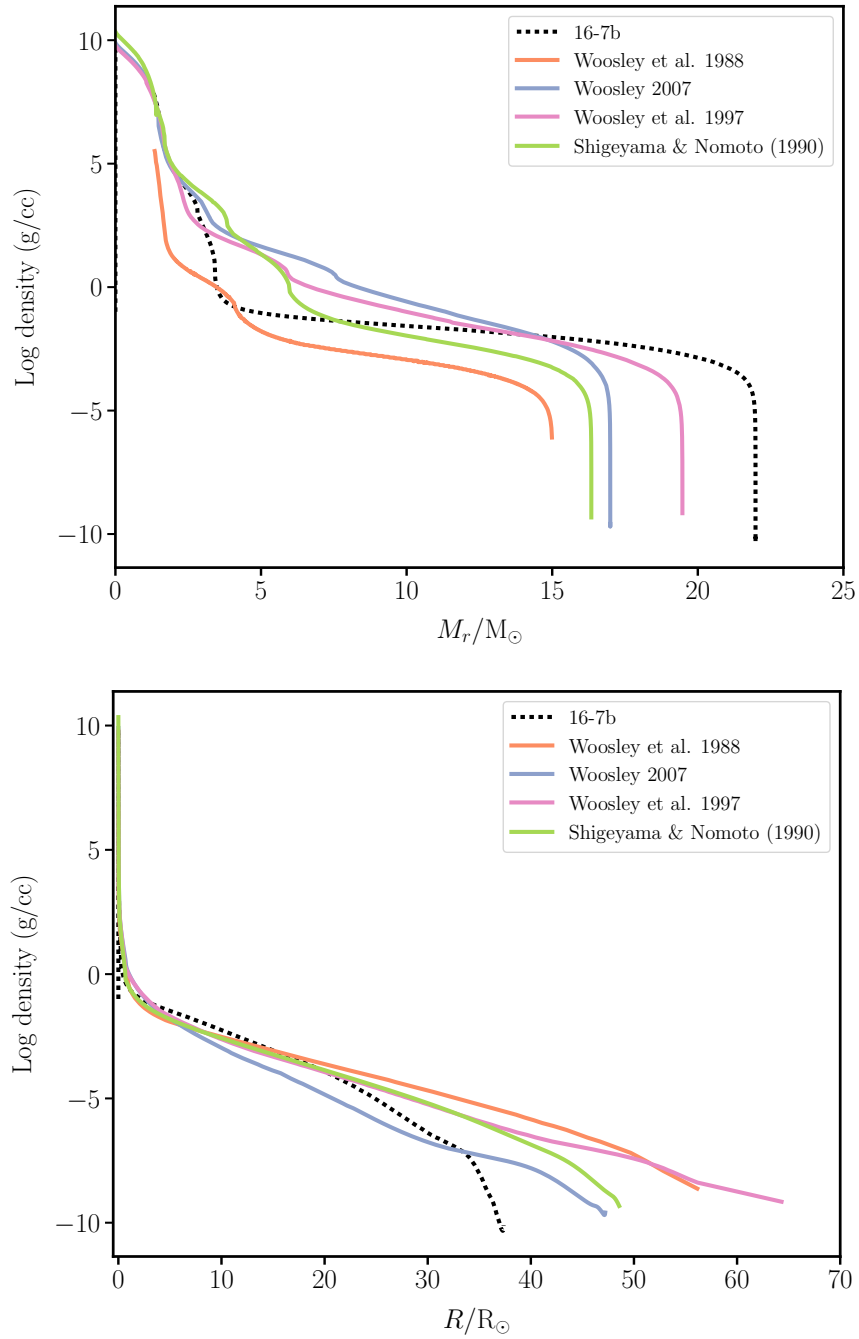


FIGURE 3.1: Density profiles of Model 16-7b and single star pre-SN models used in Utrobin et al. (2015) as a function of mass coordinate (top) and radius (bottom).

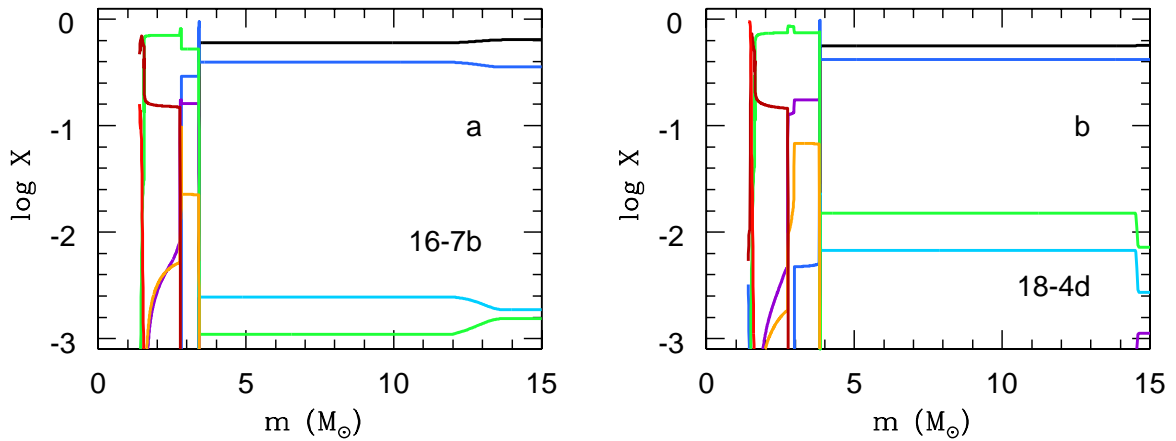


FIGURE 3.2: Chemical composition of the original pre-SN models 16-7b (a) and 18-4d (b). Mass fraction of hydrogen (black line), helium (blue line), carbon (violet line), nitrogen (cyan line), oxygen (green line), neon (orange line), silicon (firebrick line), and iron (red line).

of the star, the bolometric luminosity follows the instantaneous release of energy from the decay of ^{56}Ni to ^{56}Co and later of ^{56}Co to ^{56}Fe . This is the late light curve phase ($t > 120$ days).

Varying explosion parameters for SN 1987A

In this section, we study the effect of varying the explosion energy E , the width of boxcar mixing ΔM and the velocity of nickel v_{Ni} mixed to the surface on the light curve of SN 1987A. The nickel mass is fixed at $M_{\text{Ni}} = 0.073 M_\odot$. The mass cut in all the models is $1.4 M_\odot$. The explosion energy E is the excess above the total energy of the envelope and thus determines the kinetic energy of the ejected mass.

We demonstrate the effect of varying the above explosion parameters on Model 16-7b of Table 3.1, which is closest to the optimal model of Utrobin (2005). In Fig. 3.3, we vary the explosion energy for the ejected material between 1.7 – 2.5B. The best match for the light curve is produced for $E = 1.7$ B, at the dip at ~ 8 days and the overall fit in the middle light curve region. This result is in concurrence with the prediction of Utrobin (2005) for their optimal model, in which the synthetic H_α line profile at ~ 4.6 days reproduced the spectroscopic observations of SN 1987A at a ratio of $E/M_{\text{ej}} = 1.5\text{B}/18 M_\odot$. We hence use the same E/M_{ej} value for all our progenitor models in this study.

Next, we use an artificial procedure that mimics the mixing that arises from instabilities in the ejecta as seen in 3D simulations (such as those of after the passage of the shock-wave Kifonidis et al., 2003; Kifonidis et al., 2006; Wongwathanarat, Müller, and Janka, 2015) and has also been used in other 1D explosion studies such as those of (Pinto and Woosley, 1988; Kasen and Woosley, 2009; Dessart et al., 2013; Morozova et al., 2015). This 1D mixing is implemented via a running boxcar of width ΔM through the envelope of the star, which

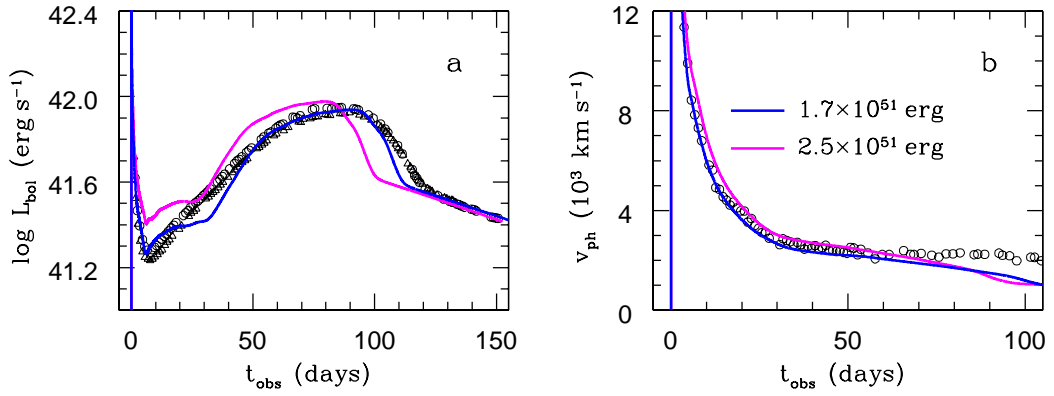


FIGURE 3.3: Dependence on the explosion energy. Bolometric light curves (panel a) and the photospheric velocity as a function of time (panel b) of Model 16-7b for the explosion energies of 1.7 B (blue line) and 2.5 B (magenta line) respectively. The computed curves are compared with the observed bolometric luminosity of SN 1987A obtained by Catchpole et al. (1987) and Catchpole et al. (1988b) (open circles) and Hamuy et al. (1988b) (open triangles), and with the velocity at the photosphere estimated by Phillips et al. (1988) with the absorption minimum of the Fe_{II} \sim 5169 Å line (open circles).

averages the composition of all chemical species other than ^{56}Ni . In Fig. 3.4, we vary the width of the running boxcar, ΔM , which effectively smoothens composition gradients in the ejecta. Increasing ΔM increases the spread of hydrogen inward (thick lines in Fig. 3.4). The boxcar width determines the distribution of hydrogen within the He core, which, in turn, determines the shape of the dome at the transition from the luminosity maximum to the radioactive tail (Fig. 3.4b). A value of $\Delta M = 2M_{\odot}$ mimics hydrogen mixing down to zero velocity which agrees with spectral observations, and produces the best match with the dome shape of SN 1987A.

After fixing the values of E and ΔM , we next selectively vary the mixing of ^{56}Ni in velocity space, keeping all other species intact (Fig. 3.5). We find that in order to have a smoothly rising light curve to maximum, a strong nickel mixing velocity of 4000 is required, which is the same result as found in previous explosion studies using evolutionary models (Shigeyama and Nomoto, 1990; Blinnikov et al., 2000; Utrobin, 2004). Using the observed value of 3000 results in a slower luminosity increase between 15 – 35 days due to the photosphere approaching the region where the internal energy of the ejecta has been radiated away and the gamma-ray energy from the radioactive decay has not been diffused yet. If ^{56}Ni is distributed out to regions moving at larger velocities, then the gamma rays diffused compensates for the drop in internal energy of the envelope and the light curve rises smoothly.

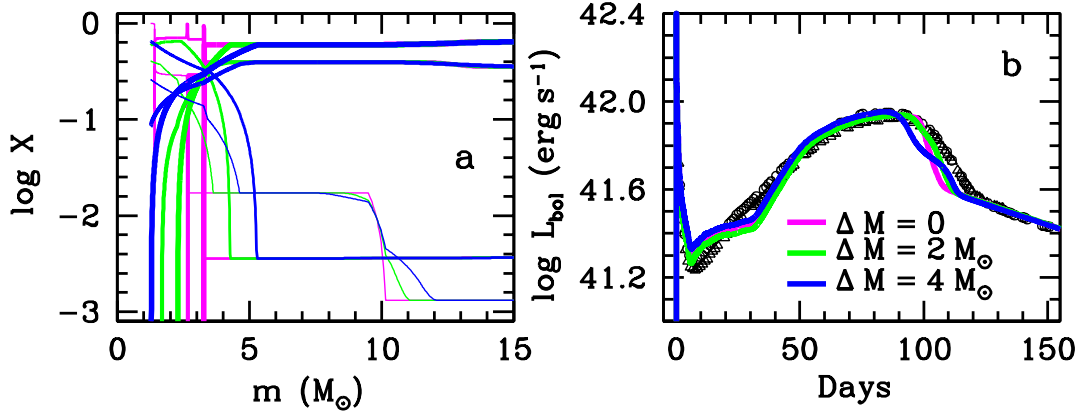


FIGURE 3.4: Dependence on the boxcar mass width ΔM . Panel a: The chemical composition of the pre-SN models based on Model 16-7b after the boxcar averaging with the mass width $\Delta M = 2 M_\odot$ (green lines), $4 M_\odot$ (blue lines) and with no mixing, $\Delta M = 0 M_\odot$ (magenta lines). Mass fractions of hydrogen (thick line), helium (medium line), CNO elements (thin line), and Fe-peak elements (tiny line) are plotted. Panel b: The corresponding bolometric light curves are compared with the observations of SN 1987A obtained by Catchpole et al. (1987) and Catchpole et al. (1988b) (open circles) and Hamuy et al. (1988b) (open triangles).

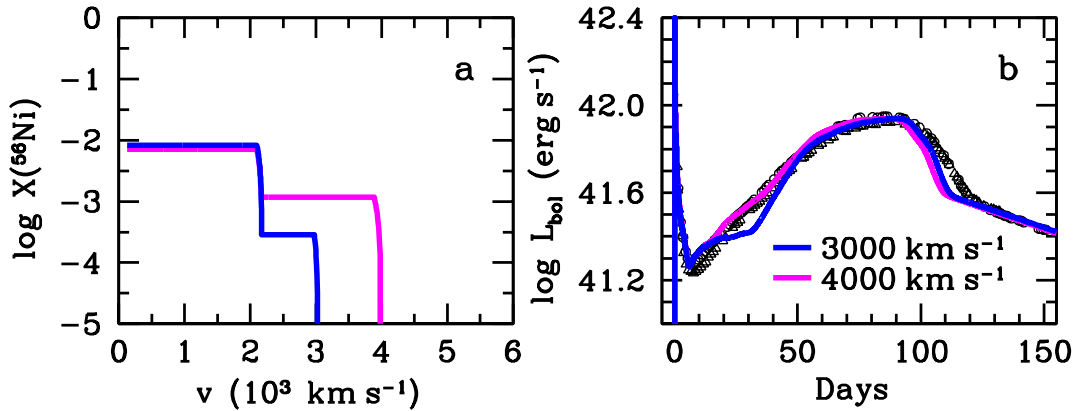


FIGURE 3.5: Dependence on the extent of mixing of radioactive ^{56}Ni . Panel a: Mass fraction of radioactive ^{56}Ni as a function of velocity at day 50 for Model 16-7b. Panel b: The corresponding bolometric light curves compared with the observations of SN 1987A obtained by Catchpole et al. (1987) and Catchpole et al. (1988b) (open circles) and Hamuy et al. (1988b) (open triangles).

Varying progenitor parameters

From the results of the previous section, we choose the following explosion parameters for the investigation into other progenitor models: $E/M_{\text{ej}} = 1.5B/18 M_\odot$, $v_{\text{Ni}} = 3000 \text{ km/s}$ and $\Delta M = 2 M_\odot$.

In Fig. 3.6, we explore how the fraction of the He shell of the He core dredged up, f_{sh} , affects the light curve shape for pre-SN models with a primary of mass $M_1 = 16 M_\odot$. These are Models 16-6a, 16-6b, 16-6c and 16-6d in Table 3.1, which have $f_{\text{sh}} = 10, 50, 90, 100\%$ and

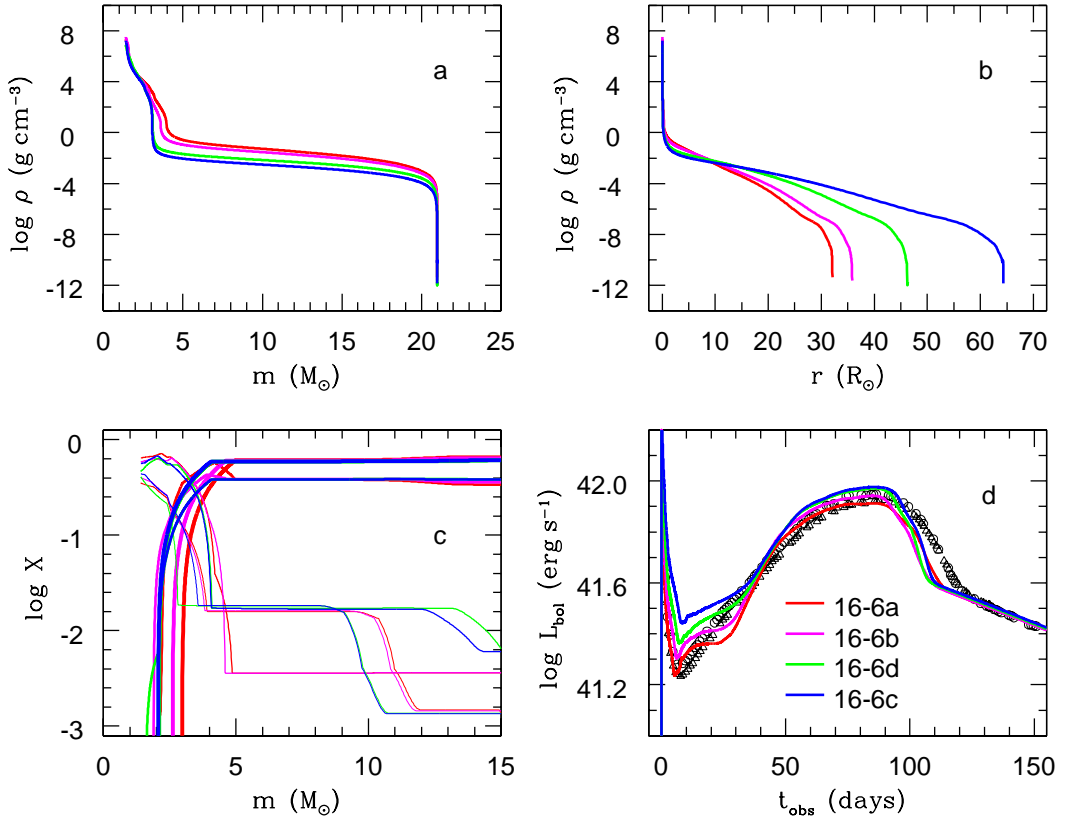


FIGURE 3.6: Variation in the fraction of the He-shell of the He core dredged up, f_{sh} : 10% (red lines), 50% (magenta lines), 90% (green lines), and 100% (blue lines) for $M_1 = 16 M_{\odot}$ and $M_2 = 6 M_{\odot}$. Panel a: density distributions as functions of interior mass for Models 16-6a, 16-6b, 16-6d, and 16-6c. Panel b: density distributions as functions of radius for the same models. Panel c: the chemical composition of the corresponding pre-SN models after the boxcar averaging with the mass width $\Delta M = 2 M_{\odot}$. Mass fractions of hydrogen (thick line), helium (medium line), CNO elements (thin line), and Fe-peak elements (tiny line) are plotted. Panel d: the calculated bolometric light curves are overlaid on the bolometric data of SN 1987A obtained by Catchpole et al. (1987) and Catchpole et al. (1988b) (open circles) and Hamuy et al. (1988b) (open triangles).

$M_2 = 6 M_{\odot}$. With increasing f_{sh} , the He core mass decreases and consequently the location of the H-rich envelope is more inward (panel c). Hence the CRW forms sooner for smaller core masses and the light curve begins to ascend earlier. In addition, with smaller core masses the models have larger radii (panel b). This reduces the expansion timescale for the envelope and decreases the role of adiabatic energy losses (Utrobin, 2005), causing the luminosity to increase between 15 and 30 days with a less pronounced bump. Thus overall, with increasing f_{sh} , the light curve ascends earlier and shifts upward.

In Fig. 3.7, we explore how the accreted secondary mass M_2 , affects the light curve shape. These are Models 16-5a, 16-6a, 16-7a and 16-8a in Table 3.1, which have $f_{\text{sh}} = 10\%$ and $M_2 = 5, 6, 7, 8 M_{\odot}$ and radii between 29 – 32.5 R_{\odot} . The density profile in the core of these models is the same (panel a, Fig. 3.6). Increasing M_2 increases the envelope mass and delays

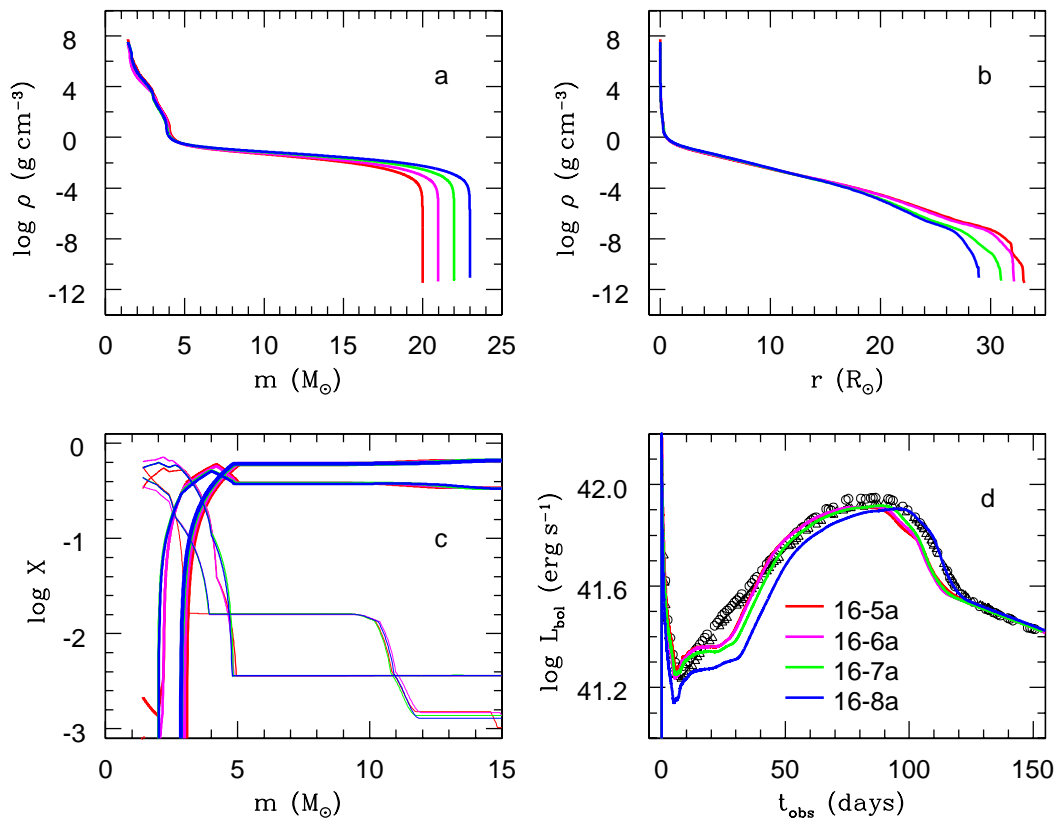


FIGURE 3.7: Variation in the secondary mass: $M_2 = 5 M_\odot$ (red lines), $6 M_\odot$ (magenta lines), $7 M_\odot$ (green lines), and $8 M_\odot$ (blue lines) for the primary mass $M_1 = 16 M_\odot$ and the fraction $f_{\text{sh}} = 10\%$. See the legend of Figure 3.6 for details.

the rise of the light curve. This is because there is less kinetic energy available per unit mass to expand the envelope, and hence the ejecta cools at a slower rate. Thus overall, the light curve shifts to the right with increasing M_2 . The bump feature between 15-30 days is also more pronounced as M_2 increases because there is less internal energy per unit mass deposited by the shock, which is then radiated away faster than the diffusion timescale of nickel decay energy.

Of the pre-SN models we analysed in this work, the best fit progenitor model for SN 1987A is Model 16-7b (Fig. 3.8) which satisfies all the observational criteria of Sk-69°202, the photospheric velocity of Fe absorption lines and the light curve Fig. 3.9. The explosion parameters are $E = 1.7 B$, $M_{\text{ej}} = 20.6 M_\odot$, $v_{\text{Ni}} = 3000 \text{ km/s}$ and $M_{\text{Ni}} = 0.073 M_\odot$.

3.3.3 Other Type II-pec SNe: SN 1998A and SN 2006V

We now extend our analysis to two other Type II-pec SNe. Table 3.2 lists the predicted progenitor properties from hydrodynamic models, semi-analytic models and scaling relations for five Type II-pec SNe.

SN 1998A which exploded in a spiral arm of the SBc galaxy IC 2627, was a more energetic explosion than SN 1987A which was recorded by Williams et al. (1998) and Woodings et al. (1998) and whose photometric data was obtained by Pastorello et al. (2005). Its bolometric luminosity exceeds that of SN 1987A at all days and from the luminosity of its Ni-decay tail, the nickel mass of this supernova is estimated to be $M_{\text{Ni}} = 0.09 - 0.11 M_{\odot}$ compared to $M_{\text{Ni}} = 0.073 M_{\odot}$ for SN 1987A (Pastorello et al., 2005; Pastorello et al., 2012). It also had a photospheric velocity higher than that of SN 1987A, on average about ~ 1.7 times more.

From a semi-analytic code that used single star pre-SN models, Pastorello et al. (2005) predicted a progenitor of radius, $R_{\text{pre-SN}} < 86.3 R_{\odot}$ and an ejecta mass of $M_{\text{ej}} = 22 M_{\odot}$ for SN 1998A by scaling with progenitor quantities from SN 1987A of $R_{\text{pre-SN}} < 71 R_{\odot}$ and $M_{\text{ej}} = 18 M_{\odot}$ for SN 1987A. SN 1998A was also estimated to have had an explosion energy 5 – 6 times more than that of SN 1987A (Pastorello et al., 2012).

Using CRAB, we tested Model 16-7b for SN 1998A, whose density distribution and chemical composition prior to the explosion are shown in Fig. 3.8. At day 50 after the explosion, the photospheric velocity is 1.5-2 times higher than the corresponding velocity in SN 1987A (panel b in Fig. 3.9 and Fig. 3.10). The higher velocities indicated the requirement of a stronger mixing of nickel than 3000 km/s for SN 1987A, further out to regions moving at 5300 km/s (panel c in Fig. 3.10). The step-like feature in the nickel distribution in both supernovae is required to account for the high absorption line velocities after day 40. Model 16-7b reproduces the light curve shape of SN 1998A and closely matches its photospheric velocity profile, with the explosion parameters of $E = 4.5 B$, $M_{\text{Ni}} = 0.12 M_{\odot}$ and $v_{\text{Ni}} = 5300 \text{ km/s}$.

SN 2006V is more luminous compared to SN 1987A and it occurred in the spiral galaxy UGC 6510 (Chen, Yang, and Lin, 2006) and its photometric data was taken by Taddia et al. (2012). Based on semi-analytic modelling and scaling relations, the progenitor expected for this supernova had $R_{\text{pre-SN}} < 50 - 75 R_{\odot}$, $M_{\text{ej}} = 17 - 20 R_{\odot}$. Due to its higher luminosity and photospheric velocities, SN 2006V was expected to have had a higher explosion energy of 2.4 B and a larger nickel mass of $0.127 M_{\odot}$ (Taddia et al., 2012). These results are scaled according to a SN 1987A progenitor model with $R_{\text{pre-SN}} = 33 R_{\odot}$, $M_{\text{ej}} = 14 M_{\odot}$, and an explosion energy of $E = 1.1 B$ and $M_{\text{Ni}} = 0.078 M_{\odot}$.

Our best fit binary merger model (Fig. 3.11), that matches the light curve and the photospheric velocity is Model 18-4d, with $R_{\text{pre-SN}} = 150.4 R_{\odot}$ and $M_{\text{ej}} = 19.1 M_{\odot}$, that was formed from the merger of a primary of mass $M_1 = 18 M_{\odot}$ and secondary of mass $M_2 = 4 M_{\odot}$. The explosion was modelled with $E = 1 B$ and $M_{\text{Ni}} = 0.15 M_{\odot}$. Unlike SN 1987A and SN 1998A in which Ni is mixed all the way down to the center (0 km/s), nickel is required to be mixed only until 1700 km/s (panel c, Fig. 3.11) and does not need the characteristic step feature of the Ni distribution as in the other two supernovae. Mixing Ni down to the centre dilutes the Ni abundance in the ejecta and causes a slower rise to maximum luminosity and a lower

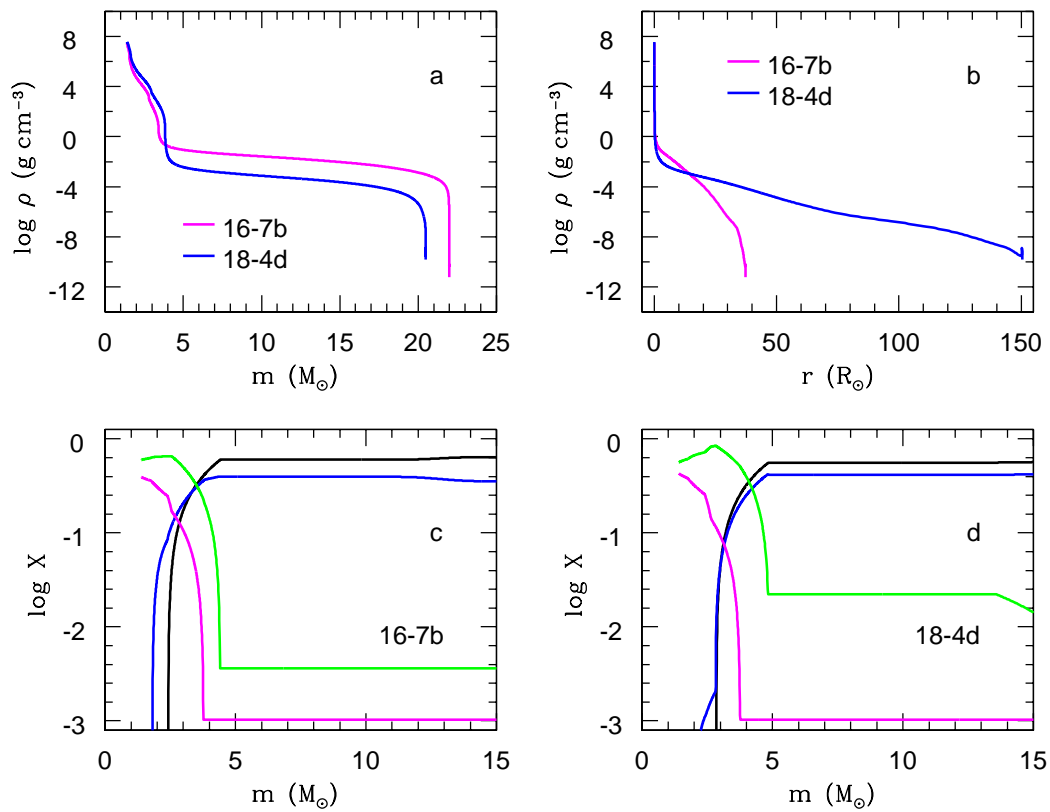


FIGURE 3.8: Pre-SN models for peculiar Type II-P supernovae. Panel a: density distributions as functions of interior mass for models 16-7b (magenta line) and 18-4d (blue line). Panel b: density distributions as functions of radius for the same models. Panel c: the chemical composition of the pre-SN model 16-7b after the boxcar averaging with the mass width $\Delta M = 2 M_{\odot}$. Mass fraction of hydrogen (black line), helium (blue line), CNO elements (green line), and Fe-peak elements (magenta line). Panel d: the same for the pre-SN model 18-4d.

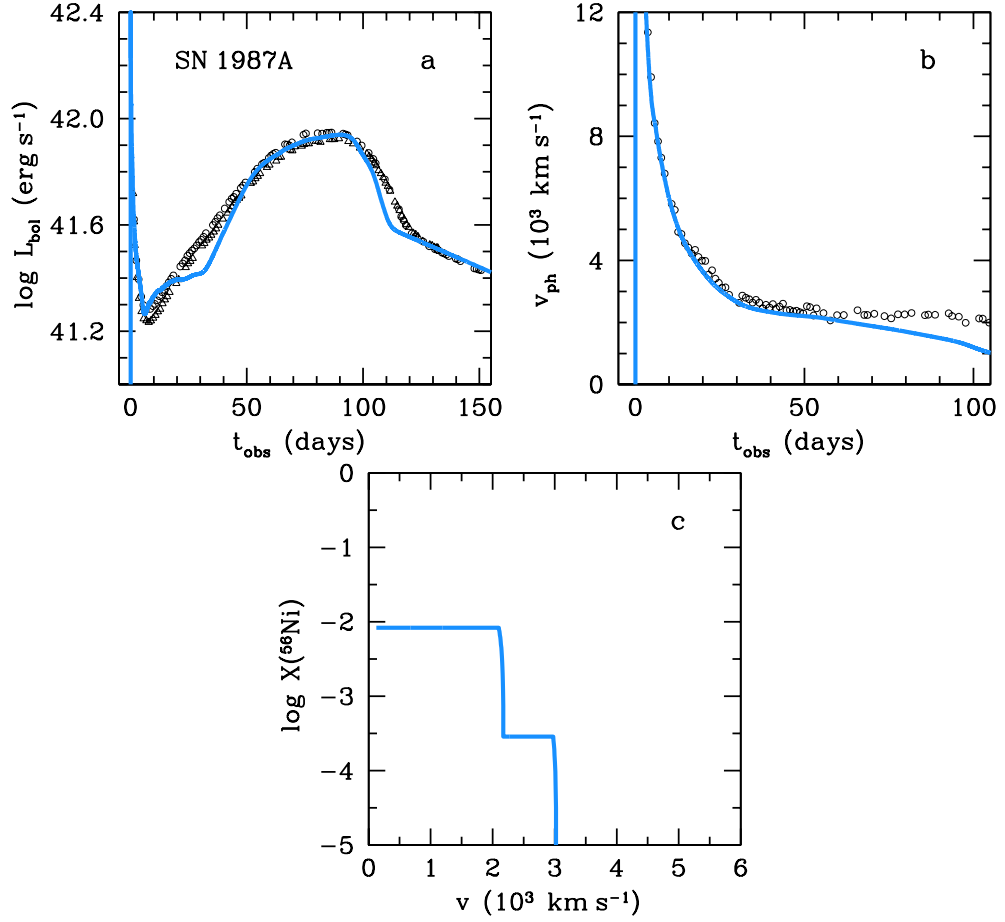


FIGURE 3.9: Hydrodynamic model for SN 1987A. Panel a: the calculated bolometric light curve is compared with the observations of SN 1987A obtained by Catchpole et al. (1987) and Catchpole et al. (1988b) (open circles) and Hamuy et al. (1988b) (open triangles). Panel b: the calculated photospheric velocity is overplotted on the velocity at the photosphere estimated by Phillips et al. (1988) with the absorption minimum of the Fe II ~ 5169 Å line (open circles). Panel c: the mass fraction of radioactive ^{56}Ni as a function of velocity at day 50.

peak luminosity than the data. This profile of Ni mixing, where the innermost Ni-ejecta travels at a velocity of 1700 km/s, was found required by the radiation hydrodynamic code to reproduce the bolometric light curve of SN 2006V.

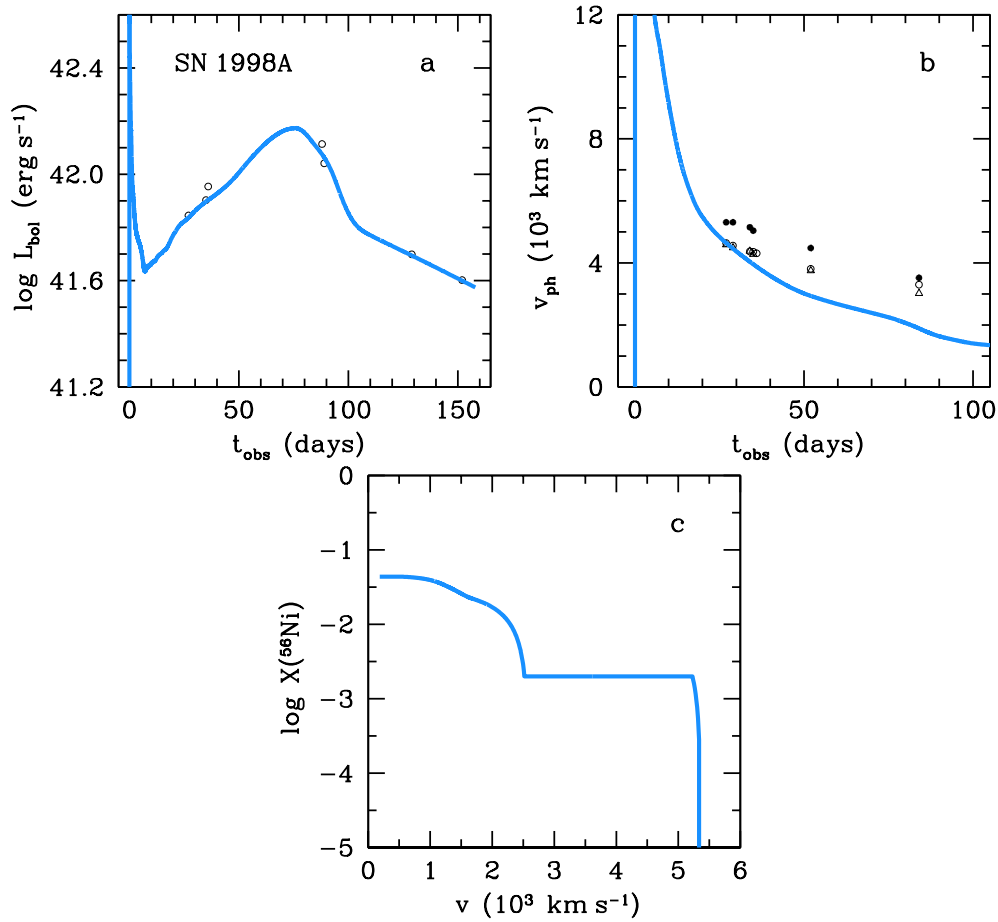


FIGURE 3.10: Hydrodynamic model for SN 1998A. Panel a: the calculated light curve is compared with the bolometric data of SN 1998A estimated by Lusk and Baron (2017) by means of direct integration (open circles). To fit the observations, the explosion date is suggested to be later by 10 days relative to that accepted by Pastorello et al. (2005). Panel b: the calculated photospheric velocity is overplotted on the velocity at the photosphere estimated by Pastorello et al. (2005) with the absorption minima of the $\text{Ba}_I I \sim 6142 \text{ \AA}$ (open circles), $\text{Fe}_{II} \sim 5169 \text{ \AA}$ (filled circles), $\text{Sc}_{II} \sim 5527 \text{ \AA}$ (open triangles) lines. Panel c: the mass fraction of radioactive ^{56}Ni as a function of velocity at day 50.

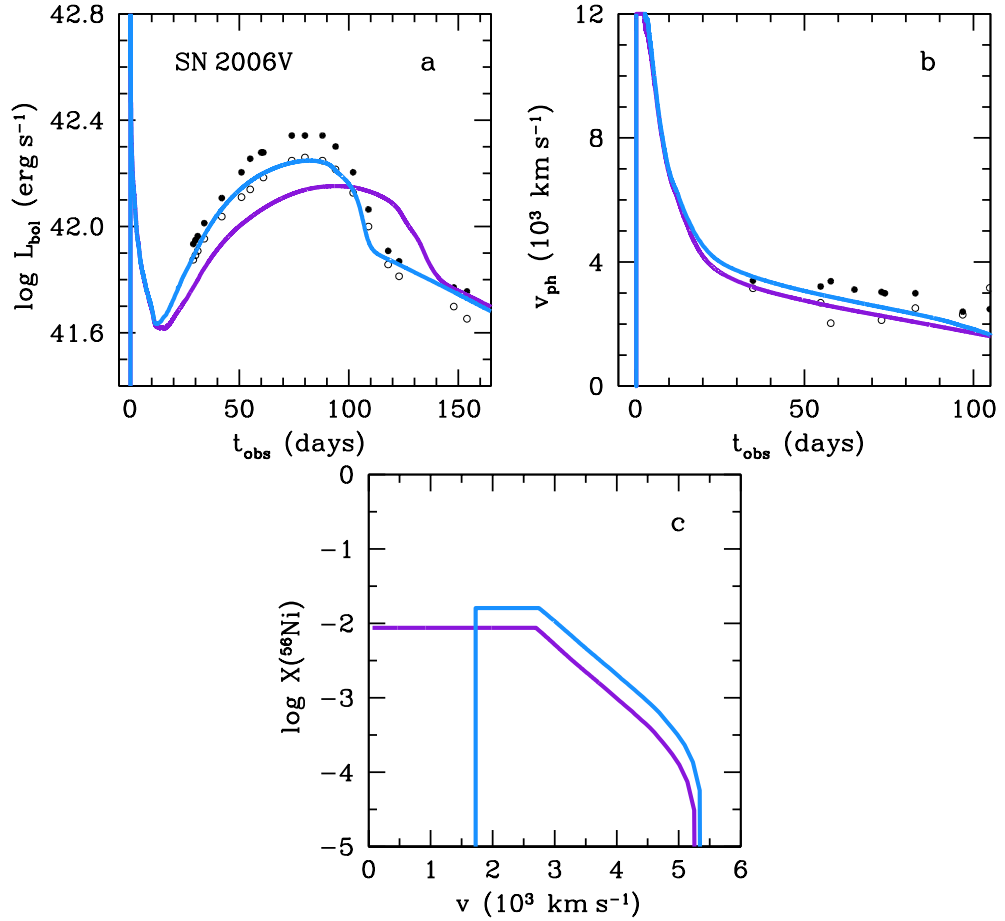


FIGURE 3.11: Hydrodynamic model for SN 2006V. Panel a: the light curves calculated for different ^{56}Ni distributions (see panel c) are compared with the bolometric data of SN 2006V estimated by Taddia et al. (2012) (open circles) and by Lusk and Baron (2017) which used direct integration (filled circles). To fit the observations, the explosion date is suggested to be earlier by 3 days relative to that accepted by Taddia et al. (2012). Panel b: the calculated photospheric velocity is overplotted on the velocity at the photosphere estimated by Taddia et al. (2012) with the absorption minima of the $\text{Ba}_{\text{II}} \sim 6142 \text{ \AA}$ (open circles), $\text{Fe}_{\text{II}} \sim 5169 \text{ \AA}$ (filled circles) lines. Panel c: the mass fraction of radioactive ^{56}Ni as a function of velocity at day 50 for the ^{56}Ni distributions within sphere (magenta line) and spherical layer (blue line).

TABLE 3.2: Predicted explosion and progenitor properties for five Type II-pec supernovae: Source: source of data, $^{56}M_{\text{ejecta}}$: ejecta mass, $R_{\text{pre-SN}}$: radius of progenitor, E : explosion energy, M_{Ni} : nickel mass from Lusk and Baron (2017). In parenthesis are the corresponding values of SN 1987A against which these parameters have been calibrated. The final column lists the method used for the calculations.

Supernova	Source	$M_{\text{ejecta}} (M_{\odot})$	$R_{\text{pre-SN}} (R_{\odot})$	$E (B)$	$^{56}M_{\text{Ni}} (M_{\odot})$	Method
SN 1998A	Pastorello et al. (2005)	22 (18)	86.3 (43.2)	5-6 (1.6)	0.11 (0.075)	Semi-analytic model
	Pastorello et al. (2012)				0.09 (0.075)	Updated results
SN 2000cb	Kleiser et al. (2011)	16.5 (14)	43.2 (43.2)	4 (1.1)	0.1	Scaling relations
	Utrobin and Chugai (2011)	17.5 (14)	43.2 (43.2)	2 (1)	0.1 ± 0.02	Hydrodynamic model
	Taddia et al. (2012)	22.3	35 ± 14	4.4	0.083	Hydrodynamic model
SN 2006V	Taddia et al. (2012)	20 (14)	< 50 (33)		< 0.127 (0.078)	Scaling relations
	Taddia et al. (2012)	17 (14)	75 (33)	2.4 (1.1)	0.127 (0.078)	Semi-analytic model
SN 2006au	Taddia et al. (2012)	20 (14)	< 50 (33)		< 0.127 (0.078)	Scaling relations
	Pastorello et al. (2012)	19.3 (14)	90 (33)	3.2 (1.1)	0.073 (0.078)	Semi-analytic model
SN 2009E	Pastorello et al. (2012)	26	86.2	1.3	0.039	Semi-analytic model
		19	100.7	0.6	0.043	Hydrodynamic model

TABLE 3.3: Hydrodynamic models of Type II-pec supernovae.

SN	Model	M_1 (M_\odot)	M_2 (M_\odot)	f_{sh} %	$M_{\text{pre-SN}}$ (M_\odot)	M_{ej} (M_\odot)	\odot (R_\odot)	E (B)	M_{Ni} (M_\odot)	$v_{\text{Ni}}^{\text{min}}$ (km s^{-1})	$v_{\text{Ni}}^{\text{max}}$ (km s^{-1})
1987A	16-7b	16	7	50	21.98	20.58	37.3	1.7	0.0734	0	3000
1998A	16-7b	16	7	50	21.98	20.58	37.3	4.5	0.12	0	5300
2006V	18-4d	18	4	90	20.48	19.08	150.4	1.0	0.15	1700	5400

3.4 Discussions and Conclusions

In this chapter, we have presented the results of the first explosion study of progenitors from binary mergers for Type II SNe. Our binary merger models for SN 1987A are significantly different from the evolutionary single star progenitor models of e.g., Woosley, Pinto, and Weaver (1988), Shigeyama and Nomoto (1990), Woosley et al. (1997), and Woosley and Heger (2007): they have smaller He core masses (3 – 4 M_\odot compared to 4 – 7.2 M_\odot), larger envelope masses (15 – 20 M_\odot compared to 9 – 14 M_\odot) and smaller radii (30 – 64 R_\odot compared to 47 – 64 R_\odot). The overall compact structure and large envelope mass of the merger progenitor model is close to the characteristics predicted ‘optimal’ non-evolutionary model of Utrobin (2005), which has a $R_{\text{pre-SN}} = 35 R_\odot$, $M_{\text{ej}} = 18 M_\odot$. The binary merger models also have a steeper density gradient at the He core- envelope interface and a smaller compactness parameter compared to single star models.

From the set of progenitor models we explored, the explosion of Model 16-7b from the merger of $M_1 = 16 M_\odot$, $M_2 = 7 M_\odot$ with $f_{\text{sh}} = 50\%$, which has $R_{\text{pre-SN}} = 37.4 R_\odot$, $M_{\text{Hec}} = 3.4 M_\odot$ and $M_{\text{ej}} = 20.6 M_\odot$, with an energy of 1.7 B, nickel mixing velocity of 3000 km/s and nickel mass of 0.073 M_\odot produces a good match with the light curve and photospheric velocity profile of SN 1987A. The fit of this model to the light curve data is a significant improvement over current explosion models from single stars, especially in matching the luminosity dip at day ~ 8 and the dome shape between day 40 – 120 (Fig. 9 in Utrobin et al., 2015). Model 16-7b also satisfies the observational constraints of the progenitor Sk –69°202, with $T_{\text{eff}}=15.8 \text{ kK}$, $\log L/L_\odot = 4.9$ and $N/C=6.9$, $N/O=1.4$ and $\text{He}/\text{H}=0.14$, making it the first evolutionary model in literature that is compatible with the observations of the progenitor and the explosion properties. These results are in agreement with the predictions of Utrobin (2004) and Utrobin (2005) from their studies of non-evolutionary models.

The ejecta mass we obtain for the pre-SN model 16-7b on including a part of the C-O core, contains $M(\text{O})=1.23 M_\odot$, $M(\text{He})=7.14 M_\odot$, and $M(\text{H})=11.50 M_\odot$. Studies of the nebular phase spectra of SN 1987A give mass estimates of these species. Oxygen, which is the most abundant of the metals and a good probe of the progenitor mass for single star models, contributes 1.2 – 2.0 M_\odot (Chugai, 1994; Kozma and Fransson, 1998; Chugai et al., 1997). The masses of helium and hydrogen are $\sim 5.8 M_\odot$ and $\sim 3.9 M_\odot$, respectively (Kozma and Fransson, 1998). The model values of oxygen and helium are comparable to the spectral values,

while the hydrogen mass of the ejecta is larger than its observational estimate by a factor of three. We have no ready explanation for the disparity found between the hydrogen masses. We can, however, make a general remark that hydrodynamic modeling of the observed light curves from the onset of the explosion to the radioactive tail involves all the ejected matter and gives better estimates of the total element masses than exploring the emission lines observed at the nebular phase which provides the element abundances only in the restricted parts, not in the whole ejecta.

The choice of initial parameters for the merger models, viz., f_{sh} , M_2 and M_1 , which determine the mass of the He core, envelope mass and the radius of the pre-SN model, also affect the light curve shape. For a given M_1 and M_2 , increasing f_{sh} causes the He core mass to decrease and the structure to become radially more extended. The explosion of progenitor models with decreasing He core mass affects the luminosity dip at day ~ 8 , causing the light curve to ascend more rapidly and shifting it upward overall. On the other hand increasing M_2 for a given M_1 and f_{sh} causes the envelope mass to increase and the radius to decrease of the pre-SN model. The explosion of these models causes the light curve to descend further at day ~ 8 and have a more pronounced delayed rise to maximum luminosity between days 15 – 40. Consequently the light curve moves further to the right as M_2 increases, and the width of the dome shape decreases.

We extended the study to investigate the explosions of our pre-SN models for two other Type II-pec SNe, SN 1998A and SN 2006V. The explosion of Model 16-7b, with $E = 4.5$ B, $M_{\text{Ni}} = 0.12 M_{\odot}$ and nickel mixing velocity up to $v_{\text{Ni}} = 5300$ km/s reproduced the light curve shape and reasonably matched the photospheric velocity evolution of SN 1998A. Using a semi-analytic model, Pastorello et al. (2005) predicted the progenitor for this supernova to have had a radius smaller than $86.3 R_{\odot}$ and ejecta mass of $22 M_{\odot}$ and to have exploded with an energy of 5 – 6 B. Thus our results are in reasonable agreement with the predictions of Pastorello et al. (2005).

According to our study SN 2006V had a much more extended progenitor, with $R_{\text{pre-SN}} = 150.4 R_{\odot}$ and $M_{\text{ej}} = 19.1 M_{\odot}$. This pre-SN model was created from the merger of a primary of $M_1 = 18 M_{\odot}$, $M_2 = 4 M_{\odot}$ with $f_{\text{sh}} = 90\%$, and had a He core mass of $3.8 M_{\odot}$, an envelope mass of $16.7 M_{\odot}$, $T_{\text{eff}} = 7.5$ kK and $\log L/L_{\odot} = 4.8$. Our progenitor for this supernova is not thus a blue supergiant, but a yellow supergiant. On the other hand, Taddia et al. (2012) who did the photometric analysis of this supernova, predicted a progenitor with $R_{\text{pre-SN}} < 50 - 75 R_{\odot}$ and $M_{\text{ej}} = 17 - 20 M_{\odot}$, based on a semi-analytic model. Thus our results for the progenitor differ significantly from those predicted by Taddia et al. (2012) and indicate that SN 2006V is an anomaly amongst Type II-pec SNe. The explosion parameters for the progenitor in our study are: $E = 1$ B, nickel mass of $0.15 M_{\odot}$ and nickel mixing in the regions with velocities of 1700 – 5400 km/s. The latter result is different from the nickel mixing velocity profiles for SN 1998A and SN 1987A in which the nickel was mixed down all the way to the centre

where the velocity was 0 km/s. Again, our explosion parameters are different from Taddia et al. (2012) who predicted an explosion energy of 2.4 B and a nickel mass of $0.127 M_{\odot}$ for SN 2006V. These results of Taddia et al. (2012) may have to do with the progenitor model assumed for SN 1987A, which had a much smaller ejecta than our progenitor model, with $M_{\text{ej}} = 14 M_{\odot}$ compared to $M_{\text{ej}} = 22 M_{\odot}$ and a smaller explosion energy of $E = 1.1$ B as against $E = 1.7$ B.

The light curve of SN 2000cb had a much broader dome than that of SN 1987A and other Type II-pec SNe and was a more energetic explosion than SN 1987A, with $E = 4$ B (Kleiser et al., 2011). The ‘optimal’ non-evolutionary progenitor model for SN 2000cb calculated by Utrobin and Chugai (2011) has $R_{\text{pre-SN}} = 35 \pm 14 R_{\odot}$ and $M_{\text{ej}} = 22 \pm 1 M_{\odot}$. Although our merger progenitor models can match these constraints on radius and ejecta mass, their structures are not suitable to reproduce the unusual light curve shape of this supernova. We also could not study SN 2006au due to data missing from the first 50 days of the supernova and SN 2009E whose nickel decay tail was not recorded.

The BSG structure of our merger models are in line with the requirements from the 3D simulations of Wongwathanarat, Müller, and Janka (2015) and Utrobin et al. (2015). These models have a smaller He core mass, a sharper density gradient at the He/H interface and smaller radii than single star models. All these characteristics can assist in the deeper penetration of Ni fingers to regions in the envelope travelling at 3000 km/s, while current explosion simulations of single star models can only mix Ni out to a velocity of 2200 km/s. Our binary merger models thus show promise in being improvements over existing single star models and can provide further insight into the physics of core-collapse supernovae and their progenitors.

3.5 Acknowledgements

The explosion models in this chapter were done by Victor Utrobin. We thank Alexandra Kozyrova and Luc Dessart for useful initial discussions on this project. We also thank Andrea Pastorello (Pastorello et al., 2005) and Francesco Taddia (Taddia et al., 2012), for providing the expansion velocities of weak absorption lines for SN 1998A and SN 2006V respectively.

Chapter 4

Low-metallicity CO+He WD post-merger models for RCB stars and their connection to low-density graphite grains

4.1 Introduction

In this work, we present 1D stellar models which have evolved from the mergers of carbon-oxygen (CO) and helium (He) white dwarfs (WDs). These models are used to explain the hydrogen-deficient carbon-rich R Coronae Borealis (RCB) stars by reproducing their position in the HR diagram and their spectral signatures. The models are created using the methodology of an earlier work, Menon et al. (2013). Since RCB stars are known to produce copious amounts of carbon dust, we investigate whether RCB stars can be a source of a subset of pre-solar graphite grains. We do this by first comparing the observed isotopic signatures of RCB stars with those of the grains and thereafter check whether our evolutionary models of RCB stars reproduce the grain signatures as well.

4.1.1 R Coronae Borealis stars

R Coronae Borealis stars (RCBs) are carbon-rich supergiants that are almost entirely deficient in hydrogen (Searle, 1961; Pollard, Cottrell, and Lawson, 1994; Asplund et al., 1997; Asplund et al., 2000). RCBs have been found in the Magellanic clouds and in the old bulge population of the Galaxy (Cottrell and Lawson, 1998; Alcock et al., 2001; Tisserand et al., 2008; Clayton, 2012; Tisserand et al., 2013) and recently also in the Andromeda Galaxy (Tang et al., 2013). The Galactic population have metallicities of $[\text{Fe}/\text{H}] < -0.6$ and the majority of RCBs have effective temperatures of $3000\text{K} \leq T_{\text{eff}} \leq 8000\text{K}$ and luminosities of $3.5 \leq \log L/L_{\odot} \leq 4.0$ (Clayton, 1996; Asplund et al., 2000; Pandey, Lambert, and Kameswara Rao, 2008) but four

RCBs have also been discovered with $T_{\text{eff}} = 15000 - 25000$ K (Alcock et al., 2001; Clayton, 1996; Clayton, 2012).

RCBs were first noted for their distinct light curves which show unpredictable declines in brightness of up to 8 orders of magnitude (Loreta, 1935; O’Keefe, 1939; Feast et al., 1997; Feast, 1997). These declines were attributed to puffs of amorphous carbon dust released from the atmosphere of the star (Feast, 1986; Clayton, 1996; García-Hernández, Rao, and Lambert, 2011), whose ejections coincided with the pulsation period of the star (Woitke, Goeres, and Sedlmayr, 1996; Crause, Lawson, and Henden, 2007; Lawson et al., 1990). Typically each puff of carbon dust has a mass of $10^{-6} - 10^{-7} M_{\odot}$ (Feast, 1986; Clayton et al., 2011).

The atmospheres of RCBs have many chemically peculiar signatures, the most remarkable of them being some of the lowest $^{16}\text{O}/^{18}\text{O}$ number ratios detected in any star, between 1 and 25 as against the solar value of ~ 500 (Clayton et al., 2007; García-Hernández et al., 2010). They also have high $^{12}\text{C}/^{13}\text{C}$ number ratios $> 40 - 100$ (Warner, 1967; Cottrell and Lambert, 1982; Hema, Pandey, and Lambert, 2012). with the exception of a few stars with $^{12}\text{C}/^{13}\text{C} = 3 - 4$ (Rao and Lambert, 2008; Hema, Pandey, and Lambert, 2012), along with enhancements in F of up to 2.7 dex (Pandey, Lambert, and Kameswara Rao, 2008) and in s-process elements (Asplund et al., 2000) compared to solar.

Historically, there have been two evolutionary channels proposed to explain the origin of RCB stars. Post-AGB stars that underwent a late thermal pulse while on or transiting toward the WD cooling track, referred to as the final He-shell flash (FF) model (Renzini, 1990; Iben, Tutukov, and Yungelson, 1996; Saio and Jeffery, 2002) and, the mergers of degenerate CO and He WDs, referred to as the double degenerate (DD) model (Webbink, 1984; Iben, Tutukov, and Yungelson, 1996). Based on the observational constraints of RCB stars, such as their surface isotopic ratios, their recorded numbers and their masses, the DD scenario appears more favourable than the FF scenario to explain the origin of the majority of RCB stars (Clayton et al., 2007; Clayton, 2012).

The evolutionary scenario that forms a DD WD system begins from a pair of main-sequence intermediate mass stars. Two common envelope episodes occur during their evolution— one when the more massive star (primary) evolves into an Asymptotic Giant Branch (AGB) star with a degenerate CO core and another when the secondary evolves into a Red Giant Branch (RGB) star with a degenerate He core (Webbink, 1984; Iben, Tutukov, and Yungelson, 1996; Solheim, 2010; Brown et al., 2016). The entire evolutionary sequence is described in Section 1.5.2. In the second common envelope phase, the entire envelope is ejected and results in a close CO+He WD binary with an orbital period of a few hours. A number of such close DD systems have been found by various observational surveys (e.g., Nelemans et al., 2005; Schreiber et al., 2009)

It is expected that some of these close DD systems will have merged within the lifetime of the Universe. Mergers have been modelled in 3D hydrodynamic simulations such as

those by Lorén-Aguilar, Isern, and García-Berro (2009), Dan et al. (2011), Staff et al. (2012), Raskin et al. (2012), Dan et al. (2014), and Moll et al. (2014). In the simulations of Staff et al. (2012), whose results we have used in this work, the He WD is tidally disrupted by the more massive CO WD and is entirely unbound. A stream of the He WD mass rapidly falls on the CO WD, creating a hot corona like structure, referred to as the Shell of Fire (SOF) around the CO WD, while the rest of the He WD material settles as a disk on the SOF. The complete disruption of the He WD, the ‘merger’ phase, lasts for a period of 100-1000 s in the simulations. The results of merger simulations by other works also report similar behaviours.

The next phase is the long-term evolution of the post-merger object. Shen et al. (2012) and Schwab et al. (2012) found that magnetic stresses redistribute angular momentum through the envelope of the post-merger object and over a period of $10^4 - 10^8$ s, the differentially-rotating post-merger remnant evolves to a spherically symmetric structure with a thermally supported envelope in solid-body rotation. Both works predict that after the viscous phase, the structure can evolve over a thermal timescale into a giant star with an extended envelope driven by convection. Zhang et al. (2014) built zero-metallicity 1D models of the ‘corona+disc’ structure indicated in the 3D merger simulations. These post-merger models passed through the RCB region in the HR diagram and were also enriched in C, N, O and F in the surface due to convection driven by He-shell flashes, during the accretion of the disc on the corona.

Menon et al. (2013) (hereby Paper I) also studied the long-term evolution of the WD merger remnant in the aim of obtaining the surface composition of RCBs and their position in the HR diagram. They constructed a 1D hybrid CO+He WD structure by mapping the chemical composition of solar metallicity CO and He WDs onto an initially homogeneous $0.90M_{\odot}$ pre-main sequence model. The temperature-density profile and isotopic abundances of the hot corona from the 3D simulations of Staff et al. (2012), which the authors had named the ‘Shell of Fire’, were mapped onto the hybrid structure as well. These post-merger models were then evolved until they passed through the RCB domain in the HR diagram.

During the post-merger evolution, it was observed that there was very little mixing occurring in the model except for a thin convective layer ($< 0.01M_{\odot}$) in the surface. The nuclear products that enrich the surface of RCBs were being formed in the interior of the model and there was no mechanism to dredge them up to the surface. Given that the envelope of the post-merger remnant is expected to evolve toward solid-body rotation (Shen et al., 2012; Schwab et al., 2012), mixing processes other than convection can arise due to rotational instabilities. The main isotopic signature that Menon et al. (2013) aimed to reproduce was the low $^{16}\text{O}/^{18}\text{O}$ ratio observed in RCBs. Given that the exact nature of rotation-driven mixing processes and their physics are highly uncertain, Menon et al. (2013) constructed an adhoc mixing recipe in the form of an Eulerian diffusion coefficient, that would help dredge

up sufficient amounts of ^{12}C and ^{18}O to the surface. With this induced mixing, the post-merger models were not only successful at reproducing $^{16}\text{O}/^{18}\text{O}$ ratios of 9 – 15 and > 100 , they could also obtain enhancements in F of 1.4 – 2.35 dex compared to solar, enhancements in s-process elements and reasonably reproduce the abundances of other species observed in RCBs. Effectively these models predicted the abundances for an RCB star if one were to form at solar-metallicity. When the abundances of the models were plotted along with the recorded abundances of the metal-poor RCB stars we observe today, they fit the extrapolated trend in the variation of the abundances with metallicity, making these models promising for an RCB star. The mixing routine and its parameter values were set at the initial point of evolution of the model and not altered at any time during the evolution or on an element-by-element basis. These results indicate a fair robustness in the mixing prescription and may provide an insight into the kind of mixing that could occur in the long term evolution of post-DD merger objects.

4.1.2 Pre-solar graphite grains

Pre-solar carbon grains are found in three forms: diamonds, silicon carbide grains and the rarest of the three, graphites (Zinner, 2014). Graphites are classified morphologically into two categories based on their density– high density (HD) and low density (LD) graphite grains. In this work we are interested in the origin of the LD graphite grains. These grains are characterised by their low $^{29}\text{Si}/^{28}\text{Si}$ and $^{30}\text{Si}/^{28}\text{Si}$ ratios, low $^{14}\text{N}/^{15}\text{N}$ ratios, high $^{26}\text{Al}/^{27}\text{Al}$ ratios and excesses in Ca and Ti isotopic ratios compared to their respective solar values (Amari, Zinner, and Lewis, 1995; Amari and Lodders, 2007). It is due to these signatures, particularly the low $^{29}\text{Si}/^{28}\text{Si}$ and $^{30}\text{Si}/^{28}\text{Si}$ ratios, which are interpreted as an excess in ^{28}Si , and the presence of ^{44}Ca , which formed from the decay of ^{44}Ti in some grains (Zinner, 2014), that massive star progenitors of Type II-plateau supernovae (Type II-P SNe) have been typically used to explain the origin of LD graphite grains (Travaglio et al., 1999; Pignatari et al., 2013; Amari, Zinner, and Gallino, 2014; Pignatari et al., 2015). Certain LD graphite grains were also found to have low $^{16}\text{O}/^{18}\text{O}$ ratios ≤ 25 and $^{12}\text{C}/^{13}\text{C} > 40$ (Amari et al., 1993; Amari et al., 2017), which matched the values observed in RCB stars.

Dust from supernovae

There is ample evidence for the presence of carbon dust grains in the environment surrounding supernova remnants; flux emitted by cold dust in the ejecta have been detected by AKARI, Herschel, Spitzer and ALMA. By fitting the sub-millimetre (submm) spectral energy distribution (SED) from the cold dust in the ejecta, a dust mass of 0.4 – 0.7 M_{\odot} has been estimated for the remnant of SN 1987A (Matsuura et al., 2011; Matsuura et al., 2015), 0.04 – 0.12 M_{\odot} for the remnant of Cas A (Barlow et al., 2010; Sibthorpe et al., 2010; Arendt et al., 2014) and 0.12 – 0.24 M_{\odot} for the remnant of Crab Nebula (Gomez et al., 2012; Temim and

Dwek, 2013). In the case of SN 1987A, Matsuura et al. (2015) deduced a composition for the dust to be $\approx 0.3 M_{\odot}$ of amorphous carbon and $\approx 0.5 M_{\odot}$ of silicates by fitting the SED of the dust. The problem with these estimates is that they exceed the nucleosynthesis yields for both these components from single-star evolutionary models, such as the $19 M_{\odot}$ model of Rauscher et al. (2002) and the $20 M_{\odot}$ model of Woosley (1988) (Matsuura et al., 2015; Dwek and Arendt, 2015). An alternative method to analyse the IR emission from the dust by Dwek and Arendt (2015), predicted a smaller dust mass of $\approx 0.5 M_{\odot}$ which has $0.4 M_{\odot}$ of silicates and $0.047 M_{\odot}$ of amorphous carbon. These estimates are within the yields from single-star progenitor models.

The predictions from independent theoretical models that consider the dust nucleation in the gas of the ejecta matched the above results obtained by fitting the observed SED. The models of Kozasa, Hasegawa, and Nomoto (1989), Todini and Ferrara (2001), and Bianchi and Schneider (2007) predicted a dust mass in the ejecta of core-collapse supernovae between $0.08 - 1 M_{\odot}$, depending on the model for dust condensation used, the mass and metallicity of the progenitor and whether the layers of the ejecta are mixed. The more recently developed model of Sarangi and Cherchneff (2013) that couples the dust nucleation phase to their condensation phase, however, expect that the dust mass produced is between $0.03 - 0.09 M_{\odot}$ and are smaller than the results derived from submm data for SN 1987A ($0.4 - 0.7 M_{\odot}$) and Crab nebula ($0.24 M_{\odot}$). Sarangi and Cherchneff (2013) state that this is because the models which predicted higher dust masses assumed a simple dust composition that consisted only of carbon and silicates, 100% condensation for both species or simpler equations to describe the depletion of elements from the ejecta gas (Sarangi and Cherchneff, 2013; Cherchneff, 2013). The nature of the carbon dust grains are mostly reported to be that of amorphous carbon; it is not clear whether graphite grains also form in the supernovae ejecta or whether there exist conditions to convert amorphous carbon to graphite in the ejecta. It is interesting to note that amorphous carbon has not been detected in meteorite grains.

A separate body of work, that does not include the physics of dust formation, investigated whether the ejecta material of Type-II P SNe can reproduce the isotopic signatures of LD graphite grains. One set of models uses partial or complete mixing of the stratified ejecta of the supernova progenitor just before the onset of core collapse, in order to form an environment with $C/O < 1$ in which carbon grains can form. The envelope of the progenitor (the layers above the iron core), consist of shells of S, Si, O, Ne, Mg, C, He and H. The models of Travaglio et al. (1999), Yoshida, Umeda, and Nomoto (2005), and Yoshida (2007) preferentially mixed the C-rich layers of the ejecta while avoiding any contamination with the O-rich layers in between. In a different model, Pignatari et al. (2013) and Pignatari et al. (2015) demonstrated that a C-rich layer in the ejecta can be formed without any preferential mixing, by ensuring the availability of He or H nuclei in the He/C and C/O regions, prior to the arrival of the supernova shockwave. On comparing the abundances due to explosive

He-burning in these He/C and C/O shells, the authors could obtain many of the isotopic ratios measured in the grains.

Although there is evidence for carbon dust in the environment surrounding supernovae remnants and models that examine the progenitor of supernovae can reproduce the composition of the grains in their ejecta, the contribution of core-collapse supernovae as a substantial source of dust grains in the Universe is still an open question.

Dust grains are at a risk of being destroyed in the ejecta itself, before being swept up in the interstellar medium. This is because after the explosion, the supernova ejecta drives a blast wave into the surrounding medium made of material ejected earlier by the progenitor star and, the interstellar matter. The blast wave gets decelerated by this surrounding matter and a reverse shock forms in the material behind the shock wave swept-up earlier by the blast wave (McKee, 1974). As the reverse shock propagates inwards, it heats up the circumstellar medium to begin emitting in the X-ray. This phase of X-ray emission has been detected around the remnant of SN 1987A (Larsson et al., 2011; Larsson et al., 2013) and in that of Cas A (McKee, 1974; Micelotta, Dwek, and Slavin, 2016). Dust grains that were condensed in the ejecta are at a risk of being heated and destroyed by the X-ray heating caused by the propagation of the reverse shock. In the particular case of the remnant of Cas A, Micelotta, Dwek, and Slavin (2016) expect that only 12 – 16% of the dust grains can survive the passage of the shock wave. Thus, considering that supernovae are moderate dust producers in the Universe Sarangi and Cherchneff (2013) and that a substantial fraction of the dust condensed in the ejecta may get destroyed, there is considerable uncertainty about the fraction of pre-solar grains that would have originated from supernovae.

Dust from RCB stars

Given that the circumstellar environment of an RCB star is rich in carbon dust, RCB stars may also be a possible source for presolar graphite grains alongside supernovae. The current observed number of RCB stars including those found in the Galaxy and the Magellanic clouds, is close to a 100 (Clayton, 1996; Alcock et al., 2001; Tisserand et al., 2008; Tisserand et al., 2013). Assuming WD mergers are the channel for their formation and given a merger rate of $1.8 \times 10^{-2} \text{ yr}^{-1}$ for CO+He WD systems (Han, 1998) Clayton (2012) estimate that 5400 – 5700 RCB stars must currently exist in our Galaxy. They also arrive at a similar number using an independent method that extrapolates the known RCB population in the LMC to that of our Galaxy. Karakas, Ruiter, and Hampel (2015) estimate a more conservative number of 150 – 540 RCB stars in the Galaxy, based on a lower CO+He WD merger rate of $1.8 \times 10^{-3} \text{ yr}^{-1}$. RCB stars are expected to eject about $10^{-6} \text{ M}_{\odot} \text{ yr}^{-1}$ (Feast, 1986) to $10^{-7} \text{ M}_{\odot} \text{ yr}^{-1}$ (Clayton et al., 2011) and have a lifetime of roughly 10^5 yr (Clayton et al., 2011; Clayton, 2012). Thus, an RCB star will eject 0.01 – 0.1 M_{\odot} of amorphous carbon dust over its lifetime. Given their estimated number in the Galaxy, Karakas, Ruiter, and Hampel (2015)

concluded that the dust production rates of RCB stars may exceed those of born-again AGB stars and novae.

Given thus that they are viable producers of dust, Karakas, Ruiter, and Hampel (2015) speculated if certain pre-solar graphite grains could have originated from RCB stars. The key signature isotopic signatures that led to this speculation were the presence of $^{16}\text{O}/^{18}\text{O} < 25$ and $^{12}\text{C}/^{13}\text{C} > 100$ reported in certain LD graphite grains (Amari et al., 1993), which are similar to the values observed in the atmosphere of RCB stars. Karakas, Ruiter, and Hampel (2015) also speculated whether the predictions of the models of Paper I could compare with the isotopic ratios measured in these grains. Although typically the sources of pre-solar grains are considered to be of solar metallicity, the RCB stars we find today are metal-poor. This means if there existed a generation of RCB stars that were born from WD mergers 4.5 Gyrs ago, they would also have been metal poor and their ejected dust would have mixed with the interstellar medium from which the solar system formed.

The RCB models of Paper I are of solar-metallicity. For the purpose of this study, we build new post-WD merger models for RCB stars with a realistic metallicity of $Z=0.0028$ ($[\text{Fe}/\text{H}] = -1.4$), using the same methodology as in Paper I. The models are evolved through the RCB phase in the HRD, during which we examine if their surfaces can reproduce the coveted low $^{16}\text{O}/^{18}\text{O}$ ratios and high $^{12}\text{C}/^{13}\text{C}$ ratios of RCB stars. We also make detailed comparisons with all the elemental abundances measured in RCB stars. We then explore how well the isotopic ratios from these models compare with those LD graphite grains that have $^{16}\text{O}/^{18}\text{O}$ ratios in the observed range of RCB stars. These grains do not have any ^{44}Ca detected in them but do have low ratios of $^{29}\text{Si}/^{28}\text{Si}$ and $^{30}\text{Si}/^{28}\text{Si}$ and high ratios of $^{26}\text{Al}/^{27}\text{Al}$, compared to solar. In Section 4.2, we describe the methodology of our work; in Section 4.3, we present the result of our comparison study and in Section 4.4, we present our conclusions and discuss their implications.

4.2 Methodology

We describe the setup of our initial post-merger models and the artificial mixing recipe. We then vary the initial parameters and build four cases to study in this paper.

4.2.1 Initial setup

The initial model for the evolutionary calculations consists of four zones which were identified in the hydrodynamic simulations of CO+He WD mergers by Staff et al. (2012): the CO core, the buffer, the Shell of Fire (SOF) and the envelope (Fig. 4.1). Material was dredged up during the merger in the simulations from the region between the CO core and the surface of the CO WD and mixed with the overlying He WD material; most of the dredged-up mass was found in the hot SOF region while the rest was in the envelope.

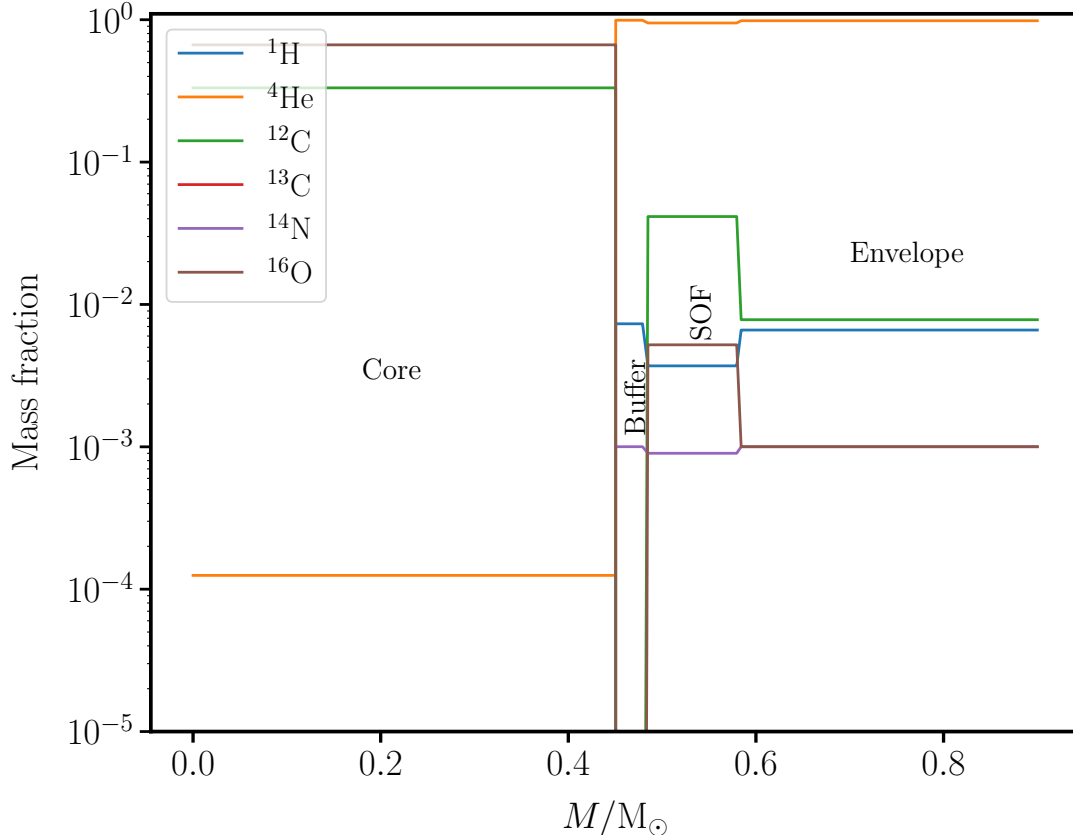


FIGURE 4.1: The four-zone profile of the initial post-merger model of Case 1 of this paper.

Our four cases are built using the initial mass distribution of Case 1 of Paper 1, which had the lowest surface $^{16}\text{O}/^{18}\text{O}$ ratio for its RCB model in that work. The initial WD masses for this case are: $M_{\text{CO WD}} = 0.53 M_{\odot}$, $M_{\text{He WD}} = 0.37 M_{\odot}$ and thus have a total mass of $M_{\text{total}} = 0.90 M_{\odot}$. We refer the reader to Section 2.1.1 of Paper I for a detailed understanding of the construction of the four zones of the initial model. We provide a brief overview of the four zones here:

- **Core** ($0.45 M_{\odot}$): CO core of the CO WD. This part does not participate in the evolution of the post-merger star.
- **Buffer** ($0.03 M_{\odot}$): A small buffer zone with the abundances of the He WD.
- **SOF** ($0.10 M_{\odot}$): A hot shell with temperatures of $T_{\text{SOF}} = 120 - 250 \text{ MK}$ and densities of $\rho_{\text{SOF}} \approx 5 \times 10^4 \text{ g/cc}$, suitable for H-burning and partial He-burning. 50% of the composition is of the dredged up mass from the CO WD and 50% is the He WD composition.
- **Envelope** ($0.32 M_{\odot}$): Relatively cold material where 90.6% of the composition is of the He WD material and 9.4% is that of the dredged up mass from the CO WD.

After the allotment of masses for the individual zones, the next step is to determine the initial composition of each zone in the model. For this we first consider the abundances

TABLE 4.1: Isotopic mass fractions from the He WD models (limited to values $> 10^{-4}$) with different envelope masses: He WD(1): $M_{\text{env}} = 6.4 \times 10^{-3} M_{\odot}$, He WD(2): $M_{\text{env}} = 10^{-2} M_{\odot}$ and from the dredged-up region of the CO WD: CO WD (DUP).

Species	He WD(1)	He WD(2)	CO WD (DUP)
^1H	7.3×10^{-3}	1.4×10^{-2}	–
^4He	0.99	0.98	0.91
^{12}C	–	–	8.3×10^{-2}
^{13}C	–	–	–
^{14}N	1.0×10^{-3}	1.0×10^{-3}	8.0×10^{-4}
^{16}O	–	–	1.0×10^{-2}
^{18}O	–	–	–

for the CO and He WDs. The abundances of the He WD are extracted from an RGB model of a $1 M_{\odot}$ main sequence star, which has a $M_{\text{HeWD}} = 0.30 M_{\odot}$. Since in the hydrodynamic simulations, the entire He WD was found to be disrupted during the merger we assume a uniform composition for the He WD mass. This composition is then normalized to the He WD mass of $M_{\text{HeWD}} = 0.37 M_{\odot}$ which was used for the merger simulation. The abundances of the CO WD are taken from an early-AGB model of a $3 M_{\odot}$ main sequence star, which has a CO WD mass of $M_{\text{CO WD}} = 0.70 M_{\odot}$. We dredge up $\sim 35\%$ of the CO WD mass, which includes the envelope and the He shell just above the CO core, which was the same region dredged up to construct models in Paper I as well. The abundances in the dredged up region are homogenised over the dredged up mass of $0.245 M_{\odot}$ and mixed in required proportions in the SOF and the envelope above it to build the initial composition profile of the model. This initial composition (Fig. 4.1) is then relaxed on a $M = 0.90 M_{\odot}$ pre-main sequence star. Table 4.1 lists the CO and He WD abundances used in this work. The abundances of the SOF are treated specially, which we shall discuss in the next section.

The RGB and AGB star models, from which the He WD and CO WD abundances were extracted respectively, were computed with the stellar evolution and nucleosynthesis post-processing codes used in Karakas and Lattanzio (2014) and Karakas and Lugaro (2016). These models were built with an initial composition by setting a global metallicity of $Z=0.0028$, where $Z=Z_{\alpha} + Z_{\text{other}}$, where $Z_{\text{other}}=Z_{\text{CNO}}+Z_{\text{Fe}}$ etc. The inferred $[\text{Fe}/\text{H}]$ value for this metallicity is -1.4 . The α -elements are individually enhanced according to the chemical evolution models of Kobayashi, Karakas, and Umeda (2011) while the non- α elements are scaled according to the solar abundances and isotopic ratios in Asplund et al. (2009).

Finally, we set up the artificial mixing routine. Menon et al. (2013) adopted an empirical mixing law in the form of an Eulerian diffusion coefficient, that drops exponentially from the surface until a cut-off point in the interior of the model. The total diffusion coefficient of the mixing model is the sum of the diffusion coefficient of convective mixing (which is only present within $< 0.01 M_{\odot}$ of the surface) and that of the additional mixing we implement. Mixing is restricted to occur only in the region between the surface and the outer

TABLE 4.2: The four cases. Abundances in the last two columns are initial amounts in the SOF and envelope, and are listed in Table 4.3.

Case	H-envelope mass	SOF conditions	SOF abundances	Envelope abundances
1	6.4×10^{-3}	cold	SOF (1)	Envelope (1)
2	1.0×10^{-2}	cold	SOF (2)	Envelope (2)
3	6.4×10^{-3}	hot	SOF (3)	Envelope (1)
4	1.0×10^{-2}	hot	SOF (4)	Envelope (2)

TABLE 4.3: Isotopic mass fractions of the SOF and envelope regions for the initial post-merger models. The composition of the material dredged up from the CO WD is the same for all SOFs and envelopes as in Table 4.1. SOF(1): Cold, from He WD(1), SOF(2): Hot, $T_{\text{SOF}}=123$ MK, from He WD(1), SOF(3): Cold, from He WD(2), SOF(4): Hot, $T_{\text{SOF}}=123$ MK. Envelope(1): From He WD(1) and Envelope(2): From He WD(2).

Species	SOF(1)	SOF(2)	SOF(3)	SOF(4)	Envelope(1)	Envelope(2)
^1H	3.7×10^{-3}	7.1×10^{-3}	–	–	6.6×10^{-3}	1.3×10^{-2}
^4He	0.95	0.95	0.93	0.86	0.98	0.98
^{12}C	4.1×10^{-2}	4.1×10^{-2}	9.4×10^{-3}	7.7×10^{-2}	7.8×10^{-3}	7.8×10^{-3}
^{13}C	–	–	–	–	–	–
^{14}N	9.3×10^{-4}	9.2×10^{-4}	1.6×10^{-3}	1.7×10^{-2}	1.0×10^{-3}	1.0×10^{-3}
^{15}N	–	1.6×10^{-3}	4.0×10^{-4}	3.6×10^{-4}	–	–
^{16}O	5.2×10^{-3}	5.2×10^{-3}	3.0×10^{-2}	2.0×10^{-2}	1.0×10^{-3}	1.0×10^{-3}
^{18}O	–	–	2.1×10^{-2}	1.6×10^{-2}	–	–
Maximum neutron density (neutrons/cm ³)	–	–	6.3×10^{11}	7.9×10^{10}	–	–

boundary of the CO core (at $0.45 M_{\odot}$ in our models) i.e., the CO core does not participate in determining the abundances of the surface. Mixing further into the CO core would cause a dredge-up of ^{16}O that would excessively exceed the abundance of ^{18}O in the surface. The additional diffusion coefficient is built such that it drops exponentially from the surface to the location of the entropy barrier arising from the energy peak of nuclear burning, which is approximated as the mass co-ordinate where the ^{14}N abundance drops to a specific fraction. For more details about the mixing routine, we encourage the reader to refer to Section 2.3 of Paper I. In this work, we use the same parameter values for the additional mixing diffusion coefficient as in Paper I.

4.2.2 The four cases of this paper

During the initial examination of the models, two important factors were found to affect the surface abundances of the models– the **H-rich envelope mass** of the He WD and, the **SOF**. The four cases we study are built so as to isolate the impact of these factors on the post-merger model.

The H-rich envelope masses for the WDs are a function of their H-free core mass (Schoenberner, 1983; Driebe et al., 1998) and are found to decrease as the H-free core mass increases. The envelope mass is determined by an analytic equation derived in Staff et al. (2012): $\log M_{\text{env}}/M_{\odot} = 4.982 M_{\text{H}}/M_{\odot} - 0.7171$, where M_{H} is the mass of the H-free core. The CO and He WD masses obtained from the AGB and RGB models are $0.7 M_{\odot}$ and $0.3 M_{\odot}$

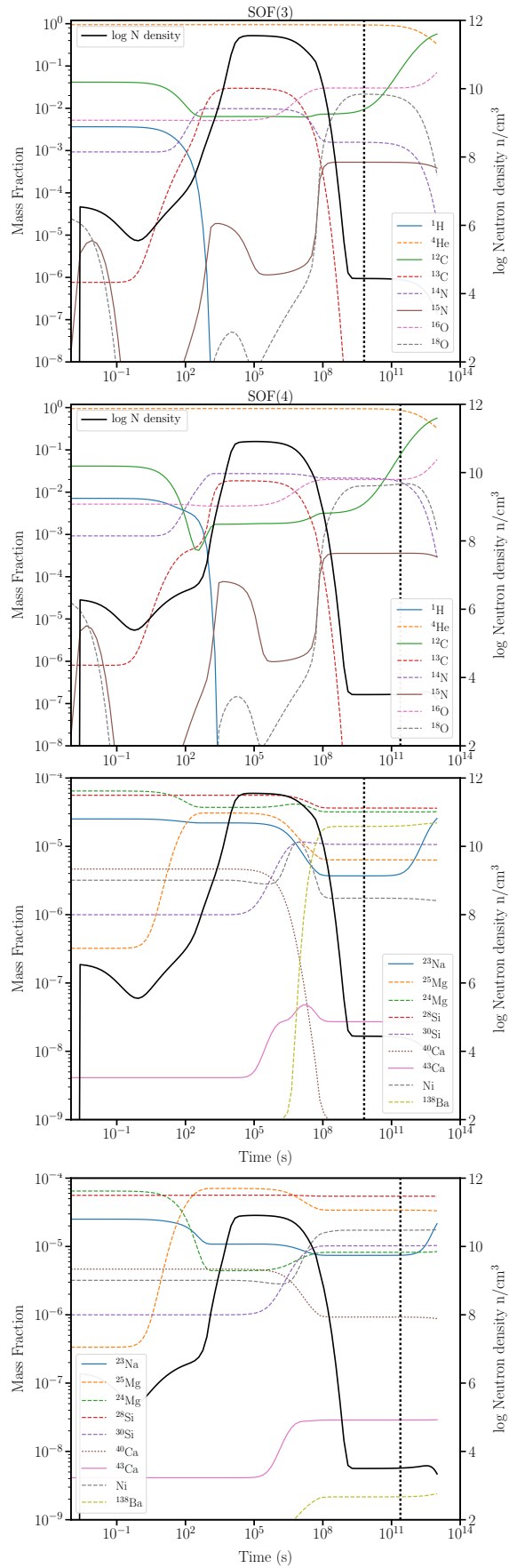


FIGURE 4.2: The abundances and neutron densities of the hot SOFs of Cases 3 (left panel) and 4 (right panel), calculated at $T = 123$ MK and $\rho \approx 3 \times 10^4$ g/cm³. The dashed vertical line is when the $^{16}\text{O}/^{18}\text{O}$ drops to ≈ 2 , and the hot SOF abundances are taken at this point.

respectively. Hence with this equation, the envelope masses for the CO and He WD are $4.4 \times 10^{-4} M_{\odot}$ and $8.6 \times 10^{-4} M_{\odot}$ respectively. On running a simulation with these envelope masses, we do not find the required low $^{16}\text{O}/^{18}\text{O}$ ratio in the models. We hence increase the envelope mass of the He WD to $6.4 \times 10^{-3} - 10^{-2} M_{\odot}$. The fact that the surface abundances are sensitive to the initial H mass was also found in Paper I. The abundances from the two He WD models with differing envelope masses are listed in Table 4.1.

With a given envelope mass for the He WD, we next construct the SOF abundances. In the hydrodynamic simulations the SOF is the hottest region during the merger, reaching temperatures of 123 – 250 MK, and hence burns prior to the stellar evolution of the model in this work. In order to understand the contribution of the SOF to the final surface abundances, we build two sub-cases for each envelope mass considered: one with a ‘cold SOF’ where the SOF is not burnt prior to the beginning of the evolution and a ‘hot SOF’ which is burnt at a constant temperature and density of $T_{\text{SOF}} = 123$ MK and $\rho \approx 5 \times 10^4$ g/cc respectively, until the order of $^{16}\text{O}/^{18}\text{O} \approx 1 - 10$ (these are the values used for the SOF in Case 1 of Paper I). Fig. 4.2 shows the evolution of abundances in the SOF region during its burning.

The four cases are listed in Table 4.2 and the abundances of the SOF and envelope for each case are listed in Table 4.3. The algorithm for the construction of each case is as follows:

1. Select the mass of the H-rich envelope of the He WD and homogenise the isotopic abundances over the mass of the He WD. The CO WD abundances are fixed for all initial models (Table 4.1)
2. Mix the He and dredged-up CO WD abundances in proportions according to the description of the four zones in Section 4.2.1.
3. Treatment of SOF: cold or hot? If cold, proceed to post-merger evolution (SOF(1) and SOF(2) in Table 4.3).
4. If hot (Fig. 4.2), burn the SOF abundances at constant T, ρ conditions, until $^{16}\text{O}/^{18}\text{O}$ is of the order of 1-10 (SOF(3) and SOF(4) in Table 4.3).
5. Use these SOF abundances in the initial model, with appropriate buffer and envelope abundances (Table 4.2) and begin post-merger evolution.

The four initial models are: Case 1 and Case 2 which differ by the H-rich envelope mass of the He WD used to build them. Both of these are ‘cold SOF’ cases, i.e, the SOF is not burnt prior to the evolution. Cases 3 and 4 are ‘hot SOF’ cases. Case 3 is constructed with the abundance of Case 1 in the core, intershell and envelope, but the SOF abundance from Case 1 is burnt until the $^{16}\text{O}/^{18}\text{O}$ drops to its lowest value. Case 4 is built in the same way as Case 3 but by using the initial abundances of Case 2.

4.2.3 Simulation algorithm

We used three codes for our work: nucleosynthesis codes from the NuGrid family; the single zone frame (Herwig et al., 2008) and the multi zone post processing frame (Pignatari et al., 2016, Ritter et al., in prep.), and the stellar evolution code MESA (version 6794) (Paxton et al., 2015).

For burning the SOF prior to constructing the initial model, we used the single-zone frame of NuGrid. Once the initial model was built, we used MESA to perform the stellar evolution calculations. The above initial profiles are relaxed onto a $0.9M_{\odot}$ pre-main-sequence model and then evolved until it passes through the region in the HR diagram where RCB stars are found: $3000\text{ K} \leq T_{\text{eff}} \leq 8000\text{ K}$ and $3.5 \leq \log L/L_{\odot} \leq 4.0$ (Clayton, 1996; Pandey, Lambert, and Kameswara Rao, 2008)– this is the RCB phase of the model. We use the Bloeker’s mass-loss formula (Bloeker, 1995) when the star is in the RCB phase $\eta = 0.02$, along with Type I OPAL tables to calculate opacities. Energy generation is followed using an 18-isotope network that follows hydrogen and helium burning reactions.

The models were then post-processed using the multi-zone post processing network frame (MPPNP) of NuGrid. Each zone of a model computed at every time-step is processed with an adaptive nuclear network that uses over 1000 isotopes, taking also into account the diffusive mixing processes in the MESA model.

4.3 Results

The evolutionary tracks are similar to those in Fig. 5 of Paper I. The RCB phase of our four post-merger models is between $6.7 - 9.2 \times 10^4$ yr, which is consistent with the expected lifetime of roughly 10^5 yr from observations.

4.3.1 Nucleosynthesis and mixing processes in the models

We examine the different phases of nuclear burning during the evolution of the models and how both burning and mixing simultaneously affect their surface abundances. In Paper I, the evolution of species between ^1H to ^{22}Ne were studied in detail. These species affected the $^{16}\text{O}/^{18}\text{O}$ and $^{12}\text{C}/^{13}\text{C}$ ratios and the abundance of ^{19}F , as these formed the main focus of that work. The nature of the evolution of the above species are the same in the cases presented in this work as well (see Section 3.2.2, Paper I).

In this work we examine the heavier species, such as the isotopes of Si, S and Ca, using Case 1 to demonstrate their evolution (Fig. 4.3). There are two stages of nuclear burning: H-shell burning followed by He-shell burning. During the post-merger evolution of the models the maximum temperatures for H burning are between 40 – 50 MK and for He burning up to ~ 250 MK. In Fig. 4.3 we show temporal snapshots of mass profiles of Case 1, with

the diffusion coefficient of mixing (D) along with the convective region (the grey shaded portion), the neutron density (in n/cm^3) and the isotopic abundance of ^1H , ^{13}C , ^{14}N , ^{29}Si , ^{30}Si and ^{32}S . The temperature-density profiles of our models are similar to those of Paper I and the reader is referred to Fig 7 of Paper I for these.

The region which participates in nuclear burning during the evolution of the post-merger model, i.e., the mass above the CO core, has $\sim 98\text{--}99\%$ of He (not shown in the snapshots of Fig. 4.3), $< 1.5\%$ of H and $\sim 0.3\%$ of metals. The first panel of Fig. 4.3 shows an early stage of post merger evolution ($t=0.13\text{Myr}$). By 0.32 Myrs, the second panel of Fig. 4.3, H has been completely burnt in the inner region of the star ($0.45 < M/M_\odot < 0.7$) and the H-shell moves toward the surface. The overall abundance of ^{14}N has increased due to proton-neutron-capture by ^{13}C , and its simultaneous mixing upto the surface. This is also the period where the Ne-Na cycle is active and ^{23}Na is created via $^{22}\text{Ne}(p,\gamma)^{23}\text{Na}$ (not shown in plot). ^{13}C is also destroyed by He burning via $^{13}\text{C}(\alpha, n)^{16}\text{O}$, which gives rise to the formation of a neutron pocket (right side of second panel). By 0.50 Myrs, the third panel of Fig. 4.3, temperatures have become hot enough for He burning to become dominant and ^{13}C is entirely destroyed in the interior of the star. At this time, the neutron pocket is diluted and spread over a mass of $0.45 - 0.58M_\odot$ by a convection zone which arises due to the triple- α reaction (right side of third panel). ^{28}Si undergoes neutron-capture in this region to produce ^{29}Si while ^{30}Si is produced more abundantly than ^{29}Si , through the more efficient neutron-capture reaction of $^{33}\text{S}(n,\alpha)^{30}\text{Si}$. All these products from H and He burning, are gradually dredged up from the interior to the surface by the artificial mixing process we implement.

This diffusion coefficient is constructed such that it cuts off at the entropy barrier arising from the peak of nuclear energy in the star, which in our models is at approximately the location where ^{14}N undergoes He capture to form ^{18}O . Therefore as the model evolves, the ^{14}N abundance profile burns and moves closer to the surface with the diffusion coefficient following simultaneously. By the time the star enters the RCB phase, mixing becomes restricted to the outer region of the model. By the end of the RCB phase, the fourth panel of Fig. 4.3, the post-merger star is 1.8 Myrs for Case 1 and the $^{30}\text{Si}/^{28}\text{Si}$ in the surface is enhanced by twice its initial amount while $^{29}\text{Si}/^{28}\text{Si}$ is not significantly enhanced compared to its initial value. About $0.05M_\odot$ is lost from the surface due to winds. The duration of the RCB phase of this model is 9.2×10^4 yr.

Prior to examining the evolution of individual elements that have been observed in RCB stars, we discuss the structural differences between the four cases during their evolution. The main difference between Cases 1 and 2 initially is their H abundance, with Case 2 having a higher H abundance than Case 1. During their evolution, the wide convection zone between $0.45 - 0.58M_\odot$ which arises in Case 1 (third panel, Fig. 4.3), does not appear during the evolution of Case 2. Both these cases attain nearly the same maximum neutron

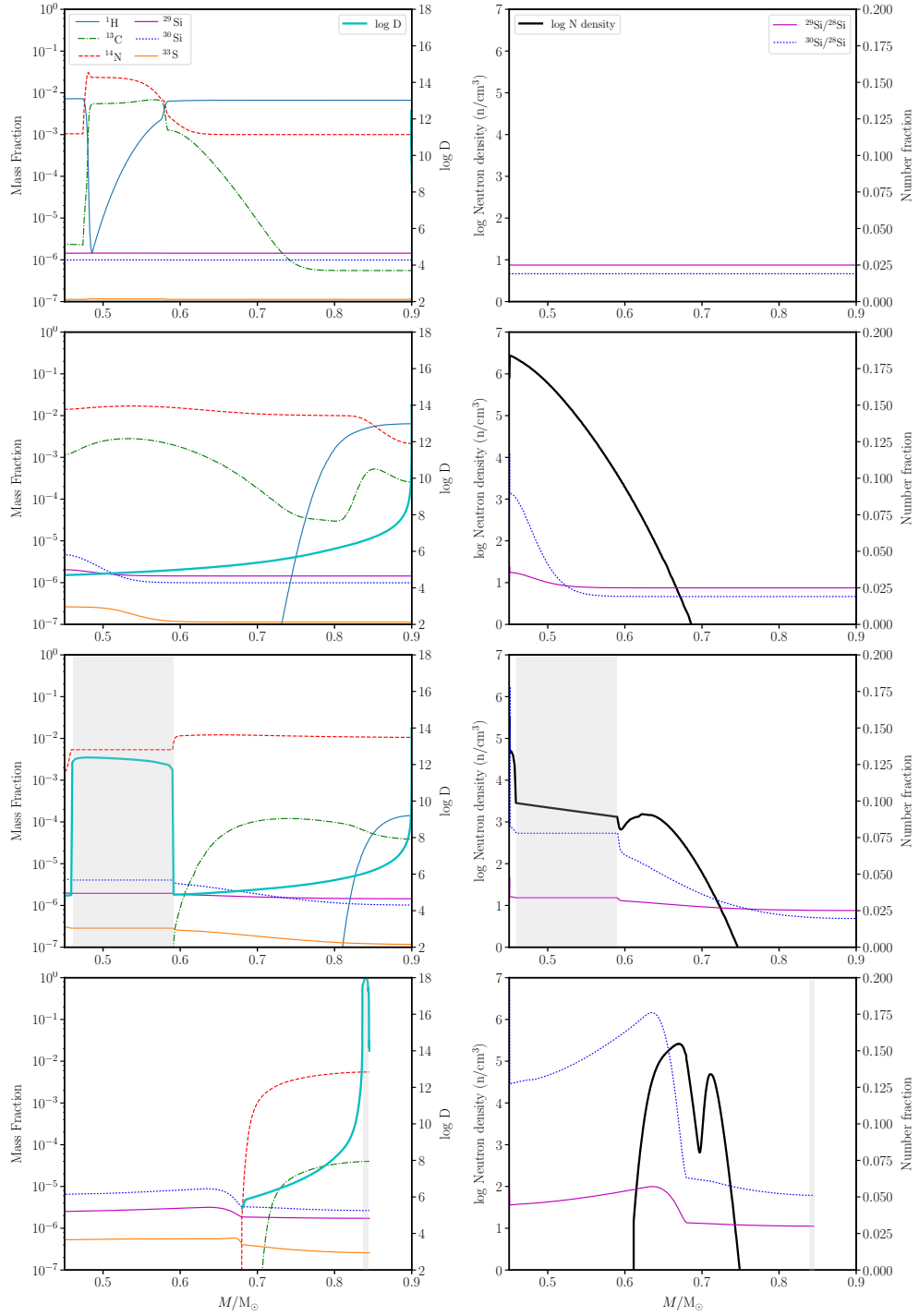


FIGURE 4.3: Snapshots of time for Case 1 from top to bottom: close to initial at $t=0.13$ Myr, $t=0.32$ Myr, $t=0.50$ Myr and at the termination of the evolution at $t=1.8$ Myr. Left: Mass fractions and diffusion coefficient ($\log D$) against mass coordinate. Right: Neutron density and number ratios of silicon isotopes against mass coordinate. Convection is shown as the grey shaded region. Since the mixing is restricted to the layers above the CO core, the mass range in this plot is restricted to $0.45 - 0.90 M_{\odot}$.

densities during their evolution, but as the wide convection zone in Case 1 causes the neutron pocket to be spread out, it produces a larger abundance of neutron-capture isotopes in Case 1 than Case 2.

The main difference between the cold (Cases 1 and 2) and their corresponding hot SOF cases (Cases 3 and 4) is that in the cold SOF cases, all the nuclear burning processes occur during the post-merger evolution of the star. In the hot SOF models, the abundances of the SOF zone of the initial profile were burnt prior to the beginning of the evolution and hence these SOFs (Fig. 4.2) are enriched in products of He burning and neutron capture.

4.3.2 Elemental abundances and comparison with RCB stars

The products of H-burning during the evolution of the post-merger model are: ^{13}C , ^{14}N and ^{23}Na and in the setup of the hot SOF is ^{25}Mg (Fig. 4.2). The products of He-burning are: ^{16}O , ^{18}O , ^{15}N , ^{19}F , ^{22}Ne and neutrons. Depending on the neutron density during the post-merger evolution the isotopes of Si, Ti, Ca, Ni, Zn, and the elements of the first s-process peak Y and Zr are affected. The prior burning of the hot SOFs also affects the abundance of these isotopes and depending on the neutron density during their burning, can also significantly enhance the abundance of the second s-process peak elements Ba and La.

We next discuss the evolution of those elements in our models that have been observed in RCB stars.

Carbon is predominantly in the form of ^{12}C in our models, which is already larger than ^{13}C in the initial composition ($^{12}\text{C}/^{13}\text{C} = 325$ initially), and is then increased further due to the triple-alpha reaction. ^{13}C is first consumed by proton capture to make ^{14}N and then entirely destroyed due to alpha capture through $^{13}\text{C}(\alpha, n)^{16}\text{O}$. The net effect of these processes is that the $^{12}\text{C}/^{13}\text{C}$ ratio at the surface is increased significantly. Since the SOFs of the hot SOF models are enhanced in ^{12}C and depleted in ^{13}C due to their prior burning (Table 4.3), the final ratio at the surface of the hot SOF cases is higher than their corresponding cold SOF cases.

Nitrogen is constituted of ^{14}N and ^{15}N in our models. Aside from the contribution of the He WD (Table 4.1), ^{14}N is also created in the star from $^{13}\text{C}(p, \gamma)^{14}\text{N}$ and then destroyed by He-burning through $^{14}\text{N}(\alpha, \gamma)^{18}\text{F}(\beta, \gamma)^{18}\text{O}$. ^{14}N is a neutron poison and creates protons through $^{14}\text{N}(n, p)^{14}\text{C}$, which allows for the production of ^{15}N through He-burning, via $^{18}\text{O}(p, \alpha)^{15}\text{N}$. ^{15}N is destroyed by further He-burning through $^{15}\text{N}(\alpha, \gamma)^{19}\text{F}$. The SOFs of the hot SOF cases produce some ^{15}N (Table 4.3) and hence these cases are initially more enhanced in $^{14}\text{N}/^{15}\text{N}$ than the corresponding cold SOF cases.

Oxygen in our models is predominantly ^{16}O followed by ^{18}O and ^{17}O . The $^{16}\text{O}/^{18}\text{O}$ number ratio from the initial composition is 1417 and that of $^{16}\text{O}/^{17}\text{O}$ is 6800. Proton capture by ^{16}O produces ^{17}O via $^{16}\text{O}(p, \gamma)^{17}\text{F}(\beta, \gamma)^{17}\text{O}$. ^{16}O is initially enhanced in all cases due to alpha

enhancement of the initial composition, and is then further produced by $^{12}\text{C}(\alpha, \gamma)^{16}\text{O}$ and $^{13}\text{C}(\alpha, n)^{16}\text{O}$ in the star. He-burning of ^{14}N produces ^{18}O in the star and also in the SOFs of the hot SOF cases (Table 4.3) leading to an overall initial enhancement of this ratio in Cases 3 and 4.

Fluorine is created in the star by the destruction of ^{15}N via $^{15}\text{N}(\alpha, \gamma)^{19}\text{F}$.

Sodium is enhanced due to the reaction from the Ne-Na cycle, $^{22}\text{Ne}(p, \gamma)^{23}\text{Na}$, and is enhanced above its initial amount during the evolution of the post-merger model; the hot SOFs destroy ^{23}Na through neutron capture and then generate it back to its initial amount through the above proton capture reaction (Fig. 4.2). Only one of the stable isotopes of **Magnesium**, ^{25}Mg , is produced in nominal amounts during the post-merger evolution at the maximum temperatures of H-burning at 40 – 50 MK, via $^{24}\text{Mg}(p, \gamma)^{25}\text{Al}(\beta, \gamma)^{25}\text{Mg}$. It is also enhanced in the hot SOFs.

Aluminium is negligibly affected during the post-merger evolution or in the hot SOFs since the temperatures of 40-50 MK are not sufficient for hot H-burning via the Mg-Al chain. $^{25}\text{Mg}(p, \gamma)^{26}\text{Al}$ weakly creates some ^{26}Al . Temperatures of > 50 MK are required to activate the Mg-Al chain for producing significant amounts of Al (Arnould, Goriely, and Jorissen, 1999; Iliadis, 2007).

We now come to elements whose isotopes are affected only by neutron capture.

The maximum values for the neutron densities are in the range of $10^5 - 10^7 \text{ n/cm}^3$ during the evolution of the four post-merger cases. On the other hand, the SOFs when burnt prior to the evolution of Cases 3 and 4 produce higher maximum neutron densities of $6.3 \times 10^{11} \text{ n/cm}^3$ in the SOF of Case 3 and $7.9 \times 10^{10} \text{ n/cm}^3$ in the SOF of Case 4 (Fig. 4.2), upto a period of 10^7 s . Since for the initial setup of Cases 3 and 4, we take the SOF abundances at a much later time ($\approx 10^{10} \text{ s}$) when the $^{16}\text{O}/^{18}\text{O}$ ratio drops to its lowest value, their SOFs are enriched in isotopes of neutron-capture and He burning (Fig 4.2 and Table 4.3), thus contributing to the overall enrichment of these species at the surface of the RCB models from Cases 3 and 4.

Silicon and sulphur are not produced in our models since temperatures required for their creation are of the order of 1 GK. Their isotopic ratios are however, affected by neutron captures as was shown in Fig 4.3.

In Fig. 4.4, we use **Ca** isotopes to illustrate the evolution of neutron-capture species and simultaneously examine the differences between hot and cold SOF cases, 1 and 3 respectively. Initially, Case 3 is more enriched in neutron-capture isotopes due to the contribution of the initially burnt SOF than Case 1 (Fig. 4.4, top panel). One of the first He-burning reactions to occur is $^{13}\text{C}(\alpha, n)^{16}\text{O}$, which gives rise to a neutron pocket (Fig. 4.4, second panel). In Case 1, the neutron pocket reaches a maximum density of $\approx 2.5 \times 10^6 \text{ n/cm}^3$ and spans a broader mass zone than Case 3 whose maximum neutron density is $\approx 6.3 \times$

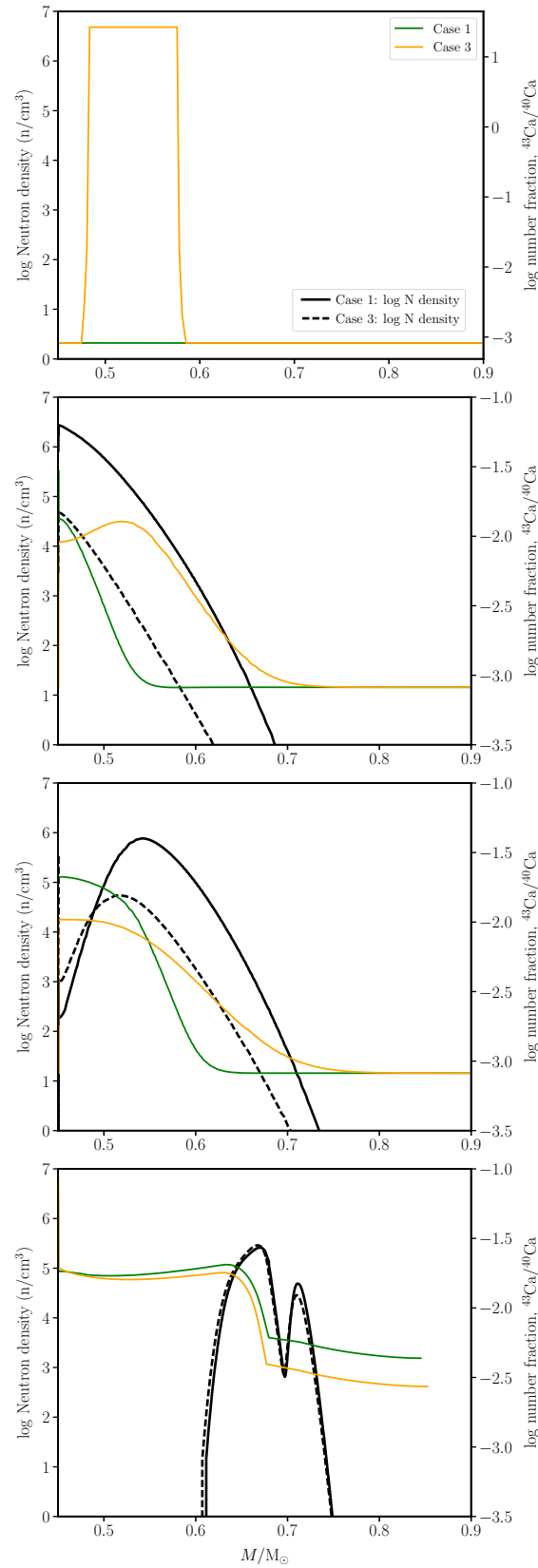


FIGURE 4.4: Snapshots of time for Cases 1 and 3, showing the evolution of the number fraction of Ca isotopes and neutron density. From top to bottom, Case 1 (Case 3): $t=0.13$ (0.11) Myr, $t=0.32$ (0.28) Myr, $t=0.34$ (0.31) Myr and $t=1.8$ (1.7) Myr.

10^4 n/cm^3 . The weaker neutron pocket of Case 3 produces a lower enhancement in the $^{43}\text{Ca}/^{40}\text{Ca}$ ratio than Case 1 (Fig. 4.4, third panel); thus in Case 3, the change in the surface value of this ratio is primarily due to the artificial mixing which dredges up the hot SOF abundances (Fig. 4.4, bottom panel). On the other hand in Case 1, the $^{43}\text{Ca}/^{40}\text{Ca}$ ratio is affected by neutron-capture occurring during the post-merger evolution. The isotopes of **Ti** evolve in a similar way as Ca isotopes. Neutron-capture reactions also produce **Ni and Zn** in our models.

The main difference between Cases 3 and 4, which are both hot SOF cases, is their initial H mass fraction. As the SOF of Case 3 has a lower initial H abundance than Case 4, only a smaller fraction of ^{13}C is destroyed to ^{14}N , making more ^{13}C available for neutron production in the SOF of Case 3 compared to that of Case 4 (Table 4.3). Thus the SOF of Case 3 has a larger maximum density of neutrons ($6.3 \times 10^{11} \text{ n/cm}^3$) than Case 4 ($7.9 \times 10^{10} \text{ n/cm}^3$). The larger neutron density of Case 3 causes elements prior to the first peak such as Ni and Zn, to undergo neutron-capture and give rise to large enhancements in elements belonging to the s-process peak elements such as **Y, Zr, Ba, La**. On the other hand, the neutron density in the SOF of Case 4 is high enough only to produce isotopes of Ni and Zn, and to a smaller extent in the s-process elements belonging to the first s-process peak, Y and Zr. Thus the net surface abundances of Ni and Zn are higher in Case 4 while those of the s-process elements are higher in Case 3. Ba and La which are second peak s-process elements, are not produced in the SOF of Case 4.

To summarise, Cases 1 and 3 have a lower initial abundance of hydrogen than Cases 2 and 4 respectively and hence have more ^{13}C , higher neutron densities and less ^{14}N . Consequently, Cases 1 and 3 produce higher amounts of neutron-capture isotopes than Cases 2 and 4. On the other hand, the abundance of proton-capture isotopes such as ^{14}N , ^{15}N , ^{17}O and ^{25}Mg are higher in Cases 2 and 4 owing to their larger H abundance than Cases 1 and 3 respectively.

We next compare individual elemental abundances between our models and those of RCB stars, taken from the database compiled by Jeffery, Karakas, and Saio (2011), (which is itself based on the data of Asplund et al., 2000 and Pandey, Lambert, and Kameswara Rao, 2008) and which was also used in Paper I. RCB stars were classified as minority and majority stars by Lambert and Rao (1994) based on their abundances– the RCB minority stars (black squares in Fig. 4.5) have a lower [Fe] abundance and higher Si/Fe and S/Fe values than the RCB majority stars (black stars in Fig. 4.5). We use the same notation as Jeffery, Karakas, and Saio (2011) to represent the elemental abundances; the abundance [X] is calculated as $[X] = \epsilon_i - \epsilon_{\text{solar},i}$, where $\epsilon_i \equiv \log n_i + C$, C being a constant and n_i the number density of species i. The individual errors are not marked in Fig. 4.5, but there is a general uncertainty of $\pm 0.2 - 0.3$ dex in the measured abundances.

For the purpose of our analysis, we divide the elements as those that are primarily

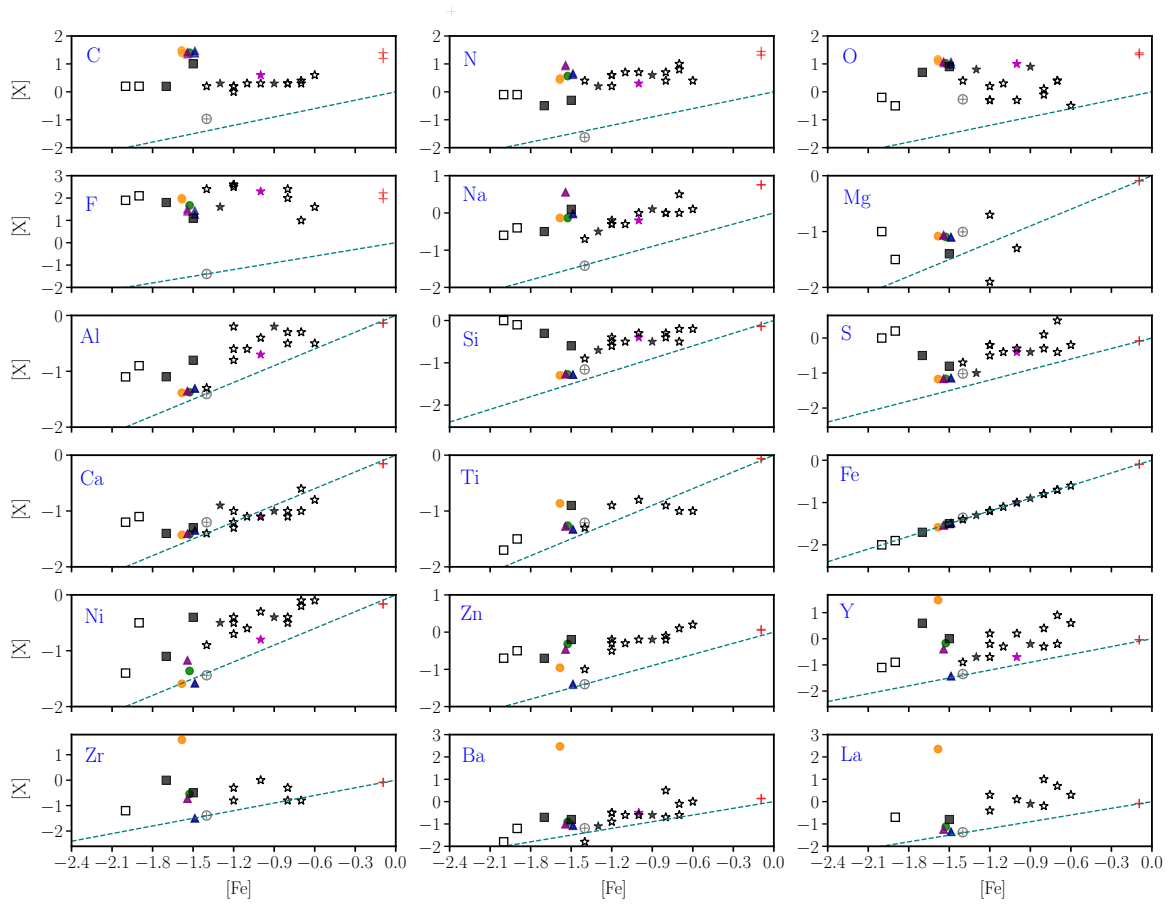


FIGURE 4.5: Comparison of the surface abundance of the four cases in this work, with observed abundances of RCB stars. Square symbols are RCB minority stars and star symbols are RCB majority stars; the two filled square symbols have $^{16}\text{O}/^{18}\text{O}$ measured from García-Hernández et al. (2010). As a reference we also plot the abundances of Case 1 of Paper I as the + symbol. The prototype, R Coronae Borealis (RCrB) is the pink \star . **Case 1** and **Case 3** are plotted as filled green and orange \circ symbols respectively, and **Case 2** and **Case 4** as filled blue and purple \triangle symbols respectively. The grey \oplus symbol is the abundance from the initial $Z=0.0028$ alpha-enhanced composition. The teal-dashed line shows the scaled-solar composition.

affected by neutron capture and those that are not. We begin with the ones whose isotopes are not affected by neutron-capture reactions: C, N, O, F, Na and Mg. Their abundances are determined mainly by H and He burning reactions within the star. In the observations of RCB stars, the $[X]$ values of these elements seem to not have a distinct correlation with metallicity, until $[\text{Fe}] < -1.5$ dex, and then decrease as $[\text{Fe}]$ decreases. Both our new metal-poor models and the solar-metallicity model of Paper I, obtain elemental abundances of these elements close to the upper limits of the values observed in RCB stars.

In our models, the abundance of C is enhanced up to 2 dex, N up to 1 dex and O up to 1.2 dex, all compared to solar. Carbon is overproduced in our models because of two reasons- the initial enhancement $[\text{C}/\text{Fe}] = 0.55$ dex and its production in the star due to the triple-alpha reaction. This ^{12}C is burnt to ^{16}O through alpha capture, and hence the $[\text{O}]$ values are also in the upper limit of the observed range. Nitrogen is enhanced due to the contribution of ^{14}N in the initial setup from the He WD and the hot SOFs (Table 4.1, Table 4.3) and the production of ^{14}N and ^{15}N during the evolution of the star and from the hot SOFs as well.

Fluorine has only one stable isotope, ^{19}F which is predominantly produced by the He-burning of ^{15}N in the star. Fluorine values are enhanced to 1 – 2.3 dex and reasonably span the entire observed range as did the solar-metallicity models of Paper I.

Sodium is enhanced in our models due to H-burning in the Ne-Na cycle in the early stages of the evolution and its abundance matches the abundances measured in RCB stars. Case 4 makes the highest amount of Na because of the contribution of ^{22}Ne seed nuclei from its hot SOF which then undergo proton capture during the post-merger evolution. The abundances of Mg and Al are unchanged from their initial alpha-enhanced values in our models because temperatures are not hot enough for the Mg-Al chain to operate. The observed abundances of Na, Mg and Al in RCB stars scale down with $[\text{Fe}]$ more or less the same way as the solar-scaled composition (the dashed teal line in Fig. 4.5) down to $[\text{Fe}] = -1.5$ dex. Lower than $[\text{Fe}] = -1.5$ dex, the elemental abundances of the three RCB stars appear more enhanced in $[\text{X}/\text{Fe}]$ than their more metal-rich counterparts. For $[\text{X}/\text{Fe}]$, we compare the offset of $[\text{X}]$ against the dashed teal line. Thus, C, N, O, F and Na are substantially produced in our models, while Mg and Al reflect only their initial values. Despite not being produced in our models, the initial abundance of Mg is sufficient to match the observational data.

The abundances of Si, S and Ca are unchanged from their initial values since temperatures high enough for O burning are required to produce them. Calcium is in fact, very close to the solar-scaled value for most of the RCB stars, except two stars that have a lower metallicity than our models and show enhancements of $[\text{Ca}/\text{Fe}] \approx 0.8$ dex. Titanium is significantly enhanced to match the observed values only in Case 3 due to the contribution of its hot SOF.

Nickel isotopes are produced by neutron capture in our models, causing an enhancement of ~ 0.4 dex in Case 4 (through its hot SOF) and ~ 0.3 dex in Case 1, compared to the initial amount. These values are not sufficiently high to match the abundances of Ni in RCB stars. The production of large amounts of Ni, like Si and S requires temperatures of at least ~ 1 GK. Zinc is sufficiently produced to match the observed abundances, again from the SOF of Case 4.

S-process elements Y, Zr, Ba and La are greatly enhanced by up to 2 – 2.5 dex compared to solar in Case 3. These values however, are much higher than observations. Cases 1 and 4 produce the required abundances of these elements that match the observations.

Our best RCB model whose surface abundances are within range of most species observed in RCB stars, is from Case 4.

4.3.3 Comparison with pre-solar graphite grains

In Figs. 4.6–4.8, we compare the number ratios of isotopes from our models with the observed LD graphite grain data, taken from the compilation of Hynes and Gyngard (2009). In Figs. 4.7–4.8, we use the δ notation to represent the isotopic ratios. It is calculated as follows: $\delta(^iX/^jX) = ((^iX/^jX)_\star / (^iX/^jX)_\odot) - 1) \times 1000$.

Although the $^{16}\text{O}/^{18}\text{O}$ ratio measured in RCB stars is less than 25, we expand the range of grain data to include those with $^{16}\text{O}/^{18}\text{O} < 40$, since Case 1 has $^{16}\text{O}/^{18}\text{O} = 29 - 33$. Due to the uncertainty in the physics of grain condensation, we assume that the gas ejected by an RCB star can be mixed with different proportions of interstellar material of solar composition before condensing into carbon dust. We hence also investigate the effect of dilution with solar material on the surface isotopic ratios of our four RCB models and how they compare with the grain composition. Each of our cases has two points, one representing the value at the start of the RCB phase and one when it leaves the RCB phase on the HR diagram. We also plot dilution lines which represent the isotopic number ratio on diluting the values from the surface of the models with different fractions of the solar value. Diluted ratios are calculated for fractions of 0.0 (direct surface value of the ratio from the model), 0.1, 0.3, 0.5, 0.7, 0.9 and 1 (solar value, not visible since the x-axis range is restricted to $^{16}\text{O}/^{18}\text{O} \leq 40$). As the ratios become increasingly diluted with solar mass fractions, the dilution lines move toward the right of the figures and asymptotically approach the solar composition (horizontal dashed black line).

There are only two common isotopic ratios that have been measured between RCB stars and LD graphite grains: and $^{16}\text{O}/^{18}\text{O}$ (Fig. 4.6a). Cases 2 and 4 which are constructed with the higher initial H-abundance, make more ^{14}N through $^{13}\text{C}(p, \gamma)^{14}\text{N}$ and thus make more ^{18}O than Cases 1 and 3 respectively. Hence Case 2 has $^{16}\text{O}/^{18}\text{O}$ in the range of 19 – 23 while Case 1 has a larger range of 29 – 33 at the surface. Introducing a burnt SOF in the initial

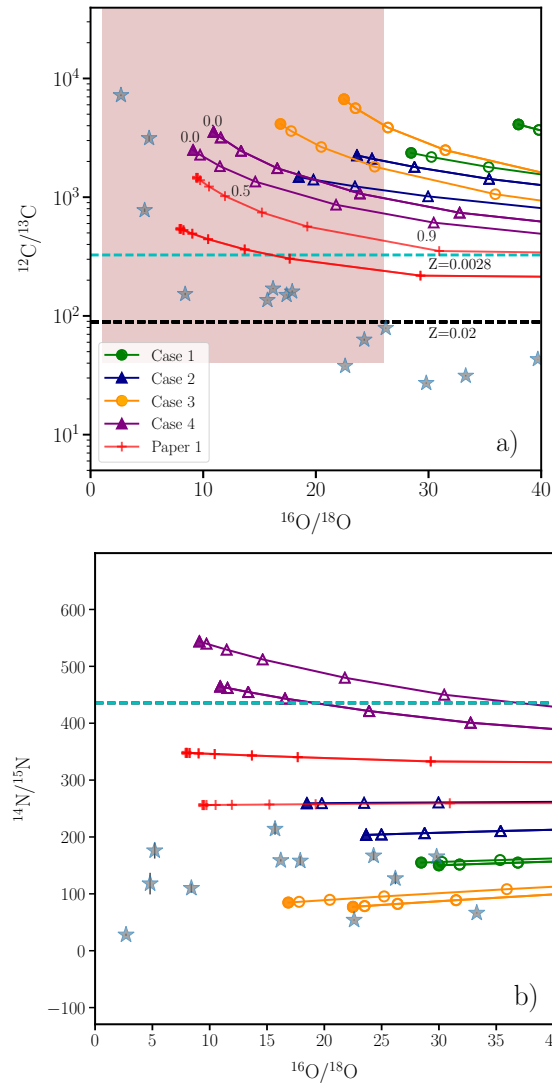


FIGURE 4.6: Number ratios of $^{12}\text{C}/^{13}\text{C}$ (a) and $^{14}\text{N}/^{15}\text{N}$ (b) against $^{16}\text{O}/^{18}\text{O}$. The grain data are the grey stars along with error bars. Error bars for $^{16}\text{O}/^{18}\text{O}$ are within the symbol. Dilution lines connect points that represent different fractions of dilution with solar material; filled symbols are directly taken from the surface of the models (without any dilution) and empty symbols represent dilution with 0.1, 0.3, 0.5, 0.7, 0.9, 1.0 fraction of solar composition. The dashed cyan line is the value for the alpha-enhanced composition at $Z = 0.0028$ and dashed black line is the solar composition. The shaded region in (a) represents the observed limits for RCB stars; the lower bound for $^{12}\text{C}/^{13}\text{C}$ is set to 40 (Hema, Pandey, and Lambert, 2012) and $^{16}\text{O}/^{18}\text{O}$ is set to 1–25 (Clayton et al., 2007; García-Hernández et al., 2010). Note: The measurements for these two ratios were obtained independently and do not belong to the same stars. Symbols and lines of this figure are used in the following figures Fig. 4.7–4.8.

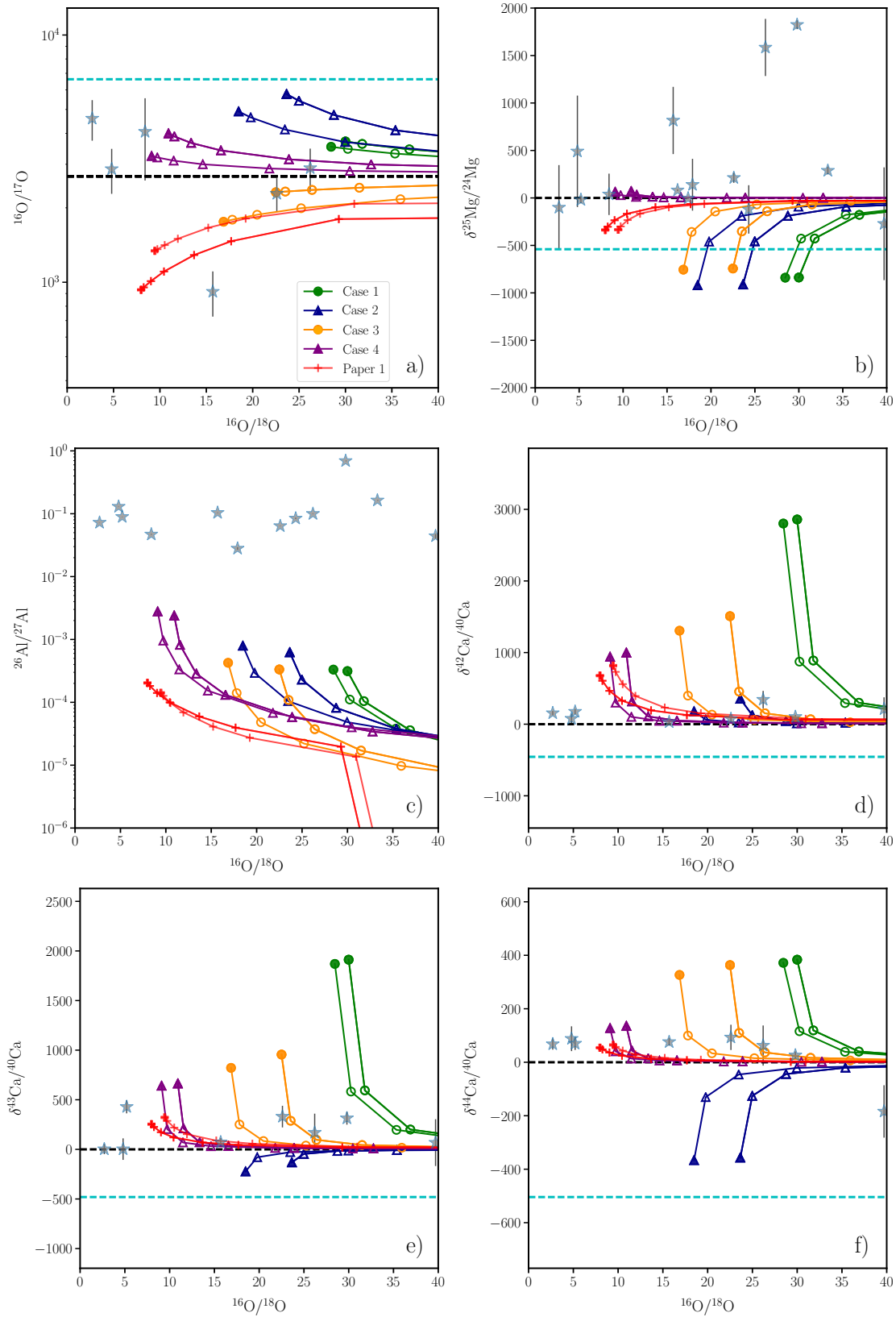


FIGURE 4.7: Number ratios of $^{16}\text{O}/^{17}\text{O}$ (a) and $^{26}\text{Al}/^{27}\text{Al}$ (c), and δ -values of $^{25}\text{Mg}/^{24}\text{Mg}$ number ratio (b), and of Ca isotopes (d), (e), (f) vs. $^{16}\text{O}/^{18}\text{O}$ for our models and the grains.

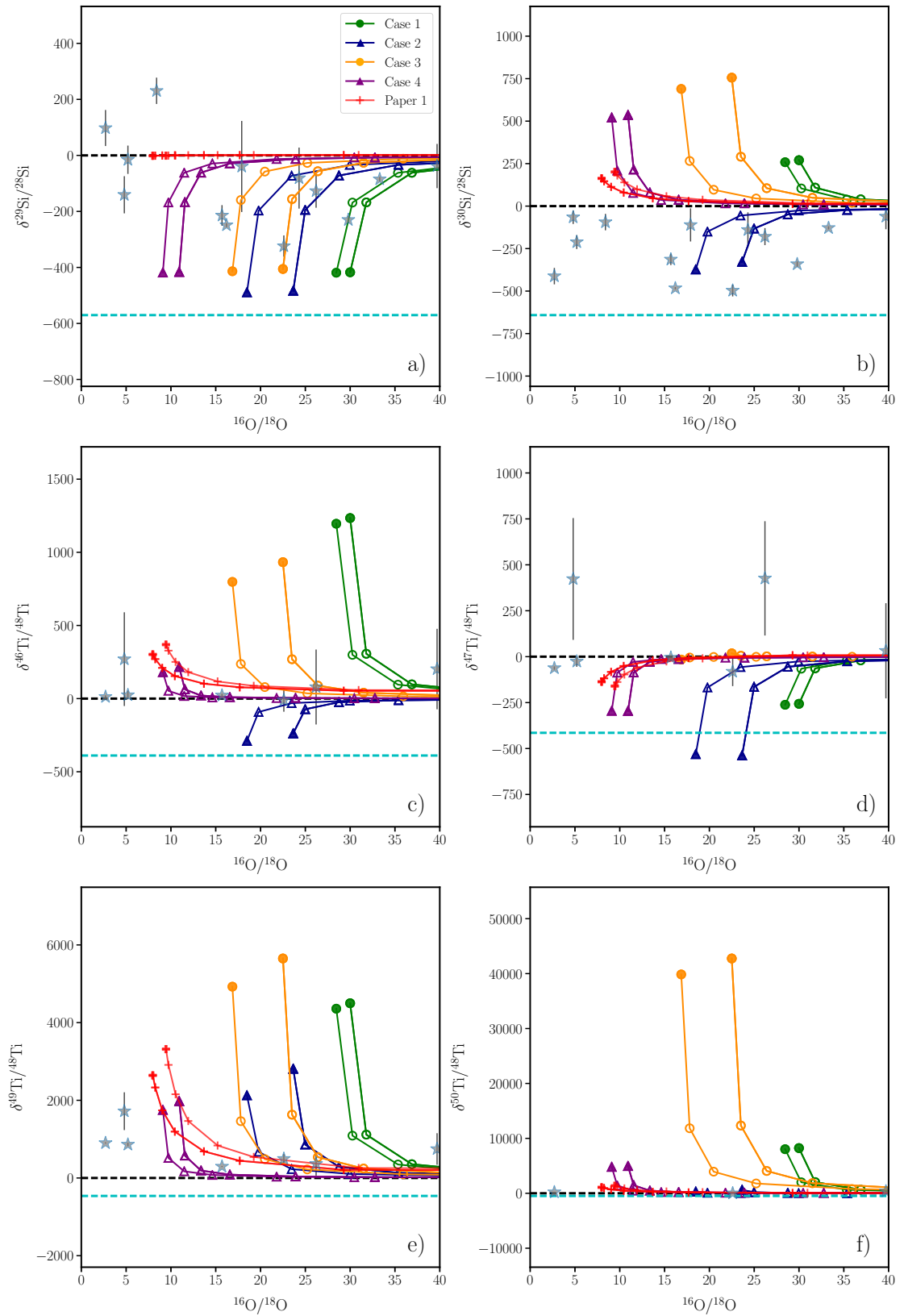


FIGURE 4.8: δ -values of Si isotopes (a) and (b), of Ti isotopes (c), (d), (e) and (f) vs. $^{16}\text{O}/^{18}\text{O}$ for our models and the grains.

setup, decreases this ratio in the hot SOF cases to 9.5 – 10.2 in Case 4 and 17 – 23 in Case 3.

The models have much higher values of $^{12}\text{C}/^{13}\text{C}$ than the grains, between 1500 and 7000 as against the grain values which are in the range of 30–200. This is because of the high initial $^{12}\text{C}/^{13}\text{C}$ ratio of 325, the production of ^{12}C and destruction of ^{13}C due to He burning. Changing the H-envelope mass does not affect the $^{12}\text{C}/^{13}\text{C}$ ratio significantly. The hot SOF cases however are initially enhanced in ^{12}C and depleted in ^{13}C in the SOF region, and thus their final C-isotopic ratios at the surface are also higher than their corresponding cold SOF cases.

Ten grains in Fig. 4.6a which have $^{16}\text{O}/^{18}\text{O} < 25$ and $^{12}\text{C}/^{13}\text{C} > 100$, fall within the observational range of RCB stars. None of our models, however, can simultaneously produce the grain values in this region of $^{16}\text{O}/^{18}\text{O}$ and $^{12}\text{C}/^{13}\text{C}$. Only three grains have $^{12}\text{C}/^{13}\text{C}$ ratios of 700 – 7400 which are comparable to the estimates from our models, but these grains also have very low $^{16}\text{O}/^{18}\text{O}$ ratios of 3–4. Our models however, only go down to 9.5 in $^{16}\text{O}/^{18}\text{O}$.

One of the major successes of our models is in obtaining the sub-solar $^{14}\text{N}/^{15}\text{N}$ values measured in these graphite grains (Fig. 4.6b); our models have a range of $^{14}\text{N}/^{15}\text{N} = 70 – 540$, three of which are below the initial amount of $^{14}\text{N}/^{15}\text{N} = 470$. The $^{14}\text{N}/^{15}\text{N}$ ratio of Case 4 exceeds the initial value of 470, because of the production of ^{14}N in the star and also from its initial hot SOF contribution.

The isotopes ^{17}O , ^{25}Mg and ^{26}Al are affected by proton capture reactions in our models. The $^{16}\text{O}/^{17}\text{O}$ ratio (Fig. 4.7a) is measured only for six grains in this set, and our models show a reasonable spread that matches the range in the grains.

Case 4 produces the highest amount of ^{25}Mg compared to the other cases (Fig. 4.7b) and $\delta^{25}\text{Mg}/^{24}\text{Mg}$ is enhanced above the initial value of -590 due to its hot SOF (Fig. 4.2). Within the error bars of the data, Case 4 matches the measured values of $\delta^{25}\text{Mg}/^{24}\text{Mg}$. Although ^{25}Mg is produced in Cases 1, 2 and 3, it is not enhanced above ^{24}Mg . Diluting with 30 % of solar mass fractions can also make Cases 2 and 3 to match the data.

^{26}Al is not produced sufficiently in our models to match the grain data while ^{27}Al remains at the initial amount in the models (Fig. 4.7c). The ratio of $^{26}\text{Al}/^{27}\text{Al}$ is 0.0003–0.003 in our models while the grains have ratios of 0.03 – 0.7. Along with the C abundance, Al is also one of the key places where our models need to be improved.

Beginning with Si in Figs. 4.8a-b, we direct our attention to the neutron-capture isotopes in our models. The evolution of $^{29}\text{Si}/^{28}\text{Si}$ and $^{30}\text{Si}/^{28}\text{Si}$ have been illustrated in Fig. 4.3. Due to the higher initial hydrogen abundance and a wider convection zone that arises due to the energy released by the triple- α reaction during the evolution, the abundances of all neutron-capture isotopes are higher in Case 1 than Case 2. Hence the abundances of ^{29}Si and ^{30}Si compared to ^{28}Si are higher in Case 1 than Case 2. Owing to higher neutron densities in the SOF, the hot SOF Case 3 has higher abundances of neutron-capture isotopes than

Case 4. All four of our models match the $\delta(^{29}\text{Si}/^{28}\text{Si})$ ratio but have much higher values than the $\delta(^{30}\text{Si}/^{28}\text{Si})$ measured in the grains, except for Case 2.

For the Ca isotopes (Figs. 4.7d-f), diluting the abundances of Cases 1, 3 and 4 with 10-30% solar material produces a reasonable match with the measured grain data. Case 2 is the least enhanced in neutron-capture isotopes, and matches the grain data without much dilution. The same trends are also observed in the Ti isotopes (Figs. 4.8c-f). With a dilution of 10 – 30 %, Cases 2 and 4 can reproduce the observed δ values of all four Ti isotopes. Cases 1 and 3 are more enhanced in the Ti isotopic ratios and hence require higher dilution fractions of $\geq 30\%$ to match the grain data.

Except for the high values of $^{14}\text{N}/^{15}\text{N}$, the case that reasonably matches the other measured isotopic ratios of our sample of graphite grains is Case 4.

4.4 Discussions and Conclusions

We have presented 1D stellar evolution models of RCB stars with an alpha-enhanced initial composition of $Z=0.0028$, initiated from hybrid post-merger structures of CO+He WD mergers, by using the methodology of Menon et al. (2013) (Paper I). Four cases were studied in the current work, which primarily differed by their initial hydrogen mass in the envelope and their Shell of Fire (SOF) abundances. We followed the evolution of the post-merger models until they passed through the RCB phase in the HR diagram and compared their isotopic abundances from their surface with those observed in RCB stars.

Our post-merger models spend $6.7 - 9.2 \times 10^4$ yr in the RCB phase, which is in line with the observational estimate of $\approx 10^5$ yr (Clayton et al., 2011; Clayton, 2012). They also have low $^{16}\text{O}/^{18}\text{O}$ ratios of 9.5 – 33, high $^{12}\text{C}/^{13}\text{C}$ ratios of > 100 , enhancements in F and s-process elements compared to solar, which agree with the measured values in RCBs. A key reason for the success of our models is the implementation of the artificial mixing routine, whose prescription and parameters were adapted from Paper I. The isotopic ratios and elemental abundances of the solar-metallicity RCB models of Paper I were also reproduced in our low-metallicity cases, indicating a fair robustness in the mixing routine we constructed.

These RCB models demonstrate that even at a particular metallicity, there can be a spread in abundances depending on the values of the initial parameters chosen to construct the post-merger structure. As there is only one data point for each metallicity, we compare the spread in abundances in our models against the entire database for each element. Elements such as C, N, O, Mg, Al, Si, S, Ca are not affected significantly by the choice of the H mass fraction or the SOF abundances. Fluorine, Na, Ti, Ni and Zn show a more noticeable spread in abundance (≈ 0.8 dex) between the models. The s-process elements, Y, Zr, Ba and La, show the largest variation in abundances between the models, particularly in Case 3 due to its lower initial H-abundance and its hot SOF. The presence of the hot SOF increases the

abundance of s-process elements compared to the cold SOF cases, and also the n-capture isotopic ratios.

Carbon is overproduced in all our models and they only match the observed upper limits of N, O and Na. The abundances of Al, Si and S, are enhanced in RCB stars but remain unchanged in our models. Similarly, Mg and Ti (except Case 3) are unchanged in our models but they are within the limits of the observed range in RCB stars. The models also do not produce sufficiently high abundances of Ni or the observed spread in Ca abundances. Lithium which has been observed to be enhanced in a few RCB stars (Asplund et al., 2000), is not produced in our models.

We compare the isotopic composition of those LD graphite grains which have $^{16}\text{O}/^{18}\text{O} < 25$ and >100 which are similar to the range observed in RCBs. We explore the effect of dilution with solar material on the surface composition of our RCB models, under the hypothesis that the gas ejected by RCBs could mix with interstellar solar material before condensing as grains.

Three of our models can reproduce the sub-solar values of $^{14}\text{N}/^{15}\text{N} = 70 - 240$ and match the grain values. They can also reproduce the low $\delta^{29}\text{Si}/^{28}\text{Si}$ ratios, which were attributed to the production of ^{28}Si from massive stars and ejected in supernova explosions in earlier studies. In our low-metallicity models, ^{28}Si is alpha enhanced in the initial composition and ^{29}Si is weakly produced by neutron capture. The $\delta^{30}\text{Si}/^{28}\text{Si}$ ratios in our models are enhanced by neutron-capture above the solar value, except for Case 2 which has a weak neutron pocket. The isotopic ratios of Ca and Ti isotopes are also enhanced above solar due to neutron capture, but these can be reduced to match with the grain data by diluting their abundances with at least 10% of the solar mass fraction.

Our best model that reproduces most of the isotopic ratios and elemental abundances of RCB stars and some of the grain signatures, is Case 4. We rule out Case 3 due to the excessive amounts of s-process elements it produces compared to what is observed in RCB stars.

Carbon in our models is higher by nearly 1 dex compared to the observed value in RCB stars and the $^{12}\text{C}/^{13}\text{C}$ ratios in our models is between 1500 and 7000 while most of the grains have $^{12}\text{C}/^{13}\text{C}$ less than 100. Thus carbon is excessively produced in our models in comparison with both, RCB stars and the graphite grains. The abundance of carbon depends greatly on its enhancement in the initial composition. In our work, initial values of $[\text{C}/\text{Fe}] = 0.55$ dex and $=325$ were chosen which are higher than the predictions from galactic chemical evolution models such as those of Kobayashi, Karakas, and Umeda (2011), and observations of stars in the solar neighbourhood. The latter show an uncertainty in the abundance prediction of carbon and can vary between $[\text{C}/\text{Fe}] = -0.4$ and 0.2 dex for the metallicity of $Z=0.0028$ which we used for our models.

We do not produce the excess in $\delta^{25}\text{Mg}/^{24}\text{Mg}$ observed in the grains except for Case

4. We also do not produce sufficiently high amounts of ^{26}Al that can match the $^{26}\text{Al}/^{27}\text{Al}$ ratios of 0.03-0.7 observed in the grains nor the enhancement of [Al] in RCB stars, of up to ≈ 0.5 dex compared to its initial value.

For our models to completely match all the elemental abundances of RCB stars and the isotopic ratios measured in the grains, we need to boost the production of ^{13}C , ^{25}Mg and ^{26}Al . One underlying mechanism can solve this problem– a layer of partial H-burning close to the surface that does not mix with the the He-burning layer below it. We did a rough test calculation for estimating whether this solution will work for ^{26}Al in Case 2. The H-burning shell of $\approx 0.1 M_{\odot}$ must sit on top of the SOF which has temperatures conducive for hot H-burning i.e, of 60 – 100 MK, and densities of $1.6 - 2.5 \times 10^3 \text{ g/cm}^3$. On burning the envelope composition of Case 2 at $T = 100 \text{ MK}$ and $\rho = 2 \times 10^3 \text{ g/cm}^3$ for $10^6 - 10^{10} \text{ s}$, the mass fraction of ^{26}Al increases to 3×10^{-6} and hence the mass of ^{26}Al produced in the H-burning shell of $0.1 M_{\odot}$ is 3×10^{-7} . If all this ^{26}Al is uniformly mixed in the entire envelope which has a mass of $0.32 M_{\odot}$, the mass fraction of ^{26}Al in the envelope is $3 \times 10^{-7}/0.32 = 9.4 \times 10^{-7}$. The abundance of ^{27}Al is unchanged at these T, ρ conditions and hence its envelope abundance is the same as the initial value of 4×10^{-6} . Thus the number ratio of $^{26}\text{Al}/^{27}\text{Al}$ in the envelope is $(9.4 \times 10^{-7}/4 \times 10^{-6}) * (27/26) = 0.244$. Our target for this ratio according to the grain data is of the order of 0.1, which we achieve by this calculation. The same calculation for ^{25}Mg can also produce high values of $\delta^{25}\text{Mg}/^{24}\text{Mg}$ that will match the grain data.

This calculation however does not produce sufficient amounts of ^{13}C that can reduce the number ratios in our models. This once again indicates that the initial carbon value and the ratio used in our calculations were quite high. In a test calculation we did for Case 1, in which the initial ^{12}C and ^{16}O were reduced by an order of magnitude, thus reducing the initial and $^{16}\text{O}/^{18}\text{O}$ ratios, but keeping the same initial ratio of carbon to oxygen, the final surface ratio of was ≈ 95 compared to 2000 but $^{16}\text{O}/^{18}\text{O}$ increased to 47 compared to 29-33. Thus the final surface ratios of and $^{16}\text{O}/^{18}\text{O}$ are highly sensitive to their initial quantities.

In conclusion, our new low-metallicity stellar evolution models for post CO+He WD merger structures, match most of the chemical signatures of RCB stars quite well, particularly the low $^{16}\text{O}/^{18}\text{O}$ ratios. The models are sensitive to the initial setup– the final surface abundances depend on the initial H-mass present in the star and the treatment of the SOF. The model predictions are in partial agreement with some of the LD graphite grain data, and show promise in being sources of LD graphite grains with low $^{16}\text{O}/^{18}\text{O}$ ratios.

Chapter 5

Conclusions and Summary

In this thesis we have examined the outcomes of two types of binary mergers: massive star mergers which form blue supergiant (BSG) progenitors such as those of Supernova SN 1987A and other Type II-pec SNe. And low-mass white dwarf mergers which produce hydrogen-deficient carbon-rich ‘R Coronae Borealis’ stars.

For the first time, we have demonstrated within a single framework, that the BSG model formed from a binary merger reproduces the observed properties of Sk –69°202, the progenitor star of SN 1987A, and its explosion reproduces a strong match with the light curve and photospheric velocity profile of SN 1987A. We also extended our study to two other Type II-pec SNe, SN 1998A and SN 2006V, and found that the explosion of our merger progenitor models also match the light curves of these supernovae as well.

The first question explored in this thesis is how viable a binary merger scenario is to form the BSG Sk –69°202 that exploded as SN 1987A and how the choice of initial parameters affect the nature of the pre-supernova (pre-SN) model. These initial parameters consisted of the primary mass $M_1 = 15, 16, 17 M_\odot$, the secondary mass $M_2 = 2 - 8 M_\odot$ and the fraction of the He shell of the He core of the primary dredged up during the merger, $f_{\text{sh}} = 10, 50, 90, 100\%$. The evolutionary model we constructed was based on the binary evolution sequence hypothesised by Podsiadlowski, Joss, and Hsu (1992) and Podsiadlowski, Morris, and Ivanova (2007), and the effective-merger prescription we employed in our models, was based on the results of the simulations of Ivanova, Podsiadlowski, and Spruit (2002) and Ivanova and Podsiadlowski (2003). In this scenario, following a Case C mass transfer event, the binary system consisting of a primary RSG containing a He-depleted core and secondary main-sequence star, merges over a period of the order of a 100 years.

Each initial system (with particular values of M_1, M_2, f_{sh}) was evolved until the onset of iron-core collapse (the pre-SN model). Two factors were found important in determining whether a star formed from a merger will become a BSG, i.e., it has $T_{\text{eff}} \geq 12 \text{ kK}$: the fraction of the He shell of the He core of the primary dredged up (f_{sh}), which determines the final He core mass, and the mass of the secondary (M_2), which determines the final envelope mass of the pre-SN model. For a given value of M_1 and M_2 , increasing f_{sh} (i.e., decreasing the He core mass) causes the effective temperature and surface luminosity of the pre-SN models to

decrease. For a given M_1 and f_{sh} , increasing M_2 (i.e., increasing the envelope mass) causes the effective temperature and luminosity of the pre-SN models to increase. The final number ratios of N/C and N/O ratios in the surface are also affected by the choices of these initial parameters: N/C and N/O ratios decrease as f_{sh} increases or when M_2 increases. The He/H ratios are not significantly affected by the initial parameter choices in our models. The duration of the BSG phase of the post-merger model depends on how close the primary star is to C-ignition in the core; the sooner the primary is to C-ignition the shorter the lifetime of the BSG before explosion.

The majority of the pre-SN models were BSGs (59 out of 84 initial models) within the initial parameter space we considered, while the rest were yellow supergiants (YSGs) with $7000 \leq T_{\text{eff}} < 12\text{kK}$. None of the 84 pre-SN models were RSGs. This indicates that mergers are highly favourable to produce hot, compact progenitors with $T_{\text{eff}} \geq 12 - 18\text{kK}$ and $R = 30 - 50R_{\odot}$. The only condition under which RSG pre-SN models could form were if there was no dredge-up of the primary's He core during the merger.

Six pre-SN models matched the observational constraints of Sk -69°202, namely $T_{\text{eff}} = 15 - 18\text{kK}$, $\log L/L_{\odot} = 5.15 - 5.45$ and number ratios of N/C = 5.8 - 7, N/O = 1.3 - 1.4, He/H = 0.13 - 0.14 in the surface. The pre-SN models computed in Appendix 2.5 of Chapter 2 have been computed with RSG primary models which have a central He mass fraction of 10^{-2} , and these pre-SN models have a BSG lifetime of the order of 10^5 kyr. By choosing an RSG model when its central He mass fraction $X_{\text{Hec}} \leq 10^{-4}$ at the time of the merger, the lifetime of the BSG is < 20 kyr which matches the value deduced from observations and does not significantly affect the above surface properties of the pre-SN model.

We next investigated the viability of our BSG pre-SN models for three Type II-pec SNe: SN 1987A, SN 1998A and SN 2006V, using a 1D radiation hydrodynamic explosion code. A pre-SN model was considered to be the best fit for a given SN, if it simultaneously matched both the bolometric light curve and the velocity profiles from the absorption minima of spectral lines in the photosphere. For SN 1987A, it was the pre-SN model 16-7b which formed from the merger of $M_1 = 16M_{\odot}$, $M_2 = 7M_{\odot}$ with $f_{\text{sh}} = 50\%$, when exploded with $E = 1.7B$, a nickel mass of $M_{\text{Ni}} = 0.073M_{\odot}$ and a nickel mixing velocity of 3000 km/s. It had a radius, $R = 37.4R_{\odot}$, an He core mass of $M_{\text{Hec}} = 3.4M_{\odot}$, and an ejecta mass of $M_{\text{ej}} = 20.6M_{\odot}$. Model 16-7b has the characteristics of the optimal progenitor model for SN 1987A determined by the non-evolutionary study of Utrobin (2005), which has $M_{\text{ej}} = 18M_{\odot}$ and $R = 35 \pm 14R_{\odot}$ and a steeper density profile at the core-envelope interface than single star progenitor models.

The progenitor model that most suited SN 1998A was also Model 16-7b, with $E = 4.5B$, $M_{\text{Ni}} = 0.12M_{\odot}$ and a nickel mixing velocity of 5300 km/s. These results are comparable to the results of Pastorello et al. (2005) from their semi-analytic code, which predicts a progenitor with $R < 86.3R_{\odot}$, $M_{\text{ej}} = 22M_{\odot}$ that exploded with $E = 5 - 6B$. The analysis

of SN 2006V, however, yielded a very different progenitor structure compared to the semi-analytic results of Taddia et al. (2012). The progenitor expected from this semi-analytic code is a BSG with $R < 50 - 75 R_{\odot}$ and $M_{\text{ej}} = 17 - 20 M_{\odot}$, which exploded with $E = 2.4 B$ and had $M_{\text{Ni}} = 0.127 M_{\odot}$. Our best fit model for SN 2006V is model 18-4d, a YSG with $R = 150 R_{\odot}$, $M_{\text{ej}} = 19.1 M_{\odot}$ and $M_{\text{HeC}} = 3.8 M_{\odot}$, formed from the merger of $M_1 = 18 M_{\odot}$, $M_2 = 4 M_{\odot}$ and with $f_{\text{sh}} = 90\%$. On this basis we can state that SN 2006V is peculiar among SN 1987A-like objects and suggest that these objects may originate from both blue and yellow supergiants.

The second investigation conducted in this thesis was that of the origin of RCB stars, which are considered to have formed from the mergers of carbon-oxygen (CO) white dwarfs (WDs) and helium (He) WDs. As RCBs are known for being producers of carbon dust, we also probed them as a source of certain pre-solar graphite grains. For this, we built 1D hybrid post-merger objects based on the methodology of Menon et al. (2013), in which RCB models from solar-metallicity were evolved from hybrid CO+He WD post-merger structures. In this work, we built a new set of models with a realistic RCB metallicity. These models were evolved with an alpha-enhanced initial composition at a metallicity of $Z=0.0028$ ($[\text{Fe}/\text{H}]=-1.4$), and their surface elemental abundances and isotopic ratios were compared with the observed values of RCBs.

The first check for our models was if they reproduce the remarkably low ratios of $^{16}\text{O}/^{18}\text{O}$ between 1 – 25 that are characteristic of RCBs. The four cases we studied in this work have $^{16}\text{O}/^{18}\text{O}$ ratios between 9 – 33 and hence successfully reproduce the observed range. We next compared their surface elemental abundances with the observed values of RCB stars. We find that our models are within range of nearly all the elemental abundances of RCB stars, viz., N, O, F, Na, Mg, Ca, Ti, Zn, Y, Zr, Ba and La, except those of C (which is overproduced), Al, Si, S and Ni (which is under-produced). Along with the initial abundances of these elements, two factors in the construction of the RCB models were found to play an important role in determining their final surface abundances– its overall H mass-fraction (X_{H}) and the abundances of the Shell of Fire (SOF). The main impact of increasing X_{H} is to increase the production of nuclei from H-burning such as ^{14}N , ^{23}Na and ^{25}Mg , and decrease the abundance of ^{13}C (due to its destruction via $^{13}\text{C}(p, \gamma)^{14}\text{N}$) and consequently decrease the production of neutrons through $^{13}\text{C}(\alpha, n)^{16}\text{O}$. Burning the SOF prior to the post-merger evolution (the ‘hot SOF cases’), increases the abundance of H-burning, He-burning and neutron-capture products compared to the cases with the unburnt SOFs (the ‘cold SOF’ cases).

The production of the *s*-process elements is particularly sensitive to the treatment of the SOF and can rise up to 2.7 dex relative to initial. The abundances of C, N, O on the other hand do not vary much between the four cases, whereas F, Na, Mg, Ca, Ti and Ni are affected by both, X_{H} and abundances of the SOF in the initial post-merger model.

Carbon is overproduced in our models to nearly 2 dex whereas the observed values

are up to 0.5 dex. There are two reasons for these high values of C in our models: the initial alpha-enhancement value, $[C/Fe]=0.55$ dex and the production of ^{12}C in the post-merger evolution via the triple-alpha reaction. The latter reason also boosts the $^{12}\text{C}/^{13}\text{C}$ values in the surface to 1700–2100 in the models whereas the values in RCB stars have a lower limit of 40–100. We find that by decreasing the initial enhancement of C, the final surface values of our models also decrease and are within range of the observed RCB values. The production of Al requires hotter H-burning temperatures than the current values in our models or a separate H-burning layer directly below the envelope and above the SOF, that can produce Al and mix it directly with the surface without mixing it to the hotter regions below. The production of Si, S and higher amounts of Ni can only occur at temperatures of ~ 1 GK, which are not found in the 3D hydrodynamic simulations based on which we built our initial post-merger structures.

We next compared our the isotopic ratios of our models with those graphite grains which have $^{16}\text{O}/^{18}\text{O}$ between 1–40. We assume that the gas ejected by an RCB star is diluted with the solar interstellar material before condensing into grains. By including a dilution recipe that mixes the surface material of the models with 10–30% of the corresponding solar mass-fraction, our models can reproduce the $^{14}\text{N}/^{15}\text{N}$ ratio, O isotopic ratios, Si isotopic ratios, $\delta^{25}\text{Mg}/^{24}\text{Mg}$, Ca and Ti isotopic ratios measured in the grains. Unfortunately s-process elements, which are produced in abundance in our models, are not measured in the grains and would have otherwise been a vital check for the validity of our RCB models.

Our RCB models do not produce the low $^{12}\text{C}/^{13}\text{C}$ ratios or the high $^{26}\text{Al}/^{27}\text{Al}$ ratios measured in the grains. Since the isotopic ratios of C and Al from our models do not match the observations of RCB stars and the graphite grains, the models require a common method to completely fit the chemical signatures of both these objects. Our rudimentary calculations indicated that the ^{13}C and ^{26}Al can be increased in the surface by including a H-burning shell just above the Shell of Fire. There is scope for our models thus to completely fit the chemical signatures of RCB stars and those graphite grains that have $^{16}\text{O}/^{18}\text{O} < 40$.

Our immediate future work will focus on improving the merger models for the BSG progenitor of Type II-pec SNe, by including the spin-up of the envelope, injection of heating during accretion, frictional luminosity, and mass lost during the common envelope phase. We will repeat our study on the progenitor and its explosion and examine how well our models match SN 1987A.

The progenitor models of this work are currently being used to study the early explosion phase of SN 1987A upto shock-breakout, using 3D hydrodynamic simulations, by the group of Dr. Thomas Janka at the Max Planck Institute, Garching. The main focus of this work is to see whether the binary merger progenitor models can obtain deeper nickel-mixing fingers that are required to explain observations, than what is currently obtained from single star models. The next step will be similar to the work done in Utrobin et al.

(2015), wherein the required 3D quantities are mapped to 1D and the radiation hydrodynamic code CRAB will be used to simulate the entire light curve until the nebular phase. The results from these studies will improve our understanding not only of SN 1987A, but of all core-collapse supernovae.

Bibliography

- Abbott, B. P. et al. (2016). “Binary Black Hole Mergers in the First Advanced LIGO Observing Run”. In: *Physical Review X* 6.4, 041015, p. 041015. DOI: [10.1103/PhysRevX.6.041015](https://doi.org/10.1103/PhysRevX.6.041015). arXiv: [1606.04856 \[gr-qc\]](https://arxiv.org/abs/1606.04856).
- Abt, H. A. (1983). “Normal and abnormal binary frequencies”. In: 21, pp. 343–372. DOI: [10.1146/annurev.aa.21.090183.002015](https://doi.org/10.1146/annurev.aa.21.090183.002015).
- Alcock, C. et al. (2001). “The MACHO Project LMC Variable Star Inventory. X. The R Coronae Borealis Stars”. In: 554, pp. 298–315. DOI: [10.1086/321369](https://doi.org/10.1086/321369). eprint: [astro-ph/0102262](https://arxiv.org/abs/astro-ph/0102262).
- Amari, S. and K. Lodders (2007). “Pre-solar grains from supernovae and novae”. In: *Highlights of Astronomy* 14, pp. 349–352. DOI: [10.1017/S1743921307010952](https://doi.org/10.1017/S1743921307010952).
- Amari, S., E. Zinner, and R. Gallino (2014). “Presolar graphite from the Murchison meteorite: An isotopic study”. In: 133, pp. 479–522. DOI: [10.1016/j.gca.2014.01.006](https://doi.org/10.1016/j.gca.2014.01.006).
- Amari, S., E. Zinner, and R. S. Lewis (1995). “Large 18O Excesses in Circumstellar Graphite Grains from the Murchison Meteorite: Indication of a Massive-Star Origin”. In: 447, p. L147. DOI: [10.1086/309573](https://doi.org/10.1086/309573).
- Amari, S. et al. (1990). “Interstellar graphite in meteorites”. In: 345, pp. 238–240. DOI: [10.1038/345238a0](https://doi.org/10.1038/345238a0).
- Amari, S. et al. (1993). “The isotopic compositions and stellar sources of meteoritic graphite grains”. In: 365, pp. 806–809. DOI: [10.1038/365806a0](https://doi.org/10.1038/365806a0).
- Amari, S. et al. (2017). “Oxygen Isotopic Composition of High-Density Presolar Graphite Grains from Murchison”. In: *Lunar and Planetary Science Conference*. Vol. 48. Lunar and Planetary Science Conference, p. 1947.
- Arendt, R. G. et al. (2014). “Interstellar and Ejecta Dust in the Cas A Supernova Remnant”. In: 786, 55, p. 55. DOI: [10.1088/0004-637X/786/1/55](https://doi.org/10.1088/0004-637X/786/1/55). arXiv: [1403.3008](https://arxiv.org/abs/1403.3008).
- Arnett, D., B. Fryxell, and E. Mueller (1989). “Instabilities and nonradial motion in SN 1987A”. In: 341, pp. L63–L66. DOI: [10.1086/185458](https://doi.org/10.1086/185458).
- Arnett, W. D. et al. (1989). “Supernova 1987A”. In: 27, pp. 629–700.
- Arnould, M., S. Goriely, and A. Jorissen (1999). “Non-explosive hydrogen and helium burnings: abundance predictions from the NACRE reaction rate compilation”. In: 347, pp. 572–582. eprint: [astro-ph/9904407](https://arxiv.org/abs/astro-ph/9904407).
- Asplund, M. et al. (1997). “Line-blanketed model atmospheres for R Coronae Borealis stars and hydrogen-deficient carbon stars.” In: 318, pp. 521–534.

- Asplund, M. et al. (2000). “The R Coronae Borealis stars - atmospheres and abundances”. In: 353, pp. 287–310.
- Asplund, M. et al. (2009). “The Chemical Composition of the Sun”. In: 47, pp. 481–522. DOI: [10.1146/annurev.astro.46.060407.145222](https://doi.org/10.1146/annurev.astro.46.060407.145222). arXiv: [0909.0948](https://arxiv.org/abs/0909.0948) [astro-ph.SR].
- Barkat, Z. and J. C. Wheeler (1989a). “SN 1987A - Was Sanduleak -69 deg 202 mixed up?” In: 342, pp. 940–944. DOI: [10.1086/167650](https://doi.org/10.1086/167650).
- (1989b). “Supernova 1987A - The progenitor corridor”. In: 341, pp. 925–933. DOI: [10.1086/167550](https://doi.org/10.1086/167550).
- Barlow, M. J. et al. (2010). “A Herschel PACS and SPIRE study of the dust content of the Cassiopeia A supernova remnant”. In: 518, L138, p. L138. DOI: [10.1051/0004-6361/201014585](https://doi.org/10.1051/0004-6361/201014585). arXiv: [1005.2688](https://arxiv.org/abs/1005.2688).
- Belczynski, K. et al. (2016). “The first gravitational-wave source from the isolated evolution of two stars in the 40-100 solar mass range”. In: 534, pp. 512–515. DOI: [10.1038/nature18322](https://doi.org/10.1038/nature18322). arXiv: [1602.04531](https://arxiv.org/abs/1602.04531) [astro-ph.HE].
- Bell, K. L. and K. A. Berrington (1987). “Free-free absorption coefficient of the negative hydrogen ion”. In: *Journal of Physics B Atomic Molecular Physics* 20, pp. 801–806. DOI: [10.1088/0022-3700/20/4/019](https://doi.org/10.1088/0022-3700/20/4/019).
- Bennett, P. D. (2010). “Chromospheres and Winds of Red Supergiants: An Empirical Look at Outer Atmospheric Structure”. In: *Hot and Cool: Bridging Gaps in Massive Star Evolution*. Ed. by C. Leitherer et al. Vol. 425. Astronomical Society of the Pacific Conference Series, p. 181. arXiv: [1004.1853](https://arxiv.org/abs/1004.1853) [astro-ph.SR].
- Bergeron, P., A. Gianninas, and S. Boudreault (2007). “The Mass Distribution of White Dwarfs: An Unwavering Obsession”. In: *15th European Workshop on White Dwarfs*. Ed. by R. Napiwotzki and M. R. Burleigh. Vol. 372. Astronomical Society of the Pacific Conference Series, p. 29. eprint: [astro-ph/0611904](https://arxiv.org/abs/astro-ph/0611904).
- Bersten, M. C. and M. Hamuy (2009). “Bolometric Light Curves for 33 Type II Plateau Supernovae”. In: 701, pp. 200–208. DOI: [10.1088/0004-637X/701/1/200](https://doi.org/10.1088/0004-637X/701/1/200). arXiv: [0906.1999](https://arxiv.org/abs/0906.1999) [astro-ph.SR].
- Bianchi, S. and R. Schneider (2007). “Dust formation and survival in supernova ejecta”. In: 378, pp. 973–982. DOI: [10.1111/j.1365-2966.2007.11829.x](https://doi.org/10.1111/j.1365-2966.2007.11829.x). arXiv: [0704.0586](https://arxiv.org/abs/0704.0586).
- Bionta, R. M. et al. (1987). “Observation of a neutrino burst in coincidence with supernova 1987A in the Large Magellanic Cloud”. In: *Physical Review Letters* 58, pp. 1494–1496. DOI: [10.1103/PhysRevLett.58.1494](https://doi.org/10.1103/PhysRevLett.58.1494).
- Blinnikov, S. et al. (2000). “Radiation Hydrodynamics of SN 1987A. I. Global Analysis of the Light Curve for the First 4 Months”. In: 532, pp. 1132–1149. DOI: [10.1086/308588](https://doi.org/10.1086/308588). eprint: [astro-ph/9911205](https://arxiv.org/abs/astro-ph/9911205).

- Bloecker, T. (1995). “Stellar evolution of low and intermediate-mass stars. I. Mass loss on the AGB and its consequences for stellar evolution.” In: 297, p. 727.
- Brandner, W. et al. (1997a). “Ring Nebula and Bipolar Outflows Associated with the B1.5 Supergiant Sher 25 in NGC 3603”. In: 475, pp. L45–L48. DOI: [10.1086/310460](https://doi.org/10.1086/310460). eprint: [astro-ph/9611046](https://arxiv.org/abs/astro-ph/9611046).
- Brandner, W. et al. (1997b). “The Hourglass Nebulae of Sher 25 and SN 1987A: Two of a Kind?” In: 489, p. L153. DOI: [10.1086/316795](https://doi.org/10.1086/316795). eprint: [astro-ph/9709138](https://arxiv.org/abs/astro-ph/9709138).
- Brott, I. et al. (2011). “Rotating massive main-sequence stars. II. Simulating a population of LMC early B-type stars as a test of rotational mixing”. In: 530, A116, A116. DOI: [10.1051/0004-6361/201016114](https://doi.org/10.1051/0004-6361/201016114). arXiv: [1102.0766](https://arxiv.org/abs/1102.0766) [[astro-ph](https://arxiv.org/abs/astro-ph).SR].
- Brown, W. R. et al. (2016). “Most Double Degenerate Low-mass White Dwarf Binaries Merge”. In: 824, 46, p. 46. DOI: [10.3847/0004-637X/824/1/46](https://doi.org/10.3847/0004-637X/824/1/46). arXiv: [1604.04269](https://arxiv.org/abs/1604.04269) [[astro-ph](https://arxiv.org/abs/astro-ph).SR].
- Burrows, A. (2013). “Colloquium: Perspectives on core-collapse supernova theory”. In: *Reviews of Modern Physics* 85, pp. 245–261. DOI: [10.1103/RevModPhys.85.245](https://doi.org/10.1103/RevModPhys.85.245). arXiv: [1210.4921](https://arxiv.org/abs/1210.4921) [[astro-ph](https://arxiv.org/abs/astro-ph).SR].
- Burrows, A. and J. M. Lattimer (1987). “Neutrinos from SN 1987A”. In: 318, pp. L63–L68. DOI: [10.1086/184938](https://doi.org/10.1086/184938).
- Burrows, C. J. et al. (1995). “Hubble Space Telescope Observations of the SN 1987A Triple Ring Nebula”. In: 452, p. 680. DOI: [10.1086/176339](https://doi.org/10.1086/176339).
- Caldwell, J. A. R. et al. (1993). “Spectroscopic and photometric observations of supernova 1987A. VII - Days 793 to 1770”. In: 262, pp. 313–324. DOI: [10.1093/mnras/262.2.313](https://doi.org/10.1093/mnras/262.2.313).
- Caramana, E. J., M. J. Shashkov, and P. P. Whalen (1998). “Formulations of Artificial Viscosity for Multi-dimensional Shock Wave Computations”. In: *Journal of Computational Physics* 144, pp. 70–97. DOI: [10.1006/jcph.1998.5989](https://doi.org/10.1006/jcph.1998.5989).
- Carroll, B. W. and D. A. Ostlie (2006). *An introduction to modern astrophysics and cosmology*.
- Castor, J. I., D. C. Abbott, and R. I. Klein (1975a). “Radiation-driven winds in Of stars”. In: 195, pp. 157–174. DOI: [10.1086/153315](https://doi.org/10.1086/153315).
- (1975b). “Radiation-driven winds in Of stars”. In: 195, pp. 157–174. DOI: [10.1086/153315](https://doi.org/10.1086/153315).
- Catchpole, R. M. et al. (1987). “Spectroscopic and photometric observations of SN 1987a. II - Days 51 to 134”. In: 229, 15P–25P.
- Catchpole, R. M. et al. (1988a). “Spectroscopic and photometric observations of SN 1987A. III - Days 135 to 260”. In: 231, 75p–89p. DOI: [10.1093/mnras/231.1.75P](https://doi.org/10.1093/mnras/231.1.75P).
- (1988b). “Spectroscopic and photometric observations of SN 1987A. III - Days 135 to 260”. In: 231, 75P.
- Chen, Y.-T., M. Yang, and C.-S. Lin (2006). “Supernova 2006V in UGC 6510”. In: *Central Bureau Electronic Telegrams* 390.

- Cherchneff, I. (2013). “Dust production in Supernovae”. In: *Proceedings of The Life Cycle of Dust in the Universe: Observations, Theory, and Laboratory Experiments (LCDU2013). 18-22 November, 2013. Taipei, Taiwan*. Editors: Anja Andersen (University of Copenhagen, Denmark), Maarten Baes (Universiteit Gent, Belgium), Haley Gomez (Cardiff University, UK), Ciska Kemper (Academia Sinica, Taiwan), Darach Watson (University of Copenhagen, Denmark). Online at http://pos.sissa.it/cgi-bin/reader/conf.cgi?confid=207, id.18, p. 18.
- Chevalier, R. A. and V. V. Dwarkadas (1995). “The Presupernova H II Region around SN 1987A”. In: 452, p. L45. DOI: [10.1086/309714](https://doi.org/10.1086/309714).
- Chevalier, R. A. and N. Soker (1989). “Asymmetric envelope expansion of supernova 1987A”. In: 341, pp. 867–882. DOI: [10.1086/167545](https://doi.org/10.1086/167545).
- Chita, S. M. et al. (2008). “Multiple ring nebulae around blue supergiants”. In: 488, pp. L37–L41. DOI: [10.1051/0004-6361:200810087](https://doi.org/10.1051/0004-6361:200810087). arXiv: [0807.3049](https://arxiv.org/abs/0807.3049).
- Chugai, N. N. (1991). “Asymmetry of the Shell of Supernova 1987A”. In: 35, p. 171.
- (1994). “The oxygen mass in SN 1987A: Making use of fluctuations in the (O I) lambda lambda 6300, 6364 profile”. In: 428, pp. L17–L19. DOI: [10.1086/187382](https://doi.org/10.1086/187382).
- Chugai, N. N. et al. (1997). “Hubble Space Telescope Spectrum of SN 1987A at an Age of 8 Years: Radioactive Luminescence of Cool Gas”. In: 483, pp. 925–940. DOI: [10.1086/304253](https://doi.org/10.1086/304253).
- Clayton, G. C. (1996). “The R Coronae Borealis Stars”. In: 108, p. 225. DOI: [10.1086/133715](https://doi.org/10.1086/133715).
- (2012). “What Are the R Coronae Borealis Stars?” In: *Journal of the American Association of Variable Star Observers (JAAVSO)* 40, p. 539. arXiv: [1206.3448](https://arxiv.org/abs/1206.3448) [[astro-ph.SR](https://arxiv.org/abs/1206.3448)].
- Clayton, G. C. et al. (2007). “Very Large Excesses of ^{18}O in Hydrogen-deficient Carbon and R Coronae Borealis Stars: Evidence for White Dwarf Mergers”. In: 662, pp. 1220–1230. DOI: [10.1086/518307](https://doi.org/10.1086/518307). eprint: [astro-ph/0703453](https://arxiv.org/abs/astro-ph/0703453).
- Clayton, G. C. et al. (2011). “The Circumstellar Environment of R Coronae Borealis: White Dwarf Merger or Final-helium-shell Flash?” In: 743, 44, p. 44. DOI: [10.1088/0004-637X/743/1/44](https://doi.org/10.1088/0004-637X/743/1/44). arXiv: [1110.3235](https://arxiv.org/abs/1110.3235) [[astro-ph.SR](https://arxiv.org/abs/1110.3235)].
- Colgan, S. W. J. et al. (1994). “Day 640 infrared line and continuum measurements: Dust formation in SN 1987A”. In: 427, pp. 874–888. DOI: [10.1086/174193](https://doi.org/10.1086/174193).
- Constantino, T. et al. (2014). “On the Necessity of Composition-dependent Low-temperature Opacity in Models of Metal-poor Asymptotic Giant Branch Stars”. In: 784, 56, p. 56. DOI: [10.1088/0004-637X/784/1/56](https://doi.org/10.1088/0004-637X/784/1/56). arXiv: [1401.7752](https://arxiv.org/abs/1401.7752) [[astro-ph.SR](https://arxiv.org/abs/1401.7752)].
- Cottrell, P. L. and D. L. Lambert (1982). “The chemical composition of R Coronae Borealis and XX Camelopardalis”. In: 261, pp. 595–611. DOI: [10.1086/160370](https://doi.org/10.1086/160370).
- Cottrell, P. L. and W. A. Lawson (1998). “Hipparcos Observations of Hydrogen-deficient Carbon Stars *”. In: 15, pp. 179–182. DOI: [10.1071/AS98179](https://doi.org/10.1071/AS98179).

- Crause, L. A., W. A. Lawson, and A. A. Henden (2007). “Pulsation-decline relationships in R Coronae Borealis stars”. In: 375, pp. 301–306. DOI: [10.1111/j.1365-2966.2006.11299.x](https://doi.org/10.1111/j.1365-2966.2006.11299.x).
- Crotts, A. P. S. and S. R. Heathcote (2000). “SN 1987A’s Circumstellar Envelope. II. Kinematics of the Three Rings and the Diffuse Nebula”. In: 528, pp. 426–435. DOI: [10.1086/308141](https://doi.org/10.1086/308141). eprint: [astro-ph/9907367](https://arxiv.org/abs/astro-ph/9907367).
- Crotts, A. P. S. and W. E. Kunkel (1991). “Using SN 1987A light echoes to determine mass loss from the progenitor”. In: 366, pp. L73–L77. DOI: [10.1086/185912](https://doi.org/10.1086/185912).
- Dan, M. et al. (2011). “Prelude to A Double Degenerate Merger: The Onset of Mass Transfer and Its Impact on Gravitational Waves and Surface Detonations”. In: 737, 89, p. 89. DOI: [10.1088/0004-637X/737/2/89](https://doi.org/10.1088/0004-637X/737/2/89). arXiv: [1101.5132 \[astro-ph.HE\]](https://arxiv.org/abs/1101.5132).
- Dan, M. et al. (2014). “The structure and fate of white dwarf merger remnants”. In: 438, pp. 14–34. DOI: [10.1093/mnras/stt1766](https://doi.org/10.1093/mnras/stt1766). arXiv: [1308.1667 \[astro-ph.HE\]](https://arxiv.org/abs/1308.1667).
- de Jager, C., H. Nieuwenhuijzen, and K. A. van der Hucht (1988). “Mass loss rates in the Hertzsprung-Russell diagram”. In: 72, pp. 259–289.
- de Kool, M. (1990). “Common envelope evolution and double cores of planetary nebulae”. In: 358, pp. 189–195. DOI: [10.1086/168974](https://doi.org/10.1086/168974).
- De Marco, O. (2009). “The Origin and Shaping of Planetary Nebulae: Putting the Binary Hypothesis to the Test”. In: 121, p. 316. DOI: [10.1086/597765](https://doi.org/10.1086/597765). arXiv: [0902.1137](https://arxiv.org/abs/0902.1137).
- De Marco, O. and R. G. Izzard (2017). “Dawes Review 6: The Impact of Companions on Stellar Evolution”. In: 34, e001, e001. DOI: [10.1017/pasa.2016.52](https://doi.org/10.1017/pasa.2016.52). arXiv: [1611.03542 \[astro-ph.SR\]](https://arxiv.org/abs/1611.03542).
- De Marco, O. et al. (2011). “On the α formalism for the common envelope interaction”. In: 411, pp. 2277–2292. DOI: [10.1111/j.1365-2966.2010.17891.x](https://doi.org/10.1111/j.1365-2966.2010.17891.x). arXiv: [1010.4374 \[astro-ph.SR\]](https://arxiv.org/abs/1010.4374).
- de Mink, S. E., O. R. Pols, and S.-C. Yoon (2008). “Binaries at Low Metallicity: Ranges For Case A, B and C Mass Transfer”. In: American Institute of Physics Conference Series 990. Ed. by B. W. O’Shea and A. Heger, pp. 230–232. DOI: [10.1063/1.2905549](https://doi.org/10.1063/1.2905549). arXiv: [0710.1010](https://arxiv.org/abs/0710.1010).
- Dessart, L. and D. J. Hillier (2008). “Time-dependent effects in photospheric-phase Type II supernova spectra”. In: 383, pp. 57–74. DOI: [10.1111/j.1365-2966.2007.12538.x](https://doi.org/10.1111/j.1365-2966.2007.12538.x). arXiv: [0710.0784](https://arxiv.org/abs/0710.0784).
- (2010). “Supernova radiative-transfer modelling: a new approach using non-local thermodynamic equilibrium and full time dependence”. In: 405, pp. 2141–2160. DOI: [10.1111/j.1365-2966.2010.16611.x](https://doi.org/10.1111/j.1365-2966.2010.16611.x). arXiv: [1003.2557 \[astro-ph.SR\]](https://arxiv.org/abs/1003.2557).
- (2011). “Non-LTE time-dependent spectroscopic modelling of Type II-plateau supernovae from the photospheric to the nebular phase: case study for 15 and 25 M progenitor stars”. In: 410, pp. 1739–1760. DOI: [10.1111/j.1365-2966.2010.17557.x](https://doi.org/10.1111/j.1365-2966.2010.17557.x). arXiv: [1008.3238 \[astro-ph.SR\]](https://arxiv.org/abs/1008.3238).

- Dessart, L., E. Livne, and R. Waldman (2010). “Determining the main-sequence mass of Type II supernova progenitors”. In: 408, pp. 827–840. DOI: [10.1111/j.1365-2966.2010.17190.x](https://doi.org/10.1111/j.1365-2966.2010.17190.x). arXiv: [1006.2268](https://arxiv.org/abs/1006.2268) [astro-ph.SR].
- Dessart, L. et al. (2013). “Type II-Plateau supernova radiation: dependences on progenitor and explosion properties”. In: 433, pp. 1745–1763. DOI: [10.1093/mnras/stt861](https://doi.org/10.1093/mnras/stt861). arXiv: [1305.3386](https://arxiv.org/abs/1305.3386) [astro-ph.SR].
- Doherty, C. L. et al. (2015). “Super- and massive AGB stars - IV. Final fates - initial-to-final mass relation”. In: 446, pp. 2599–2612. DOI: [10.1093/mnras/stu2180](https://doi.org/10.1093/mnras/stu2180). arXiv: [1410.5431](https://arxiv.org/abs/1410.5431) [astro-ph.SR].
- Doherty, C. L. et al. (2017). “Super-AGB Stars and their role as Electron Capture Supernova progenitors”. In: *ArXiv e-prints*. arXiv: [1703.06895](https://arxiv.org/abs/1703.06895) [astro-ph.SR].
- Driebe, T. et al. (1998). “The evolution of helium white dwarfs. I. The companion of the millisecond pulsar PSR J1012+5307”. In: 339, pp. 123–133. eprint: [astro-ph/9809079](https://arxiv.org/abs/astro-ph/9809079).
- Duchêne, G. and A. Kraus (2013). “Stellar Multiplicity”. In: 51, pp. 269–310. DOI: [10.1146/annurev-astro-081710-102602](https://doi.org/10.1146/annurev-astro-081710-102602). arXiv: [1303.3028](https://arxiv.org/abs/1303.3028) [astro-ph.SR].
- Dwek, E. and R. G. Arendt (2015). “The Evolution of Dust Mass in the Ejecta of SN1987A”. In: 810, 75, p. 75. DOI: [10.1088/0004-637X/810/1/75](https://doi.org/10.1088/0004-637X/810/1/75). arXiv: [1507.07019](https://arxiv.org/abs/1507.07019) [astro-ph.SR].
- Eggenberger, P., G. Meynet, and A. Maeder (2002). “The blue to red supergiant ratio in young clusters at various metallicities”. In: 386, pp. 576–582. DOI: [10.1051/0004-6361:20020262](https://doi.org/10.1051/0004-6361:20020262). eprint: [astro-ph/0202478](https://arxiv.org/abs/astro-ph/0202478).
- Eggleton, P. (2011). *Evolutionary Processes in Binary and Multiple Stars*.
- Eggleton, P. P. (1983). “Approximations to the radii of Roche lobes”. In: 268, p. 368. DOI: [10.1086/160960](https://doi.org/10.1086/160960).
- Eggleton, P. P. and C. A. Tout (1989). “The evolution of moderately close and moderately wide binaries”. In: 50, pp. 165–177. DOI: [10.1007/BF00215928](https://doi.org/10.1007/BF00215928).
- Ellinger, C. I. et al. (2012). “A Case Study of Small-scale Structure Formation in Three-dimensional Supernova Simulations”. In: 755, 160, p. 160. DOI: [10.1088/0004-637X/755/2/160](https://doi.org/10.1088/0004-637X/755/2/160). arXiv: [1206.1834](https://arxiv.org/abs/1206.1834) [astro-ph.SR].
- Erickson, E. F. et al. (1988). “Observation of Fe II (26.0 microns) in SN 1987A”. In: 330, pp. L39–L41. DOI: [10.1086/185200](https://doi.org/10.1086/185200).
- Falk, S. W. and W. D. Arnett (1977). “Radiation Dynamics, Envelope Ejection, and Supernova Light Curves”. In: 33, p. 515. DOI: [10.1086/190440](https://doi.org/10.1086/190440).
- Feast, M. W. (1979). “Recent Work on the R-Coronae Stars”. In: *IAU Colloq. 46: Changing Trends in Variable Star Research*. Ed. by F. M. Bateson, J. Smak, and I. H. Urch. Vol. 46, p. 246.
- (1986). “The RCB stars and their circumstellar material”. In: *IAU Colloq. 87: Hydrogen Deficient Stars and Related Objects*. Ed. by K. Hunger, D. Schoenberner, and N. Kameswara

- Rao. Vol. 128. Astrophysics and Space Science Library, pp. 151–161. DOI: [10.1007/978-94-009-4744-3_15](https://doi.org/10.1007/978-94-009-4744-3_15).
- (1997). “The R Coronae Borealis stars - II. Further inferences from the infrared data”. In: 285, pp. 339–357. DOI: [10.1093/mnras/285.2.339](https://doi.org/10.1093/mnras/285.2.339).
- Feast, M. W. et al. (1997). “The R Coronae Borealis stars - I. Infrared photometry and long-term variations”. In: 285, pp. 317–338. DOI: [10.1093/mnras/285.2.317](https://doi.org/10.1093/mnras/285.2.317).
- Ferguson, J. W. et al. (2005). “Low-Temperature Opacities”. In: 623, pp. 585–596. DOI: [10.1086/428642](https://doi.org/10.1086/428642). eprint: [astro-ph/0502045](https://arxiv.org/abs/astro-ph/0502045).
- Fischer, D. A. and G. W. Marcy (1992). “Multiplicity among M dwarfs”. In: 396, pp. 178–194. DOI: [10.1086/171708](https://doi.org/10.1086/171708).
- France, K. et al. (2011). “HST-COS Observations of Hydrogen, Helium, Carbon, and Nitrogen Emission from the SN 1987A Reverse Shock”. In: 743, 186, p. 186. DOI: [10.1088/0004-637X/743/2/186](https://doi.org/10.1088/0004-637X/743/2/186). arXiv: [1111.1735](https://arxiv.org/abs/1111.1735) [[astro-ph](https://arxiv.org/abs/astro-ph).SR].
- Fransson, C. (1988). “The circumstellar emission from SN 1987A”. In: *Proceedings of the Astronomical Society of Australia* 7, pp. 520–526.
- Fransson, C. et al. (1989). “Narrow ultraviolet emission lines from SN 1987A - Evidence for CNO processing in the progenitor”. In: 336, pp. 429–441. DOI: [10.1086/167022](https://doi.org/10.1086/167022).
- Friend, D. B. and D. C. Abbott (1986). “The theory of radiatively driven stellar winds. III - Wind models with finite disk correction and rotation”. In: 311, pp. 701–707. DOI: [10.1086/164809](https://doi.org/10.1086/164809).
- Fryxell, B., D. Arnett, and E. Mueller (1991). “Instabilities and clumping in SN 1987A. I - Early evolution in two dimensions”. In: 367, pp. 619–634. DOI: [10.1086/169657](https://doi.org/10.1086/169657).
- García-Hernández, D. A., N. K. Rao, and D. L. Lambert (2011). “Dust around R Coronae Borealis Stars. I. Spitzer/Infrared Spectrograph Observations”. In: 739, 37, p. 37. DOI: [10.1088/0004-637X/739/1/37](https://doi.org/10.1088/0004-637X/739/1/37). arXiv: [1107.1185](https://arxiv.org/abs/1107.1185) [[astro-ph](https://arxiv.org/abs/astro-ph).SR].
- García-Hernández, D. A. et al. (2010). “Oxygen Isotopic Ratios in Cool R Coronae Borealis Stars”. In: 714, pp. 144–154. DOI: [10.1088/0004-637X/714/1/144](https://doi.org/10.1088/0004-637X/714/1/144). arXiv: [1003.2901](https://arxiv.org/abs/1003.2901) [[astro-ph](https://arxiv.org/abs/astro-ph).SR].
- Gavrila, M. (1967). “Elastic Scattering of Photons by a Hydrogen Atom”. In: *Physical Review* 163, pp. 147–155. DOI: [10.1103/PhysRev.163.147](https://doi.org/10.1103/PhysRev.163.147).
- Gear, C. W. (1971). *Numerical initial value problems in ordinary differential equations*.
- Gilmozzi, R. et al. (1987). “The progenitor of SN1987A”. In: 328, pp. 318–320. DOI: [10.1038/328318a0](https://doi.org/10.1038/328318a0).
- Gomez, H. L. et al. (2012). “A Cool Dust Factory in the Crab Nebula: A Herschel Study of the Filaments”. In: 760, 96, p. 96. DOI: [10.1088/0004-637X/760/1/96](https://doi.org/10.1088/0004-637X/760/1/96). arXiv: [1209.5677](https://arxiv.org/abs/1209.5677).
- Gvaramadze, V. V. et al. (2015). “The blue supergiant MN18 and its bipolar circumstellar nebula”. In: 454, pp. 219–237. DOI: [10.1093/mnras/stv1995](https://doi.org/10.1093/mnras/stv1995). arXiv: [1508.06288](https://arxiv.org/abs/1508.06288) [[astro-ph](https://arxiv.org/abs/astro-ph).SR].

- Hairer, E., S. P. Norsett, and G. Wanner (1993). *Solving Ordinary Differential Equations I, Nonstiff Problems*. Second Revised. Springer-Verlag Berlin Heidelberg.
- Hairer, E. and G. Wanner (1996). *Solving Ordinary Differential Equations II, Stiff and Differential-Algebraic Problems*. Second Revised. Springer-Verlag Berlin Heidelberg.
- Hamann, W.-R., G. Gräfener, and A. Liermann (2006). “The Galactic WN stars. Spectral analyses with line-blanketed model atmospheres versus stellar evolution models with and without rotation”. In: 457, pp. 1015–1031. DOI: [10.1051/0004-6361:20065052](https://doi.org/10.1051/0004-6361:20065052). eprint: [astro-ph/0608078](https://arxiv.org/abs/astro-ph/0608078).
- Hamann, W.-R., L. Koesterke, and U. Wessolowski (1995). “Spectral analyses of the Galactic Wolf-Rayet stars: hydrogen-helium abundances and improved stellar parameters for the WN class”. In: 299, p. 151.
- Hammer, N. J., H.-T. Janka, and E. Müller (2010). “Three-dimensional Simulations of Mixing Instabilities in Supernova Explosions”. In: 714, pp. 1371–1385. DOI: [10.1088/0004-637X/714/2/1371](https://doi.org/10.1088/0004-637X/714/2/1371). arXiv: [0908.3474](https://arxiv.org/abs/0908.3474) [[astro-ph.SR](https://arxiv.org/abs/astro-ph.SR)].
- Hamuy, M. (2003). “Observed and Physical Properties of Core-Collapse Supernovae”. In: 582, pp. 905–914. DOI: [10.1086/344689](https://doi.org/10.1086/344689). eprint: [astro-ph/0209174](https://arxiv.org/abs/astro-ph/0209174).
- (2004). “Review on the Observed and Physical Properties of core Collapse Supernovae”. In: *Astrophysics and Space Science Library*. Ed. by C. L. Fryer. Vol. 302. Astrophysics and Space Science Library, pp. 39–64. DOI: [10.1007/978-0-306-48599-2_2](https://doi.org/10.1007/978-0-306-48599-2_2).
- Hamuy, M. et al. (1988a). “SN 1987A in the LMC - UBVRI photometry at Cerro Tololo”. In: 95, pp. 63–83. DOI: [10.1086/114613](https://doi.org/10.1086/114613).
- (1988b). “SN 1987A in the LMC - UBVRI photometry at Cerro Tololo”. In: 95, pp. 63–83. DOI: [10.1086/114613](https://doi.org/10.1086/114613).
- Han, Z. (1998). “The formation of double degenerates and related objects”. In: 296, pp. 1019–1040. DOI: [10.1046/j.1365-8711.1998.01475.x](https://doi.org/10.1046/j.1365-8711.1998.01475.x).
- Han, Z. et al. (2002). “The origin of subdwarf B stars - I. The formation channels”. In: 336, pp. 449–466. DOI: [10.1046/j.1365-8711.2002.05752.x](https://doi.org/10.1046/j.1365-8711.2002.05752.x). eprint: [astro-ph/0206130](https://arxiv.org/abs/astro-ph/0206130).
- Hanuschik, R. W. and J. Dachs (1987). “The H-alpha velocity structure during the first month of SN 1987a in the LMC”. In: 182, p. L29.
- Heger, A. and N. Langer (1998). “The spin-up of contracting red supergiants”. In: 334, pp. 210–220. eprint: [astro-ph/9803005](https://arxiv.org/abs/astro-ph/9803005).
- (2000). “Presupernova Evolution of Rotating Massive Stars. II. Evolution of the Surface Properties”. In: 544, pp. 1016–1035. DOI: [10.1086/317239](https://doi.org/10.1086/317239). eprint: [astro-ph/0005110](https://arxiv.org/abs/astro-ph/0005110).
- Heger, A., N. Langer, and S. E. Woosley (2000). “Presupernova Evolution of Rotating Massive Stars. I. Numerical Method and Evolution of the Internal Stellar Structure”. In: 528, pp. 368–396. DOI: [10.1086/308158](https://doi.org/10.1086/308158). eprint: [astro-ph/9904132](https://arxiv.org/abs/astro-ph/9904132).

- Heger, A., S. E. Woosley, and H. C. Spruit (2005). “Presupernova Evolution of Differentially Rotating Massive Stars Including Magnetic Fields”. In: 626, pp. 350–363. DOI: [10.1086/429868](https://doi.org/10.1086/429868). eprint: [astro-ph/0409422](https://arxiv.org/abs/astro-ph/0409422).
- Heger, A. et al. (2002). “Massive star evolution: nucleosynthesis and nuclear reaction rate uncertainties”. In: 46, pp. 463–468. DOI: [10.1016/S1387-6473\(02\)00184-7](https://doi.org/10.1016/S1387-6473(02)00184-7). eprint: [astro-ph/0110015](https://arxiv.org/abs/astro-ph/0110015).
- Heger, A. et al. (2003). “How Massive Single Stars End Their Life”. In: 591, pp. 288–300. DOI: [10.1086/375341](https://doi.org/10.1086/375341). eprint: [astro-ph/0212469](https://arxiv.org/abs/astro-ph/0212469).
- Hema, B. P., G. Pandey, and D. L. Lambert (2012). “The Galactic R Coronae Borealis Stars: The C₂ Swan Bands, the Carbon Problem, and the ¹²C/¹³C Ratio”. In: 747, 102, p. 102. DOI: [10.1088/0004-637X/747/2/102](https://doi.org/10.1088/0004-637X/747/2/102). arXiv: [1201.1357](https://arxiv.org/abs/1201.1357) [[astro-ph](https://arxiv.org/abs/astro-ph).SR].
- Hendry, M. A. et al. (2008). “The blue supergiant Sher 25 and its intriguing hourglass nebula”. In: 388, pp. 1127–1142. DOI: [10.1111/j.1365-2966.2008.13347.x](https://doi.org/10.1111/j.1365-2966.2008.13347.x). arXiv: [0803.4262](https://arxiv.org/abs/0803.4262).
- Herant, M. and W. Benz (1991). “Hydrodynamical instabilities and mixing in SN 1987A - Two-dimensional simulations of the first 3 months”. In: 370, pp. L81–L84. DOI: [10.1086/185982](https://doi.org/10.1086/185982).
- Herant, M., W. Benz, and S. Colgate (1992). “Postcollapse hydrodynamics of SN 1987A - Two-dimensional simulations of the early evolution”. In: 395, pp. 642–653. DOI: [10.1086/171685](https://doi.org/10.1086/171685).
- Herwig, F. (2005). “Evolution of Asymptotic Giant Branch Stars”. In: 43, pp. 435–479. DOI: [10.1146/annurev.astro.43.072103.150600](https://doi.org/10.1146/annurev.astro.43.072103.150600).
- Herwig, F. et al. (2008). “Nucleosynthesis simulations for a wide range of nuclear production sites from NuGrid”. In: *Nuclei in the Cosmos (NIC X)*. arXiv: [0811.4653](https://arxiv.org/abs/0811.4653).
- Herwig, F. et al. (2011). “Convective-reactive Proton-¹²C Combustion in Sakurai’s Object (V4334 Sagittarii) and Implications for the Evolution and Yields from the First Generations of Stars”. In: 727, 89, p. 89. DOI: [10.1088/0004-637X/727/2/89](https://doi.org/10.1088/0004-637X/727/2/89). arXiv: [1002.2241](https://arxiv.org/abs/1002.2241) [[astro-ph](https://arxiv.org/abs/astro-ph).SR].
- Hillebrandt, W. and F. Meyer (1989). “A common envelope model for SN 1987A”. In: 219, pp. L3–L6.
- Hirata, K. et al. (1987). “Observation of a neutrino burst from the supernova SN1987A”. In: *Physical Review Letters* 58, pp. 1490–1493. DOI: [10.1103/PhysRevLett.58.1490](https://doi.org/10.1103/PhysRevLett.58.1490).
- Hirschi, R., G. Meynet, and A. Maeder (2004). “Stellar evolution with rotation. XII. Pre-supernova models”. In: 425, pp. 649–670. DOI: [10.1051/0004-6361:20041095](https://doi.org/10.1051/0004-6361:20041095). eprint: [astro-ph/0406552](https://arxiv.org/abs/astro-ph/0406552).
- Hungerford, A. L., C. L. Fryer, and M. S. Warren (2003). “Gamma-Ray Lines from Asymmetric Supernovae”. In: 594, pp. 390–403. DOI: [10.1086/376776](https://doi.org/10.1086/376776). eprint: [astro-ph/0301120](https://arxiv.org/abs/astro-ph/0301120).

- Hunter, I. et al. (2008a). “The VLT-FLAMES survey of massive stars: atmospheric parameters and rotational velocity distributions for B-type stars in the Magellanic Clouds”. In: 479, pp. 541–555. DOI: [10.1051/0004-6361:20078511](https://doi.org/10.1051/0004-6361:20078511). arXiv: [0711.2264](https://arxiv.org/abs/0711.2264).
- Hunter, I. et al. (2008b). “The VLT FLAMES Survey of Massive Stars: Rotation and Nitrogen Enrichment as the Key to Understanding Massive Star Evolution”. In: 676, L29, p. L29. DOI: [10.1086/587436](https://doi.org/10.1086/587436). arXiv: [0711.2267](https://arxiv.org/abs/0711.2267).
- Hunter, J. D. (2007). “Matplotlib: A 2D graphics environment”. In: *Computing In Science & Engineering* 9.3, pp. 90–95. DOI: [10.1109/MCSE.2007.55](https://doi.org/10.1109/MCSE.2007.55).
- Hynes, K. M. and F. Gyngard (2009). “The Presolar Grain Database: <http://presolar.wustl.edu/~pgd>”. In: *Lunar and Planetary Science Conference*. Vol. 40. Lunar and Planetary Inst. Technical Report, p. 1198.
- Iben Jr., I. and M. Livio (1993). “Common envelopes in binary star evolution”. In: 105, pp. 1373–1406. DOI: [10.1086/133321](https://doi.org/10.1086/133321).
- Iben Jr., I. and A. V. Tutukov (1984). “The evolution of low-mass close binaries influenced by the radiation of gravitational waves and by a magnetic stellar wind”. In: 284, pp. 719–744. DOI: [10.1086/162455](https://doi.org/10.1086/162455).
- (1987). “Evolutionary scenarios for intermediate-mass stars in close binaries”. In: 313, pp. 727–742. DOI: [10.1086/165011](https://doi.org/10.1086/165011).
- Iben Jr., I., A. V. Tutukov, and L. R. Yungelson (1996). “On the Origin of Hydrogen-deficient Supergiants and Their Relation to R Coronae Borealis Stars and Non-DA White Dwarfs”. In: 456, p. 750. DOI: [10.1086/176694](https://doi.org/10.1086/176694).
- Iglesias, C. A. and F. J. Rogers (1996). “Updated Opal Opacities”. In: 464, p. 943. DOI: [10.1086/177381](https://doi.org/10.1086/177381).
- Iliadis, C. (2007). *Nuclear Physics of Stars*. Wiley-VCH Verlag. DOI: [10.1002/9783527692668](https://doi.org/10.1002/9783527692668).
- Irwin, A. W. (1981). “Polynomial partition function approximations of 344 atomic and molecular species”. In: 45, pp. 621–633. DOI: [10.1086/190730](https://doi.org/10.1086/190730).
- Ivanova, N. (2002). “Slow mergers of massive stars”. PhD thesis. University of Oxford.
- Ivanova, N. and P. Podsiadlowski (2002a). “Massive Star Mergers: Induced Mixing and Nucleosynthesis”. In: 281, pp. 191–194. DOI: [10.1023/A:1019553109023](https://doi.org/10.1023/A:1019553109023). eprint: [astro-ph/0112039](https://arxiv.org/abs/astro-ph/0112039).
- (2002b). “The Slow Merger of Massive Stars: Merger Types and Post-Merger Evolution”. In: *Exotic Stars as Challenges to Evolution*. Ed. by C. A. Tout and W. van Hamme. Vol. 279. Astronomical Society of the Pacific Conference Series, p. 245.
- (2003). “The Slow Merger of Massive Stars”. In: *From Twilight to Highlight: The Physics of Supernovae*. Ed. by W. Hillebrandt and B. Leibundgut, p. 19. DOI: [10.1007/10828549_3](https://doi.org/10.1007/10828549_3). eprint: [astro-ph/0210368](https://arxiv.org/abs/astro-ph/0210368).
- Ivanova, N., P. Podsiadlowski, and H. Spruit (2002). “Hydrodynamical simulations of the stream-core interaction in the slow merger of massive stars”. In: 334, pp. 819–832. DOI: [10.1046/j.1365-8711.2002.05543.x](https://doi.org/10.1046/j.1365-8711.2002.05543.x). eprint: [astro-ph/0109524](https://arxiv.org/abs/astro-ph/0109524).

- Ivanova, N. et al. (2013). “Common envelope evolution: where we stand and how we can move forward”. In: *The Astronomy and Astrophysics Review* 21.1, p. 59. ISSN: 1432-0754. DOI: [10.1007/s00159-013-0059-2](https://doi.org/10.1007/s00159-013-0059-2). URL: <https://doi.org/10.1007/s00159-013-0059-2>.
- Izzard, R. G. et al. (2012). “Common envelope evolution”. In: *IAU Symposium*. Vol. 283. IAU Symposium, pp. 95–102. DOI: [10.1017/S1743921312010769](https://doi.org/10.1017/S1743921312010769).
- Janev, R. K., W. D. Langer, and K. Evans (1987). *Elementary processes in Hydrogen-Helium plasmas - Cross sections and reaction rate coefficients*.
- Janka, H.-T. (2012). “Explosion Mechanisms of Core-Collapse Supernovae”. In: *Annual Review of Nuclear and Particle Science* 62, pp. 407–451. DOI: [10.1146/annurev-nucl-102711-094901](https://doi.org/10.1146/annurev-nucl-102711-094901). arXiv: [1206.2503](https://arxiv.org/abs/1206.2503) [astro-ph.SR].
- Janka, H.-T. et al. (2007). “Theory of core-collapse supernovae”. In: 442, pp. 38–74. DOI: [10.1016/j.physrep.2007.02.002](https://doi.org/10.1016/j.physrep.2007.02.002). eprint: [astro-ph/0612072](https://arxiv.org/abs/astro-ph/0612072).
- Jeffery, C. S. (1996). “Surface properties of extreme helium stars”. In: *Hydrogen Deficient Stars*. Ed. by C. S. Jeffery and U. Heber. Vol. 96. Astronomical Society of the Pacific Conference Series, p. 152.
- Jeffery, C. S., A. I. Karakas, and H. Saio (2011). “Double white dwarf mergers and elemental surface abundances in extreme helium and R Coronae Borealis stars”. In: 414, pp. 3599–3616. DOI: [10.1111/j.1365-2966.2011.18667.x](https://doi.org/10.1111/j.1365-2966.2011.18667.x). arXiv: [1103.1556](https://arxiv.org/abs/1103.1556) [astro-ph.SR].
- Karakas, A. I. and J. C. Lattanzio (2014). “The Dawes Review 2: Nucleosynthesis and Stellar Yields of Low- and Intermediate-Mass Single Stars”. In: 31, e030, e030. DOI: [10.1017/pasa.2014.21](https://doi.org/10.1017/pasa.2014.21). arXiv: [1405.0062](https://arxiv.org/abs/1405.0062) [astro-ph.SR].
- Karakas, A. I. and M. Lugaro (2016). “Stellar Yields from Metal-rich Asymptotic Giant Branch Models”. In: 825, 26, p. 26. DOI: [10.3847/0004-637X/825/1/26](https://doi.org/10.3847/0004-637X/825/1/26). arXiv: [1604.02178](https://arxiv.org/abs/1604.02178) [astro-ph.SR].
- Karakas, A. I., A. J. Ruitter, and M. Hampel (2015). “R Coronae Borealis Stars Are Viable Factories of Pre-solar Grains”. In: 809, 184, p. 184. DOI: [10.1088/0004-637X/809/2/184](https://doi.org/10.1088/0004-637X/809/2/184). arXiv: [1507.06367](https://arxiv.org/abs/1507.06367) [astro-ph.SR].
- Kasen, D. and S. E. Woosley (2009). “Type II Supernovae: Model Light Curves and Standard Candle Relationships”. In: 703, pp. 2205–2216. DOI: [10.1088/0004-637X/703/2/2205](https://doi.org/10.1088/0004-637X/703/2/2205). arXiv: [0910.1590](https://arxiv.org/abs/0910.1590).
- Kifonidis, K. et al. (2003). “Non-spherical core collapse supernovae. I. Neutrino-driven convection, Rayleigh-Taylor instabilities, and the formation and propagation of metal clumps”. In: 408, pp. 621–649. DOI: [10.1051/0004-6361:20030863](https://doi.org/10.1051/0004-6361:20030863). eprint: [astro-ph/0302239](https://arxiv.org/abs/astro-ph/0302239).
- Kifonidis, K. et al. (2006). “Non-spherical core collapse supernovae. II. The late-time evolution of globally anisotropic neutrino-driven explosions and their implications for SN 1987A”. In: 453, pp. 661–678. DOI: [10.1051/0004-6361:20054512](https://doi.org/10.1051/0004-6361:20054512). eprint: [astro-ph/0511369](https://arxiv.org/abs/astro-ph/0511369).

- Kiminki, D. C. and H. A. Kobulnicky (2012). “An Updated Look at Binary Characteristics of Massive Stars in the Cygnus OB2 Association”. In: 751, 4, p. 4. DOI: [10.1088/0004-637X/751/1/4](https://doi.org/10.1088/0004-637X/751/1/4). arXiv: [1203.2156](https://arxiv.org/abs/1203.2156) [astro-ph.SR].
- Kippenhahn, R., A. Weigert, and A. Weiss (2012). *Stellar Structure and Evolution*. DOI: [10.1007/978-3-642-30304-3](https://doi.org/10.1007/978-3-642-30304-3).
- Kleiser, I. K. W. et al. (2011). “Peculiar Type II supernovae from blue supergiants”. In: 415, pp. 372–382. DOI: [10.1111/j.1365-2966.2011.18708.x](https://doi.org/10.1111/j.1365-2966.2011.18708.x). arXiv: [1101.1298](https://arxiv.org/abs/1101.1298) [astro-ph.CO].
- Kobayashi, C., A. I. Karakas, and H. Umeda (2011). “The evolution of isotope ratios in the Milky Way Galaxy”. In: 414, pp. 3231–3250. DOI: [10.1111/j.1365-2966.2011.18621.x](https://doi.org/10.1111/j.1365-2966.2011.18621.x). arXiv: [1102.5312](https://arxiv.org/abs/1102.5312).
- Kobulnicky, H. A. et al. (2014). “Toward Complete Statistics of Massive Binary Stars: Penultimate Results from the Cygnus OB2 Radial Velocity Survey”. In: 213, 34, p. 34. DOI: [10.1088/0067-0049/213/2/34](https://doi.org/10.1088/0067-0049/213/2/34). arXiv: [1406.6655](https://arxiv.org/abs/1406.6655) [astro-ph.SR].
- Kozasa, T., H. Hasegawa, and K. Nomoto (1989). “Formation of dust grains in the ejecta of SN 1987A”. In: 344, pp. 325–331. DOI: [10.1086/167801](https://doi.org/10.1086/167801).
- Kozma, C. and C. Fransson (1992). “Gamma-ray deposition and nonthermal excitation in supernovae”. In: 390, pp. 602–621. DOI: [10.1086/171311](https://doi.org/10.1086/171311).
- (1998). “Late Spectral Evolution of SN 1987A. II. Line Emission”. In: 497, pp. 431–457. DOI: [10.1086/305452](https://doi.org/10.1086/305452). eprint: [astro-ph/9712224](https://arxiv.org/abs/astro-ph/9712224).
- Kudritzki, R.-P. and J. Puls (2000). “Winds from Hot Stars”. In: 38, pp. 613–666. DOI: [10.1146/annurev.astro.38.1.613](https://doi.org/10.1146/annurev.astro.38.1.613).
- Kurucz, R. L. (2002). “Atomic and Molecular Data Needs for Astrophysics”. In: *Atomic and Molecular Data and Their Applications*. Ed. by D. R. Schultz, P. S. Krstic, and F. Ownby. Vol. 636. American Institute of Physics Conference Series, pp. 134–143. DOI: [10.1063/1.1516330](https://doi.org/10.1063/1.1516330).
- Lada, C. J. (2006). “Stellar Multiplicity and the Initial Mass Function: Most Stars Are Single”. In: 640, pp. L63–L66. DOI: [10.1086/503158](https://doi.org/10.1086/503158). eprint: [astro-ph/0601375](https://arxiv.org/abs/astro-ph/0601375).
- Lambert, D. L. and N. K. Rao (1994). “The R Coronae Borealis stars - A few mere facts”. In: *Journal of Astrophysics and Astronomy* 15, pp. 47–67. DOI: [10.1007/BF03010404](https://doi.org/10.1007/BF03010404).
- Langer, N. (1991). “Evolution of massive stars in the Large Magellanic Cloud - Models with semiconvection”. In: 252, pp. 669–688.
- (2012). “Presupernova Evolution of Massive Single and Binary Stars”. In: 50, pp. 107–164. DOI: [10.1146/annurev-astro-081811-125534](https://doi.org/10.1146/annurev-astro-081811-125534). arXiv: [1206.5443](https://arxiv.org/abs/1206.5443) [astro-ph.SR].
- Larsson, J. et al. (2011). “X-ray illumination of the ejecta of supernova 1987A”. In: 474, pp. 484–486. DOI: [10.1038/nature10090](https://doi.org/10.1038/nature10090). arXiv: [1106.2300](https://arxiv.org/abs/1106.2300) [astro-ph.SR].

- Larsson, J. et al. (2013). “The Morphology of the Ejecta in Supernova 1987A: A Study over Time and Wavelength”. In: 768, 89, p. 89. DOI: [10.1088/0004-637X/768/1/89](https://doi.org/10.1088/0004-637X/768/1/89). arXiv: [1212.5051](https://arxiv.org/abs/1212.5051) [[astro-ph.SR](#)].
- Larsson, J. et al. (2016). “Three-dimensional Distribution of Ejecta in Supernova 1987A at 10,000 Days”. In: 833, 147, p. 147. DOI: [10.3847/1538-4357/833/2/147](https://doi.org/10.3847/1538-4357/833/2/147). arXiv: [1609.04413](https://arxiv.org/abs/1609.04413) [[astro-ph.HE](#)].
- Lawson, W. A. et al. (1990). “The Photometric Characteristics of Cool Hydrogen Deficient Carbon Stars”. In: 247, p. 91.
- Lodders, K. and S. Amari (2005). “Presolar grains from meteorites: Remnants from the early times of the solar system”. In: *Chemie der Erde / Geochemistry* 65, pp. 93–166. DOI: [10.1016/j.chemer.2005.01.001](https://doi.org/10.1016/j.chemer.2005.01.001). eprint: [astro-ph/0501430](https://arxiv.org/abs/astro-ph/0501430).
- Longland, R. et al. (2011). “Nucleosynthesis during the Merger of White Dwarfs and the Origin of R Coronae Borealis Stars”. In: 737, L34, p. L34. DOI: [10.1088/2041-8205/737/2/L34](https://doi.org/10.1088/2041-8205/737/2/L34). arXiv: [1107.2233](https://arxiv.org/abs/1107.2233) [[astro-ph.SR](#)].
- Lorén-Aguilar, P., J. Isern, and E. García-Berro (2009). “High-resolution smoothed particle hydrodynamics simulations of the merger of binary white dwarfs”. In: 500, pp. 1193–1205. DOI: [10.1051/0004-6361/200811060](https://doi.org/10.1051/0004-6361/200811060).
- Loreta, E. (1935). “Nota sulle stelle variabili R Coronidi”. In: *Astronomische Nachrichten* 254, p. 151.
- Lucy, L. B. and P. M. Solomon (1970). “Mass Loss by Hot Stars”. In: 159, p. 879. DOI: [10.1086/150365](https://doi.org/10.1086/150365).
- Lugaro, M. (2005). *Stardust from meteorites. An introduction to presolar grains*.
- Lundqvist, P. and C. Fransson (1996). “The Line Emission from the Circumstellar Gas around SN 1987A”. In: 464, p. 924. DOI: [10.1086/177380](https://doi.org/10.1086/177380). eprint: [astro-ph/9512025](https://arxiv.org/abs/astro-ph/9512025).
- Lusk, J. A. and E. Baron (2017). “Bolometric Light Curves of Peculiar Type II-P Supernovae”. In: 129.4, p. 044202. DOI: [10.1088/1538-3873/aa5e49](https://doi.org/10.1088/1538-3873/aa5e49). arXiv: [1608.08631](https://arxiv.org/abs/1608.08631) [[astro-ph.SR](#)].
- Maeder, A. (1987). “Pre-supernova evolution of SN 1987A”. In: *European Southern Observatory Conference and Workshop Proceedings*. Ed. by I. J. Danziger. Vol. 26. European Southern Observatory Conference and Workshop Proceedings, pp. 251–269.
- (1999). “Stellar evolution with rotation IV: von Zeipel’s theorem and anisotropic losses of mass and angular momentum”. In: 347, pp. 185–193.
- Maeder, A. and G. Meynet (2000). “The Evolution of Rotating Stars”. In: 38, pp. 143–190. DOI: [10.1146/annurev.astro.38.1.143](https://doi.org/10.1146/annurev.astro.38.1.143). eprint: [astro-ph/0004204](https://arxiv.org/abs/astro-ph/0004204).
- Maran, S. P. et al. (2000). “Physical Conditions in Circumstellar Gas Surrounding SN 1987A 12 Years after Outburst”. In: 545, pp. 390–398. DOI: [10.1086/317809](https://doi.org/10.1086/317809). eprint: [astro-ph/0009403](https://arxiv.org/abs/astro-ph/0009403).

- Marigo, P. and B. Aringer (2009). “Low-temperature gas opacity. *ÆSOPUS*: a versatile and quick computational tool”. In: 508, pp. 1539–1569. DOI: [10.1051/0004-6361/200912598](https://doi.org/10.1051/0004-6361/200912598). arXiv: [0907.3248](https://arxiv.org/abs/0907.3248) [[astro-ph.SR](#)].
- Marks, M. et al. (2012). “Evidence for top-heavy stellar initial mass functions with increasing density and decreasing metallicity”. In: 422, pp. 2246–2254. DOI: [10.1111/j.1365-2966.2012.20767.x](https://doi.org/10.1111/j.1365-2966.2012.20767.x). arXiv: [1202.4755](https://arxiv.org/abs/1202.4755).
- Matsuura, M. et al. (2011). “Herschel Detects a Massive Dust Reservoir in Supernova 1987A”. In: *Science* 333, p. 1258. DOI: [10.1126/science.1205983](https://doi.org/10.1126/science.1205983). arXiv: [1107.1477](https://arxiv.org/abs/1107.1477) [[astro-ph.SR](#)].
- Matsuura, M. et al. (2015). “A Stubbornly Large Mass of Cold Dust in the Ejecta of Supernova 1987A”. In: 800, 50, p. 50. DOI: [10.1088/0004-637X/800/1/50](https://doi.org/10.1088/0004-637X/800/1/50). arXiv: [1411.7381](https://arxiv.org/abs/1411.7381) [[astro-ph.SR](#)].
- Mattila, S. et al. (2010). “Abundances and Density Structure of the Inner Circumstellar Ring Around SN 1987A”. In: 717, pp. 1140–1156. DOI: [10.1088/0004-637X/717/2/1140](https://doi.org/10.1088/0004-637X/717/2/1140). arXiv: [1002.4195](https://arxiv.org/abs/1002.4195) [[astro-ph.SR](#)].
- Mazzali, P. A. and N. N. Chugai (1995). “Barium in SN 1987A and SNe II-P.” In: 303, p. 118.
- Mazzali, P. A., L. B. Lucy, and K. Butler (1992). “Barium and other s-process elements in the early-time spectrum of SN 1987A”. In: 258, pp. 399–411.
- McKee, C. F. (1974). “X-Ray Emission from an Inward-Propagating Shock in Young Supernova Remnants”. In: 188, pp. 335–340. DOI: [10.1086/152721](https://doi.org/10.1086/152721).
- Melena, N. W. et al. (2008). “The Massive Star Content of NGC 3603”. In: 135, pp. 878–891. DOI: [10.1088/0004-6256/135/3/878](https://doi.org/10.1088/0004-6256/135/3/878). arXiv: [0712.2621](https://arxiv.org/abs/0712.2621).
- Menon, A. et al. (2013). “Reproducing the Observed Abundances in RCB and HdC Stars with Post-double-degenerate Merger Models Constraints on Merger and Post-merger Simulations and Physics Processes”. In: 772, 59, p. 59. DOI: [10.1088/0004-637X/772/1/59](https://doi.org/10.1088/0004-637X/772/1/59). arXiv: [1211.3392](https://arxiv.org/abs/1211.3392) [[astro-ph.SR](#)].
- Menon, Athira and Alexander Heger (2017). “The quest for blue supergiants: binary merger models for the evolution of the progenitor of SN 1987A”. In: *Monthly Notices of the Royal Astronomical Society* 469.4, pp. 4649–4664. DOI: [10.1093/mnras/stx818](https://doi.org/10.1093/mnras/stx818). eprint: [/oup/backfile/content_public/journal/mnras/469/4/10.1093_mnras_stx818/1/stx818.pdf](https://oup/backfile/content_public/journal/mnras/469/4/10.1093_mnras_stx818/1/stx818.pdf). URL: [+http://dx.doi.org/10.1093/mnras/stx818](http://dx.doi.org/10.1093/mnras/stx818).
- Menzies, J. W. et al. (1987). “Spectroscopic and photometric observations of SN 1987a - The first 50 days”. In: 227, 39P–49P. DOI: [10.1093/mnras/227.1.39P](https://doi.org/10.1093/mnras/227.1.39P).
- Micelotta, E. R., E. Dwek, and J. D. Slavin (2016). “Dust destruction by the reverse shock in the Cassiopeia A supernova remnant”. In: 590, A65, A65. DOI: [10.1051/0004-6361/201527350](https://doi.org/10.1051/0004-6361/201527350). arXiv: [1602.02754](https://arxiv.org/abs/1602.02754).
- Mihalas, D. and B. W. Mihalas (1984). *Foundations of radiation hydrodynamics*.

- Moe, M. and R. Di Stefano (2013). “The Close Binary Properties of Massive Stars in the Milky Way and Low-metallicity Magellanic Clouds”. In: 778, 95, p. 95. DOI: [10.1088/0004-637X/778/2/95](https://doi.org/10.1088/0004-637X/778/2/95). arXiv: [1309.3532](https://arxiv.org/abs/1309.3532) [[astro-ph.SR](#)].
- (2015). “Early-type Eclipsing Binaries with Intermediate Orbital Periods”. In: 810, 61, p. 61. DOI: [10.1088/0004-637X/810/1/61](https://doi.org/10.1088/0004-637X/810/1/61). arXiv: [1501.03152](https://arxiv.org/abs/1501.03152) [[astro-ph.SR](#)].
- Moll, R. et al. (2014). “Type Ia Supernovae from Merging White Dwarfs. I. Prompt Detonations”. In: 785, 105, p. 105. DOI: [10.1088/0004-637X/785/2/105](https://doi.org/10.1088/0004-637X/785/2/105). arXiv: [1311.5008](https://arxiv.org/abs/1311.5008) [[astro-ph.HE](#)].
- Morozova, V. et al. (2015). “Light Curves of Core-collapse Supernovae with Substantial Mass Loss Using the New Open-source SuperNova Explosion Code (SNEC)”. In: 814, 63, p. 63. DOI: [10.1088/0004-637X/814/1/63](https://doi.org/10.1088/0004-637X/814/1/63). arXiv: [1505.06746](https://arxiv.org/abs/1505.06746) [[astro-ph.HE](#)].
- Morris, T. and P. Podsiadlowski (2006). “Anisotropic mass ejection in binary mergers”. In: 365, pp. 2–10. DOI: [10.1111/j.1365-2966.2005.09645.x](https://doi.org/10.1111/j.1365-2966.2005.09645.x). eprint: [astro-ph/0502288](https://arxiv.org/abs/astro-ph/0502288).
- (2007). “The Triple-Ring Nebula Around SN 1987A: Fingerprint of a Binary Merger”. In: *Science* 315, pp. 1103–. DOI: [10.1126/science.1136351](https://doi.org/10.1126/science.1136351). eprint: [astro-ph/0703317](https://arxiv.org/abs/astro-ph/0703317).
- (2009). “A binary merger model for the formation of the Supernova 1987A triple-ring nebula”. In: 399, pp. 515–538. DOI: [10.1111/j.1365-2966.2009.15114.x](https://doi.org/10.1111/j.1365-2966.2009.15114.x).
- Müller, B. (2017). “The Core-Collapse Supernova Explosion Mechanism”. In: *ArXiv e-prints*. arXiv: [1702.06940](https://arxiv.org/abs/1702.06940) [[astro-ph.SR](#)].
- Müller, B., H.-T. Janka, and A. Heger (2012). “New Two-dimensional Models of Supernova Explosions by the Neutrino-heating Mechanism: Evidence for Different Instability Regimes in Collapsing Stellar Cores”. In: 761, 72, p. 72. DOI: [10.1088/0004-637X/761/1/72](https://doi.org/10.1088/0004-637X/761/1/72). arXiv: [1205.7078](https://arxiv.org/abs/1205.7078) [[astro-ph.SR](#)].
- Nagataki, S., T. M. Shimizu, and K. Sato (1998). “Matter Mixing from Axisymmetric Supernova Explosion”. In: 495, pp. 413–423. DOI: [10.1086/305258](https://doi.org/10.1086/305258). eprint: [astro-ph/9709152](https://arxiv.org/abs/astro-ph/9709152).
- Nelemans, G. and C. A. Tout (2005). “Reconstructing the evolution of white dwarf binaries: further evidence for an alternative algorithm for the outcome of the common-envelope phase in close binaries”. In: 356, pp. 753–764. DOI: [10.1111/j.1365-2966.2004.08496.x](https://doi.org/10.1111/j.1365-2966.2004.08496.x). eprint: [astro-ph/0410301](https://arxiv.org/abs/astro-ph/0410301).
- Nelemans, G. et al. (2000). “Reconstructing the evolution of double helium white dwarfs: envelope loss without spiral-in”. In: 360, pp. 1011–1018. eprint: [astro-ph/0006216](https://arxiv.org/abs/astro-ph/0006216).
- Nelemans, G. et al. (2005). “Binaries discovered by the SPYproject. IV. Five single-lined DA double white dwarfs”. In: 440, pp. 1087–1095. DOI: [10.1051/0004-6361:20053174](https://doi.org/10.1051/0004-6361:20053174). eprint: [astro-ph/0506231](https://arxiv.org/abs/astro-ph/0506231).
- Nieuwenhuijzen, H. and C. de Jager (1990a). “Parametrization of stellar rates of mass loss as functions of the fundamental stellar parameters M, L, and R”. In: 231, pp. 134–136.

- Nieuwenhuijzen, H. and C. de Jager (1990b). “Parametrization of stellar rates of mass loss as functions of the fundamental stellar parameters M, L, and R”. In: 231, pp. 134–136.
- Nomoto, K. et al. (1988). “New developments in theoretical modelling of SN 1987A”. In: *Proceedings of the Astronomical Society of Australia* 7, pp. 490–504.
- O’Keefe, J. A. (1939). “Remarks on Loreta’s Hypothesis Concerning R Coronae Borealis.” In: 90, p. 294. DOI: [10.1086/144107](https://doi.org/10.1086/144107).
- Paczyński, B. (1971). “Evolutionary Processes in Close Binary Systems”. In: 9, p. 183. DOI: [10.1146/annurev.aa.09.090171.001151](https://doi.org/10.1146/annurev.aa.09.090171.001151).
- Paczynski, B. (1976). “Common Envelope Binaries”. In: *Structure and Evolution of Close Binary Systems*. Ed. by P. Eggleton, S. Mitton, and J. Whelan. Vol. 73. IAU Symposium, p. 75.
- Pakmor, R. et al. (2012). “Normal Type Ia Supernovae from Violent Mergers of White Dwarf Binaries”. In: 747, L10, p. L10. DOI: [10.1088/2041-8205/747/1/L10](https://doi.org/10.1088/2041-8205/747/1/L10). arXiv: [1201.5123 \[astro-ph.HE\]](https://arxiv.org/abs/1201.5123).
- Panagia, N. et al. (1996). “On the Nature of the Outer Rings around SN 1987A”. In: 459, p. L17. DOI: [10.1086/309930](https://doi.org/10.1086/309930).
- Pandey, G., D. L. Lambert, and N. Kameswara Rao (2008). “Fluorine in R Coronae Borealis Stars”. In: 674, 1068-1077, pp. 1068–1077. DOI: [10.1086/526492](https://doi.org/10.1086/526492). arXiv: [0711.2363](https://arxiv.org/abs/0711.2363).
- Passy, J.-C. et al. (2011). “Simulations of the Common Envelope Interaction Between a Red Giant Branch Star and Low-Mass Companions”. In: *Evolution of Compact Binaries*. Ed. by L. Schmidtbreick, M. R. Schreiber, and C. Tappert. Vol. 447. Astronomical Society of the Pacific Conference Series, p. 107.
- Pastorello, A. et al. (2005). “SN 1998A: explosion of a blue supergiant”. In: 360, pp. 950–962. DOI: [10.1111/j.1365-2966.2005.09079.x](https://doi.org/10.1111/j.1365-2966.2005.09079.x). eprint: [astro-ph/0504114](https://arxiv.org/abs/astro-ph/0504114).
- Pastorello, A. et al. (2012). “SN 2009E: a faint clone of SN 1987A”. In: 537, A141, A141. DOI: [10.1051/0004-6361/201118112](https://doi.org/10.1051/0004-6361/201118112). arXiv: [1111.2497 \[astro-ph.SR\]](https://arxiv.org/abs/1111.2497).
- Paxton, B. et al. (2015). “Modules for Experiments in Stellar Astrophysics (MESA): Binaries, Pulsations, and Explosions”. In: 220, 15, p. 15. DOI: [10.1088/0067-0049/220/1/15](https://doi.org/10.1088/0067-0049/220/1/15). arXiv: [1506.03146 \[astro-ph.SR\]](https://arxiv.org/abs/1506.03146).
- Penny, L. R. and D. R. Gies (2009). “A FUSE Survey of the Rotation Rates of Very Massive Stars in the Small and Large Magellanic Clouds”. In: 700, pp. 844–858. DOI: [10.1088/0004-637X/700/1/844](https://doi.org/10.1088/0004-637X/700/1/844). arXiv: [0905.3681 \[astro-ph.SR\]](https://arxiv.org/abs/0905.3681).
- Petermann, I. et al. (2015). “Blue supergiants as descendants of magnetic main sequence stars”. In: 584, A54, A54. DOI: [10.1051/0004-6361/201526302](https://doi.org/10.1051/0004-6361/201526302). arXiv: [1509.05805 \[astro-ph.SR\]](https://arxiv.org/abs/1509.05805).
- Phillips, M. M. and S. R. Heathcote (1989). “Satellite emission features in the line profiles of SN 1987A”. In: 101, pp. 137–146. DOI: [10.1086/132414](https://doi.org/10.1086/132414).
- Phillips, M. M. et al. (1988). “An optical spectrophotometric atlas of Supernova 1987A in the LMC. I - The first 130 days”. In: 95, pp. 1087–1110. DOI: [10.1086/114705](https://doi.org/10.1086/114705).

- Pignatari, M. et al. (2013). “Production of Carbon-rich Presolar Grains from Massive Stars”. In: 767, L22, p. L22. DOI: [10.1088/2041-8205/767/2/L22](https://doi.org/10.1088/2041-8205/767/2/L22). arXiv: [1303.3374](https://arxiv.org/abs/1303.3374) [astro-ph.SR].
- Pignatari, M. et al. (2015). “Carbon-rich Presolar Grains from Massive Stars: Subsolar $^{12}\text{C}/^{13}\text{C}$ and $^{14}\text{N}/^{15}\text{N}$ Ratios and the Mystery of ^{15}N ”. In: 808, L43, p. L43. DOI: [10.1088/2041-8205/808/2/L43](https://doi.org/10.1088/2041-8205/808/2/L43). arXiv: [1506.09056](https://arxiv.org/abs/1506.09056) [astro-ph.SR].
- Pignatari, M. et al. (2016). “NuGrid Stellar Data Set. I. Stellar Yields from H to Bi for Stars with Metallicities $Z = 0.02$ and $Z = 0.01$ ”. In: 225, 24, p. 24. DOI: [10.3847/0067-0049/225/2/24](https://doi.org/10.3847/0067-0049/225/2/24). arXiv: [1307.6961](https://arxiv.org/abs/1307.6961) [astro-ph.SR].
- Pinto, P. A. and S. E. Woosley (1988). “X-ray and gamma-ray emission from supernova 1987A”. In: 329, pp. 820–830. DOI: [10.1086/166426](https://doi.org/10.1086/166426).
- Podsiadlowski, P. (1992). “The progenitor of SN 1987 A”. In: 104, pp. 717–729. DOI: [10.1086/133043](https://doi.org/10.1086/133043).
- (2001). “Common-Envelope Evolution and Stellar Mergers”. In: *Evolution of Binary and Multiple Star Systems*. Ed. by P. Podsiadlowski et al. Vol. 229. Astronomical Society of the Pacific Conference Series, p. 239.
- (2008a). “The Evolution of Close Binaries”. In: *RS Ophiuchi (2006) and the Recurrent Nova Phenomenon*. Ed. by A. Evans et al. Vol. 401. Astronomical Society of the Pacific Conference Series, p. 63.
- (2008b). “The Formation of Hydrogen-Deficient Stars in Binaries”. In: *Hydrogen-Deficient Stars*. Ed. by A. Werner and T. Rauch. Vol. 391. Astronomical Society of the Pacific Conference Series, p. 323.
- Podsiadlowski, P. and P. C. Joss (1989). “An alternative binary model for SN1987A”. In: 338, pp. 401–403. DOI: [10.1038/338401a0](https://doi.org/10.1038/338401a0).
- Podsiadlowski, P., P. C. Joss, and J. J. L. Hsu (1992). “Presupernova evolution in massive interacting binaries”. In: 391, pp. 246–264. DOI: [10.1086/171341](https://doi.org/10.1086/171341).
- Podsiadlowski, P., P. C. Joss, and S. Rappaport (1990). “A merger model for SN 1987 A”. In: 227, pp. L9–L12.
- Podsiadlowski, P., T. S. Morris, and N. Ivanova (2006). “Massive Binary Mergers: A Unique Scenario for the sgB[e] Phenomenon?” In: *Stars with the B[e] Phenomenon*. Ed. by M. Kraus and A. S. Miroshnichenko. Vol. 355. Astronomical Society of the Pacific Conference Series, p. 259.
- (2007). “The progenitor of SN 1987A”. In: *Supernova 1987A: 20 Years After: Supernovae and Gamma-Ray Bursters*. Ed. by S. Immler, K. Weiler, and R. McCray. Vol. 937. American Institute of Physics Conference Series, pp. 125–133. DOI: [10.1063/1.3682893](https://doi.org/10.1063/1.3682893).
- Pollard, K. R., P. L. Cottrell, and W. A. Lawson (1994). “An Abundance Analysis of R-Coronae Stars in the Galaxy and the Large Magellanic Cloud”. In: 268, p. 544. DOI: [10.1093/mnras/268.2.544](https://doi.org/10.1093/mnras/268.2.544).

- Portegies Zwart, S. F. and E. P. J. van den Heuvel (2016). “Was the nineteenth century giant eruption of Eta Carinae a merger event in a triple system?” In: 456, pp. 3401–3412. DOI: [10.1093/mnras/stv2787](https://doi.org/10.1093/mnras/stv2787). arXiv: [1511.06889](https://arxiv.org/abs/1511.06889) [[astro-ph.SR](#)].
- Potekhin, A. Y. et al. (2006). “Nonideal strongly magnetized plasmas of neutron stars and their electromagnetic radiation”. In: *Journal of Physics A Mathematical General* 39, pp. 4453–4458. DOI: [10.1088/0305-4470/39/17/S21](https://doi.org/10.1088/0305-4470/39/17/S21). eprint: [astro-ph/0512088](https://arxiv.org/abs/astro-ph/0512088).
- Poveda, A., C. Allen, and L. Parrao (1982). “Statistical studies of visual double and multiple stars. I - Incompleteness of the IDS, intrinsic fraction of visual doubles and multiples, and number of optical systems”. In: 258, pp. 589–604. DOI: [10.1086/160110](https://doi.org/10.1086/160110).
- Puls, J., J. S. Vink, and F. Najarro (2008). “Mass loss from hot massive stars”. In: 16, pp. 209–325. DOI: [10.1007/s00159-008-0015-8](https://doi.org/10.1007/s00159-008-0015-8). arXiv: [0811.0487](https://arxiv.org/abs/0811.0487).
- Raghavan, D. et al. (2010). “A Survey of Stellar Families: Multiplicity of Solar-type Stars”. In: 190, pp. 1–42. DOI: [10.1088/0067-0049/190/1/1](https://doi.org/10.1088/0067-0049/190/1/1). arXiv: [1007.0414](https://arxiv.org/abs/1007.0414) [[astro-ph.SR](#)].
- Rao, N. K. (2005). “Surface Compositions of R Coronae Borealis Stars and Extreme Helium Stars – Some Connections”. In: *Cosmic Abundances as Records of Stellar Evolution and Nucleosynthesis*. Ed. by T. G. Barnes III and F. N. Bash. Vol. 336. Astronomical Society of the Pacific Conference Series, p. 185. eprint: [astro-ph/0410648](https://arxiv.org/abs/astro-ph/0410648).
- Rao, N. K. and D. L. Lambert (1996). “Surface composition of the RCB stars - refinement of a few mere facts”. In: *Hydrogen Deficient Stars*. Ed. by C. S. Jeffery and U. Heber. Vol. 96. Astronomical Society of the Pacific Conference Series, p. 43.
- (2008). “High-resolution spectroscopy of the R Coronae Borealis star V Coronae Australis”. In: 384, pp. 477–488. DOI: [10.1111/j.1365-2966.2007.12643.x](https://doi.org/10.1111/j.1365-2966.2007.12643.x). arXiv: [0710.5030](https://arxiv.org/abs/0710.5030).
- Raskin, C. et al. (2012). “Remnants of Binary White Dwarf Mergers”. In: 746, 62, p. 62. DOI: [10.1088/0004-637X/746/1/62](https://doi.org/10.1088/0004-637X/746/1/62). arXiv: [1112.1420](https://arxiv.org/abs/1112.1420) [[astro-ph.HE](#)].
- Rauscher, T. et al. (2002). “Nucleosynthesis in Massive Stars with Improved Nuclear and Stellar Physics”. In: 576, pp. 323–348. DOI: [10.1086/341728](https://doi.org/10.1086/341728). eprint: [astro-ph/0112478](https://arxiv.org/abs/astro-ph/0112478).
- Reipurth, B. et al. (2014). “Multiplicity in Early Stellar Evolution”. In: *Protostars and Planets VI*, pp. 267–290. DOI: [10.2458/azu_uapress_9780816531240-ch012](https://doi.org/10.2458/azu_uapress_9780816531240-ch012). arXiv: [1403.1907](https://arxiv.org/abs/1403.1907) [[astro-ph.SR](#)].
- Renzini, A. (1990). “Evolutionary scenarios for R CrB stars”. In: *Confrontation Between Stellar Pulsation and Evolution*. Ed. by C. Cacciari and G. Clementini. Vol. 11. Astronomical Society of the Pacific Conference Series, pp. 549–556.
- Ritter, Christian (in press).
- Rose, W. K. (1998). *Advanced Stellar Astrophysics*, p. 494.
- Ryan, S. G. and A. J. Norton (2010). *Stellar Evolution and Nucleosynthesis*.

- Sadavoy, S. I. and S. W. Stahler (2017). “Embedded binaries and their dense cores”. In: 469, pp. 3881–3900. DOI: [10.1093/mnras/stx1061](https://doi.org/10.1093/mnras/stx1061). arXiv: [1705.00049](https://arxiv.org/abs/1705.00049) [astro-ph.SR].
- Saio, H. (2008). “Radial and Nonradial Pulsations in RCB and EHe-B Stars”. In: *Hydrogen-Deficient Stars*. Ed. by A. Werner and T. Rauch. Vol. 391. Astronomical Society of the Pacific Conference Series, p. 69.
- Saio, H. and C. S. Jeffery (2002). “Merged binary white dwarf evolution: rapidly accreting carbon-oxygen white dwarfs and the progeny of extreme helium stars”. In: 333, pp. 121–132. DOI: [10.1046/j.1365-8711.2002.05384.x](https://doi.org/10.1046/j.1365-8711.2002.05384.x).
- Saio, H., K. Nomoto, and M. Kato (1988). “Why did the progenitor of SN 1987A undergo the blue-red-blue evolution?” In: 331, pp. 388–393. DOI: [10.1086/166565](https://doi.org/10.1086/166565).
- Sana, H., E. Gosset, and C. J. Evans (2009). “The massive star binary fraction in young open clusters - II. NGC6611 (Eagle Nebula)”. In: 400, pp. 1479–1492. DOI: [10.1111/j.1365-2966.2009.15545.x](https://doi.org/10.1111/j.1365-2966.2009.15545.x). arXiv: [0909.0486](https://arxiv.org/abs/0909.0486) [astro-ph.SR].
- Sana, H. et al. (2012). “Binary Interaction Dominates the Evolution of Massive Stars”. In: *Science* 337, pp. 444–. DOI: [10.1126/science.1223344](https://doi.org/10.1126/science.1223344). arXiv: [1207.6397](https://arxiv.org/abs/1207.6397) [astro-ph.SR].
- Sana, H. et al. (2013). “The VLT-FLAMES Tarantula Survey. VIII. Multiplicity properties of the O-type star population”. In: 550, A107, A107. DOI: [10.1051/0004-6361/201219621](https://doi.org/10.1051/0004-6361/201219621). arXiv: [1209.4638](https://arxiv.org/abs/1209.4638) [astro-ph.SR].
- Sarangi, A. and I. Cherchneff (2013). “The Chemically Controlled Synthesis of Dust in Type II-P Supernovae”. In: 776, 107, p. 107. DOI: [10.1088/0004-637X/776/2/107](https://doi.org/10.1088/0004-637X/776/2/107). arXiv: [1309.5887](https://arxiv.org/abs/1309.5887) [astro-ph.SR].
- Schoenberner, D. (1983). “Late stages of stellar evolution. II - Mass loss and the transition of asymptotic giant branch stars into hot remnants”. In: 272, pp. 708–714. DOI: [10.1086/161333](https://doi.org/10.1086/161333).
- Schreiber, M. R. et al. (2009). “White dwarf post common envelope binaries from the SDSS”. In: *Journal of Physics Conference Series*. Vol. 172. Journal of Physics Conference Series, p. 012024. DOI: [10.1088/1742-6596/172/1/012024](https://doi.org/10.1088/1742-6596/172/1/012024).
- Schwab, J. et al. (2012). “The viscous evolution of white dwarf merger remnants”. In: 427, pp. 190–203. DOI: [10.1111/j.1365-2966.2012.21993.x](https://doi.org/10.1111/j.1365-2966.2012.21993.x). arXiv: [1207.0512](https://arxiv.org/abs/1207.0512) [astro-ph.HE].
- Searle, L. (1961). “An Abundance Analysis of R Coronae Borealis.” In: 133, p. 531. DOI: [10.1086/147056](https://doi.org/10.1086/147056).
- Shen, K. J. et al. (2012). “The Long-term Evolution of Double White Dwarf Mergers”. In: 748, 35, p. 35. DOI: [10.1088/0004-637X/748/1/35](https://doi.org/10.1088/0004-637X/748/1/35). arXiv: [1108.4036](https://arxiv.org/abs/1108.4036) [astro-ph.HE].
- Shigeyama, T. and K. Nomoto (1990). “Theoretical light curve of SN 1987A and mixing of hydrogen and nickel in the ejecta”. In: 360, pp. 242–256. DOI: [10.1086/169114](https://doi.org/10.1086/169114).
- Sibthorpe, B. et al. (2010). “AKARI and BLAST Observations of the Cassiopeia A Supernova Remnant and Surrounding Interstellar Medium”. In: 719, pp. 1553–1564. DOI: [10.1088/0004-637X/719/2/1553](https://doi.org/10.1088/0004-637X/719/2/1553). arXiv: [0910.1094](https://arxiv.org/abs/0910.1094) [astro-ph.HE].

- Smartt, S. J. (2009). “Progenitors of Core-Collapse Supernovae”. In: 47, pp. 63–106. DOI: [10.1146/annurev-astro-082708-101737](https://doi.org/10.1146/annurev-astro-082708-101737). arXiv: [0908.0700](https://arxiv.org/abs/0908.0700) [astro-ph.SR].
- Smartt, S. J. et al. (2002). “The evolutionary status of Sher 25 - implications for blue supergiants and the progenitor of SN 1987A”. In: 391, pp. 979–991. DOI: [10.1051/0004-6361:20020829](https://doi.org/10.1051/0004-6361:20020829). eprint: [astro-ph/0205242](https://arxiv.org/abs/astro-ph/0205242).
- Smartt, S. J. et al. (2009). “The death of massive stars - I. Observational constraints on the progenitors of Type II-P supernovae”. In: 395, pp. 1409–1437. DOI: [10.1111/j.1365-2966.2009.14506.x](https://doi.org/10.1111/j.1365-2966.2009.14506.x). arXiv: [0809.0403](https://arxiv.org/abs/0809.0403).
- Smith, L. J. et al. (1998). “Ejected Nebulae as Probes of the Evolution of Massive Stars in the Large Magellanic Cloud”. In: 503, pp. 278–296. DOI: [10.1086/305980](https://doi.org/10.1086/305980).
- Smith, N. (2007). “Discovery of a Nearby Twin of SN 1987A’s Nebula around the Luminous Blue Variable HD 168625: Was Sk -69 202 an LBV?” In: 133, pp. 1034–1040. DOI: [10.1086/510838](https://doi.org/10.1086/510838). eprint: [astro-ph/0611544](https://arxiv.org/abs/astro-ph/0611544).
- (2014). “Mass Loss: Its Effect on the Evolution and Fate of High-Mass Stars”. In: 52, pp. 487–528. DOI: [10.1146/annurev-astro-081913-040025](https://doi.org/10.1146/annurev-astro-081913-040025). arXiv: [1402.1237](https://arxiv.org/abs/1402.1237) [astro-ph.SR].
- Smith, N., J. Bally, and J. Walawender (2007). “And in the Darkness Bind Them: Equatorial Rings, B[e] Supergiants, and the Waists of Bipolar Nebulae”. In: 134, pp. 846–859. DOI: [10.1086/518563](https://doi.org/10.1086/518563). arXiv: [0705.3054](https://arxiv.org/abs/0705.3054).
- Smith, N. et al. (2013). “The ring nebula around the blue supergiant SBW1: pre-explosion snapshot of an SN 1987A twin”. In: 429, pp. 1324–1341. DOI: [10.1093/mnras/sts418](https://doi.org/10.1093/mnras/sts418). arXiv: [1211.4612](https://arxiv.org/abs/1211.4612) [astro-ph.SR].
- Solheim, J.-E. (2010). “AM CVn Stars: Status and Challenges”. In: 122, p. 1133. DOI: [10.1086/656680](https://doi.org/10.1086/656680).
- Sonneborn, G., B. Altner, and R. P. Kirshner (1987). “The progenitor of SN 1987A - Spatially resolved ultraviolet spectroscopy of the supernova field”. In: 323, pp. L35–L39. DOI: [10.1086/185052](https://doi.org/10.1086/185052).
- Sonneborn, G. et al. (1997). “The Evolution of Ultraviolet Emission Lines From Circumstellar Material Surrounding SN 1987A”. In: 477, pp. 848–864. eprint: [astro-ph/9610021](https://arxiv.org/abs/astro-ph/9610021).
- Spruit, H. C. (2004). “Angular Momentum Transport and Mixing by Magnetic Fields (Invited Review)”. In: *Stellar Rotation*. Ed. by A. Maeder and P. Eenens. Vol. 215. IAU Symposium, p. 356.
- Staff, J. E. et al. (2012). “Do R Coronae Borealis Stars Form from Double White Dwarf Mergers?” In: 757, 76, p. 76. DOI: [10.1088/0004-637X/757/1/76](https://doi.org/10.1088/0004-637X/757/1/76). arXiv: [1208.0732](https://arxiv.org/abs/1208.0732) [astro-ph.SR].
- Sugerman, B. E. K. et al. (2005a). “A New View of the Circumstellar Environment of SN 1987A”. In: 627, pp. 888–903. DOI: [10.1086/430396](https://doi.org/10.1086/430396). eprint: [astro-ph/0502268](https://arxiv.org/abs/astro-ph/0502268).
- (2005b). “The Three-dimensional Circumstellar Environment of SN 1987A”. In: 159, pp. 60–99. DOI: [10.1086/430408](https://doi.org/10.1086/430408). eprint: [astro-ph/0502378](https://arxiv.org/abs/astro-ph/0502378).

- Sukhbold, T. et al. (2016). “Core-collapse Supernovae from 9 to 120 Solar Masses Based on Neutrino-powered Explosions”. In: 821, 38, p. 38. DOI: [10.3847/0004-637X/821/1/38](https://doi.org/10.3847/0004-637X/821/1/38). arXiv: [1510.04643](https://arxiv.org/abs/1510.04643) [astro-ph.HE].
- Sutherland, R. S. (1998). “Accurate free-free Gaunt factors for astrophysical plasmas”. In: 300, pp. 321–330. DOI: [10.1046/j.1365-8711.1998.01687.x](https://doi.org/10.1046/j.1365-8711.1998.01687.x).
- Sutherland, R. S. and M. A. Dopita (1993). “Cooling functions for low-density astrophysical plasmas”. In: 88, pp. 253–327. DOI: [10.1086/191823](https://doi.org/10.1086/191823).
- Taddia, F. et al. (2012). “The Type II supernovae 2006V and 2006au: two SN 1987A-like events”. In: 537, A140, A140. DOI: [10.1051/0004-6361/201118091](https://doi.org/10.1051/0004-6361/201118091). arXiv: [1111.2509](https://arxiv.org/abs/1111.2509).
- Taddia, F. et al. (2013). “A metallicity study of 1987A-like supernova host galaxies”. In: 558, A143, A143. DOI: [10.1051/0004-6361/201322276](https://doi.org/10.1051/0004-6361/201322276). arXiv: [1308.5545](https://arxiv.org/abs/1308.5545).
- Tang, S. et al. (2013). “R Coronae Borealis Stars in M31 from the Palomar Transient Factory”. In: 767, L23, p. L23. DOI: [10.1088/2041-8205/767/2/L23](https://doi.org/10.1088/2041-8205/767/2/L23). arXiv: [1303.1820](https://arxiv.org/abs/1303.1820) [astro-ph.SR].
- Teachout, R. R. and R. T. Pack (1971). “The Static Dipole Polarizabilities of All the Neutral Atoms in Their Ground States”. In: *Atomic Data* 3, p. 195. DOI: [10.1016/S0092-640X\(71\)80007-4](https://doi.org/10.1016/S0092-640X(71)80007-4).
- Temim, T. and E. Dwek (2013). “The Importance of Physical Models for Deriving Dust Masses and Grain Size Distributions in Supernova Ejecta. I. Radiatively Heated Dust in the Crab Nebula”. In: 774, 8, p. 8. DOI: [10.1088/0004-637X/774/1/8](https://doi.org/10.1088/0004-637X/774/1/8). arXiv: [1302.5452](https://arxiv.org/abs/1302.5452).
- Thimm, G. J., R. W. Hanuschik, and T. Schmidt-Kaler (1989). “The H-alpha flux in SN 1987A during the first 111 D”. In: 238, 15P–23P. DOI: [10.1093/mnras/238.1.15P](https://doi.org/10.1093/mnras/238.1.15P).
- Tisserand, P. et al. (2008). “R Coronae Borealis stars in the Galactic bulge discovered by EROS-2”. In: 481, pp. 673–690. DOI: [10.1051/0004-6361:20078814](https://doi.org/10.1051/0004-6361:20078814). arXiv: [0801.1680](https://arxiv.org/abs/0801.1680).
- Tisserand, P. et al. (2013). “The ongoing pursuit of R Coronae Borealis stars: the ASAS-3 survey strikes again”. In: 551, A77, A77. DOI: [10.1051/0004-6361/201220713](https://doi.org/10.1051/0004-6361/201220713). arXiv: [1211.2475](https://arxiv.org/abs/1211.2475) [astro-ph.SR].
- Todini, P. and A. Ferrara (2001). “Dust formation in primordial Type II supernovae”. In: 325, pp. 726–736. DOI: [10.1046/j.1365-8711.2001.04486.x](https://doi.org/10.1046/j.1365-8711.2001.04486.x). eprint: [astro-ph/0009176](https://arxiv.org/abs/astro-ph/0009176).
- Travaglio, C. et al. (1999). “Low-Density Graphite Grains and Mixing in Type II Supernovae”. In: 510, pp. 325–354. DOI: [10.1086/306551](https://doi.org/10.1086/306551).
- Tremblay, P.-E. et al. (2016). “The field white dwarf mass distribution”. In: 461, pp. 2100–2114. DOI: [10.1093/mnras/stw1447](https://doi.org/10.1093/mnras/stw1447). arXiv: [1606.05292](https://arxiv.org/abs/1606.05292) [astro-ph.SR].
- Ugliko, M. et al. (2012). “Progenitor-explosion Connection and Remnant Birth Masses for Neutrino-driven Supernovae of Iron-core Progenitors”. In: 757, 69, p. 69. DOI: [10.1088/0004-637X/757/1/69](https://doi.org/10.1088/0004-637X/757/1/69). arXiv: [1205.3657](https://arxiv.org/abs/1205.3657) [astro-ph.SR].

- Utrobin, V. (1993). “Hydrodynamic study of supernova 1987A - Near the peak luminosity”. In: 270, pp. 249–258.
- Utrobin, V. P. (2004). “The Light Curve of Supernova 1987A: The Structure of the Presupernova and Radioactive Nickel Mixing”. In: *Astronomy Letters* 30, pp. 293–308. DOI: [10.1134/1.1738152](https://doi.org/10.1134/1.1738152). eprint: [astro-ph/0406410](https://arxiv.org/abs/astro-ph/0406410).
- (2005). “Supernova 1987A: The Envelope Mass and the Explosion Energy”. In: *Astronomy Letters* 31, pp. 806–815. DOI: [10.1134/1.2138767](https://doi.org/10.1134/1.2138767).
- (2007). “An optimal hydrodynamic model for the normal type IIP supernova 1999em”. In: 461, pp. 233–251. DOI: [10.1051/0004-6361:20066078](https://doi.org/10.1051/0004-6361:20066078). eprint: [arXiv:astro-ph/0609642](https://arxiv.org/abs/astro-ph/0609642).
- Utrobin, V. P. and N. N. Chugai (2011). “Supernova 2000cb: high-energy version of SN 1987A”. In: 532, A100, A100. DOI: [10.1051/0004-6361/201117137](https://doi.org/10.1051/0004-6361/201117137). arXiv: [1107.2145](https://arxiv.org/abs/1107.2145) [[astro-ph.SR](https://arxiv.org/abs/1107.2145)].
- Utrobin, V. P., N. N. Chugai, and A. A. Andronova (1995). “Asymmetry of SN 1987A: Fast Ni-56 clump”. In: 295, pp. 129–135.
- Utrobin, V. P. et al. (2015). “Supernova 1987A: neutrino-driven explosions in three dimensions and light curves”. In: 581, A40, A40. DOI: [10.1051/0004-6361/201425513](https://doi.org/10.1051/0004-6361/201425513). arXiv: [1412.4122](https://arxiv.org/abs/1412.4122) [[astro-ph.SR](https://arxiv.org/abs/1412.4122)].
- van den Heuvel, E. P. J. (2002). “Evolutionary concepts of binaries with compact objects”. In: *The Century of Space Science, Volume I*. Ed. by J. A. Bleeker, J. Geiss, and M. C. E. Huber. Kluwer Academic Publishers, p. 759.
- Vanbeveren, D., C. De Loore, and W. Van Rensbergen (1998). “Massive stars”. In: 9, pp. 63–152. DOI: [10.1007/s001590050015](https://doi.org/10.1007/s001590050015).
- Vanbeveren, D. et al. (2013). “Blue supergiant progenitor models of type II supernovae”. In: 552, A105, A105. DOI: [10.1051/0004-6361/201321072](https://doi.org/10.1051/0004-6361/201321072). arXiv: [1212.4285](https://arxiv.org/abs/1212.4285) [[astro-ph.SR](https://arxiv.org/abs/1212.4285)].
- Verner, D. A. and D. G. Yakovlev (1995). “Analytic FITS for partial photoionization cross sections.” In: 109, pp. 125–133.
- Verner, D. A. et al. (1996). “Atomic Data for Astrophysics. II. New Analytic FITS for Photoionization Cross Sections of Atoms and Ions”. In: 465, p. 487. DOI: [10.1086/177435](https://doi.org/10.1086/177435). eprint: [arXiv:astro-ph/9601009](https://arxiv.org/abs/astro-ph/9601009).
- Vink, J. S. and A. de Koter (2005). “On the metallicity dependence of Wolf-Rayet winds”. In: 442, pp. 587–596. DOI: [10.1051/0004-6361:20052862](https://doi.org/10.1051/0004-6361:20052862). eprint: [astro-ph/0507352](https://arxiv.org/abs/astro-ph/0507352).
- Vink, J. S., A. de Koter, and H. J. G. L. M. Lamers (2000). “New theoretical mass-loss rates of O and B stars”. In: 362, pp. 295–309. eprint: [astro-ph/0008183](https://arxiv.org/abs/astro-ph/0008183).
- (2001). “Mass-loss predictions for O and B stars as a function of metallicity”. In: 369, pp. 574–588. DOI: [10.1051/0004-6361:20010127](https://doi.org/10.1051/0004-6361:20010127). eprint: [astro-ph/0101509](https://arxiv.org/abs/astro-ph/0101509).

- Voronov, G. S. (1997). "A Practical Fit Formula for Ionization Rate Coefficients of Atoms and Ions by Electron Impact: $Z = 1-28$ ". In: *Atomic Data and Nuclear Data Tables* 65, p. 1. DOI: [10.1006/adnd.1997.0732](https://doi.org/10.1006/adnd.1997.0732).
- Walborn, N. R. et al. (1987). "The composite image of Sanduleak -69 deg 202, candidate precursor to supernova 1987 A in the Large Magellanic Cloud". In: 321, pp. L41–L44. DOI: [10.1086/185002](https://doi.org/10.1086/185002).
- Walborn, N. R. et al. (1989). "The spectrograms of Sanduleak -69.202 deg, precursor to supernova 1987A in the Large Magellanic Cloud". In: 219, pp. 229–236.
- Wampler, E. J. et al. (1990). "Observations of the nebulosities near SN 1987A". In: 362, pp. L13–L16. DOI: [10.1086/185836](https://doi.org/10.1086/185836).
- Warner, B. (1967). "The hydrogen-deficient carbon stars". In: 137, p. 119. DOI: [10.1093/mnras/137.2.119](https://doi.org/10.1093/mnras/137.2.119).
- Weaver, T. A., G. B. Zimmerman, and S. E. Woosley (1978). "Presupernova evolution of massive stars". In: 225, pp. 1021–1029. DOI: [10.1086/156569](https://doi.org/10.1086/156569).
- Webbink, R. F. (1984). "Double white dwarfs as progenitors of R Coronae Borealis stars and Type I supernovae". In: 277, pp. 355–360. DOI: [10.1086/161701](https://doi.org/10.1086/161701).
- Weiss, A., W. Hillebrandt, and J. W. Truran (1988). "Rotation-induced mixing and the nitrogen abundance in SN 1987A". In: 197, pp. L11–L14.
- Werner, K. and F. Herwig (2006). "The Elemental Abundances in Bare Planetary Nebula Central Stars and the Shell Burning in AGB Stars". In: 118, pp. 183–204. DOI: [10.1086/500443](https://doi.org/10.1086/500443). eprint: [astro-ph/0512320](https://arxiv.org/abs/astro-ph/0512320).
- Weymann, R. (1966). "The Energy Spectrum of Radiation in the Expanding Universe". In: 145, p. 560. DOI: [10.1086/148795](https://doi.org/10.1086/148795).
- Willems, B. and U. Kolb (2004). "Detached white dwarf main-sequence star binaries". In: 419, pp. 1057–1076. DOI: [10.1051/0004-6361:20040085](https://doi.org/10.1051/0004-6361:20040085). eprint: [astro-ph/0403090](https://arxiv.org/abs/astro-ph/0403090).
- Williams, A. et al. (1998). "Supernova 1998A in IC 2627". In: 6805.
- Willson, L. A. (2000). "Mass Loss From Cool Stars: Impact on the Evolution of Stars and Stellar Populations". In: 38, pp. 573–611. DOI: [10.1146/annurev.astro.38.1.573](https://doi.org/10.1146/annurev.astro.38.1.573).
- Wishart, A. W. (1979). "The bound-free photo-detachment cross-section of H-". In: 187, 59P–61P.
- Woitke, P., A. Goeres, and E. Sedlmayr (1996). "On the gas temperature in the shocked circumstellar envelopes of pulsating stars. II. Shock induced condensation around R Coronae Borealis stars." In: 313, pp. 217–228.
- Wongwathanarat, A., E. Müller, and H.-T. Janka (2015). "Three-dimensional simulations of core-collapse supernovae: from shock revival to shock breakout". In: 577, A48, A48. DOI: [10.1051/0004-6361/201425025](https://doi.org/10.1051/0004-6361/201425025). arXiv: [1409.5431 \[astro-ph.HE\]](https://arxiv.org/abs/1409.5431).
- Wood, P. R. (1988). "The progenitor star and its evolution". In: *Proceedings of the Astronomical Society of Australia* 7, pp. 386–389.

- Woodings, S. J. et al. (1998). “Light curves of SN 1998A and comparison with similar unusual SNe”. In: 301, pp. L5–L9. DOI: [10.1046/j.1365-8711.1998.02120.x](https://doi.org/10.1046/j.1365-8711.1998.02120.x).
- Woosley, S. E. (1988). “SN 1987A - After the peak”. In: 330, pp. 218–253. DOI: [10.1086/166468](https://doi.org/10.1086/166468).
- Woosley, S. E. and A. Heger (2007). “Nucleosynthesis and remnants in massive stars of solar metallicity”. In: 442, pp. 269–283. DOI: [10.1016/j.physrep.2007.02.009](https://doi.org/10.1016/j.physrep.2007.02.009). eprint: [astro-ph/0702176](https://arxiv.org/abs/astro-ph/0702176).
- Woosley, S. E., A. Heger, and T. A. Weaver (2002). “The evolution and explosion of massive stars”. In: *Reviews of Modern Physics* 74, pp. 1015–1071. DOI: [10.1103/RevModPhys.74.1015](https://doi.org/10.1103/RevModPhys.74.1015).
- Woosley, S. E., P. A. Pinto, and T. A. Weaver (1988). “Recent results on SN 1987A”. In: *Proceedings of the Astronomical Society of Australia* 7, pp. 355–370.
- Woosley, S. E. et al. (1997). “SN 1987A - Presupernova Evolution and the Progenitor Star”. In: *ArXiv Astrophysics e-prints*. eprint: [astro-ph/9705146](https://arxiv.org/abs/astro-ph/9705146).
- Woosley, S.E. (2012). *Supernovae: The Tenth Santa Cruz Workshop in Astronomy and Astrophysics, July 9 to 21, 1989, Lick Observatory*. Santa Cruz Summer Workshops in Astronomy and Astrophysics. Springer New York. ISBN: 9781461229889. URL: <https://books.google.co.in/books?id=TRnSBwAAQBAJ>.
- Yamada, S. and K. Sato (1991). “Rayleigh-Taylor instability in the asymmetric supernova explosion”. In: 382, pp. 594–602. DOI: [10.1086/170746](https://doi.org/10.1086/170746).
- Yoshida, T. (2007). “Supernova Mixtures Reproducing Isotopic Ratios of Presolar Grains”. In: 666, pp. 1048–1068. DOI: [10.1086/520631](https://doi.org/10.1086/520631).
- Yoshida, T., H. Umeda, and K. Nomoto (2005). “Si Isotopic Ratios in Supernovae for Presolar Grains”. In: 631, pp. 1039–1050. DOI: [10.1086/432654](https://doi.org/10.1086/432654).
- Young, T. R. (2004). “A Parameter Study of Type II Supernova Light Curves Using 6 M_{solar} He Cores”. In: 617, pp. 1233–1250. DOI: [10.1086/425675](https://doi.org/10.1086/425675). eprint: [astro-ph/0409284](https://arxiv.org/abs/astro-ph/0409284).
- Zhang, X. et al. (2014). “Post-merger evolution of carbon-oxygen + helium white dwarf binaries and the origin of R Coronae Borealis and extreme helium stars”. In: 445, pp. 660–673. DOI: [10.1093/mnras/stu1741](https://doi.org/10.1093/mnras/stu1741). arXiv: [1408.5500 \[astro-ph.SR\]](https://arxiv.org/abs/1408.5500).
- Zinner, E. (2014). “Presolar Grains”. In: *Meteorites and Cosmochemical Processes*. Ed. by A. M. Davis, pp. 181–213.